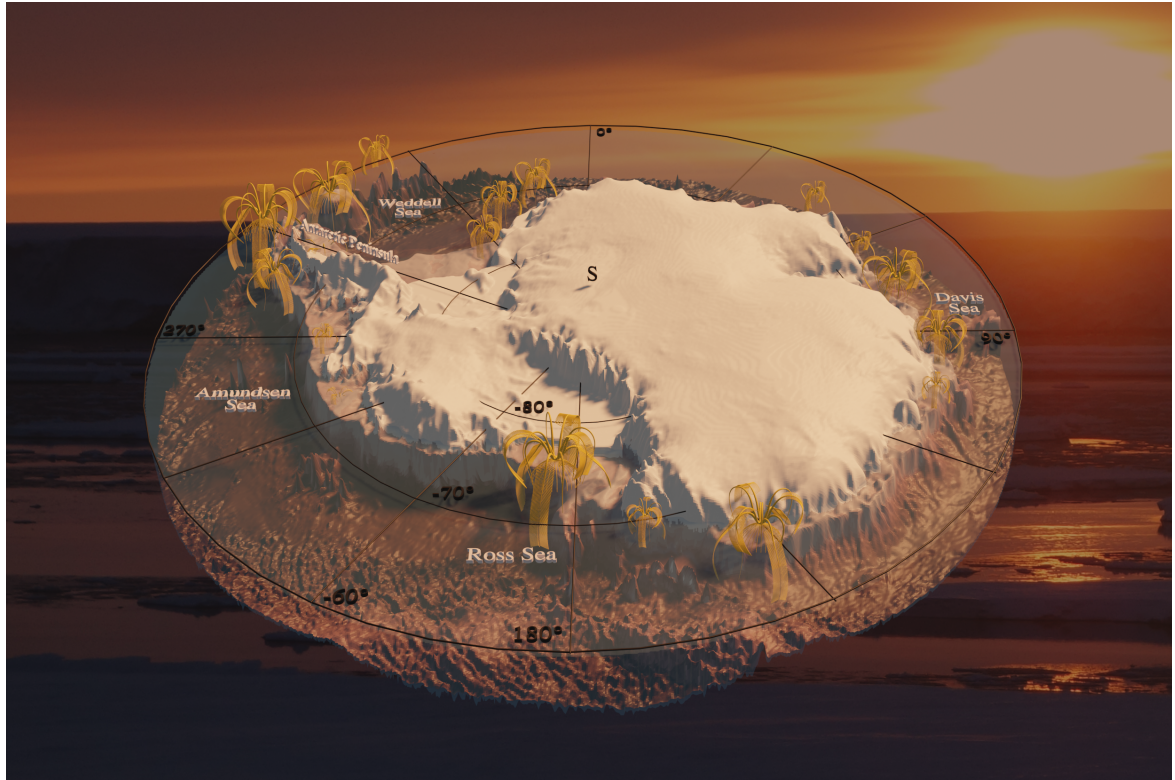


A computational approach of locomotion, energy demand and dispersal of the common comatulid crinoid *Promachocrinus kerguelensis* (Echinodermata) and its circum-Antarctic success



Von der Fakultät für Mathematik und Naturwissenschaften der Carl von Ossietzky Universität Oldenburg zur Erlangung des Grades und Titels eines

Doctor rerum naturalium

Dr. rer. nat.

angenommene Dissertation
von Herrn Nils Owsianowski
geboren am 24.09.1976 in Berlin

Erstgutachter: Prof. Dr. Julian Gutt

Zweitgutachter: Prof. Dr. Pedro Martínez Arbizu

Weitere Gutachterinnen und Gutachter:

Prof. Dr. Antonia B. Kesel

Prof. Dr. Dirk Carl Albach

Tag der Disputation: 21.12.2021

Selbstständigkeitserklärung

Hiermit erkläre ich, dass ich die vorliegende Arbeit selbstständig und ohne fremde Hilfe verfasst und keine anderen Hilfsmittel als die angegebenen verwendet habe. Die Dissertation hat weder in ihrer Gesamtheit noch in Teilen einer anderen wissenschaftlichen Hochschule zur Begutachtung in einem Promotionsverfahren vorgelegen. Des Weiteren erkläre ich hiermit, dass mir die Leitlinien guter wissenschaftlicher Praxis der Carl von Ossietzky Universität Oldenburg bekannt sind und von mir befolgt wurden. Außerdem habe ich keine kommerzielle Vermittlungs- oder Beratungsdienste (Promotionsberatung) im Zusammenhang mit dem Promotionsvorhaben in Anspruch genommen.

Insbesondere versichere ich, dass ich alle wörtlichen und sinngemäßen Übernahmen aus anderen Werken als solche kenntlich gemacht habe.

(Ort, Datum)

(Unterschrift)

CONTENTS

Contents	I
List of Figures	V
List of Tables	VII
Nomenclature	IX
Zusammenfassung	1
1 Abstract	3
2 Introduction	5
3 Additional Background Information	11
3.1 Crinoid’s Morphology	11
3.2 Crinoid’s Locomotion	13
3.3 Biological Fluid Dynamics	15
3.4 Inverse Dynamics	18
3.4.1 Kinematics	18
3.4.2 Anthropometry	19
3.4.3 Moment of Inertia	19
3.4.4 Added Mass	19
3.4.5 Work, Power, and Energy	20
3.5 Dispersal	22
4 Methodology	27
4.1 Morphology and the Virtual Design	27
4.1.1 Brachials	27
4.1.2 Pinnule segments	27
4.1.3 Calyx, Primibrachials and Cirri	29
4.1.4 Density, Mass and Weight in Water	30
4.2 Locomotion Kinematics	33
4.2.1 Image Scaling and Rectification of the Perspective Viewing Angle	34
4.2.2 Deriving an Averaged Kinematic Model	41
4.2.3 Pinnule Pose	43
4.3 Analytical Fluid Dynamics	46
4.3.1 Fluid Properties of Seawater	46
4.3.2 Thrust from Drag	48
4.3.3 Drag Coefficient	50
4.3.4 Drag Force	50

4.3.5	Brachial Motion	51
4.3.6	Pinnule Motion	51
4.3.7	Body Drag	52
4.3.8	Total Forces of Swimming Crinoid	53
4.3.9	The Iterative Process of the Locomotion Parameters (Speed and Weight)	54
4.4	Inverse Dynamics	59
4.4.1	Added Mass	62
4.4.2	Moment of Inertia	63
4.5	Work, Energy, and Power	64
4.6	Maximum Range Velocity (MRV)	64
4.7	Environment and Boundaries	69
4.7.1	Net Primary Production <i>NPP</i>	71
4.7.2	Energy Flux from the Surface to the Seafloor	76
4.7.3	Tide	77
4.8	Dispersal	79
4.8.1	Dispersal by Reproduction	79
4.8.2	Dispersal and the Migration Model	81
5	Results	87
5.1	Morphological-Physiological Computer Model	87
5.2	Locomotion Kinematics	91
5.3	Fluid Dynamics	98
5.3.1	Weight and Payload	104
5.4	Inverse Dynamics	106
5.5	Energetics: Cost Of Transport <i>COT</i>	107
5.6	Maximum Range Velocity <i>MRV</i>	109
5.7	Environmental Boundary Conditions	111
5.8	Dispersal	130
6	Discussion	139
6.1	Morphological Simplification and Kinematics	139
6.2	Fluid Dynamics	142
6.3	Inverse Dynamics	144
6.4	Dispersal	149
6.5	Evaluation of the Model	152
	Bibliography	159
	Data Sources	172
	Software	173

A	List of scale coefficients	175
B	Tables of viscosity and density coefficients	177
C	Morphological data	179
	Appendix	175
	Acknowledgements	181
	Biography	183
	Selection of publications	184
	First author publications	184
	Data publications	184

LIST OF FIGURES

2.1	Mature forms of crinoids	6
2.2	Flow diagram of the locomotion analysis	9
2.3	Flow diagram of the migration model	10
3.1	Schematic drawing a crinoid from the Antedon family	12
3.2	Schematic drawing of a stroke cycle	14
3.3	Added mass coefficient	20
3.4	Ontogenetic life cycle of comatulid crinoids	25
4.1	Arm morphology	28
4.2	Virtual pinnule geometry	29
4.3	Cirri	30
4.4	Crinoid dimensions from video recordings	32
4.5	Overview of the Weddell Sea	34
4.6	Image rectification	35
4.7	Compensation of the orientation angle	37
4.8	Perspective arm rotation	38
4.9	Spline slicing process	40
4.10	Segment kinematics	42
4.11	Automated pinnule flap	45
4.12	Flow nomenclature	48
4.13	Cylinder movement and thrust components	49
4.14	Flow components of the pinnules	53
4.15	Thrust components of horizontal swimming	56
4.16	Schematic representation of an iterative cycle	58
4.17	Schematic of a segmented body	66
4.18	Free body diagram	67
4.19	Cylinder added mass	68
4.20	General overview of the Southern Ocean	70
4.21	Tidal drift	79
4.22	Projection geometry	82
4.23	Graphical representation of the propagation algorithm	85
5.1	Dimensions of brachial	89
5.2	Pinnular dimensions	90
5.3	Dimension of cirri	90
5.4	Reference image	91
5.5	Swim track	92
5.6	Size compensation	93
5.7	Angular arm kinematics	95
5.8	Linear arm kinematics	96

5.9	Pinnule position during stroke phases	97
5.10	Range of Reynolds numbers	99
5.11	Thrust force and velocity versus frequency	100
5.12	Force components	101
5.13	Thrust distribution over stroke cycle and over arm	101
5.14	Swimming velocity	102
5.15	Travelled distances during a sequence	103
5.16	Internal forces	106
5.17	Internal moments	107
5.18	Cost Of Transport <i>COT</i>	108
5.19	Cost of transport over swimming velocity	110
5.20	Sea-ice thickness	113
5.21	Oceanic chlorophyll	114
5.22	Ice chlorophyll	115
5.23	Cloud fraction	116
5.24	Light radiation <i>PAR</i>	117
5.25	The oceanic Net Primary Production <i>NPP</i>	118
5.26	Net Primary Production <i>NPP</i> of sea ice	119
5.27	Total Net Primary Production <i>NPP</i>	120
5.28	Available energy on the seabed	121
5.29	Metabolic and reproductive costs	123
5.30	Annual excess productivity from 2003 to 2018	124
5.31	Frequency of available energy	124
5.32	Ocean currents	127
5.33	Tidal current	128
5.34	Monthly tide cycle	129
5.35	Limits of spatial dispersal	133
5.36	Dispersal: full parameter set	134
5.37	Dispersal: 10 pelagic days	137
5.38	Dispersal: no swimming	138
6.1	Arm morphology	139
6.2	Virtual model of <i>P. kerguelensis</i>	141
6.3	Maritime Cost Of Transport <i>COT</i>	145
6.4	Energy-dependent possible occurrence ranges of <i>P. kerguelensis</i>	157
6.5	Early stage of recolonisation of an iceberg scour	158

LIST OF TABLES

2.1	Taxonomy of <i>Promachocrinus kerguelensis</i>	5
4.1	Metadata of the sample stations	33
4.2	ROV orientation and number of sample	33
4.3	List of inverse-dynamic parameters	60
4.4	List of stroke-cycle frequencies	64
4.5	Solar radiation coefficients	73
4.6	Sea ice chlorophyll	75
4.7	Tidal constituents	78
5.1	Composition of the virtual model	87
5.2	Morphology of the passive body parts	88
5.3	Observed and calculated swimming velocities	102
5.4	Body weight and payload	104
5.5	Influence of pinnule's angle of attack	104
5.6	Fluid properties	105
5.7	Transport costs for different speeds	109
5.8	Costs for living	122
5.9	Boundary conditions	131
5.10	Source localities	132
6.1	Motion energetics of <i>P. kerguelensis</i> vs. fish	147
6.2	Net Primary Production <i>NPP</i> of sea ice	154
A.1	Scaling coefficients	175
B.1	Volumetric expressions	177
B.2	Viscosity coefficients v1 to v6	177
B.3	Viscosity parameter I, J and n	178
B.4	Viscosity parameter n^0	178
C.1	Arm length	179
C.2	Number of brachials	179
C.3	Body volume	180
C.4	Body weight	180
C.5	Body weight in water	180

NOMENCLATURE

Abbreviations

<i>asc</i>	Associated (brachial linked to a pinnule)
<i>bra</i>	Brachial
<i>CoM</i>	Centre of mass
<i>E</i>	Einstein (unit)
<i>fsd</i>	Fused (joined brachial and pinnule)
<i>H₂O</i>	Water
<i>i</i>	Counter i, the <i>ith</i> of something between 1...n
<i>IBr₁</i>	First primibrachial
<i>IBr₂</i>	Primibrachial axillary
<i>ldrf</i>	Location dependent rectification factor (image distortion)
<i>n</i>	Number for something (e.g. brachials)
<i>NaCl</i>	Abbreviation for salt for sodium chloride
<i>pin</i>	Pinnule
<i>COT</i>	Cost Of Transport
<i>MRV</i>	Maximum Range Velocity
<i>NPP</i>	Net Primary Production
AP	Antarctic Peninsula
AS	Amundsen Sea
fps	Frames per second
GIOMAS	Global Ice Ocean Modeling and Assimilation System
IBCSO	International Bathymetric Chart of the Souther Ocean
KP	Kerguelen Plateau
MODIS	Moderate Resolution Imaging Spectroradiometer

NEO	NASA Earth Observations
ROV	Remotely Operated Vehicle
RS	Ross Sea
TMD	Tide Model Driver
WS	Weddell Sea

Symbols

α	Angular acceleration	rad s^{-2}
α_c	Solar elevation angle	$^{\circ}$
α_v	Camera's pitch angle	rad
x_{scl}^-	Horizontal centre between laser points	px
y_{scl}^-	Vertical centre between laser points	px
χ	Organism's orientaion on the image	rad
γ_h	Enclosed horizontal angle of an image pixel	rad
γ_v	Enclosed vertical angle of an image pixel	rad
μ	Dynamic viscosity	mPa s
ν	Kinematic viscosity	$\text{m}^2 \text{s}^{-1}$
ω	Angular velocity	rad s^{-1}
$\overline{PAR}(0^+)$	Photosynthetic radiation on the Surface	E m^{-2}
ϕ	Angle	rad
ϕ	Organism's real heading	rad
Φ_h	Absolute horizontal angle	rad
Φ_v	Absolute vertical angle	rad
ψ	Camera's roll angle	rad
ψ	Pinnule angle	rad
Ψ_h	Absolute horizontal angle to reference laser	rad

X

Ψ_l	Light utilization index	$g_C g_{Chl}^{-1} (\text{E m}^{-2})^{-1}$
Ψ_v	Absolute vertical angle to reference laser	rad
ρ	Density	g cm^{-3}
$PAR(0^+)$	Solar radiation at the Earth's surface	$\text{J m}^{-2} \text{d}^{-1}$
$PAR(0^+)_{clear}$	Solar radiation at clear sky	$\text{J m}^{-2} \text{d}^{-1}$
Θ	Segment's orientation	rad
θ	Solar angle to zenith	°
A	Area	m^2
a	Linear acceleration	m s^{-2}
b'_h	Rectified horizontal length	px
b'_v	Rectified vertical length	px
b_h	Horizontal arc length (unit circle)	px
b_v	Vertical arc length (unit circle)	px
c	Cloud fraction	—
c_a	Added mass coefficient	—
$C_{flux(z)}$	Carbon at given depth	$\text{g}_C \text{m}^{-2} \text{d}^{-1}$
C_{prod}	Produced carbon at surface (equal to NPP)	$\text{g}_C \text{m}^{-2} \text{d}^{-1}$
cd	Drag coefficient	—
Chl_{sat}	Chlorophyll from satellite measurements	mg m^{-3}
Chl_{tot}	Column integrated chlorophyll content	g m^{-2}
D	Fluid dynamic drag force	N
d	Current distance Earth Sun	m
d	Diameter	m
d_0	Average distance Earth Sun	m
E_{avl}	Available energy	$\text{cal m}^{-2} \text{d}^{-1}$
E_{swim}	Locomotion energy	cal h^{-1}

E_{uab}	Usable energy	cal d^{-1}
F	Force	N
F_g	Gravitational force (weight)	N
f_{scl}	Image scale factor	m px^{-1}
h_{eff}	Relative light intensity	m
I	Solar irradiation	$\text{W m}^{-2} \text{d}^{-1}$
I_0	Moment of inertia	kg m^2
I_{rel}	Relative light intensity	0...1
im	Image index	$im = 1, \dots, I_{max}$
is	Segment index	$is = 1, \dots, S_{max}$
l	Length	m
$ldr f_h$	Horizontal rectification factor	—
$ldr f_v$	Vertical rectification factor	—
M	Moment	Nm
m	Mass	kg
m_{add}	Added mass	kg
m_{ia}	Mass in air	kg
m_{iw}	Mass in water	kg
m_w	Mass of water	kg
P	Net production of carbon	$\text{gC m}^{-2} \text{d}^{-1}$
P	Tracking point vector	
p	Pressure	Mpa
P_A	Tracked arm point vector	m
P'_A	Rotated arm point vector	m
p_{abs}	Absolute pressure	$kpond \text{ cm}^{-2}$
P_o	Power	W

R	Rotation matrix	–
r	Radius	m^3
R_d	Farce at distal joint	Nm
r_e	Ration of elliptical axes	–
R_p	Farce at proximal joint	N
S	Slicing point vector	
s	Spline length	m
scl	Spline scale factor	–
t	Time	s
T_c	Temperature	°C
T_k	Temperature	°K
u	East velocity	m s^{-1}
u	Linear velocity	m s^{-1}
U_c	Current velocity	m s^{-1}
U_s	Swimming velocity	m s^{-1}
V	Volume in general	m^3
v	North velocity	m s^{-1}
V_0	Cylinder volume	m^3
V_0	Cylinder volume	m^3
W	Work	J
$x_{abs_{rect}}$	Transformed and corrected absolute horizontal coordinate	px
x_{abs}	Absolute horizontal coordinate	px
x_{off}	Horizontal distance from image to global origin	px
$y_{abs_{rect}}$	Transformed and corrected absolute vertical coordinate	px
y_{abs}	Absolute vertical coordinate	px
y_{off}	Vertical distance from image to global origin	px

PAR	Light radiation	$\text{J m}^{-2} \text{d}^{-1}$
WIW	Weight In Water	g

Constants

β_h	Horizontal enclosed camera angle	45°
β_v	Vertical enclosed camera angle	29°
Δt	Time between two adjacent frames	$\frac{1}{15} \text{ s}$
γ	Fluid dynamic constant	0.577216
res_h	Horizontal resolution	1280 px
res_v	Vertical resolution	720 px

ZUSAMMENFASSUNG



Crinoiden existieren fast unverändert seit mehr als zweihundert Millionen Jahren. Sie sind in allen Ozeanen, von den Tropen bis zu den Polarregionen, zu finden und kommen sowohl in flachen Küstengewässern als auch in der Tiefsee vor. Es werden zwei Haupttypen unterschieden: Gestielte Crinoiden (Seelilien) und ihre jüngeren Familienmitglieder, die stiellosen Comatuliden (Haarsterne). Mit dem Verlust ihres Stiels erlangten sie eine freie Lebensweise, die mit einer eingeschränkten Schwimmfähigkeit einhergeht, was wahrscheinlich zu einer deutlichen Dominanz von Comatuliden geführt hat. Unter ihnen ist *Promachocrinus kerguelensis* die am häufigsten vorkommende Art im Südpolarmeer, dem Kontinentalschelf der Antarktis und den subantarktischen Inseln. Obwohl die ökologische Bedeutung von *P. kerguelensis* nicht vollständig verstanden ist, sind sie häufig Teil der benthischen Gemeinschaften, welche perfekt an die vorherrschenden extremen Umweltbedingungen angepasst sind.

Im Rahmen dieser Arbeit habe ich einen numerischen Ansatz aufgestellt, um die Schwimmfähigkeit von *P. kerguelensis* in Hinblick auf ihr zirkumantarktisches Vorkommen, ihre Migration sowie die Mechanismen, die zu ihrer weiten Ausbreitung geführt haben, zu bewerten, beides mit Blick auf den Vorteil ihrer Fähigkeit zur aktiven Fortbewegung und der Drift als Plankton während ihres ontogenetischen Larvenstadiums.

Der erste Teil dieser Studie befasst sich mit einer umfänglichen Lokomotionsanalyse von *P. kerguelensis*. Ein idealisiertes Berechnungsmodell eines schwimmenden Comatuliden wurde aus Messungen an Crinoidenproben und von Videoaufnahmen abgeleitet. Mithilfe einer analytischen Strömungs- und inversen Dynamik wurden die Schwimgeschwindigkeit und der entsprechende Energiebedarf zur Fortbewegung bestimmt. Aus deren gegenseitiger Abhängigkeit konnte anschließend die energieeffizienteste Geschwindigkeit, die Maximum Range Velocity (MRV), abgeleitet werden.

Im zweiten Teil dieser Arbeit wird ein Migrations- und Ausbreitungsmodell zur Analyse von *P. kerguelensis* zirkum-antarktischem Erfolg berechnet. Das Modell basiert auf ihrer Schwimmleistung, ihrer pelagischen Lebensphase als Plankton, ihrem energetischen Grundbedarf, verfügbare Nahrung als Energiequelle und den Meeres- sowie Gezeitenströmungen. Die Schwimmleistung von *P. kerguelensis* ergab dabei eine energieeffiziente Reisegeschwindigkeit von $\sim 3 \text{ cm s}^{-1}$ bei einem Energiebedarf von $\sim 12 \text{ cal h}^{-1}$, was, in Relation zum Körpergewicht gesetzt, ähnlich dem von schwimmenden Säugetieren ist. Ihr täglicher Grundbedarf beträgt zusätzlich $\sim 3,5 \text{ cal day}^{-1}$. Aus der Nettoprimärproduktion wurden Regionen mit ausreichendem Nahrungsvorkommen abgeleitet, die mindestens ihren Tagesbedarf decken. Die Vorhersagen stimmen sehr gut mit den Gebieten überein, an denen *P. kerguelensis* bisher gefunden wurde. Produktivitätsanalysen über einen Zeitraum von sechzehn Jahren zeigen, dass eine zirkum-antarktische Ausbreitung nur in sehr produktiven Jahren möglich ist. Basierend auf dieser Einschränkung führte das Modell zu einer zirkumantarktischen Ausbreitung in etwa 5.000 Jahren. Simulationen, die zu einer vollständigen Ausbreitung führten, erforderten jedoch aktives Schwimmen, eine jährliche Larvendrift von 75 Tagen und einen Ursprung in der Westantarktis. Die küstennahen Strömungen fördern

eine westliche Ausbreitung, die im Weddellmeer endet. Zeitliche Variationen von reichen und mageren Jahren deuten auf einen fortlaufenden dynamischen Prozess hin, der empfindlich auf wechselnde Umgebungsbedingungen reagiert, wobei die zirkumantarktische Ausbreitung von *P. kerguelensis* seit der letzten Kältephase vor 15.000 Jahren dreimal stattgefunden haben könnte.



1. ABSTRACT

Crinoids have existed almost unchanged for more than two hundred million years. They are found in all oceans, from the tropics to polar regions, and occur both in shallow coastal waters and in the deep sea. Crinoids are divided into two main types: stalked crinoids (sea lilies) and their more recent family members the stalkless comatulids (feather stars). With the loss of their stalk, they acquired a free-living life accompanied by a limited ability to swim, which probably led to the marked dominance of the comatulids. Among them, *Promachocrinus kerguelensis* is the most abundant species in the Southern Ocean, on the Antarctic continental shelf and around the sub-Antarctic islands.

In this work, I set up a computational approach to assess the locomotory capability of *P. kerguelensis* in terms of their circum-Antarctic occurrence, their migration pattern, and the mechanisms that led to their wide dispersal. Both with regard to the advantage of their locomotory capacity and in relation to their pelagic larval drift during their ontogenetic development.

The first part of this study is devoted to a comprehensive locomotion analysis of *P. kerguelensis*. An idealised computational model of a swimming comatulid was derived from morphological measurements on crinoid specimens and their kinematics tracked on video footage. Swimming speed and corresponding energy demand were determined with the help of analytical fluid and inverse dynamics. The most energy-efficient locomotion speed, the maximum range velocity, could be derived from their mutual dependence. The information on *P. kerguelensis*' swimming performance, its pelagic life phase, their cost of living, the available food as a source of energy, and the ocean and tidal currents form the basis for a migration and dispersal model in the second part of this thesis.

The swimming performance of *P. kerguelensis* resulted in an energy-efficient cruising speed of $\sim 3 \text{ cm s}^{-1}$ with an energy requirement of $\sim 12 \text{ cal h}^{-1}$, which, when related to body weight, is similar to that of swimming mammals. Their daily subsistence costs are an additional $\sim 3.5 \text{ cal day}^{-1}$. Locations of potential occurrences, that at least cover their daily requirements, were derived from the net primary production. The predictions correspond very well with the locations where *P. kerguelensis* has been found so far. Productivity analyses over a period from 2003 to 2018 show that circum-Antarctic dispersal is only possible in very productive years. Based on this constraint, the model led to circum-Antarctic settling in about 5,000 years. However, simulations leading to full dispersal required active swimming, an annual larval drift of at least 75 days and were restricted to an origin in the West Antarctic. Coastal currents promote a westerly dispersal ending in the Weddell Sea. Temporal variations of rich and lean years indicate an ongoing dynamic process sensitive to changing environmental conditions, where the circum-Antarctic dispersal of *P. kerguelensis* may have occurred three times since the last cold phase 15,000 years ago.



2. INTRODUCTION

Crinoids, along with starfish, sea cucumbers, sea urchins and brittle stars, represent a distinct group of echinoderms characterised by a pentametric symmetry. They are divided into two main types: stalked crinoids sea lilies and stalkless comatulids *feather stars* (Fig. 2.1). For a complete taxonomic listing, see table 2.1. Crinoids are the older representatives, with fossil records dating back to the Cambrian (250 million years ago) (Paul and Smith, 1984). Comatulid crinoids, on the other hand, lost their stalk in the course of evolutionary development and thus acquired a free way of life. Their ability to swim gave them an existential advantage and led to their enormous success and dispersal (Meyer, 1985; Meyer and Macurda, 1977; Janevski and Baumiller, 2009). More than 600 recent crinoid species have been described so far, with comatulids representing the vast majority with ~ 550 species. Crinoids, with less than a hundred representatives, occur far less frequently than their conspecific swimmer (Ameziane and Roux, 1997). This was not always the case, crinoids were the clearly dominant group of crinoids at the beginning (Bottjer and Jablonski, 1988). They are native to all oceans from shallow water to deep sea (Clark, 1967; Hess et al., 2003), one crinoid species was even discovered in a 9000 m deep ocean trench (Oji et al., 2009). While comatulids occur in shallower regions, crinoids have retreated to deeper areas (Oji, 1996). Crinoids occur both in tropical regions (Ameziane and Roux, 1997) and in the coldest waters of the Southern Ocean around Antarctica (Broyer et al., 2014). Three of the five circum-Antarctic species are feather stars: *Anthometrina adriani*, *Florometra mawsoni*, and *Promachocrinus kerguelensis*, exceptions among the sea lilies are *Feracrinus heinzelleri* (Eléaume et al., 2014) and *Bathycrinus australis*, which is native to the South Atlantic and sub-Antarctic islands (Gutt et al., 2011). *P. kerguelensis* is by far the most common species with the greatest diversity in shape, colour and morphology accounting for about 60% among the Antarctic comatulids (Clark, 1967). They have been found to date at depths of 10 to 2200 m (Speel and Dearborn, 1983) and were first described by their discoverer Carpenter (1879).

Tab. 2.1 Taxonomy of *Promachocrinus kerguelensis*. According to WoRMS: <http://www.marinespecies.org>

Kingdom	Animalia
Phylum	Echinodermata
Class	Crinoidea
Order	Comatulida
Family	Antedonidea
Genus	<i>Promachocrinus</i>
Species	<i>Promachocrinus kerguelensis</i> Carpenter, 1879

All circum-Antarctic comatulid crinoids belong to the family Antedonidae, which

2. Introduction

are considered to be free-living and able to swim (Clark, 1915, 1921). Technically, crinoids are not sessile organisms, with most of them being able to crawl. Swimming crinoids have been the subject of several studies dating back to the second half of the nineteenth century. Carpenter (1866) was the first who describe the swimming ability of *Antedon bifida*, this was further elaborated in the following decades by Marshall (1884), Moore (1923) and Langeloh (1937). However, the work of Chadwick (1907) is still considered the standard of swimming 10-armed comatulid crinoids. First qualitative studies on *Florometra serratissima* to investigate endurance and swimming speed were carried out by Shaw and Fontaine (1990). A fluid dynamics approach to determine the forces exerted and the resulting maximum payload of *Florometra serratissima* is the latest research in crinoid locomotion (Janevski and Baumiller, 2009). The significance and importance of crinoid mobility was discussed by Meyer and Macurda (1977). The decline of stalked crinoids and their retreat to deeper waters in contrast to the emerging dominance of comatulid crinoids on continental shelves provide hints for predation pressure (Oji, 1996; Messing, 1997). Nevertheless, locomotion generally provides not only the ability to escape, but also the opportunity to find new food sources and potential mating partners (Gray, 1968). Although the swimming abilities of comatulids are limited, it obviously gives them a great advantage in competition with their family members. *P. kerguelensis* in particular is perfectly adapted to the harsh conditions in the Southern Ocean (Broyer et al., 2014).

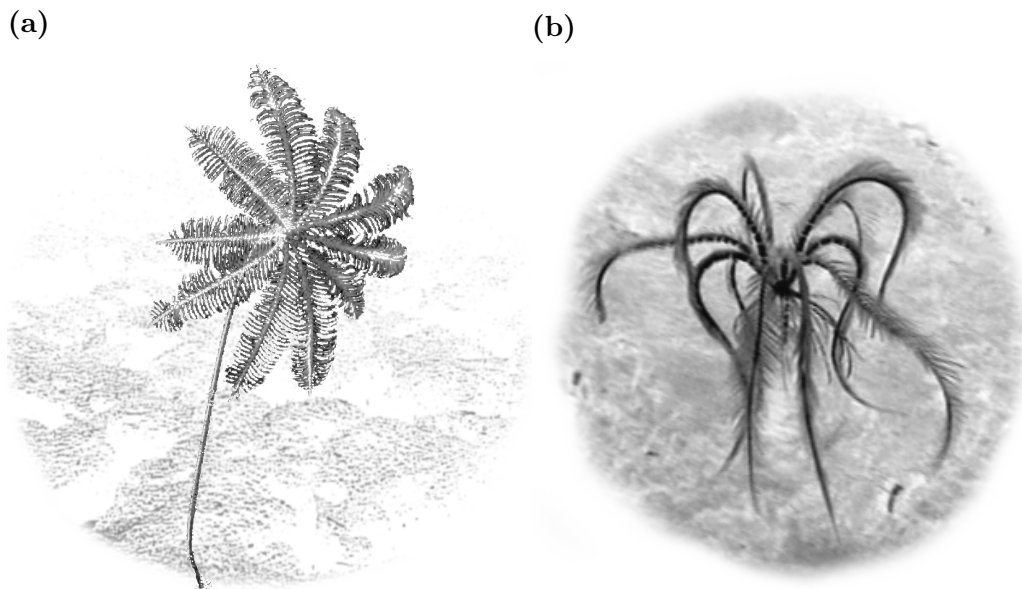


Fig. 2.1 Mature forms of crinoids. **a** Stalked crinoid also known as sea lilies. **b** A stalkless comatulid crinoid commonly named a feather star.

Although *Promachocrinus kerguelensis* is the most abundant feather star in the Southern Ocean, little is known about its dispersal journey, migration pattern and the secret of its circumpolar success. The key question of this paper is: what role does their swimming ability and physiological adaptations play in their circumpolar



dispersal, and how did this lead to such marked dominance and large abundance among Antarctic crinoids? To assess their swimming performance, it is important to know how long and how fast they can swim? Endurance depends, firstly, on their energy requirements, their cost of locomotion, in relation to the food available as an energy source. The first question is: How much food is needed to swim for a certain period of time and, on the other side, how much food is available for this? Secondly, how fast are they moving? The idea is to apply analytical fluid dynamics to calculate all the forces involved in the swimming of *P. kerguelensis*. Thrust, the force that propels the organism forward, and the resistance *drag* it faces in doing so. The swimming speed and the corresponding energy demand can be derived from the generated force field. In order to be able to carry out such an analytical fluid-dynamic approach, a detailed model of the body shape (morphology), the body weight and its density (physiology) as well as the swimming movements (kinematics) is required first.

The concept of this locomotion analysis is shown in the flow chart figure 2.2. The idea is to measure crinoid specimens to create a constructive plan of their morphology, derive their swimming motions from video recordings and determine their weight and density using given information from the literature. The challenges posed to the model are: How can such a complex and fragile structure be expressed mathematically? The concept is to develop a set of equations to create an idealised but simplified plan of *P. kerguelensis*' morphology (Fig. 2.2 x.1). The movement patterns derived from the video material are transferred to the model to give it a realistic kinematic component (Fig. 2.2 x.2). A kinematic model in combination with density and weight form the virtual model as the basis for the fluid-dynamic analysis used to calculate swimming speed and payload (Fig. 2.2 x.3).

Furthermore, the question arises: How can we obtain information about their swimming effort and thus their energy requirement? This has not yet been determined for crinoids, probably for two reasons. Their swimming strokes are very short (less than one minute) and they need a relatively large space which, due to its volume, contains a lot of water (swimming distance up to 5 m) (Shaw and Fontaine, 1990). It is precisely this combination that makes it difficult to determine experimentally reliable oxygen consumptions. Here I propose an indirect calculation method based on the conservation of energy approach, inverse dynamics. Winter (2009) provides a comprehensive description of how to derive costs for locomotion from externally applied forces and physiological data of the organism. Inverse dynamics is used to derive the internal load on muscles and skeleton from the external applied forces. These forces are determined using the preceding fluid dynamics (Fig. 2.2 x.4), which in turn allows to derive the energy demand (Fig. 2.2 x.5) and the most efficient swimming speed as well as the maximum range velocity (MRV) (Fig. 2.2 x.6), using the movement patterns obtained in the kinematic part.

The second question is dedicated to the circum-Antarctic success of *P.kerguelensis*: What are the driving factors that have led to such marked dominance among Antarctic crinoids and what role does its ability to swim play and how much does it contribute in circumnavigating the continent?

2. Introduction

For this, I have developed a computational model based on food availability, ocean and tidal currents (Fig. 2.3 x.7 "Currents") as well as energy demand, swimming speed and reproductive life cycles (Fig. 2.3 x.8) to model and analyse the circum-Antarctic migration of *P. kerguelensis*. The simulation area is restricted to 60° S, with the water depth given by the International Bathymetric Chart of Southern Ocean (IBCSO) (Arndt et al., 2013). The concept is divided into two main questions: How much energy - as a measure of food - is available on the seabed? And secondly, what is the influence of ocean and tidal currents on their circum-Antarctic dispersal? The idea to answer the first question is to derive the available food from the beginning of the food chain, when algae (phytoplankton) produce organic carbon through photosynthesis in the process of Net Primary Production *NPP* (Fig. 2.3 x.7 "net primary production"). Consumption in the food chain reduces the amount that reaches the seabed. This can finally be expressed as an energetic content (Fig. 2.3 x.7 "Available energy"). Since organisms need a certain amount of energy to live, not all food can be used for swimming. Both metabolism and the cost of reproduction reduce the daily amount of energy available for swimming. Since it is very difficult to estimate the individual willingness to swim and to include their group dynamics, I assume an absolutely optimal situation in which all surplus energy is used for locomotion. Although this leads to an underestimated time requirement for migration, albeit, it should have no influence on the degree of spatial dispersal. Currents, on the other hand, are a passive drive that transports larvae and swimming adults without additional effort (Fig. 2.3 x.7 "Currents").

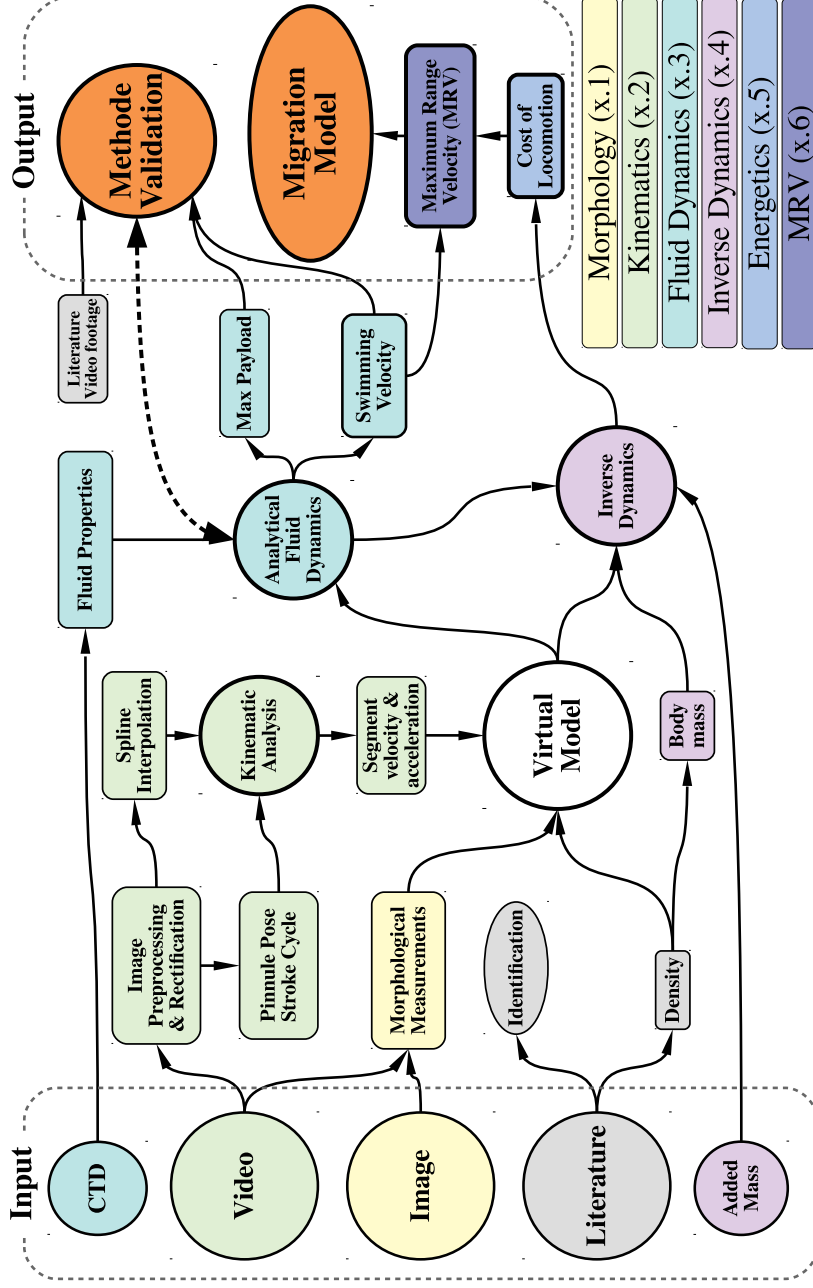
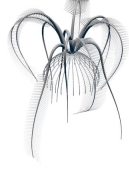


Fig. 2.2 Flow diagram of the locomotion analysis. Schematic representation of the workflow from the input data (video footage, images, literature and measurements) to the swimming-related outputs maximum range velocity (MRV), cost of locomotion and maximum payload. The outputs on the right swimming speed and maximum payload are used to validate the model. The properties maximum range velocity and energy demand are passed to the migration model (Fig. 2.3). The virtual model was composed of the crinoid's morphology, their kinematic movements and their physiological properties. Dynamic analysis of the virtual model yields thrust, swimming speed and cost of locomotion. Subsections (x.n) of the methodology (4.n) and results (5.n) are colour-coded (see legend).



2. Introduction

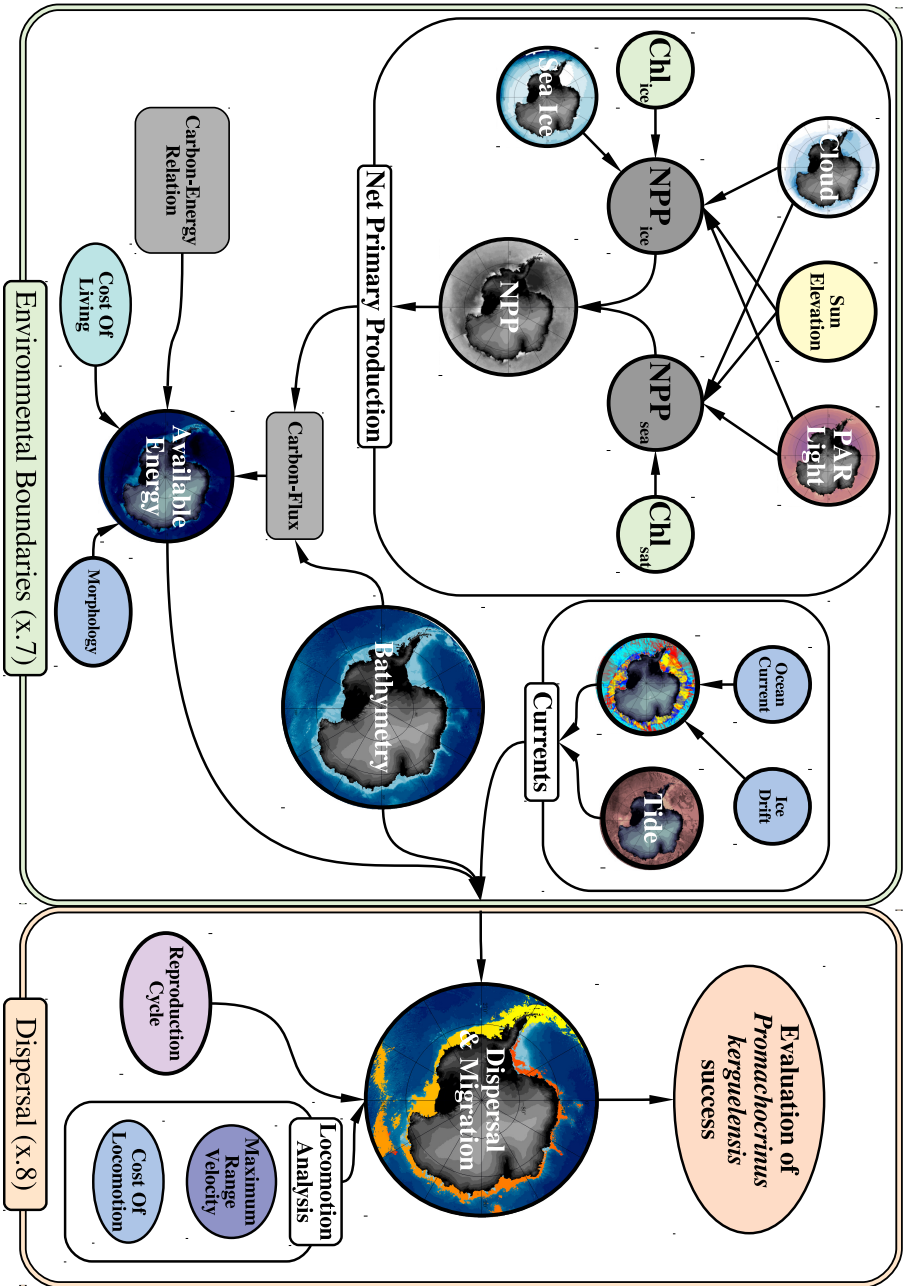


Fig. 2.3 Flow diagram of the migration model. Schematic representation of the workflow from environmental input and locomotion analysis results to the circum-Antarctic migration simulation and dispersal model. The organic carbon, synthesised in the process of Net Primary Production *NPP*, that reaches the seabed is expressed in available energy. It provides life support costs and determines swimming duration (cost of locomotion). Swimming and pelagic drift of larvae is driven by ocean and tidal currents. Their respective drift duration depends on the pelagic lifetime in the reproductive cycle or their swimming duration. Subsections (x.n) of methodology (4.n) and results (5.n) are highlighted by the coloured borders.



3. ADDITIONAL BACKGROUND INFORMATION

3.1 Crinoid's Morphology

The morphology of *Promachocrinus kerguelensis* formed the basis for an abstracted virtual model (Fig. 3.1) (Clark, 1915, p.60). The part of the body that can be considered the trunk is called the *calyx*. This is relatively small in relation to the size of the whole organism. The calyx is surrounded by 30 to 60 cirri (subdivided into 20 to 30 cirrals), small appendages with which it can anchor itself to the substrate. The arms are evenly distributed around the calyx. *Promachocrinus kerguelensis* belongs to a rare genus that can have from 12 to 22 arms within their species (Clark, 1967). They always form a pair of arms called a *ray* and thus occur predominantly even-numbered. A twelve-armed representative with six rays was chosen as the subject of this study. The arm segments are called *brachials*, of which the first two, the primibrachials, occur only singly in the ray, which then splits into two arms. The second segment, the primibrachial axillary, connects the two arms. They can reach a length of up to 250 mm and consist of over a hundred brachials. Pinnules are the small branches attached at regular intervals on either side of each arm, they consist of 20 to 26 pinnulars with a length of 10 to 20 mm (Clark, 1967).

3. Additional Background Information

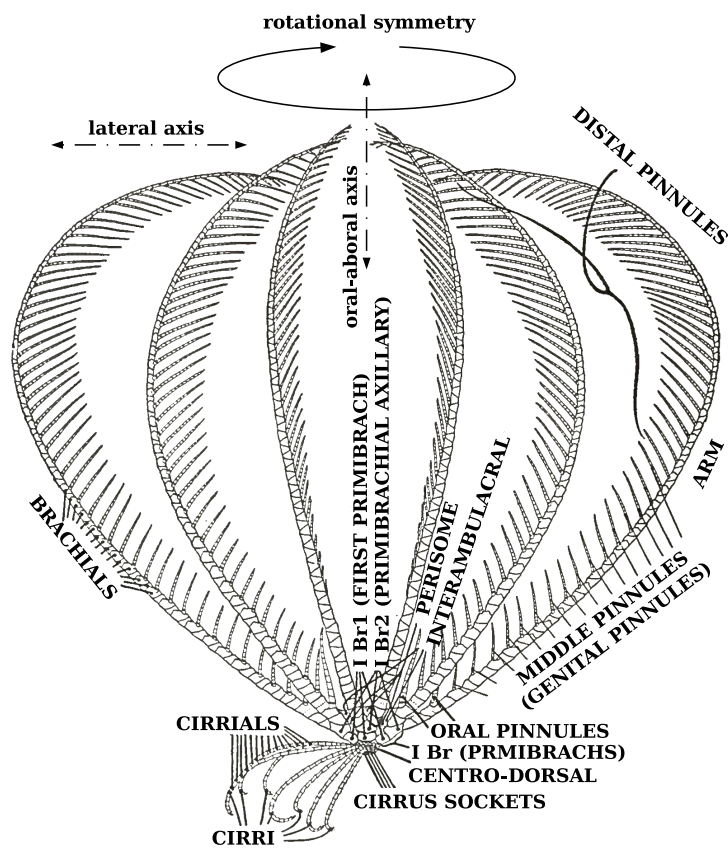
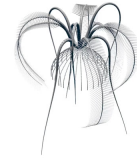


Fig. 3.1 Schematic drawing of a crinoid from the Antedon family. Modified after Clark (Clark, 1915, p.60). The side view shows the main body parts of the crinoid's morphology. The arms on the opposite side are omitted.



3.2 *Crinoid's Locomotion*

3.2 Crinoid's Locomotion

Locomotion is generally understood to be the movement to cover distances by walking or running on land, flying in the air and swimming in water (Gray, 1968). A similar form of terrestrial locomotion on land is used by benthic organisms on the sea floor. Crinoids belong to the benthic community of the oceans, spending most of their time motionless on the seabed or sitting on other organisms while filtering the water and feeding on plankton. *Promachocrinus kerguelensis* belongs to a subgroup of crinoids, the comatulids, which have evolved the ability to temporarily leave their location and swim for a limited time. To do this, they perform paddle-like arm movements, similar to those of cilia, in order to be able to lift off the ground. A stroke cycle describes a recurring movement pattern for this purpose. This is divided into two phases: the power stroke and the recovery stroke. Thrust is only generated during the power stroke. The arm is first stretched out to the side while the pinnules are unfolded to increase the effective area, finally the arm is pulled back against the swimming direction to propel the organism forward. A power stroke is followed by a recovery stroke in which the arm is brought forward again. The pinnules are aligned inwards, towards the axis of the arm, and the arm is then pushed forward close to the centre of the body (Fig. 3.2). All arms perform the same stroke pattern in succession in pairs of three or four to ensure a stable and continuous thrust (Shaw and Fontaine, 1990).

3. Additional Background Information

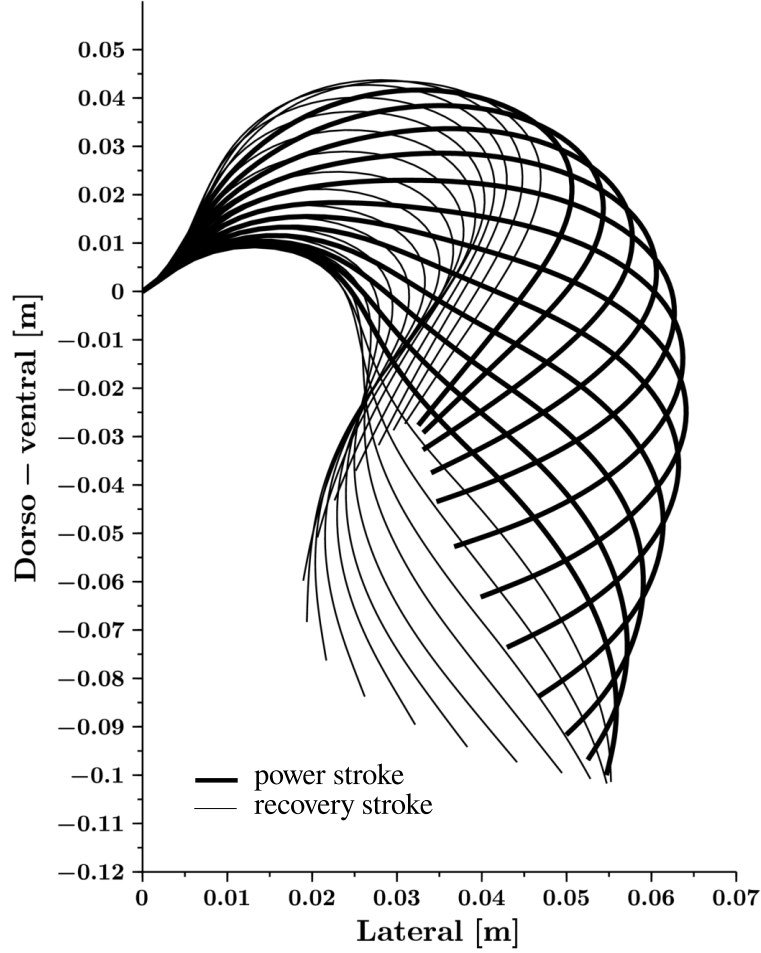


Fig. 3.2 Schematic drawing of a stroke cycle. Lateral view of the right arm of a crinoid. The power stroke is highlighted by thick lines while the recovery stroke is represented by thin lines. The plotted stroke pattern represents an idealised average of 53 stroke cycles. The y-axis represents the oral-aboral midline of the organism. The time interval between two adjacent steps is $\frac{1}{15}$ s.



3.3 Biological Fluid Dynamics

Fluid dynamics is a branch of physics that deals with the quantitative description of processes and their effects on objects in moving fluids. Characteristic parameters are usually forces that are generated by or exerted on an object. In biological fluid mechanics, these can be the drag or lift of a wing, fin or fluke, but also the generated propulsion of a moving animal. Fluid dynamics is divided into two interlocking areas: experimental and theoretical fluid dynamics. Experimentally, fluid dynamic properties are determined on models in wind or water channels. Flow field patterns can be visualised by *PIV* (Particle Image Velocimetry) analyses ([Stamhuis et al., 2002](#)). [Kato and Kamimura \(2008\)](#) gives a good overview of biological fluid dynamics. The Triantafyllou brothers are considered the modern fathers of biomechanics who conducted experiments on fish-like swimming robots ([Triantafyllou et al., 1993](#); [Triantafyllou and Triantafyllou, 1995](#)). More recent studies on undulating aerofoils were carried out by [Sonntag and Kesel \(2011\)](#); [Sonntag et al. \(2018\)](#).

On the other side exists the theoretical fluid mechanics, which provides an analytical and a numerical approach. Analytical fluid mechanics describes the expresses fluid dynamic characteristic properties and conditions in mathematical equations, e.g. the drag of a geometric shape (cylinders, plates or spheres). Fundamental work was done by [Stokes \(1850\)](#), [Burgess \(1916\)](#), and [Lamb \(1932\)](#). Their work was continued and summarised by [Hoerner \(1965, 1975\)](#), [Oertel et al. \(2009\)](#), [Durst \(2006\)](#), [Schlichting et al. \(2006\)](#), and [Sigloch \(2008\)](#), to name but a few pioneers.

A modern and nowadays more frequently used method is a numerical model, the numerical fluid dynamics. It is extremely flexible and can therefore describe complex flow fields and intricate geometries. However, due to its high demand for computing capacity, it quickly reaches its limits, especially when unsteady flow conditions encounter moving objects with large deflections. The required spatial and temporal resolution leads to extremely long computation times. A comprehensive collection of simulation-based biological fluid dynamics was compiled by [Liu \(2005\)](#). Numerical investigations of swimming and undulating two-dimensional fish locomotion were presented by [Owsianowski and Kesel \(2008\)](#).

Extensive works of biologically applied fluid dynamics have been compiled from a more scientific point of view by [Vogel \(1996\)](#) and from a technical point of view by [Oertel \(2008\)](#). [Lighthill \(1969\)](#) is one of the great pioneers in the field of aquatic animal locomotion. His work "Hydrodynamics of Aquatic Animal Locomotion" is nowadays one of the basic standards. While swimming fish is the most studied aquatic locomotion, comparatively little is known about swimming crustaceans and even less about echinoderms. The only significant work on swimming comatulids (stalkless crinoids) was done by [Shaw and Fontaine \(1990\)](#) and [Janevski and Baumiller \(2009\)](#). The role of cirri (anchoring appendages), which may be involved in crinoid locomotion, was the subject of [Baumiller and Janevski \(2011\)](#).

The fragile morphology of crinoids in combination with complex locomotion kinematics requires a very detailed model with high spatial and temporal resolution, which

3. Additional Background Information

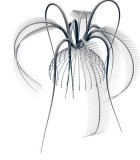
has discouraged numerical approaches so far. Since analytical calculations can only compute simple and ideal geometric shapes, advanced methods are needed to evaluate the properties of crinoid locomotion. Blade element theory (also called *blade element analysis* or *blade element method* in the literature) is an approach to solve a known function for a given parameter over a given dimension either by integrating or by summing a finite number of cross-sectional elements. Drzewiecki is considered the father of the blade element theory. He published the first method for calculating the thrust of aerial screws as early as 1892 and applied it to propellers (Drzewiecki, 1892, 1900, 1901). Since analytical fluid dynamics is mostly limited to steady laminar flow conditions at low Reynolds numbers $Re \leq 2,000$, it is applicable to either small dimensions, very slow velocities or a high kinematic viscosity (Eq. 3.1). Flow conditions at higher Reynolds numbers are increasingly dominated by turbulent effects, which are difficult or impossible to solve analytically. Swimming animals cover a wide Reynolds range, e.g. marine isopods are in the range of Re 4,000, swimming fish in the order of Re 100,000, and marine mammals even reach a Re value of up to two million. Consequently, only very small and slow swimmers come to Reynold's numbers below 2,000 (Vogel, 1996). It has been demonstrated that the blade element theory is a well-suited method for studying the locomotion of aquatic animals. Analyses of swimming fish were carried out by Colgate and Lynch (2004). Hui (1988) was also able to adequately determine the hydrodynamic properties of penguins flying under water. Recent studies on pectoral fins and their validation by robotic models were performed on an oscillating system by Bi et al. (2014) and including passive feathering by Behbahani and Tan (2016). Recent approaches extend blade element theory to include transient effects. The unsteady blade element theory was applied to flapping wings by Au et al. (2017) and compared with computational fluid dynamics. Swimming crinoids are at Re less than 2,000 and thus fall within the range of analytical fluid dynamic solutions. Here I use a morphological approach to divide the crinoid's body into small simple geometric shapes and determine their fluid dynamic drag for each time step of the swimming motion. The net generated thrust of a stroke cycle is then calculated by summing up all temporal instances.

Reynolds Number

Dimensionless ratios, such as the Reynolds number Re , offer the possibility to compare the properties of different systems. The Reynolds number expresses the relationship of size and velocity to the viscosity of the surrounding medium, which has a direct influence on the forces of lift and drag involved in locomotion.

$$Re_x = \frac{u x}{\nu} = \frac{\rho u x}{\mu} \quad (3.1)$$

The velocity u , in $[\text{m s}^{-1}]$ and the size x , in $[\text{m}]$, are related to the kinematic viscosity ν , in $[\text{m}^2 \text{s}^{-1}]$, of the surrounding medium, this can be transformed into a function of the dynamic viscosity μ , in $[\text{Pa s}]$ with the relation $\nu = \frac{\mu}{\rho}$, where ν is a function of (μ) and the density of the fluid ρ , in $[\text{kg m}^3]$ (Schlichting et al., 2006, p. 160, Eq.



3.3 Biological Fluid Dynamics

6.56) The analytical solution for the axial and radial flow around a cylinder must be differentiated, since a radial inflow is pressure-dominant, while an axial flow around is friction-dominant. The equation for the Reynolds number remains the same, but the characteristic length x must be adjusted. The reference value for radial flow is the diameter of the cylinder, while for axial flow the length of the cylinder is taken as the characteristic value.

3.4 Inverse Dynamics

Inverse dynamics in the field of biomechanics is a method that couples anatomy and kinetics with mechanical dynamics. The beginnings of biomechanics go back to Leonardo da Vinci, Galileo, Lagrange, Bernoulli, Euler and Young. It describes, analyses and evaluates the dynamics of biological movement and locomotion. The forces and moments that occur in this process characterise the system statics and dynamics. They are derived from kinematic analysis and anthropometric measurements and provide conclusions about loads and energy requirements. Winter describes the method of inverse dynamics when applied to human locomotion. He uses measured ground reaction forces and the kinematic motion data from video analyses to derive the internal forces and moments of musculoskeletal interaction (Winter, 2009). Nowadays, the mechanical analysis of biological systems is of great interest for robotics, orthopaedics and medical technology. Various studies on locomotion of land animals have been conducted to design biologically inspired machines (Buchli et al., 2009; Saunders et al., 2010; Kalakrishnan et al., 2010; Hopkins et al., 2015), even fast movements of jumping frogs have been studied in this way (Porro et al., 2017). Only a few approaches were successful in the field of aquatic locomotion, as the measurement of externally acting forces in the interaction with the fluid is difficult (Richards, 2008; Lauer et al., 2016).

In inverse dynamics, relationships between externally applied loads on a body and its resulting linear and angular accelerations are determined (Eq. 4.69). The components necessary to solve the equations are derived from kinematics, anthropometric data and fluid dynamic forces. The energy required for the movement can accordingly be derived from the moments acting on the joints and the resulting movement speeds. Necessary steps are briefly presented in the following sections. A schematic flow diagram in figure 2.2 clarifies the successive steps and the dynamic dependencies.

3.4.1 Kinematics

Kinematics is the theory of the movement of a body with the parameters displacement, velocity and acceleration, in the polar coordinate system these are correspondingly angle, angular velocity and angular acceleration. Displacement and angle are determined by subtracting two points or segment angles recorded in time. These points can be joints and are, for example, ankle, knee and hip. Each segment connecting two joints is considered a rigid bar performing an individual cyclic repetitive motion. This simplified representation proves more complex when considering the invertebrate or limbless locomotion of snakes, fish or the paddling arm movement of crinoids. Both the spinal column of fish and snakes, but also the arms of crinoids, consist of many small segments that are difficult to grasp individually. However, the large number and their short length make their movement appear fluid like a wavy line. However, this movement pattern can be described either as a wave function or by an extensive polynomial, a cubic spline. The cubic spline has been shown to be able to map natural motion and perfectly reproduce different amplitudes, wavelengths and frequencies.



3.4 Inverse Dynamics

Kinematics is generally the basis of all motion analyses, Hertel (1963) gives a good overview of the flying and swimming of insects, birds, fish and water snakes, his focus here is on fluid dynamics. Gray (1968) gives a more comprehensive insight into the locomotion of vertebrates and invertebrates in terms of their kinetics and musculoskeletal anatomy. A more general introduction to animal swimming, flying and running, including an energetic consideration, is summarised by Alexander (2006). Winter (2009) describes a detailed methodology for analysing human walking from kinematics to energy requirements.

3.4.2 Anthropometry

Physiology as the study of the properties of biological bodies, their dimensions and masses is called anthropometry. In order to solve the equations of inverse dynamics, the physiological properties of the individual segments are required. There are methods for determining these properties, but their potential applicability is limited. Large segment weights of thighs or whole legs can still be determined quite well, but properties of small body parts can often only be estimated if a non-destructive examination is required. The weight can be approximated by volumetric measurements and determination of the average density of the segments. The moment of inertia can subsequently be derived from the segment shape and weight (Winter, 2009).

3.4.3 Moment of Inertia

The moment of inertia I_0 is the resistance of a body to a change in its current rotation (angular velocity), it is dependent on both the shape and its specific mass distribution. The force necessary to change its rotational speed is the moment of inertia, it is the equivalent of the body mass and the associated mass inertia in linear motion.

3.4.4 Added Mass

Euler's formulation of Newton's second law $\vec{F} = m\vec{a}$ states that a resulting force F exerted on an object is proportional to its momentum $\dot{P} = m\dot{v}$ assuming constant mass m . However, the force required to accelerate an object of a given mass surrounded by a fluid is much higher. This difference is called the *acceleration reaction*. If the acceleration applied is of the same magnitude, the additional energy required comes from the extra mass, the so-called *added mass*.

An immersed body displaces the same amount of fluid as its own volume. The movement of the body with constant velocity displaces fluid portions and results in a fluid dynamic force acting on the object (Lamb, 1932; Batchelor, 1967). If the velocity of the object is now changed either accelerated or decelerated, a part of the surrounding fluid must also change its velocity. This part of the fluid depends on the shape and orientation of the body and is expressed as the *added mass coefficient* c_a which represents the fraction of the body's volume (Vogel, 1996). The total mass

3. Additional Background Information

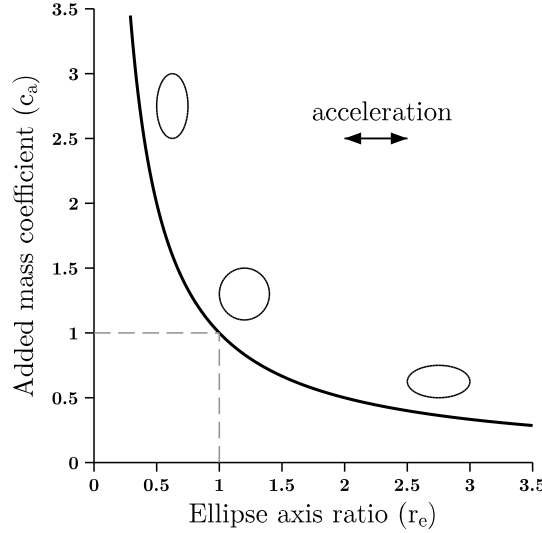


Fig. 3.3 Added mass coefficient. The additional mass of the fluid surrounded by an elliptical cylinder, which must also be accelerated by an acceleration of the cylinder, is expressed as a function of its axial ratio with respect to its direction of motion. The mass coefficient c_a is a volume factor of the cylinder.

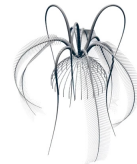
m_{tot} is then the mass of the body m_{body} plus the mass of the surrounding medium it influences.

$$m_{tot} = m_{body} + c_a \rho V_{body} \quad (3.2)$$

The mass coefficient c_a for a cylinder with a circular cross-section is 1.0 (Batchelor, 1967). However, if a cylinder is cut other than perpendicular to its major axis, i.e. exposed to a current at an angle, the result is an elliptical cross-section. The coefficient of added mass c_a for an ellipse is proportional to the ratio of its axes $c_a = b/a$, where a is perpendicular to the acceleration (Fig. 3.3) (Daniel, 1984).

3.4.5 Work, Power, and Energy

Work, in [J], is the energy transferred from one object to another over a period of time, that is, one body A does work on another body B . If body A is a muscle and body B is a segment, the energy required to move the segment is the work done by the muscle. According to Newton's law of conservation, energy cannot be consumed or destroyed, only a transformation into another form of energy is possible. Since not all work done by a muscle is converted into kinetic or potential energy, some is lost in heat or elastic deformation. It is expressed as a percentage between input and output, where 1 refers



3.4 Inverse Dynamics

to a theoretical 100% energy transfer with no loss and 0 refers to no expected output. [Hill \(1950\)](#) assumes a muscle power efficiency of 25%, i.e. the muscles must provide four times the required energy for the movement. Muscle power is the product of net muscle moment M and joint angular velocity ω . The latter is determined in the kinematic analysis of locomotion and the moment M can be determined using inverse dynamics.

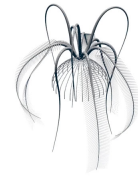
3.5 Dispersal

Migration simulations are based on environmental factors under which the dispersal of organisms serves as a study for ecological predictions. They have great significance for ecological management, e.g. for the definition of protected areas, which play an important role in biological networks. Impacts of industrial interventions by tidal power plants, wind farms and resource extraction can thus be minimised. Impacts on aquatic communities - partly caused by climate fluctuations, but also by humans - can be predicted and help prevent irreversible damage to the biosphere. Especially habitats under extreme conditions in the polar regions or in the deep sea are sensitive to changes in the environment.

In order to make reliable predictions about ecological scenarios, various approaches from different perspectives have become established. [Willis \(2011\)](#) provides a comprehensive treatise on different simulation methods and their implementation concepts.

Most recent studies to analyse dispersal and migration of marine organisms use a coupled Euler-Lagrangian strategy. Here, numerical fluid are combined with particle simulations so that ocean currents as well as individual and group dynamics can be modelled ([Hirt et al., 1974](#)). The Navier-Stokes equation of the Eulerian part is used to determine the general flow field of ocean currents ([Batchelor, 1967](#)), while individual and group behaviour are captured by Lagrangian particle dynamics ([Hirt et al., 1970](#)). While the computing power required for fluid-based flow simulations did not reach a sufficient level until the end of the twentieth century, the first motion simulations of terrestrial migration patterns date back to the 1960s ([Siniff and Jessen, 1969](#)). Today, however, modern computers are capable of calculating complex and high-resolution models, so that large-scale dispersal and migration predictions of marine organisms can be described sufficiently well. Migration of salmon shoals ([Byron and Burke, 2014](#)) and collisions of marine mammals with tidal turbines ([Lake, 2017](#); [Rossington and Benson, 2020](#)) underline the importance for interdisciplinary collaboration between science and industry. A more comprehensive approach from fertilisation through larval stages to adult migration was presented by [Allen et al. \(2018\)](#). Major improvements on larval dispersal during their pelagic life stage have been made within the last decade by [Shanks \(2009\)](#); [Staaterman and Paris \(2013\)](#); [Swearer et al. \(2019\)](#). A simulation of phytoplankton and their distribution by ocean currents is among the most recent studies in this field ([Soontiens et al., 2019](#)). Further studies extend the dispersion models by implementing the behaviour of single individuals to achieve better predictions of more natural dynamics. The so-called individual-based model, or more generally agent-based model, is already used in various simulations to improve predictions of group dynamics. A standard protocol for this method is provided by [Grimm et al. \(2006\)](#).

The ability to move independently of the environment is considered a fundamental advantage for the success of a species. However, locomotion is associated with high transport costs compared to dormant metabolism. The main advantages lie in the



3.5 Dispersal

search for new food sources, escape from predators or the pursuit of prey and the search for potential mating partners. It has been debated by scientists which of these factors led to the swimming abilities of comatulids. Observational and behavioural studies conclude that most likely avoidance of benthic hunters provides the greatest benefit to stalkless crinoids (comatulids) (Meyer and Macurda, 1977). Foraging behaviour, swimming activities and ecological influences on crinoids were summarised by Macurda and Meyer (1983); Meyer et al. (1984). Although generally assumed evolutionary hunting pressure led to a stalkless physiology of comatulids that enabled swimming, there is no evidence for the influence on their dispersal rate. Evolutionary success can have different reasons, either adaptation follows survival pressure or well-adapted organisms start to colonise new habitats. Since crinoids have been discovered around the globe and their physiology has not changed significantly over millions of years, they seem to be perfectly adapted to their needs and have been able to colonise the most remote habitats (Clark, 1967). The dispersal of sessile organisms, unable to leave their habitat, depends essentially on three factors: On the duration of the larval pelagic life stage of their offspring, on the direction and strength of the ocean currents that transport them and on the mobility of the larvae themselves (Swearer et al., 2019). The latter usually plays a subordinate role and is negligible to the transport by tides and ocean currents. Free-living organisms, in contrast to sessile species, have the possibility to influence the direction of migration and therefore a much larger radius of action. Comatulid crinoids are known to be more abundant than their stalked family members, but the extent of their success is not yet fully understood. *Promachocrinus kerguelensis* is, as far as known, the most successful crinoid in the southern oceans. They occur in a unique morphological diversity, there are representatives with 12 to 22 arms, which occur at depths of up to 2,200 m. Extensive surveys around the Antarctic continent prove their clear dominance, of the 2,450 samples taken so far on the entire Antarctic continental shelf, 1,451 belong to the species *Promachocrinus kerguelensis* (Speel and Dearborn, 1983; Eléaume et al., 2014).

The approach of this study follows a different concept than the methods presented above. An analytical method derived from geometric relationships was chosen to express the migration processes in simple mathematical relationships and thus predict how quickly and to what extent comatulids are able to colonise new areas or recolonise devastated regions. Comatulids as mobile benthic species belong to the pioneer species and thus represent the basis for new communities. Especially the seafloor on the Antarctic continental shelf, which is repeatedly destroyed by icebergs, seems to play a major role in the ecology of primary populations. Studies by Gutt (2001) indicate that the Antarctic seabed is disturbed every 340 yr in regions shallower than 500 m. Very shallow areas are said to be disturbed more often. Very shallow areas are even said to be affected by icebergs at a rate of 30% per year (Peck et al., 2010; Barnes, 2016; Barnes et al., 2018).

3. Additional Background Information

Mechanisms of Migration

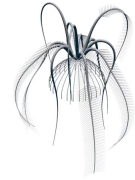
Migration is achieved by two mechanisms: active swimming of adults and passive drift of juveniles. Maximum daily swimming performance is given by the ratio of required and available energy. Pelagic drift on the other hand depends on the period an organism spend in the water column.

The energy available to organisms is mainly provided in the form of carbon and nitrogen, initially produced by primary production in the process of photosynthesis in the upper water layers by phytoplankton. Organic material is then transported downwards to the seabed. Since the entire food chain benefits from the primarily produced energy, it is subject to constant consumption on its way down, i.e. only a fraction of the organic material produced eventually arrives at the bottom as a food source for benthic communities. Where and how fast this process takes place depends on currents, tides and the local occurrence of chlorophyll *a*. Recent studies on food availability in Antarctic oceans show the mutual influence of net primary production, sea ice conditions, currents and bathymetry (Jansen et al., 2017). In situ sediment sampling formed the basis for describing the loss through the food chain as a function of depth. Flux rates were derived from sediment traps at different depths for this purpose, but these locally collected results are often based on seasonal data only (Isla et al., 2006, 2009). Very few studies cover sampling periods over more than a couple of months (Wefer and Fischer, 1991; Palanques et al., 2002; Smith et al., 2008).

Passive migration through drift is part of the reproductive cycle during crinoid's juvenile larval life stage.

Reproduction

The reproductive cycle and ontogenetic development of crinoids involves a pelagic stage in the water column. Figure 3.4 illustrates the ontogenetic development of comatulids and clarifies their main stages. The individual stages are species-dependent and may vary slightly. Especially the period of larval pelagic life ranges from a few days to several months (Mladenov and Chia, 1983). *Promachocrinus kerguelensis* has an annual reproductive cycle in which spawning probably occurs from November to December. Fecundity has been estimated to average 29,000 eggs per female (McClintock and Pearse, 1987). The family Antedonidea has doliolarian larvae whose bilateral symmetry does not completely change to the typical pentametric radial symmetry during metamorphosis. The larvae are surrounded by cilia bands that allow limited mobility. They have an adhesive pit that serves to anchor the organism to a substrate. *Promachocrinus kerguelensis* belongs to a group with an exceptionally long lecthotrophic (non-feeding) (McEdward and Miner, 2001) pelagic life phase, settlement most likely occurs after 2 to 3 months. However, this conclusion is based on data from other Antarctic echinoderms and has not yet been verified. A density slightly lower than that of seawater gives buoyancy to the offspring, suggesting a long larval period (McClintock and Pearse, 1987). Tropical species usually settle in less than a week, e.g. *Florometra serratissima* in 4 to 5 days (Mladenov and Chia, 1983). Once attached to



3.5 Dispersal

the substrate, the larva forms a stalk and arms with which it is then able to capture food. Comatulid species eventually lose their stalk and begin a free-living adult life (McEdward and Miner, 2001).

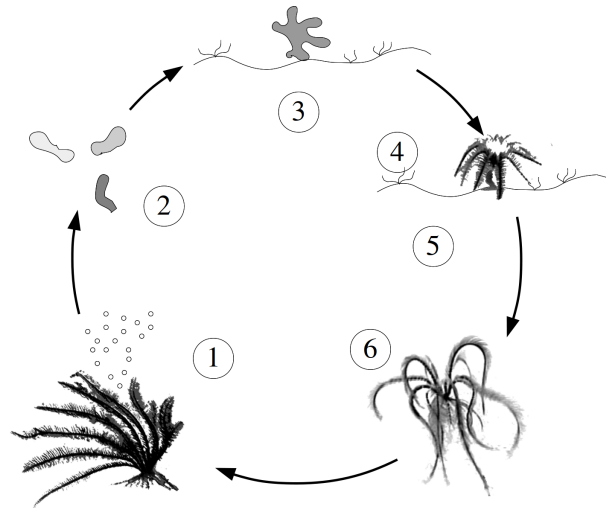


Fig. 3.4 Ontogenetic life cycle of comatulid crinoids. Schematic representation according to the description by McEdward and Miner (2001). 1) Release of eggs into the water. 2) Temporary pelagic life as non-feeding larvae. 3) Settling on the seabed after a species-dependent period of several days to several months. 4) Formation of body appendages - stalk and arms. Start of feeding by filtering plankton from the water. 5) The shedding of the stalk initiates the beginning of a free lifestyle. 6) Adult life and beginning of the next reproductive cycle.

3. Additional Background Information



4. METHODOLOGY

This chapter gives a comprehensive and detailed insight into the process of how an extensive analysis of swimming feather stars (comatulid crinoids) of the species *Pro-machocrinus kerguelensis* was carried out from video recordings and sample measurement. The results obtained and third-party environmental data were then used to develop a computer model to simulate their migration patterns and dispersal around the Antarctic continent. The methodology is a collection of approaches presented by scientists in the literature, extended and compiled by methods developed for this thesis, as highlighted in each section. All steps listed were part of this study and had to be calculated for this task in order to achieve the required spatial and temporal resolution. The equations, external data and coefficients used are either referenced or highlighted as part of this study. The level of detail and listing of third party equations is intended to allow the process to be reproduced in its entirety without having to go back to their origins.

4.1 Morphology and the Virtual Design

A virtual morphological model, the spatial framework, formed the basis for the computational analysis. The aim was to reconstruct an idealised but relatively realistic three-dimensional (3D) model derived from detailed morphological measurements and describing their anatomical relationships as far as possible mathematically. Arm, pinnule, cirri and calyx dimensions were determined on eight individuals of the Antedon family sampled on the *Polarstern* cruise ANT XXI/2 in the Weddell Sea (2003). They were caught with an AGT (Agassiz trawl) at a depth of 350 m at station 65/29-2 (54° 31.5 S 003° 12.8 E) and stored in formalin. Eight arm samples were photographed and multiple images stitched together to create high resolution pictures. Dimensions of the arm segments were then digitally measured on the scaled pictures using Fiji software (based on ImageJ v1.52, University of Wisconsin-Madison) (Fig. 4.1).

4.1.1 Brachials

Length and width of all brachials were digitally measured and their brachial length as well as the brachial width were related to their position on the arm axis by means of exponential regression as a rule of measure. The segment numbers start with one after the primibrachial axillary IBr_2 . Distal arm parts of the virtual design had to be extrapolated due to the fragmented and incomplete nature of the samples.

4.1.2 Pinnule segments

Pinnules ($n=63$) were removed at regular intervals from 8 arms. The photos were digitised and the length and width measurements of the pinnules were regressed as

4. Methodology

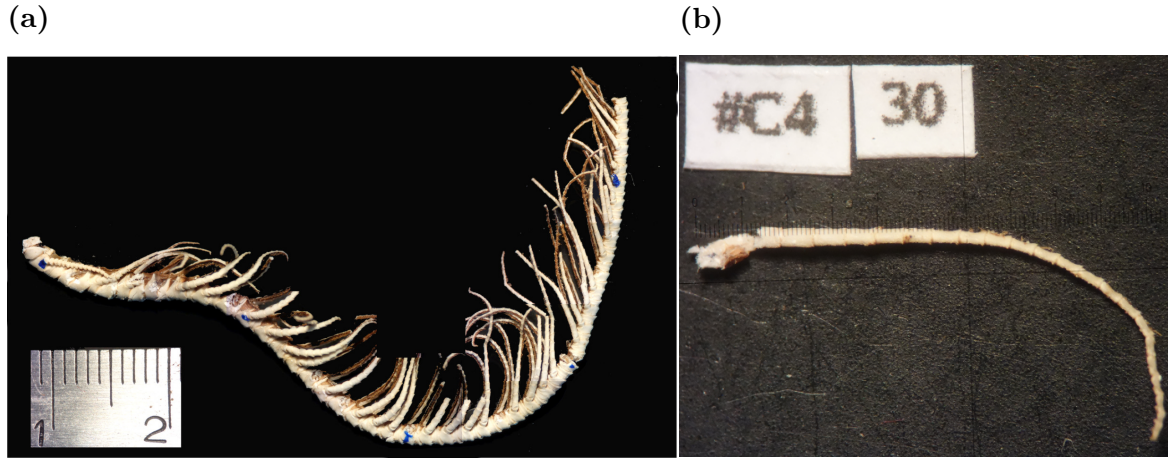


Fig. 4.1 Arm morphology. **a** Composite image of crinoid arm specimen #C4 separated between the first brachial IBr_1 and the primibrachial axillary IBr_2 on the left side on the image (scale in centimetres). The pinnules were taken at the positions marked by blue dots. **b** Image of the corresponding pinnule number 30 (scale in millimetres).

already done for the brachials. Here, the length of the pinnulars was also linked to their proximal-distal position on the pinnule, only the width of the pinnulars was expressed in relation to the width of the associated brachial, i.e. the width regression is given as the ratio of the arm thickness at the base of the pinnule.

The correlation between width and length of a pinnule was also needed to calculate the volume-preserving brachial diameter during recovery strokes when pinnules are folded inwards and aligned to the brachial axis. To create a simple geometric shape, brachial and aligned pinnules are fused to form a volume-preserving cylinder (Fig. 4.2). Here, the base of the pinnules was assumed to be etched in the middle of a brachial.

$$V_{(fsd)} = V_{(bra)} + \sum_1^n \pi r_{(pin)}^2 l_{(bra)} \quad (4.1)$$

The volume of the fused segments $V_{(fsd)}$ is the volume of the brachial $V_{(bra)}$ plus the sum of all laterally parallel pinnulars, their radius was taken from the length-width regression (Fig. 5.2).

$$r_{(pin)} = \frac{0.0004l^2 - 0.0251l + 0.3675}{2} \quad (4.2)$$

The length l is the distance from brachial where the pinnule attaches to the brachial to be fused according to the brachial length regression in (Fig. 5.1).

$$l_{(pin)} = \int_{i_{(asc)}}^{i_{(fsd)}} 0.179 \exp^{-0.109i+2.319} + 1.57 \quad (4.3)$$



4.1 Morphology and the Virtual Design

Length integration over the segments to be fused $i_{(f_{sd})}$ to the brachial at the base of the pinnule $i_{(asc)}$.

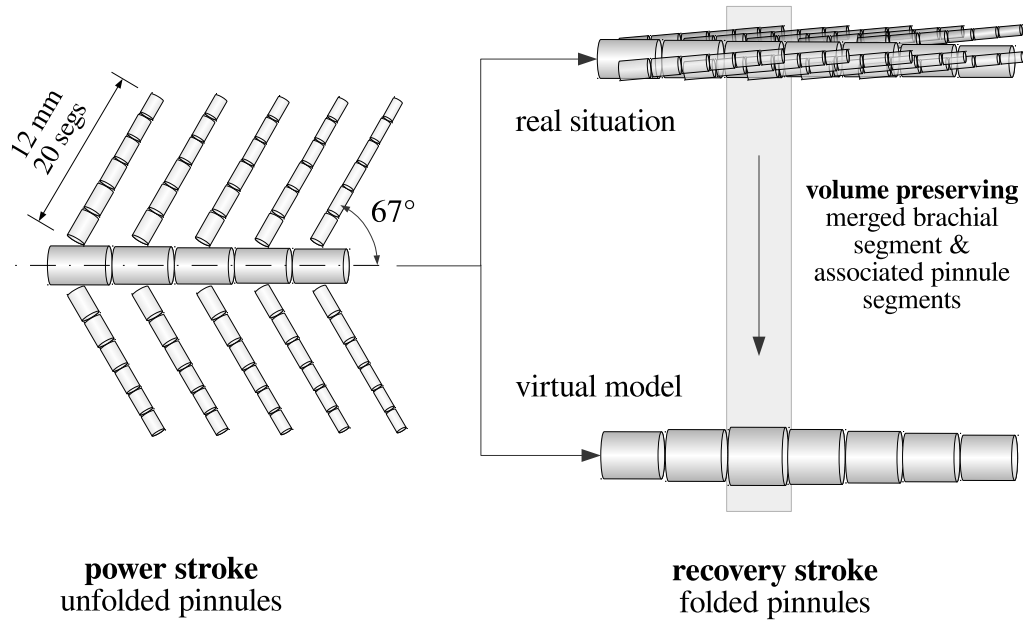


Fig. 4.2 Virtual pinnule geometry. Schematic drawing of the arrangements of the pinnules during power stroke and recovery stroke. The power stroke pose is shown on the left. The pinnules are folded out laterally at an angle of 67° to the arm axis. On the right, the realistic situation is shown in comparison to the fused model. While the pinnules are folded inwards, in the virtual model they merge into a volume-preserving cylinder.

4.1.3 Calyx, Primibrachials and Cirri

The calyx is the part of the body of a crinoid without arms and cirri, which can be circular in oral projection but roundish to conical in lateral perspective. Adult representatives of *Promachocrinus kerguelensis* have a rather conical calyx with a diameter of about 7 mm and a length of 8 mm. The primibrachials (IBr_1) and (IBr_2) are together about 5 mm long and wide. They share a pair of arms and thus occur six times in a twelve-armed crinoid. The number of cirri ranges from 30 to 65 with a length of 40 to 130 mm, consisting of 25 to 30 cirrals (Clark, 1967, p.433). The dimensions of the cirri and their cylindrical regressions were measured digitally on photographs of 5 cirri samples (Fig. 4.3).

The calyx, primibrachials and cirri were considered passive body parts. They are thus not actively involved in swimming, but still contribute to body weight and re-

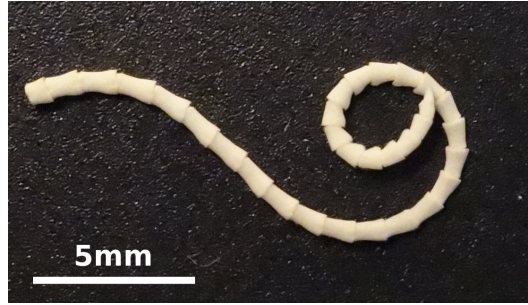


Fig. 4.3 Cirri. Image of a cirri.

sistance. None of the eight specimens examined were in a complete state, the strong fragmentation therefore did not allow measurements on a complete organism and only one of the crinoid specimens clearly belonged to the genus *Promachocrinus kerguelensis*. This sample has a calyx with a diameter of 6.6 mm. Clark speaks of highly developed individuals with an arm length of up to 250 mm, however all organisms observed had arm lengths around 150 mm. This size is rather at the lower limit of Clark's data and correlates with the recorded crinoids (Fig. 4.4). A geometric sphere 7 mm in diameter was considered suitable to represent the virtual calyx. Cylinders, 3 mm in length and diameter, represent the six primibrachials one and two. The number of 30 cirri was approximated from the video images. They consist of interconnected cylinders according to the regression of their length and width (Fig. 5.3). The total length of the cirri of 42 mm leads to an average of 29 cirrals.

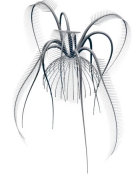
4.1.4 Density, Mass and Weight in Water

The mass of an individual is defined as its wet weight in air. Since an object displaces exactly the same volume of water (Heath, 1897), the weight in water is then the difference between the wet weight of the organism and its corresponding volume of water mass. If an organism has a density higher than that of water (say 1 g cm^{-3}) it has negative buoyancy and sinks. It follows that an object is positive buoyant if its density is less than that of water. Since the individuals were only observed and not sampled, the weight could not be determined directly. Therefore, density values were derived from the literature (Janevski and Baumiller, 2009) and used to calculate their weight.

$$WIW = V (\rho_{(organism)} - \rho_{(water)}) \quad (4.4)$$

The Weight in Water WIW in [g] is the product of the volume V in [cm^3] and the difference between the density of the organism $\rho_{organism}$ and the density of the water ρ_{water} (both in [g cm^{-3}]).

Janevski and Baumiller provide WIW for 10 individuals of the family Antedonidae, including one representative of the species *Promachocrinus kerguelensis*. The data



4.1 Morphology and the Virtual Design

show a strong dependence of density on species, so that the density of *P. kerguelensis* is based on only one sample, despite the lack of statistical support. It is a 20-armed individual with a brachial width of 1.53 mm in the middle of the arm and an arm length of 137.4 mm (Janevski and Baumiller, 2009, Supplementary Data 3.). The weight in water of 0.46 g was reconstructed using a modelled arm with approximately the same dimensions in order to determine the density of the crinoids. For this purpose, the recorded arm *E* from the video sequence RS610012_7186-7244 with 137 mm arm length was used.

$$\rho = \frac{WIW}{20 V_{(arm)} + V_{(centrodorsal)}} \quad (4.5)$$

The density ρ of *P. kerguelensis*, in $[g\text{ cm}^{-3}]$ was determined from the Weight In Water *WIW* of 0.46 g divided by the volume of a comparably sized virtual model of the arm, in $[cm^3]$. The resulting density of 0.056 g cm^{-3} in water was used to calculate the *WIW* of all samples. To obtain the wet weight of the individual in air, the same volume of seawater was simply added to its weight in water.

$$m_{(in\ water)} = V_{(individual)} \rho \quad (4.6)$$

$$m_{(in\ air)} = m_{(in\ water)} + V_{(individual)} \rho_{(seawater)} \quad (4.7)$$

4. Methodology

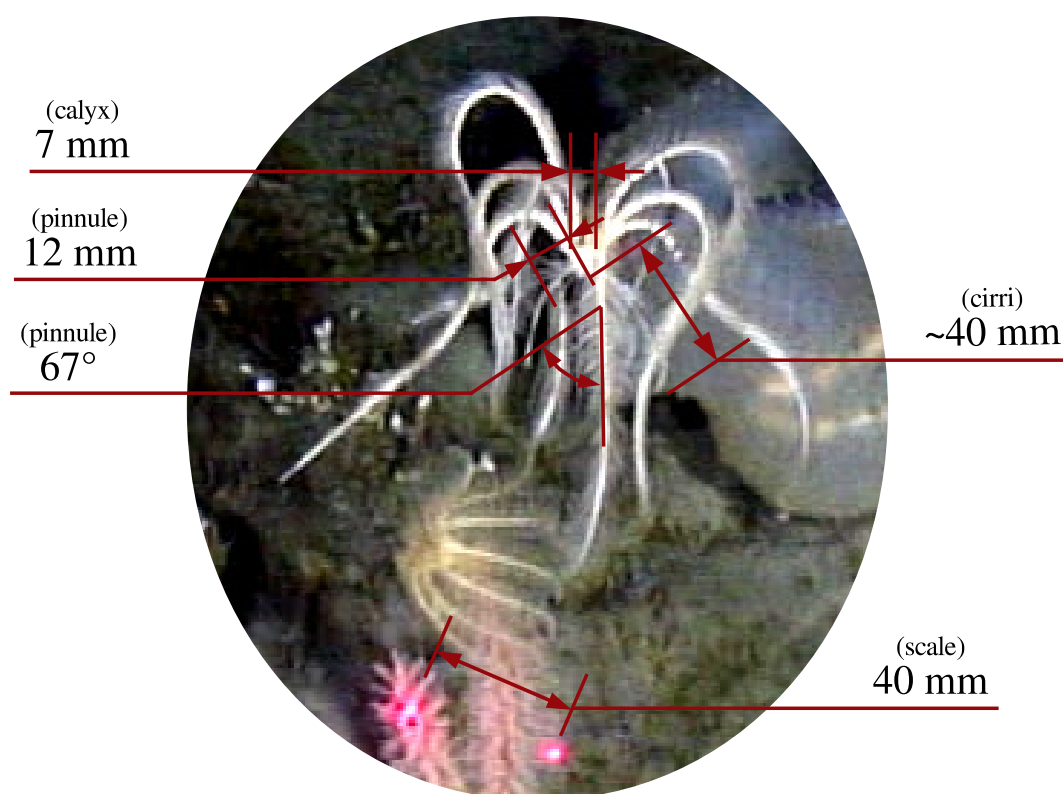
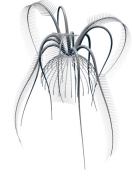


Fig. 4.4 Crinoid dimensions from video recordings. Dimensions were measured on a filmed individual. Cirri length, calyx diameter, pinnule length and angle were taken from the scaled image. The image was taken on the *Polarstern* cruise PS82 [crii].



4.2 Locomotion Kinematics

4.2 Locomotion Kinematics

The kinematics of locomotion of *Promachocrinus kerguelensis* defines the movement sequence of the arm stroke during swimming. The movement sequences are taken from video recordings made during the *Polarstern* cruise PS82 in the Weddell Sea (2014). The footage of the swimming crinoids was taken by an Ocean Modules V8Sii Remotely Operated Vehicle (ROV) at depths between 240 m and 280 m [cri, crii] (Tab. 4.1). Four organisms with five to six arm flapping cycles each provided 53 complete movement sequences, which were interpolated using a third-order spline (Tab. 4.2). For this purpose, the videos were converted to 15 frames per second at a resolution of 1280x720 using the software ffmpeg [FFP].

Tab. 4.1 Metadata of the sample stations. Position of the ROV stations where the swimming crinoids were filmed. The time is given as Coordinated Universal Time (UTC).

Date (UTC)	Station	Filename	Depth [m]	Latitude	Longitude
2014-01-08 04:13	PS82-049	RS610012	240	76.3203 S	29.0261 W
2014-01-19 17:48	PS82-128	RS619007	274	75.4950 S	27.4537 W
2014-01-19 19:16	PS82-128	RS620008	278	75.4950 S	27.4597 W
2014-01-19 19:57	PS82-128	RS620018	281	75.4929 S	27.4628 W

Tab. 4.2 ROV orientation and number of samples. Summary of relevant parameters regarding camera perspective and number of samples.

Filename	Arms	Stroke-cycle	n	Heading	Roll	Pitch
RS610012	6	1	6	116°	1°	-40°
RS619007	5-6	2	11	346°	2°	-47°
RS620008	6	1	6	347°	2°	-43°
RS620018	6	5	30	337°	1°	-44°

Image sequences with a time difference $\Delta t = \frac{1}{15}$ s between two adjacent images were reduced to whole stroke cycles, 25 to 30 images.

The centre of the calyx (referred to here as the *body track*) and a prominent feature on the seabed (*reference track*) were tracked on all images to extract the *motion path* of the organism from the camera motion (Fig. 5.5). The arm motion could be tracked along the arm axis for each frame and interpolated by third-order polynomial B-splines (Farin, 1990; Farin and Hansford, 2000). A subsequent correction of the position of the tracking points was used for optimisation to ensure coherent splines-arm axes (Fig.

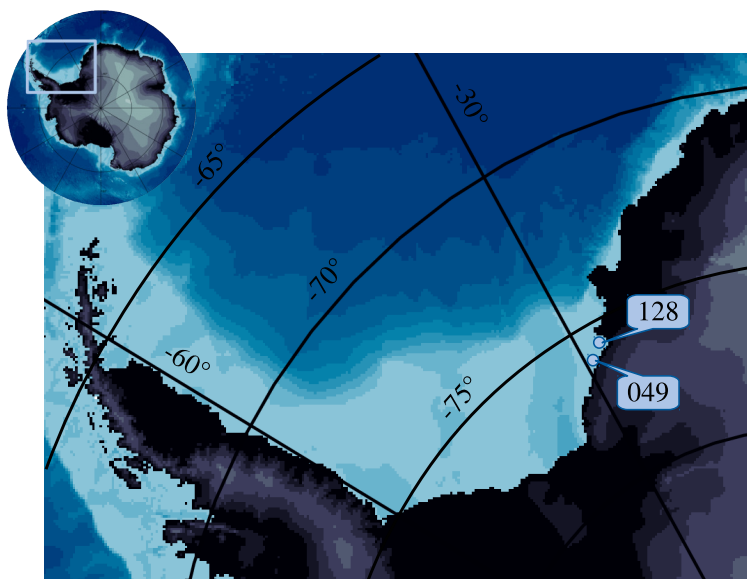


Fig. 4.5 Overview of the Weddell Sea. Section of the Weddell Sea with sample stations 049 and 128 during *RV Polarstern* cruise PS082 in the season 2013/2014. The map is based on the bathymetric model IBCSO [bc] (Arndt et al., 2013). For details see also table 4.1.

5.4). Tracking and interpolation were programmed in Scilab-5.5.2 [SCI]¹.

4.2.1 Image Scaling and Rectification of the Perspective Viewing Angle

Image distortions caused by the angle of view perspective and camera optics had to be corrected to ensure a true-to-scale reconstruction. Reference scale, lens geometry, camera angle and object orientation had to be eliminated to obtain the correct relations of the actual dimensions of the organism.

- image scaling according to the reference laser
- rectification of lens geometry and camera pitch
- correction of the orientation and rotation of the crinoids

Rectification of Lens Geometry and Camera Pitch

The video footage is from a Kongsberg OE14-502 camera with a resolution of 1080i, 30 fps (frames per second), which was converted into an image sequence of res_h : 1280,

¹A script on B-spline interpolation has been published by Professor Kirby Baker of the UCLA Mathematics Department in Los Angeles <https://www.math.ucla.edu/~baker/149.1.02w/handouts/> (January 2019)



4.2 Locomotion Kinematics

res_v : 720 pixels, 15 fps. The lens geometry and corresponding field of view covers a range of β_v : 29° vertically and β_h : 45° horizontally.

To correct the distorted images with their vertical and horizontal length errors due to camera tilt and aperture angle, I have developed a method that determines the true distances depending on the image pixel position. A common method is to first rectify the image and then track the scaled values. In this approach, however, tracking is done first and all rectification is done in a second step. The advantage here is that lens distortion, perspective view due to camera tilt and image scale (reference laser) can be corrected in a single operation.

The reference coordinate origin is assumed to be a point on the global horizon above the centre of the image (referred to here as the *absolute coordinate system*). All image points with their pixel coordinates were transformed into the new absolute coordinate system. Image points to a plane vertically related to the camera orientation were rectified with a location-dependent factor $ldrf$ (Fig. 4.6).

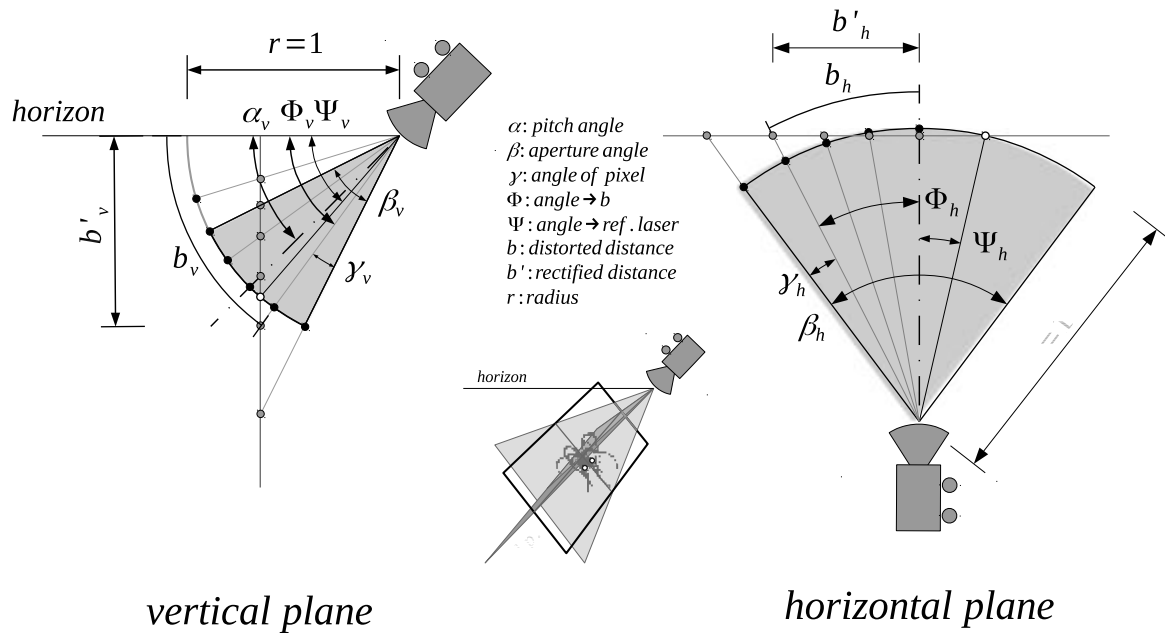


Fig. 4.6 Image rectification. Schematic representation of the rectified tracking points (grey dots). Image coordinates in pixels (black dots) are perspective compressed. Correct projection onto the vertical and horizontal planes is achieved by determining a position-dependent factor $ldrf$ with respect to a reference plane. The rectification is a function of the absolute angle $\Phi_h \Phi_v$ and a plane intersecting with the reference laser (circle).

First, tracking points are transformed into absolute global coordinates.

$$\begin{aligned} x_{abs} &= x_{off} + x \\ y_{abs} &= y_{off} + y \end{aligned} \tag{4.8}$$

4. Methodology

With the corresponding offsets x_{off} and y_{off} to the reference origin.

$$\begin{aligned} x_{off} &= -\frac{1}{2}res_h \\ y_{off} &= \frac{\alpha_v}{\gamma_v} - \frac{1}{2}res_v \end{aligned} \quad (4.9)$$

The absolute angles Φ_h and Φ_v of a location are obtained by multiplying with γ_h and γ_v respectively.

$$\begin{aligned} \gamma_h &= \frac{\beta_h}{res_h} \\ \gamma_v &= \frac{\beta_v}{res_v} \end{aligned} \quad (4.10)$$

$$\begin{aligned} \Phi_h &= x_{abs} \gamma_h \\ \Phi_v &= y_{abs} \gamma_v \end{aligned} \quad (4.11)$$

The desired scaled vertical plane intersects the field of view, assumed to be a unit circle, at the location of the reference lasers. The corresponding absolute angles Ψ_h and Ψ_v to the reference lasers are determined from the mean x-location x_{scl}^- and the mean y-location y_{scl}^- as the midpoint between the two laser points.

$$\begin{aligned} \Psi_h &= (x_{off} + x_{scl}^-) \gamma_h \\ \Psi_v &= (y_{off} + y_{scl}^-) \gamma_v \end{aligned} \quad (4.12)$$

Rectified lengths in the reference plane b'_h and b'_v can thus be derived trigonometrically.

$$\begin{aligned} b'_h &= \cos(\Psi_h) \tan(\Phi_h) \\ b'_v &= \cos(\Psi_v) \tan(\Phi_v) \end{aligned} \quad (4.13)$$

In a unit circle with radius $r = 1$, the arc length is equal to the angle enclosing it as radian measure.

$$\begin{aligned} b &= 2\pi r \\ \Rightarrow b_h &= \Phi_h \\ \Rightarrow b_v &= \Phi_v \end{aligned} \quad (4.14)$$

The rectification factors $ldrf_h$ and $ldrf_v$ are then the ratio between observed and rectified lengths.

$$\begin{aligned} ldrf_h &= \frac{b'_h}{\Phi_h} \\ ldrf_v &= \frac{b'_v}{\Phi_v} \end{aligned} \quad (4.15)$$

Observed absolute points are transformed into new coordinates $x_{abs_{rect}}$ and $y_{abs_{rect}}$ by these rectification factors.

$$\begin{aligned} x_{abs_{rect}} &= x_{abs} ldrf_h \\ y_{abs_{rect}} &= y_{abs} ldrf_v \end{aligned} \quad (4.16)$$



4.2 Locomotion Kinematics

Crinoid's Orientation and Camera's Rotation

The relative orientation of the crinoid is given by the angle between the oral-aboral axis and the vertical axis of the image χ . The real heading ϕ is then its relative orientation, compensated by the roll angle of the camera ψ (Fig. 4.7).

$$\phi = \chi + \psi \quad (4.17)$$

The oral-aboral body axis are taken from the video footage and the tracked arm points P_A are rotated to ϕ using a rotation matrix R_ϕ .

$$R_\phi = \begin{pmatrix} \cos \phi & -\sin \phi \\ \sin \phi & \cos \phi \end{pmatrix} \quad (4.18)$$

$$P'_A = P_A R_\phi \quad (4.19)$$

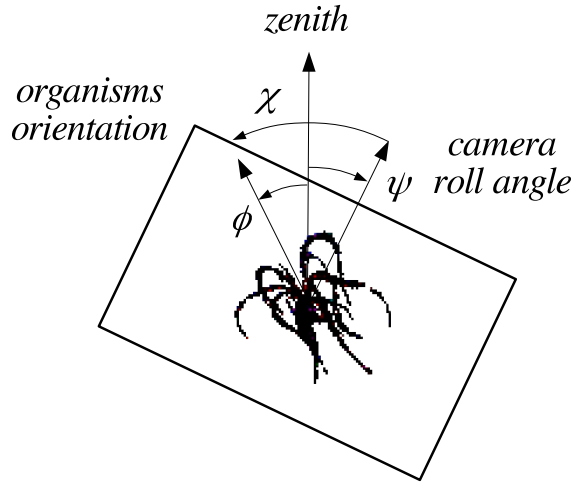


Fig. 4.7 Compensation of the orientation angle. The direction of the real organism was derived from the orientation χ and the roll angle of the camera ψ .

Since crinoids are axially symmetrical about their oral-aboral axis, body rotation only affects the x-components of the arms, which are not aligned with the image plane. A twelve-armed crinoid has an included angle between two arms of $\pi/6$ or 30° . Only the six most lateral arms $A-F$ could be tracked (Fig. 4.8), i.e. two arms were considered to be oriented perpendicular to the camera, while the other four arms are extended at an angle of 30° to the image plane. Therefore, the x-components P_{Ax} of these arms were corrected by rotation around the oral-aboral axis. When the distance between camera and object is much larger than the lateral object extension, the real P'_{Ax} can be approximated by trigonometric relations to the observed points P_{Ax} .

$$P'_{Ax} = \cos 30 P_{Ax} \quad (4.20)$$

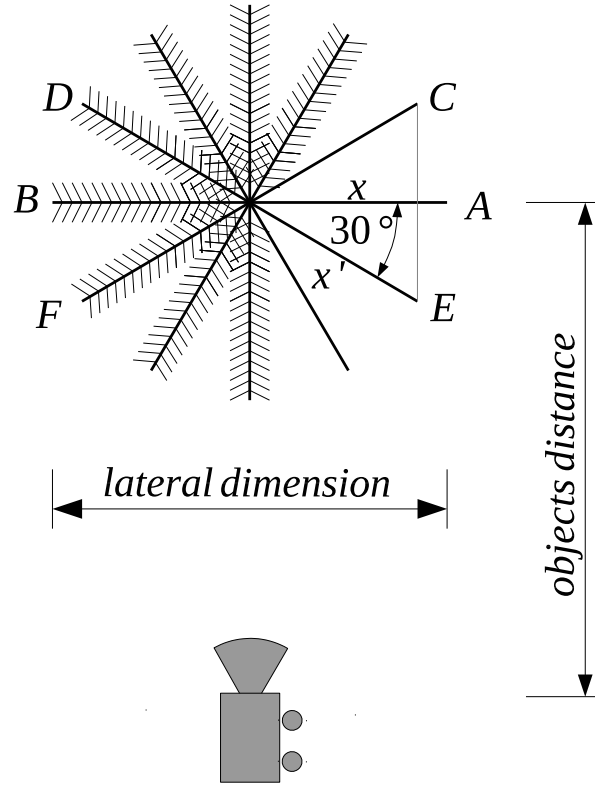


Fig. 4.8 Perspective arm rotation. Oral view of the organism. Arms *A* and *B* are aligned with the image plane. The arms *C* to *F* point at an angle of 30° to this plane.

Image Scaling in Relation to Camera Movement

After all image corrections had been made, the pixel coordinates could be converted into metric dimensions. Parallel lasers were used as reference on the images. Their distance represents a length of 0.04 m independent of the distance of the camera. An image-specific distance-to-pixel ratio is given as a scaling factor f_{scl} .

$$f_{scl} = \frac{0.04 \text{ m}}{n \text{ px}} \quad (4.21)$$

f_{scl} is the distance in metres between two adjacent pixels. Since true scales could only be obtained on images where organisms and reference lasers were on the same depth plane, one suitable image was selected at a time to determine the size of the organism represented by the arm length. All images of the same individual could now be scaled according to the arm length. Demonstrated here using the example of RS620018.

The image sequence contains 147 frames and includes five complete stroke cycles. Camera motion and crinoid movement have changed the scale and perspective throughout the video sequence. Image 128 (Fig. 5.4) was assigned as the reference image, since both lasers are pointing at the crinoid, the true scale can be seen in this image.



4.2 Locomotion Kinematics

Assuming that the arm length is the same in all images, the real dimensions can be related to this image. A linear regression was used to scale tracked splines on the same arm (Fig. 5.6). Splines were then subdivided according to brute dimensions. To eliminate length differences, all splines on the same arm were scaled with respect to the average spline length.

$$scl_i = \frac{a(ref.image) + b}{ai + b} \quad (4.22)$$

$$SPL_i = SPL_i scl_i \quad (4.23)$$

The scaling factor scl of the i^{th} image is the ratio to the reference image. The i^{th} -spline SPL is then scaled by the corresponding factor. The coefficients a , b and the reference images for all arms are listed in the table A.1.

Spline Split and Segment Kinematics

The splines were divided into segments according to the brachial length regression (Fig. 5.1). Due to the complexity of the parametric shape of the spline, an iterative approach based on Newtonian approximation has been developed, which divides the spline into unequal segments (Fig. 4.9). An essential part of this procedure is the determination of polynomial spline length elements, which were calculated by the following integral (Beyer et al., 1977):

$$s = \int_{t_1}^{t_2} \sqrt{(x'(t))^2 + (y'(t))^2} dt \quad (4.24)$$

With the exponential condition for the brachial length.

$$f(x) = 0.179e^{-0.109x+2.319} + 1.570, \text{ for } l = 1, \dots, n \quad (4.25)$$

This procedure was solved iteratively until the terminating residual of 10^{-6} m was reached. The iterative loop is shown in figure 4.9.

The generated slicing points S represent intersections of two adjacent segments (brachials). A segment itself was defined as a cylinder with its centre C midway between the two slicing points. Index is along the arm segments and index im through the images I have ranges of validity, $is = 1, \dots, S_{max} - 1$ and $im = 1, \dots, I_{max}$ for the following equations 4.26, 4.27 and 4.28. Considering that a stroke cycle is a repetitive process, the index $im + 1$ is 1 if im is I_{max} , or $im - 1$ is I_{max} if im is 1.

$$C_{is,im} = \frac{S_{is,im} + S_{is+1,im}}{2} \quad (4.26)$$

Once all splines of an arm are processed, each brachial has an equivalent segment on each image of the sequence. Linear and angular velocities, as well as their accelerations, can be derived for each segment by changing position and rotation from one image to

4. Methodology

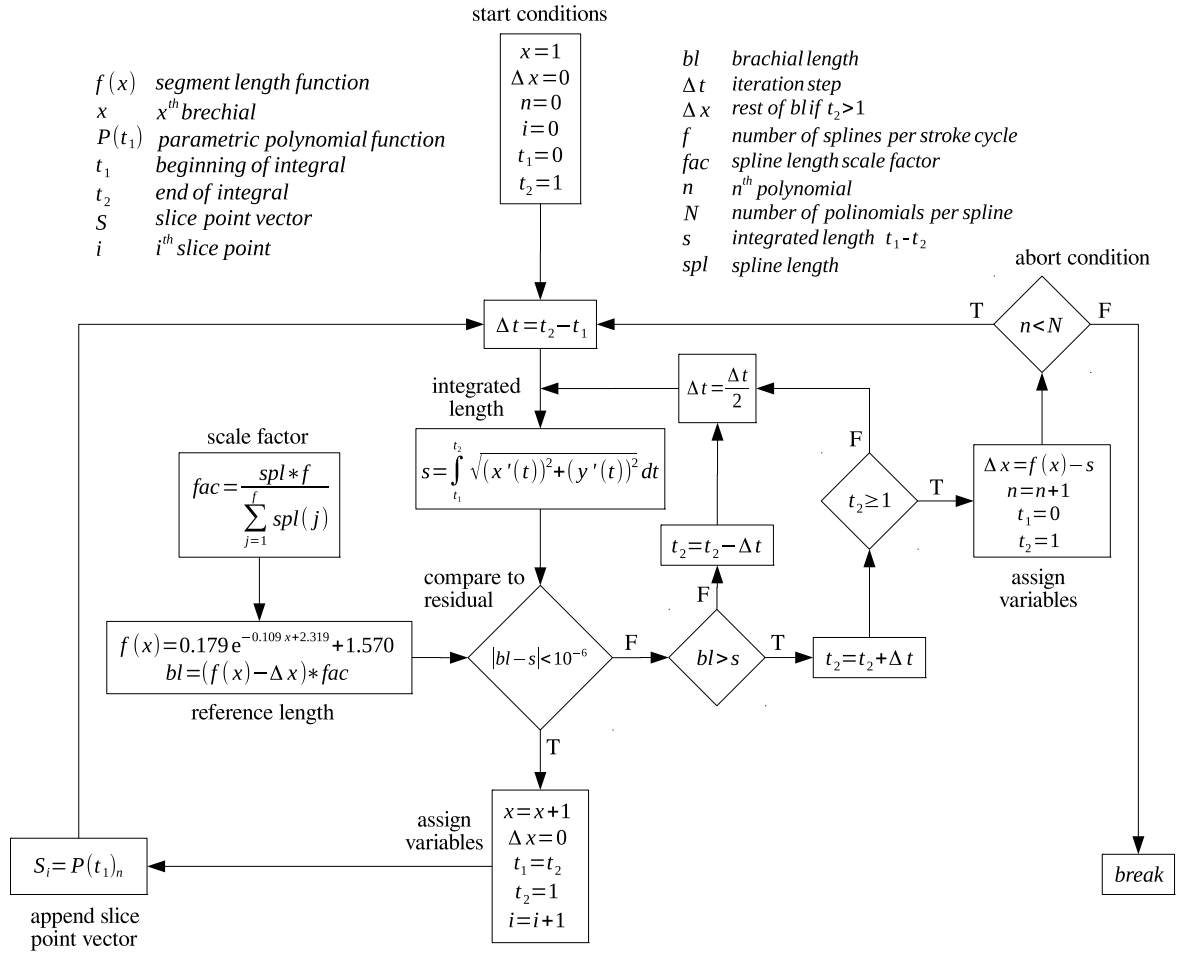


Fig. 4.9 Spline slicing process. The flowchart shows the iterative process for slicing a spline according to the brachial length regression. To ensure the same number of segments for all splines of the same arm, the splines were scaled to an average length.

the next. The time difference Δt , between two adjacent images I is $\frac{1}{15}$ of a second (Fig. 4.10).

$$\begin{aligned}
 u_{is,im}^{-\frac{1}{2}} &= \frac{C_{is,im} - C_{is,im-1}}{\Delta t} \\
 u_{is,im}^{+\frac{1}{2}} &= \frac{C_{is,im+1} - C_{is,im}}{\Delta t} \\
 u_{is,im} &= \frac{u_{is,im}^{+\frac{1}{2}} + u_{is,im}^{-\frac{1}{2}}}{2} \\
 a_{is,im} &= \frac{u_{is,im}^{+\frac{1}{2}} - u_{is,im}^{-\frac{1}{2}}}{\Delta t}
 \end{aligned} \tag{4.27}$$



4.2 Locomotion Kinematics

As a stroke cycle starts over in a repeating loop, velocities u and accelerations a are distinguished circularly. Velocities represent averages between two temporal instances, so their values are averaged at the current time step. Velocities before are given as $-\frac{1}{2}$ and after the current instance as $+\frac{1}{2}$.

$$\begin{aligned}
 \phi_{is,im} &= \tan\left(\frac{Sy_{is+1,im} - Sy_{is,im}}{Sx_{is+1,im} - Sx_{is,im}}\right) \\
 \omega_{is,im}^{-\frac{1}{2}} &= \frac{\phi_{is,im} - \phi_{is,im-1}}{\Delta t} \\
 \omega_{is,im}^{+\frac{1}{2}} &= \frac{\phi_{is,im+1} - \phi_{is,im}}{\Delta t} \\
 \omega_{is,im} &= \frac{\omega_{is,im}^{+\frac{1}{2}} + \omega_{is,im}^{-\frac{1}{2}}}{2} \\
 \alpha_{is,im} &= \frac{\omega_{is,im}^{+\frac{1}{2}} - \omega_{is,im}^{-\frac{1}{2}}}{\Delta t}
 \end{aligned} \tag{4.28}$$

Tracking inaccuracies increase with each differentiation. Small errors in locations can lead to large discrepancies of velocity and acceleration. A suitable and simple method for smoothing data points is a moving average filter (Eq. 4.29). The magnitude of a given vector is averaged from its previous, subsequent and own value. The degree of smoothing is controlled by the number of cycles or by increasing the number of grid points, e.g. five instead of three. There is a danger of over-filtering; too many cycles can distort the data and flatten the peak values. Assuming that the acceleration can only change smoothly and not erratically, the data sets were filtered until the acceleration followed a continuous course. Reasonable results were obtained by applying the filter twice to each data set using three grid points. The linear and angular velocities were derived from the filtered distances respectively angles, and the linear and angular accelerations were in turn derived from the filtered velocities. Data sets D in the range $i = 2, \dots, n - 1$.

$$D_i = \frac{D_{i+1} + D_i + D_{i-1}}{3} \tag{4.29}$$

$$N \in \mathbb{N} := \{3 \leq N + 2m \leq i \mid m \in \mathbb{N}\} : n \in \mathbb{Z} := \left\{ \frac{-N+1}{2} \leq n \leq \frac{N-1}{2} \right\}$$

4.2.2 Deriving an Averaged Kinematic Model

The final virtual model was averaged from morphology and kinematics. To be able to build an average kinematics from the individual arm dimensions and the different beat cycle lengths, I developed a method to scale each arm and its beat pattern in size and duration. Due to the varying number of beat cycles per individual, a model

4. Methodology

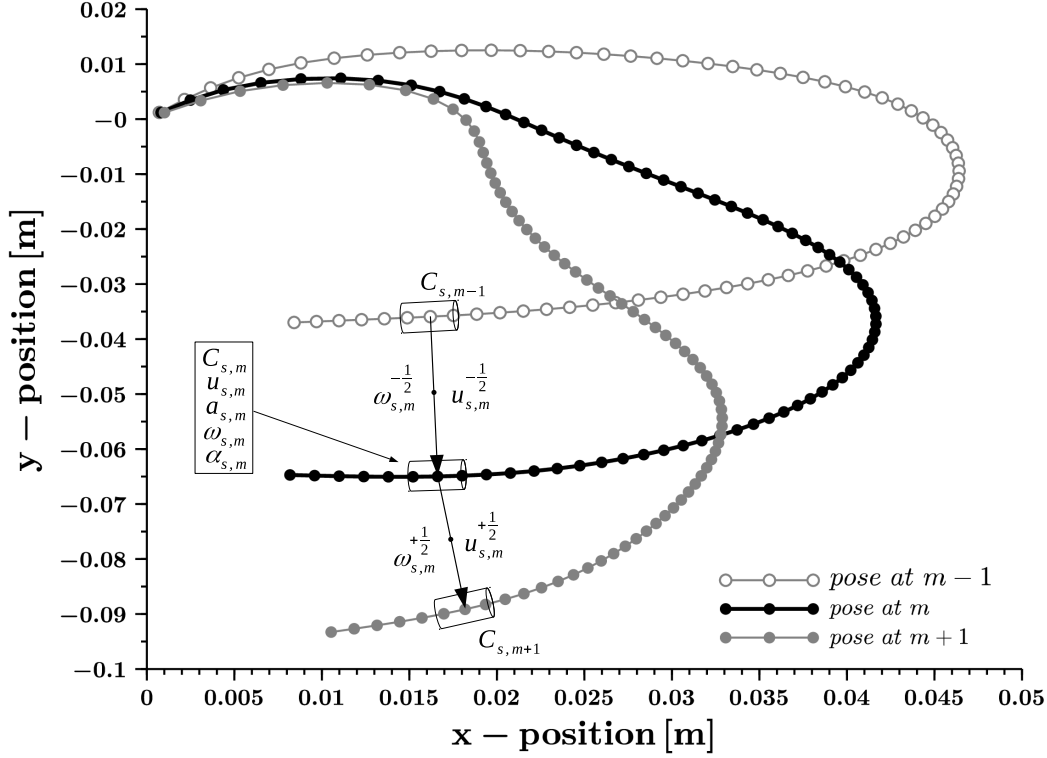


Fig. 4.10 Segment kinematics. Illustration of arm poses at three consecutive times $im - 1$, im and $im + 1$. To clean up the scene, the time difference Δt between two instances was chosen as $3/15$ s. A segment around its centre C changes position and orientation simultaneously. The linear and angular velocities as well as their accelerations were derived from the change in segment orientation and centre point positions.

of each organism was averaged before a mean species model could be created. Arm length was used as a measure of the size of the organism (Eq. 4.30).

$$\bar{l}_{arm} = \frac{\sum_1^4 \left(\frac{\sum_{i=1}^n l_i}{n} \right)}{4} \quad (4.30)$$

To form a cross-species average, the mean arm lengths of the individual organisms were first formed. All 53 arms were scaled to fit the length of the total average arm (Eq. 4.31).

$$P'_{arm} = P_{arm} \frac{\bar{l}_{arm}}{l_{arm}} \quad (4.31)$$



4.2 Locomotion Kinematics

tracking points P_{arm} were scaled by the ratio of average arm length to individual arm length.

The scaled points P'_{arm} were again spline-interpolated and intersected according to the morphological ratios (chapter 4.1). Since each beat cycle has an individual period, all 53 cycles had to be temporally averaged (Eq. 4.32). For this purpose, the orientation angles of the brachial segments were calculated (see above description). In order to reduce or increase the number of temporal steps to achieve an average stroke length, the step angles between the temporal instances were linearly interpolated (Eq. 4.34). A final step was necessary to create a complete averaged model. The arms were synchronised to a common start of the stroke cycle, here the start of the power stroke was chosen. At the end, each angle of each segment was averaged in space and time for a given instance.

$$\bar{T} = \frac{\sum_{i=1}^{53} T_i}{53} \sum_{i=1}^{53} T_i \quad (4.32)$$

$$\Delta t' = \frac{\bar{T}}{15T} \quad (4.33)$$

Mean period \bar{T} in [s]) is the average over all stroke cycles. The scaling Δt between two frames was determined as a ratio to the mean period \bar{T} . The factor 15 is thereby the original frame rate.

$$\phi'_i = (\phi_{j+1} - \phi_j) \frac{\Delta t'}{\Delta t} + \phi_j \quad := \{j \mid i\Delta t < (j+1)\Delta t' \ \& \ i\Delta t \geq j\Delta t'\} \quad (4.34)$$

Index $i = \{0, \dots, n\}$ with $n = \bar{T} * 15$ and index $j = \{0, \dots, m\}$ where m is the number of frames from the original stroke cycle. The new angle ϕ' at the run-time variable i is linearly interpolated at the position j where the condition on the right-hand side is fulfilled.

$$\bar{\phi}'_i = \frac{\sum_{j=1}^{53} \phi_j}{53} \quad (4.35)$$

Here index i stands for the runtime variable of the segments over the arm and index j for the tracked arm itself. After averaging the movement pattern of an arm swing, the entire kinematics for the new standardised movement had to be calculated again.

4.2.3 Pinnule Pose

The pinnules are unfolded laterally at an angle of 67.1° to the arm axis during power strokes ($n=29, \pm 7.1^\circ$), while they align along the arm axis during recovery strokes (Fig. 4.2). An approach to automate flapping as a function of thrust generation was therefore developed. Assuming that pinnules in the unfolded state increase fluid dynamic drag, they would only contribute productively in a backstroke faster than the forward swimming speed, i.e., the power stroke is characterised by thrust generation,

4. Methodology

while a recovery stroke is dominated by drag. A power stroke was divided into three subphases. The initial phase, in which the arm is first moved outwards, the general power phase and a retraction phase, in which the arm is pulled towards the oral-aboral axis of the body. During the first and third parts of a force stroke, the lateral velocities are dominant. To account for both phases, the algorithm was modified to consider the arm movement as a power stroke if the backward movement is greater than 60% of the lateral velocity. With this constraint, the folded and unfolded states of the pinnules were determined automatically. Since the swimming velocity must be known to determine the force or recovery stroke state, and this is a result of the fluid dynamic analysis, but these in turn depend on the pose of the pinnules, the whole process was solved iteratively until a predefined residual of 10^{-5} was reached.



4.2 Locomotion Kinematics

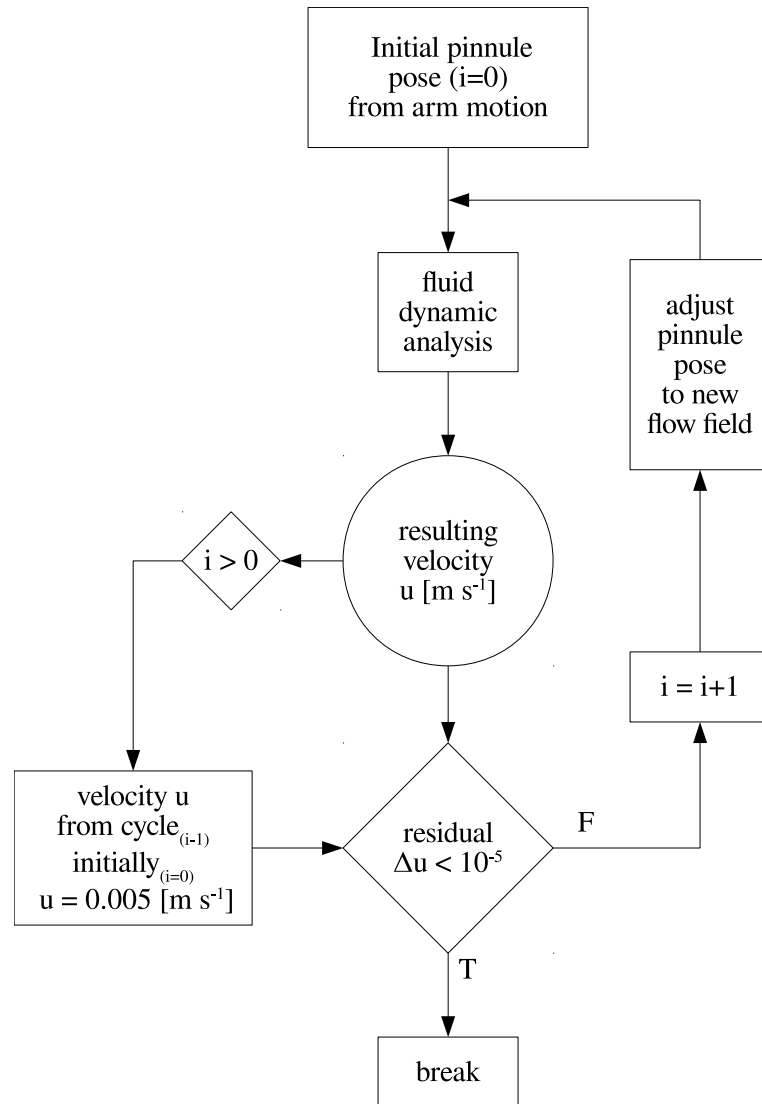


Fig. 4.11 Automated pinnule flap. Flow chart showing the iterative adjustment of the pinnules position within the fluid dynamic analysis.

4.3 Analytical Fluid Dynamics

4.3.1 Fluid Properties of Seawater

The resistance that an object generates during a relative movement in a fluid depends on the fluid properties density and viscosity in addition to the speed of movement. The higher both values are, the more drag is generated and vice versa. This relationship is expressed as a dimensionless characteristic factor, the drag coefficient cd in the equations 4.44 and 4.45. The drag coefficient is also a function of the Reynolds number Re (Eq. 3.1), which describes the relationship between the size and velocity of an object to the ratio of the density and viscosity of the fluid. Aquatic organisms live in an environment surrounded by seawater, the properties of which are strongly dependent on temperature, salinity and pressure. Especially in the waters on the Antarctic continental shelf, extreme environmental conditions prevail with water temperatures even below freezing, high salinity and deep waters with high pressures. Dr. Jörg Kuder from the Leibniz Institute for Applied Geophysics in Hannover provides a method for calculating density and viscosity for saltwater², whose method is based on the work of Rowe and Chou (1970).

Density of seawater

The density ρ , in $[\text{kg m}^{-3}]$, is a function of pressure, salinity $NaCl$ and temperature according to Kuder (2011, Eq. 8, p. 5).

$$V = A(T_k) - pB(T_k) - p^2C(T_k) - xD(T_k) + x^2E(T_k) - xpF(T_k) - x^2pG(T_k) - \frac{1}{2}xp^2H(T_k) \quad (4.36)$$

Specific volume V in $[\text{cm}^3 \text{g}^{-1}]$, temperature T_k in $[\text{K}]$, absolute pressure p in $[\text{kpond cm}^{-2}]$, and the mass fraction x of the salt $NaCl$. If the pressure is given in $[\text{MPa}]$, the absolute pressure can be calculated with the following equation. The expressions A-H are given in the table B.1 on page 177.

$$p_{abs} = \frac{p \cdot 100}{g} \quad (4.37)$$

Absolute pressure in $[\text{kpond cm}^{-2}]$ is derived from pressure p , in $[\text{MPa}]$.

$$\rho = \frac{1,000}{v} \quad (4.38)$$

The density ρ in $[\text{kg m}^{-3}]$ is derived from the specific volume V in $[\text{cm}^3 \text{g}^{-1}]$ from equation 4.36.

²Technical report for methods for determining fluid properties is available at <https://www.liag-hannover.de/fileadmin/produkte/20110503152409.pdf> (July 2019)



4.3 Analytical Fluid Dynamics

Viscosity of seawater

Analogous to density, the viscosity of a liquid is changed by its properties temperature, pressure and salt content $NaCl$. Kuder also provides a method for this purpose (Kuder, 2011, Eq. 16, p. 13). The concept is based on the hypothesis that the total viscosity of a liquid is composed of the viscosities their individual components.

The first contribution is sodium chloride $NaCl$ with its dynamic viscosity μ_{NaCl} , in [mPas]. It depends on the temperature and its specific weight fraction w respectively mass contribution.

$$w_{H_2O} + w_{NaCl} = 1 \quad (4.39)$$

With this relationship, the dynamic viscosity of $NaCl$ is determined as follows:

$$\mu_{NaCl} = \frac{\exp\left(\frac{v1(1-w_{H_2O})^{v2}+v3}{v4T_c+1}\right)}{v5(1-w_{H_2O})^{v6}+1} \quad (4.40)$$

The coefficients $v1$ to $v5$ are listed in the table B.2 on page 177. T_c [°C] is its temperature and w_{H_2O} refers to the weight fraction of water.

Secondly, the dynamic viscosity of pure water is calculated according to the IAPWS-IF 97 standard, see (Kuder, 2011, Eq. 13, p. 11) and (Wagner et al., 2000).

$$\Gamma = \sum_{i=1}^{19} \left(n_i \left(\frac{\rho}{317.763 \text{ kg m}^{-3}} - 1 \right)^{I_i} \left(\frac{647.226 \text{ K}}{T_k} - 1 \right)^{J_i} \right) \quad (4.41)$$

The equation for calculating the dynamic viscosity for pure water μ_{H_2O} was divided into two parts. The temperature T_k , in [°K] and the density ρ in [kg m^{-3}]. The coefficients I_i , J_i and n_i in the term Γ are given in the table B.3 on page 178.

$$\mu_{H_2O} = \frac{55.071 \cdot 10^{-6} \text{ Pa s}}{\sqrt{\frac{647.226 \text{ K}}{T}} \sum_{i=0}^3 \left(n_i^0 \left(\frac{647.226 \text{ K}}{T} \right)^i \right)} \exp\left(\frac{\rho}{317.763 \text{ kg m}^{-3}} \Gamma \right) \quad (4.42)$$

Using Γ from equation 4.41, the dynamic viscosity of pure water μ_{H_2O} , in [Pa s], is calculated with the coefficient n_i^0 given in table B.4 on page 178.

$$\mu = \exp\left(w_{H_2O} \log(\mu_{H_2O}) + w_{NaCl} \log(\mu_{NaCl}/1,000) \right) \quad (4.43)$$

Finally, the dynamic viscosity of seawater μ , in [Pa s], is obtained by multiplying the weight fraction of its components by the logarithm of their specific viscosities. Since μ_{NaCl} is given in [mPa s], it must be divided by 1,000 to obtain [Pa s].

4. Methodology

4.3.2 Thrust from Drag

The kinematic data described in section *Locomotion Kinematics* (4.2) and the fluid properties from section *Fluid Properties of Seawater* (4.3.1), form the basis for the analytical fluid dynamics. Here I have developed an approach to quantify the hydrodynamic properties of a swimming crinoid. The entire body structure of the crinoid was composed of small cylinders, with the only exception being the calyx (the body), this was simplified as a sphere. Analytical solutions exist for both geometric shapes if the system to be calculated is laminar and has a Reynolds number less than 2,000. The general concept is to calculate the drag forces for each segment at all temporal instances of a stroke cycle. In a resistance-based prediction, the difference between drag and thrust is found only in the direction of action of the force vector; a decelerating force is called drag and an accelerating force is called thrust. Calyx, cirri and primi-brachials are only pulled through the water and are therefore called passive elements whereby they also only produce drag. Active parts of the arms (brachials and pinnules) can either generate drag when they are pulled forward during the recovery stroke, but also generate thrust when they are moved backwards during the power stroke. When the total thrust generated overcomes the net resistance plus the gravitational force, the resulting force vector accelerates the organism until the increasing drag equals the thrust, so that a final velocity is established.

The flow around a cylinder can be divided into two components. Normal to its major axis - perpendicular to the cylindrical surface - and along the major axis parallel to it (Fig. 4.12). In contrast, a sphere, due to its geometric nature, has only one component normal to the surface in all direction.

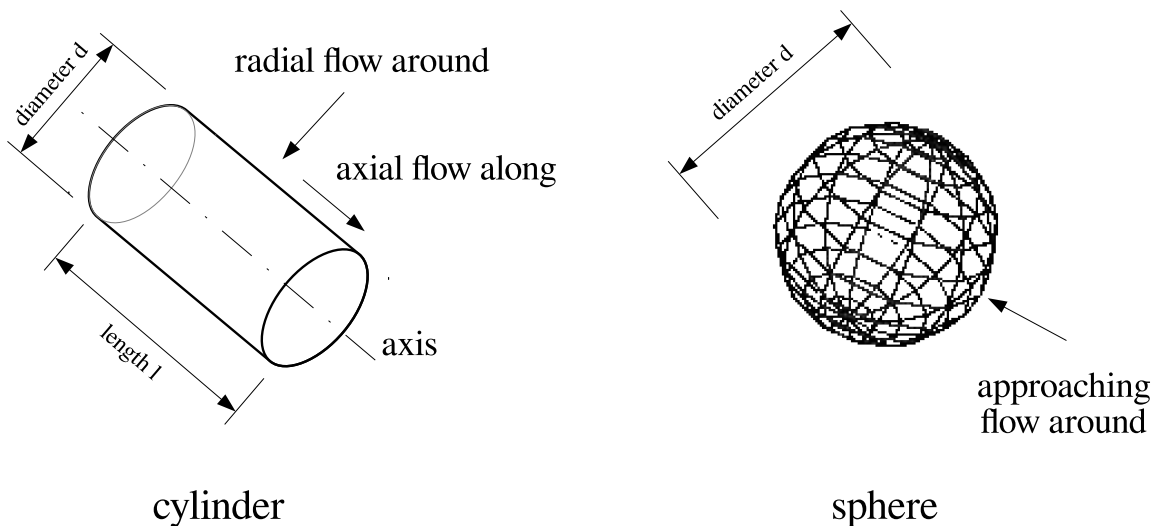
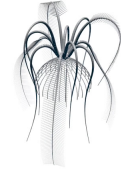


Fig. 4.12 Flow nomenclature. Basic concept of flow around cylinder and sphere. The component that points normal to the axis is the radial flow, the axial flow is parallel to the cylinder. A sphere has only one component due to its spherical symmetry.



4.3 Analytical Fluid Dynamics

Each cylinder has its individual orientation according to its position, direction of movement and rotation. Both orientation and direction change continuously during the swimming movement. Figure 4.13 illustrates the transformation of direction of motion, its radial and axial components and again its horizontal and vertical components. The resistance generated by the radial and axial flow has an analytical solution. Vertical in this context refers to the oral-aboral axis or the swimming direction, therefore only vertical forces contribute to the thrust. The horizontal vectors cancel each other out assuming a symmetrical pattern of movement through opposing arms.

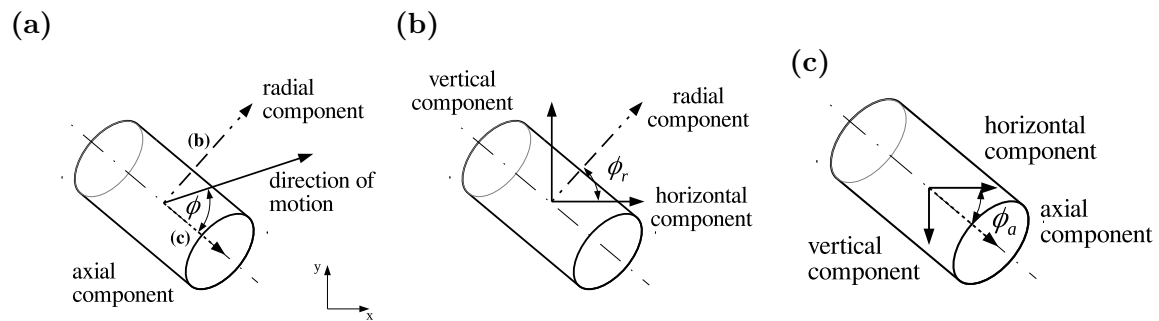


Fig. 4.13 Cylinder movement and thrust force components. Illustration to show the relationship between the direction of force and the direction of movement of the cylinder. **a** Its radial and axial parts have global x and y components. **b** shows the vertical and horizontal components of the radial part and **c** highlights them for the axial part. Only vertical components contribute to the positive thrust force. Horizontal components result in a lateral force.

The coordinate transformation angle ϕ between the motion vector and the orientation of the cylinder determines the radial and axial velocity components. ϕ_r describes the relationship between the radial component and its vertical and horizontal velocities and ϕ_a correspondingly the axial velocities.

The following sections describe the process of analytical fluid dynamics in which the thrust and drag forces involved in locomotion are calculated from the kinematics of the movement and the morphology of the animals. To do this, the Reynolds numbers for each body segment must first be determined, as they form the basis for an applicability of the analytical analysis. This only has a range of validity for Reynolds numbers Re smaller than 2,000 (Eq. 3.1).

4.3.3 Drag Coefficient

In order to be able to determine the resistance force of an object, the drag coefficient cd can first be calculated. This puts the occurring force in relation to the speed of movement, the geometry and the fluid properties. Since the drag coefficient is also a function of the Reynolds number of an object, it can be determined for both the radial and the axial incident flow without knowledge of the occurring forces.

Radial Flow Around Cylinder

The Lamb method provides a way to determine the dimensionless drag coefficient cd for the radial flow around a cylinder, but with the restriction of the Reynolds range smaller than 1 (Lamb, 1932). The Lamb equation 4.44 can be converted into a Reynolds-based form 4.45.

$$cd = \frac{8 \pi \mu}{\frac{1}{2} - \gamma - \log(\frac{U d}{8 \nu})} \quad (4.44)$$

$$cd = \frac{8 \pi}{Re (2 - \log(Re))} \quad (4.45)$$

Kümmel (2007) describes an equation from which the drag coefficient for an extended Reynolds range $1 \leq Re \leq 2,000$ can be calculated analytically (Kümmel, 2007, p. 233).

$$cd = 0.94 + \frac{10}{\sqrt[3]{Re^2}} \quad (4.46)$$

Axial Flow Along Cylinder

The resistance caused by a fluid flowing along the cylinder surface, and therefore only shear forces, was considered as flow over a flat plate. The calculation of the drag coefficient of a flat plate can be determined from the Reynolds number as follows (Schlichting et al., 2006, p.160, Eq. 6.59)

$$cd = \frac{1.328}{\sqrt{Re}} \quad (4.47)$$

4.3.4 Drag Force

The force F can now be derived for both cases from the drag coefficient cd , a specific area A and the relative velocity between object and fluid u .

$$F = \frac{1}{2 \rho cd A u^2} \quad (4.48)$$



4.3 Analytical Fluid Dynamics

The drag force F , in [N], depends on the density ρ of the fluid, in [kg m^{-3}], the drag coefficient cd , a specific area A , in [m^2], and the relative velocity u , in [m s^{-1}]. The specific area A ($A = l d$) of the radial incident flow is the cross-section resulting from the length l and diameter d . Fluid flowing along a cylinder in the axial direction and interacting with the surface has a specific surface area A in the form of $A = d \pi l$ (Oertel, 2006, p. 35, Eq. 1.3).

4.3.5 Brachial Motion

Only force components in the swimming direction, which result from either radial or axial movement, contribute to the forward thrust. As long as the orientation of the crinoid is vertical, the y-components of the force vectors point in the swimming direction. For the motion kinematics of a cylinder, the radial u_r and axial u_a velocity components were transformed using the rotation matrix R_ϕ (Eq. 4.49). Figure 4.13 illustrates the relationship between the direction of motion, its normal and axial components and the forward and sideways components respectively.

$$R_\phi = \begin{pmatrix} \cos \phi & -\sin \phi \\ \sin \phi & \cos \phi \end{pmatrix} \quad (4.49)$$

$$\begin{pmatrix} u_a \\ u_r \end{pmatrix} = R_{-\phi} \begin{pmatrix} u_x \\ u_y \end{pmatrix} \quad (4.50)$$

Axial u_a and radial velocity u_r , in [m s^{-1}], are derived from the direction of the absolute velocity and the negative angle $-\phi$ of the cylinder orientation. Then the two velocity components are transformed back into absolute x- and y-components.

$$\begin{pmatrix} u_{ax} \\ u_{ay} \end{pmatrix} = R_\phi \begin{pmatrix} u_a \\ 0 \end{pmatrix} \quad (4.51)$$

$$\begin{pmatrix} u_{rx} \\ u_{ry} \end{pmatrix} = R_{\phi+\pi/2} \begin{pmatrix} u_r \\ 0 \end{pmatrix} \quad (4.52)$$

The transformation angle requires special attention in all three rotations. Remember that the angle ϕ is the absolute orientation of the cylinder. In the first step, axial and radial components are obtained from the absolute motion vector by rotating it through the negative orientation angle $-\phi$. In the second step, the absolute x and y components are derived from the axial and radial motion. Each vector has only one x-value from a local point of view, therefore the y-component is zero in both cases. The axial part is rotated back by the positive angle ϕ , since the radial vector is normal to the axis, $\pi/2$ is added to ϕ (Fig. 4.13b and c).

4.3.6 Pinnule Motion

Pinnules require an additional transformation to account for the three-dimensional character of the unfolded structures. If pinnules were perpendicular to their associ-

4. Methodology

ated brachials, they would have a global orientation along the z-axis normal to the arm coordinates. Due to their rotational symmetry, axial and radial flow vectors from brachial motion would always point normally to a pinnule cylinder. However, since pinnules exhibit an angle of attack smaller than 90° , the axial velocity field leads to an additional warping component that necessitates a further transformation. Radial components flow vectors, on the other hand, continue to be normal on the pinnule segments. Both motion components are determined analogously to the brachial transformation in the section 4.3.5. The system now obtains a three-dimensional structure, whereby the z-components of the opposing pinnules cancel each other out and can thus be neglected. The first step is to obtain the local components of the pinnules from the global axial flow. The pinnule angle ψ relative to the brachial orientation is determined as 67.1° (for detailed information see section 4.2.3).

$$\begin{pmatrix} u_{pa} \\ u_{pr} \end{pmatrix} = R_\psi \begin{pmatrix} u_a \\ 0 \end{pmatrix} \quad (4.53)$$

Local pinnule velocities in axial u_{pa} and radial direction u_{pr} are used to calculate a local force field according to the procedure explained earlier in this section. Forces acting on the pinnule segments must be transformed back into global vectors. These forces have three dimensions, but the z-field is neglected because of symmetry. The re-orientation can therefore be simplified as shown in equation 4.54. The two-dimensional force vector F_a with its x- and y-components in the direction of the brachials is obtained by rotating backwards by the pinnule angle $-\psi$. Figure 4.14 illustrates the relation to the brachial segment and the three-dimensional character of the pinnular components.

$$\begin{pmatrix} F_{ax} \\ F_{ay} \end{pmatrix} = R_{-\psi} \begin{pmatrix} F_{pa} \\ F_{pr} \end{pmatrix} \quad (4.54)$$

Finally, the axial force vector is reduced to global components.

$$\begin{pmatrix} F_x \\ F_y \end{pmatrix} = R_\phi \begin{pmatrix} F_{ax} \\ F_{ay} \end{pmatrix} \quad (4.55)$$

As described in the section *Morphology and the Virtual Design* (4.1), the pinnules are unfolded during the power stroke, during the recovery stroke they are collapsed and merge with the brachials to form a solid cylinder. This fact has a fundamental influence on the force calculation. Pinnular forces are only relevant during the power stroke, whereas they do not have to be calculated during the recovery stroke. Instead, the fused segments are calculated according to the scheme of the brachial segments (Sec. 4.1).

4.3.7 Body Drag

The only exception within the computer model is the calyx (body), which was assumed simplified as a sphere. The drag force F_{cal} for laminar flow $Re < 2,000$ is determined



4.3 Analytical Fluid Dynamics

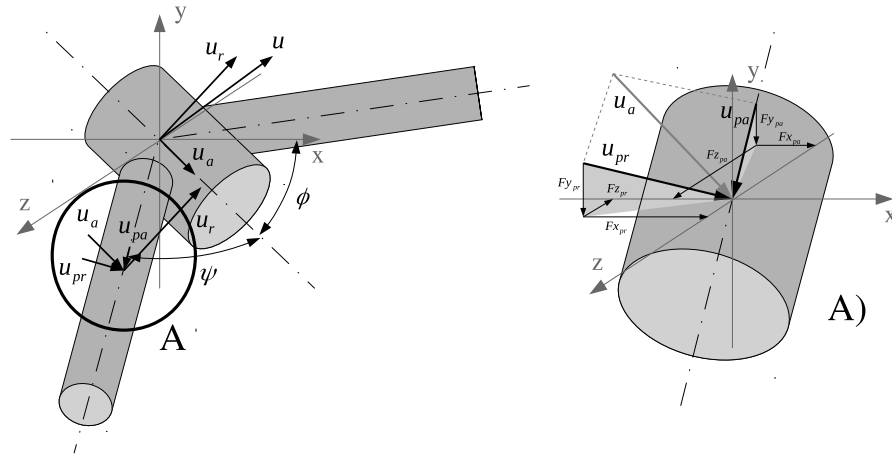


Fig. 4.14 Fluid components of the pinnules. Illustration of the fluid dynamic components of the pinnules. The left side shows a brachial segment with the associated pinnules. The brachial is inclined by the angle ϕ and the pinnules are unfolded at the angle ψ . The direction of movement u has a radial u_r and axial u_a component of velocity. As shown, u_r is also normal to the pinnule axis, while u_a has the local pinnule components u_{pr} and u_{pa} . Detail A) shows the relation to the three-dimensional force vector F . The F_z components cancel each other out due to the symmetrical orientation of the pinnule pairs.

directly from the fluid dynamic viscosity μ , in [Pa s], the velocity u , in [m s^{-1}], and the diameter d , in [m], of the sphere itself (Stokes, 1850; Lamb, 1932).

$$F_{cal} = 3\pi\mu ud \quad (4.56)$$

4.3.8 Total Forces of Swimming Crinoid

The sum of all individual components results in the total thrust of the swimming organism, which leads to acceleration and the swimming speed derived from it.

A total of 53 virtual models were calculated, which originate from a total of 4 organisms, each with 6 arms and different numbers of stroke cycles. A model always consists of a passive part with a calyx, the associated cirri and the primibrachials. The active components are represented, according to the morphology of *Promachocrinus kerguelensis*, by 12 arms composed of brachials (arm segments) each with two associated pinnules. Each model was assembled for a single arm and a specific flapping cycle. That is, each model was composed of a passive part and twelve identical arms. In addition, the kinematically averaged model was calculated accordingly.

$$F_{res} = 12(F_{bra} + F_{pin}) + F_{dor} + F_{cir} + 6F_{pri} + F_g \quad (4.57)$$

The resultant force F_{res} is a twelvefold of the arm, which consists of brachial F_{bra}

4. Methodology

and pinnule F_{pin} components. Opposed to this are the drag forces from calyx F_{cal} , cirri F_{cir} and primibrachial F_{pri} as well as the sum of all segment weights F_g .

In equation 4.57 all forces acting on all segments involved are combined. The arms generate the thrust that propels the organism forward, while the resistance of the body and the weight act in the opposite direction. According to the morphology in the section 4.1, all arms have an individual number of brachial segments nob . Each brachial is connected to two pinnules with a specific number of pinnulars $nops$, so from this relationship the two terms $\sum F_{bra}$ and $\sum F_{pin}$ sum up over the arm.

$$F_{bra} = \sum_{i=1}^{nob} F_{bra_i} \quad (4.58)$$

$$F_{pin} = 2 \sum_{i=1}^{nob} \sum_{j=1}^{nops} F_{pin_{ij}} \quad (4.59)$$

The cirri and primibrachials were formed analogously to the ratios given in the section 4.1.3. The calyx is surrounded by 6 primibrachials and 30 cirri noc with 29 segments $nocs$.

$$F_{cir} = \sum_{i=1}^{noc} \sum_{j=1}^{nocs} F_{cir_{ij}} \quad (4.60)$$

The last term, the gravitational influence counteracting the thrust forces, is determined from the volume V and density ρ of the whole organism.

$$F_g = \left(\sum V_{bra} + \sum V_{pin} + \sum V_{pri} + \sum V_{cir} + V_{dor} \right) \rho \quad (4.61)$$

This calculation only includes the state of one time instance. However, a stroke cycle comprises a stroke frequency-dependent number of frames nof determined by the frame rate with 15 frames per second. The total net force over the entire cycle is therefore the average F_{avg} of all time instances.

$$F_{avg} = \frac{\sum_{i=1}^{nof} F_{res_i}}{nof} \quad (4.62)$$

The following section describes how the vertical swimming speed, the maximum weight and the horizontal locomotion speed can be derived from the net forces.

4.3.9 The Iterative Process of the Locomotion Parameters (Speed and Weight)

The parameters characteristic of locomotion, swimming speed and maximum payload, were used to evaluate the fluid dynamic calculations and form the basis for the migration model. Since the hydrodynamic force components, thrust and drag, are functions of the relative velocity between fluid and object, which in turn are dependent on the flow field at a specific swimming speed, both parameters can only be solved numerically.



4.3 Analytical Fluid Dynamics

Maximum Organism Mass

The maximum payload of an organism is considered to be the condition where weight and thrust are equal. As a result of this equilibrium, the resulting swimming speed is zero, i.e. the organism is just able to maintain its height above the seabed without experiencing a vertical change in position. The numerical procedure for finding this equilibrium is determined by successively adjusting the mass of the organism. The schematic drawing in Figure 4.16 shows the general iterative process based on a Newton's approximation. For this, a starting weight of the organism of 3 g was used. The evaluation criterion of the process is the resulting thrust from the fluid dynamics. The difference between thrust force F_{thr} and weight force F_g must be zero if both forces are in equilibrium. A limit value smaller than 10^{-5} was assumed as the residual ΔF , here $\Delta F = F_g - F_{thr}$. In the running process, the runtime variable var is successively adjusted according to ΔF . If ΔF is greater than zero, the mass is greater than the generated thrust, then the mass is reduced by half from the adjustment of Δvar , otherwise the mass must be increased.

Residual condition:

$$F_g - (12(F_{bra} + F_{pin}) + F_{dor} + F_{cir} + 6F_{pri}) = 0 \quad (4.63)$$

Maximum Vertical Swimming Velocity

The procedure for finding the maximum swimming speed is analogous to the procedure for finding the maximum payload (Fig. 4.16). The only difference here is the runtime variable. Here, the mass is kept constant and the swimming speed is successively adjusted. The same iteration cycle starts with an initial value for the swimming speed of 50 mm s^{-1} . The residual of the swimming is reached when the thrust for a given speed is equal to the weight plus the drag.

Residual condition:

$$F_g + F_{dor} + F_{cir} + 6F_{pri} - 12(F_{bra} + F_{pin}) = 0 \quad (4.64)$$

Maximum Horizontal Swimming Velocity

For the migration model, only the horizontal swimming speed is considered. Assuming that a crinoid tilts its locomotion vector in one direction and thus also the thrust vector, the latter receives a vertical and a horizontal component. The y-component controls the regulation of the height above ground, while the x-component causes the horizontal locomotion. Let us assume the situation: The pitch axis comes to a point where the vertical y-component just compensates for the weight, then the organism would remain at a constant height above the seabed. The remaining thrust, now coming from the x-component, pushes the organism forward with a horizontal velocity that reaches an equilibrium of horizontal thrust to horizontal drag (Fig. 4.15).

Since the maximum vertical swimming speed was calculated in previous steps, the total thrust force F_{thr} generated by the arm movements is known, as well as the

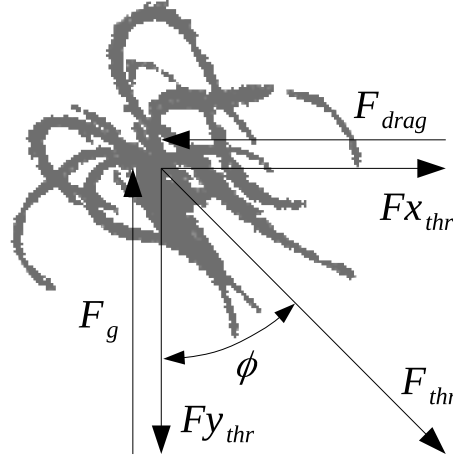


Fig. 4.15 Thrust components of horizontal swimming. Swimming crinoid at an angle of inclination where the vertical thrust $F_{y_{thr}}$ compensates for the weight F_g and the horizontal thrust component $F_{x_{thr}}$ is in equilibrium with the horizontal drag F_{drag} .

weight F_g of the organism has already been determined. If now the y-component of the thrust $F_{y_{thr}}$ is equal to the weight force, the horizontal thrust $F_{x_{thr}}$ is obtained by the trigonometric relation:

$$F_{x_{thr}} = \sqrt{F_{thr}^2 - F_g^2} \quad (4.65)$$

In the following iteration loop with the residual condition of the equation 4.66, the horizontal swimming speed is adjusted until resistance F_{drag} and thrust $F_{x_{thr}}$ are equal. The procedure follows the scheme in figure 4.16.

$$F_{dor} + F_{cir} + 6F_{pri} - F_{x_{thr}} = 0 \quad (4.66)$$

After all locomotion parameters were solved for 53 virtual models, an average was taken as a measure of characteristic values for *Promachocrinus kerguelensis*. All fluid dynamics were solved only once for the averaged kinematic and morphological model.

Tracked Vertical Swimming Velocity

The distances covered during vertical swimming were determined from the video footage in order to later assess the quality of the model. The projected position on the seabed was estimated on each first and last frame of the swimming sequences. The scale was adjusted - if not available for the respective image - as a fraction of the displayed organism size. The height of the calyx centre above the estimated position on the seabed was measured in image pixels and then geometrically corrected according to the method described in section *Rectification of Lens Geometry and Camera Pitch*



4.3 Analytical Fluid Dynamics

(4.2.1). The swimming speed is then the distance – difference between start and end height – multiplied by the number of images at a frame rate of 15 fps. The maximum and minimum distances, the mean values of which were arithmetically calculated, are derived from the areas of stay on the seabed.

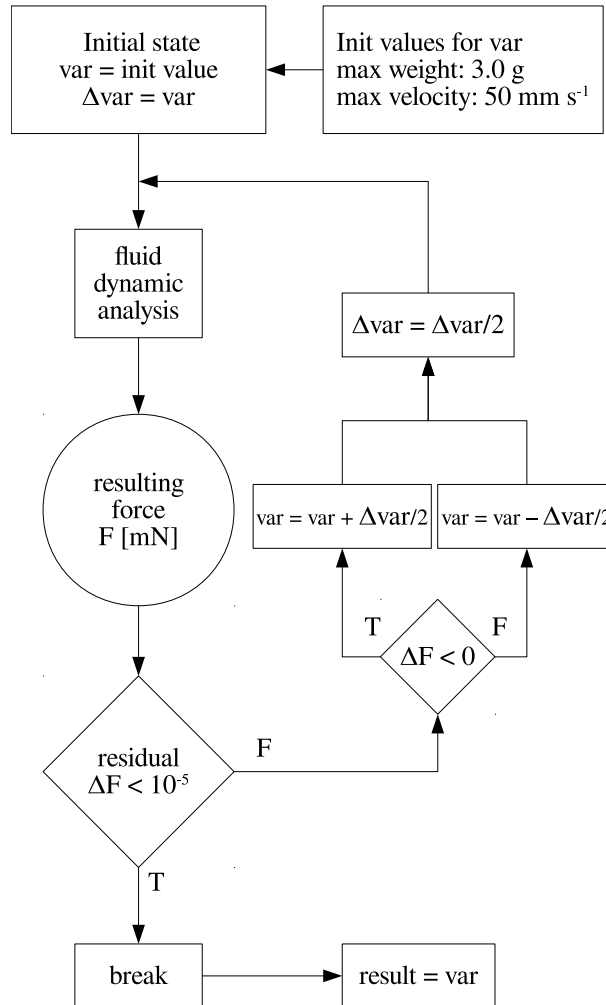


Fig. 4.16 Schematic representation of an iterative cycle. Flow chart of Newton's approximation to determine the maximum weight, vertical and horizontal swimming speed. The runtime variable var is adjusted after each iteration until the residual is less than 10^{-5} .



4.4 Inverse Dynamics

4.4 Inverse Dynamics

Here I describe how the inverse dynamics method can be applied to a swimming crinoid *Promachocrinus kerguelensis*. With this method it is possible to derive the load within a dynamic system from the movement of the structure and the external forces acting on it. Kinematic data, the quantitative description of the locomotor motion sequences with their parameters velocity and acceleration, were obtained from video recordings of swimming *P. kerguelensis* in their natural environment on the Antarctic continental shelf (chapter 4.2). More detailed information on the required data of the physiology and morphology of the organisms is given in chapter *Morphology and the Virtual Design* (4.1). Inverse dynamics is a common method in human physiology, but is rarely applied to animal locomotion. Winter (2009) describes in detail the method and its background for the analysis of human gait. The basic difference to Winter's method is the determination of the external loads on the skeletal system. Terrestrial organisms use the ground reaction forces on substrates, which counteract the acceleration of the organism. Aquatic animals, on the other hand, depend on the inertial effects of the surrounding medium. Swimmers propell themselves through the water column with the necessary reaction forces being applied by the inertia of the surrounding water. While it is still possible to determine the total thrust, measuring the hydrodynamic forces on the individual body segments is very difficult. These can nevertheless be calculated using an analytical approach, see chapter *Fluid Properties of Seawater* (4.3.1).

The inverse dynamics is based on three equations (for a two-dimensional case). The first two equations define that the sum of all forces in both x- and y-directions F_x , F_y is equal to the total net force of their motion vectors, given as mass times acceleration. The third equation applies analogously to the moments M . The sum of all moments is equal to the mass times the moment of inertia I_0 , from the rotational motion.

$$\begin{aligned} 1. \quad & \sum F_x = m a_x \\ 2. \quad & \sum F_y = m a_y \\ 3. \quad & \sum M = I_0 \alpha \end{aligned} \tag{4.67}$$

To apply inverse dynamics to brachials, the anatomical structure must be decomposed into free-body segments, as shown in figure 4.17. All the necessary variables of a single brachial are presented in figure 4.18.

The term *segment* is used in this context for subsections of the arm that include a brachial *bra* and all associated pinnules *pin*. Fluid dynamic forces and masses of arm segments are always the sum of all involved segments and forces.

$$\begin{aligned} D &= D_{bra} + 2(\sum_{i=1}^n D_{pin}) \\ m &= m_{bra} + 2(\sum_{i=1}^n m_{pin}) \end{aligned} \tag{4.68}$$

The number of pinnulars n depends on the length of the pinnule and their morpho-

4. Methodology

logical size ratio (Sec. *Morphology and the Virtual Design* (4.1)).

Table 4.3 summarises all components involved in solving the three equations of inverse dynamics (Eq. 4.67). The parameters are distinguished into known and unknown variables. Force and moment acting on a distal joint are unknown until solved for the proximal end of the distally adjacent segment. According to the principle of reaction forces, they act in opposite directions with the same magnitude. Starting with the last segment at the tip of the arm, this has an open end and no adjacent segment, therefore no forces and moments that occur distally. This situation allows the system of equations to be solved. Then all other segments can be calculated sequentially. The following equation system (Eq. 4.67) is solved for the unknown components at the proximal joint R_{xp} , R_{yp} and M_p .

Tab. 4.3 list of inverse-dynamic parameters. Known and unknown components of a free-body segment.

	variable	unit	description
known	a_x, a_y	$[\text{m s}^{-2}]$	linear acceleration at CoM
	α	$[\text{rad s}^{-2}]$	angular acceleration
	Θ	$[\text{rad}]$	angle in plane movement
	x_p, y_p, x_d, y_d	$[\text{m}]$	horizontal and vertical distances <i>CoM</i> to joints
	l	$[\text{m}]$	length of segment
	R_{xd}, R_{yd}	$[\text{N}]$	forces at distal joint
	M_d	$[\text{Nm}]$	moment at distal joint
	D_x, D_y	$[\text{N}]$	fluid-dynamic forces
	F_g	$[\text{N}]$	gravitational force $F_g = m g$
	I_0	$[\text{kg m}^2]$	moment of inertia
unknown	R_{xp}, R_{yp}	$[\text{N}]$	forces at proximal joint
	M_p	$[\text{Nm}]$	moment at proximal joint



4.4 Inverse Dynamics

$$1. \quad \sum R_x = m a_x$$

$$R_{xp} + R_{xd} + D_x = m a_x \quad (4.69)$$

$$\Rightarrow R_{xp} = m a_x - R_{xd} - D_x$$

$$2. \quad \sum R_y = m a_y$$

$$R_{yp} + R_{yd} + D_y + F_g = m a_y \quad (4.70)$$

$$\Rightarrow R_{yp} = m a_y - R_{yd} - D_y - F_g$$

$$3. \quad \sum M = I_0 \alpha$$

$$R_{xp} y_p + R_{yp} x_p + R_{xd} y_d + R_{yd} x_d + M_d + M_p = I_0 \alpha \quad (4.71)$$

$$\Rightarrow M_p = I_0 \alpha - R_{xp} y_p - R_{yp} x_p - R_{xd} y_d - R_{yd} x_d - M_d$$

Except for the first brachial at the tip of the arm, the same applies to all other segments:

$$1. \quad R_{xd} = -R_{xp}$$

$$2. \quad R_{yd} = -R_{yp} \quad (4.72)$$

$$3. \quad M_d = -M_p$$

The accelerations a_x , a_y and α are obtained from the kinematic video analysis as explained in section *Spline Split and Segment Kinematics* (4.2.1). The weight of a segment is defined as mass times gravity $F_g = m g$ with g 9.81 m s^{-2} . In contrast to fluid dynamics, where in principle the weight in water is calculated, here the real mass on which inertia acts is necessary. The fluid dynamic external drag forces D_x and D_y are the results of the hydro-dynamic analysis in the section *Thrust from Drag* (4.3.2). The characteristic distances x_p , x_d , y_p and y_d are trigonometrically derived from the kinematic segment parameters length l and orientation of the segment Θ . The centre of gravity is always in the middle of the symmetrical cylinders at $l/2$. Further details are given in the section *Spline Split and Segment Kinematics* (4.2.1). The moment of inertia I_0 has unique solutions for cylinders and can thus be applied to the abstracted brachial and pinnule segments, see subsection *Moment of Inertia* (4.4.2). The mass of a segment m is determined from its volume and the corresponding density, see subsection *Density, Mass and Weight in Water* (4.1.4) for more details on the determination of the weight in water and the subsection *Added Mass* (4.4.1) for the mass contribution arising from the added mass.

4. Methodology

4.4.1 Added Mass

The total mass m in this context is made up of two components and is referred to as the *virtual mass*. One is the mass of the object itself, which is assumed to be the mass in air m_{ia} . The mass of the air occupied by the object itself is comparatively small and can be neglected. Secondly, a virtual component, the so-called *added mass* m_{add} . The term refers to the mass of the fluid that surrounds the segment and undergoes a change in velocity as the segment accelerates. This change in motion of the fluid requires additional energy and becomes more important the higher the density and thus the mass of the fluid.

$$m = m_{ia} + m_{add} \quad (4.73)$$

The mass used so far in fluid dynamics has been the relative mass in water (Sec. 4.1.4). If the mass in air m_{ia} is not known, it can be taken as the mass in water m_{iw} plus the mass of the displaced water m_w itself.

$$m_{ia} = m_{iw} + m_w \quad (4.74)$$

The added mass m_{add} , expressed in the second term of the equation 4.73, depends on the shape and orientation of an object. Since the morphology of brachials and pinnulars have been simplified as cylindrical volumes, the added mass corresponding to the respective volume of the cylinder V_0 and its relative orientation to the acceleration vector, is expressed as a coefficient of the added mass c_a (Eq. 4.75).

$$m_{add} = \rho V_0 c_a \quad (4.75)$$

The added mass coefficient for a cylinder accelerated perpendicular to its major axis is 1 (Batchelor, 1967) and is thus exactly the amount of water replaced by the cylinder itself. Acceleration in directions other than normal to the principal axis reduces the cross-sectional area and the corresponding additional mass. Projected areas in any direction are elliptical. The relation between the coefficient of added mass c_a and the relation between the major and minor axes of an ellipse r_e is determined for this purpose as $c_a = r_e^{-1}$ (Vogel, 1996; Daniel, 1984) (Fig. 3.3). The added mass for an elliptical extrusion thus corresponds to the volume of a cylinder with the radius of its minor axis or the projected length perpendicular to the direction of acceleration (Fig. 4.19).

The added mass is finally calculated for a cylindrical segment as a function of the included angle between the major axis of the cylinder and the direction of acceleration Φ , the segment volume $V_0 = \pi r^2 l$ and the density of the fluid ρ .

$$m_{add} = \rho V_0 \cos \Phi \quad (4.76)$$



4.4 Inverse Dynamics

4.4.2 Moment of Inertia

The moment of inertia I_0 , in $[\text{kg m}^2]$, is the resistance of an object that must be overcome when the object changes its angular velocity, i.e. the torque required for angular acceleration. It depends on the mass distribution around the object's axis of rotation. Since the virtual model of the swimming crinoid was composed of simple geometric cylinders, I_0 is given for the rotation around the centre of mass and an axis perpendicular to the rotational symmetry of the cylinder.

$$I_{0_x} = I_{0_y} = \frac{1}{4}mr^2 + \frac{1}{12}ml^2 \quad (4.77)$$

I_0 is a function of the dimension of the cylinder: radius r and length l , in $[\text{m}]$, and a specific mass m , in $[\text{kg}]$, see also section 4.4.1.

The moment of inertia for a cylinder rotating about its principal axis is:

$$I_{0_z} = \frac{1}{2}mr^2 \quad (4.78)$$

Both relationships were used to determine the total moment of inertia of an arm segment. An arm segment is composed of one brachial and two pinnules, so that the total moment of inertia I_0 consists of the components of the brachial and two pinnules. The brachial cylinder rotates about an axis perpendicular to the principal axis, while the pinnules point sideways at an angle of 67° . The rotational component of the pinnular cylinder normal to the major axis was neglected and only the rotation in the z-direction was considered. In the section *Pinnule Pose* (4.2.3) it is explained how folded and unfolded states of pinnules change the geometry of the virtual model. Consequently, the moment of inertia of the pinnules only has an effect during power strokes. During the recovery strokes, the pinnules are fused with the brachials and do not need to be calculated separately.

$$I_0 = \frac{1}{4}m_{bra}r_{bra}^2 + \frac{1}{12}m_{bra}l_{bra}^2 + 2 \sum_{i=1}^n \frac{1}{2}m_{pin_i}r_{pin_i}^2 \quad (4.79)$$

I for the brachial cylinder plus twice the sum of the pinnulars n . In the folded state, during the recovery strokes, the pinnules merge with the brachial cylinders and increase the dimension and mass of the brachial cylinder. The equation for I_0 then simplifies and consists only of the first term.

$$I_0 = \frac{1}{4}m_{bra}r_{bra}^2 + \frac{1}{12}m_{bra}l_{bra}^2 \quad (4.80)$$

Mass, radius and length are taken from a cylinder with equal volume of the sum of its components.

4.5 Work, Energy, and Power

Mechanical parameters form the basis for deriving the energy requirement for locomotion. The following describes how the necessary energy content in [kcal] can be calculated from the ratio of internal moments M and angular velocities ω .

$$Po = |M \omega| \quad (4.81)$$

power Po , in watts [W], is the product of momentum M , in [Nm], and angular velocity ω , in [rad s^{-1}]. Considering that mechanical work W , in [J], is power over time Δt .

$$W = Po \Delta t \quad (4.82)$$

And the relationship between joules and calories is:

$$cal = \frac{J}{4.1868} \quad (4.83)$$

The energy needed to swim for one hour can be calculated as follows:

$$E = 3.6 \left(\frac{12 \sum_{i=1}^n \sum_{j=1}^m W_{ij}}{4.1868 m \Delta t} \right) \quad (4.84)$$

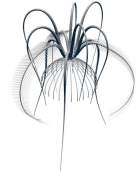
Energy E , in [kcal h^{-1}], is the sum of all arm segments n over all temporal instances of a stroke cycle m for a period between two instances Δt . The factor 12 represents the number of arms. The output of the term in the brackets has the unit [cal s^{-1}], it is converted to [kcal h^{-1}] by a factor of 3.6.

4.6 Maximum Range Velocity (MRV)

Tab. 4.4 List of stroke-cycle frequencies. Relationship between frame rate settings and paddle frequency used to determine maximum range velocity. *original fps of the observed crinoids.

fps	6	7	8	9	10	11	12	13	14	15*
stroke-cycle [s]	4.76	4.17	3.57	3.17	2.87	2.57	2.38	2.20	2.04	1.90
frequency [Hz]	0.21	0.24	0.28	0.32	0.36	0.39	0.42	0.45	0.49	0.53

The maximum range velocity is defined as the swimming speed at which the energy required over the distance is minimal (Videler, 1993; Alexander, 2006). Since it is not known how the arm kinematics of swimming comatulids change with varying speed, a simplified approach was applied by reducing the arm paddle frequency to emulate



4.6 Maximum Range Velocity (MRV)

different locomotion speeds. The original frame rate of the tracked arms was 15 frames per second *fps*. The paddle frequency can be changed by increasing the time span or decreasing the frame rate (Tab. 4.4). Kinematics, fluid and inverse dynamics were thus calculated for 10 different frequencies.

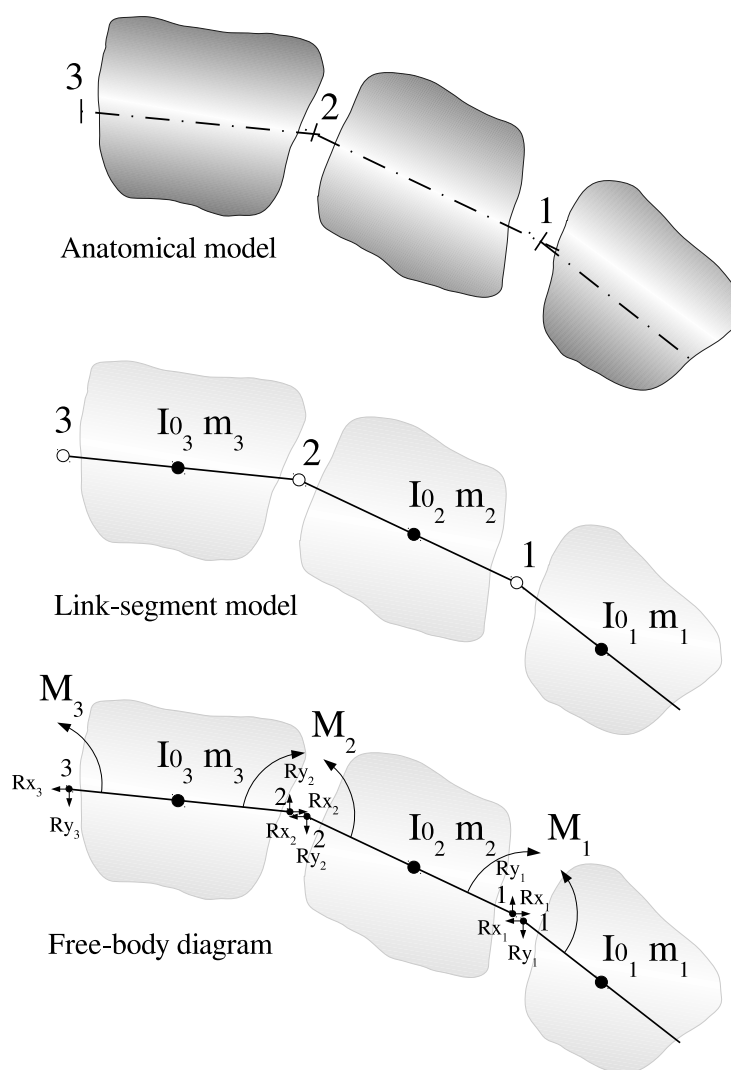


Fig. 4.17 Schematic of a segmented body. Schematic drawing illustrating the steps from the anatomical model via the linked segment model to the free-body diagram. The example shows the three most distal brachials of an arm tip of a crinoid, while the other proximal segments follow the same principle as segments two and three.



4.6 Maximum Range Velocity (MRV)

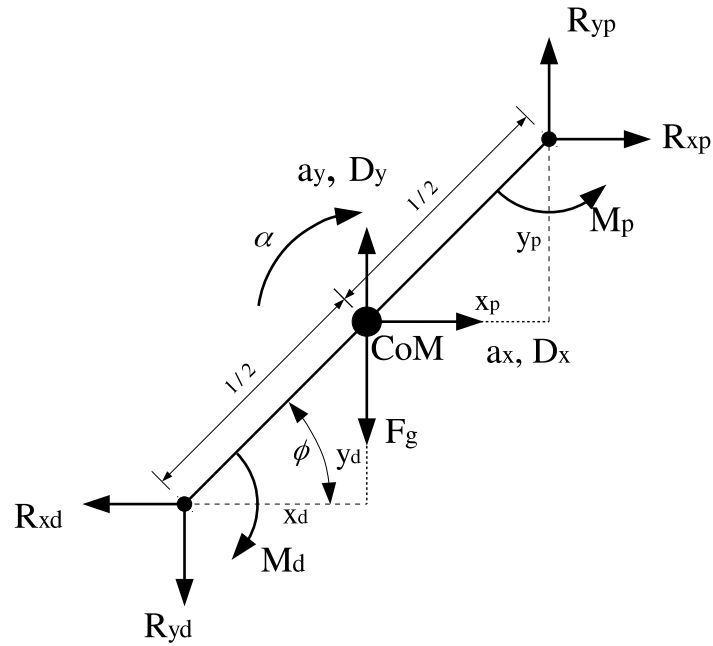


Fig. 4.18 Free body diagram. Arm segment with the involved forces, moments, accelerations and dimensions necessary for the calculation of the inverse dynamics. All forces are given in [N], moments in [Nm], accelerations in [m s^{-2}] and length in [m]. R_{xp} and R_{yp} are forces acting at the proximal end of the segment; R_{xd} and R_{yd} are correspondingly forces at the distal end; M_p and M_d are the net muscle moments at the proximal and distal joints; D_x and D_y represent the net fluid dynamic forces acting on the segment at the centre of mass CoM ; Gravitational force F_g ; Linear accelerations of the segment a_x and a_y and angular acceleration α in [rad s^{-2}]; Length between CoM and joints are x_d , y_d , x_p , y_p and l ; Orientation angle Θ is given in [rad]. The table 4.3 summarises the information about all variables once again.

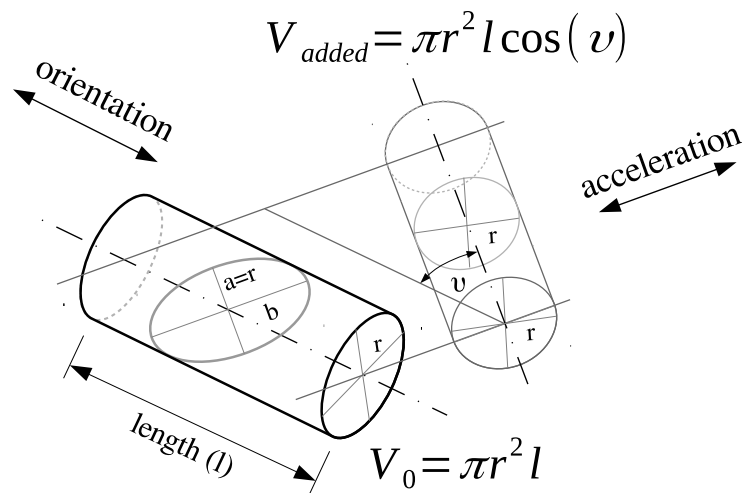


Fig. 4.19 Cylinder added mass. Relationship of the added mass to the acceleration direction and orientation of the cylinder. The cross-section of a cylinder cut at an angle other than normal to its major axis is elliptical. The volume of the added mass is determined by the projected length perpendicular to the acceleration as a cylinder with the same radius of the minor axis of the ellipse.



4.7 Environment and Boundaries

4.7 Environment and Boundaries

All of the following calculations were performed for a uniformly spaced grid within the following limits:

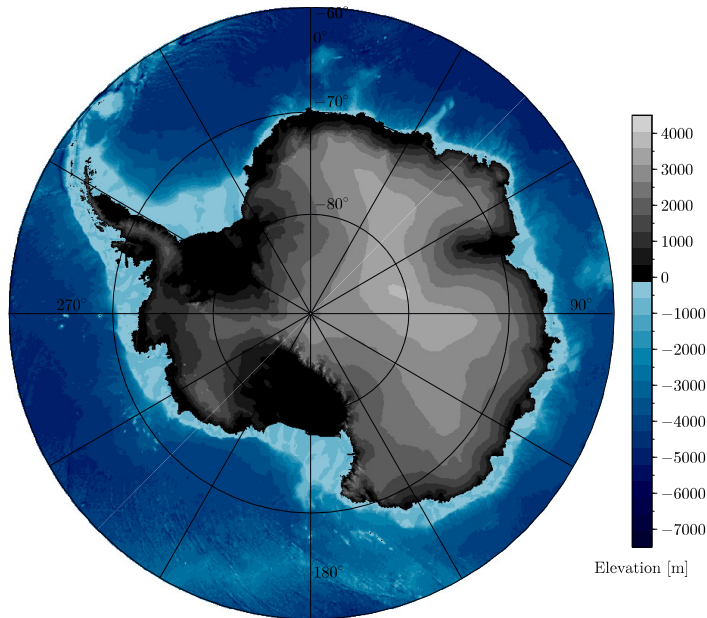
- projection: polar stereographic south, EPSG:3031
- latitudinal boundaries: 60° south to 80° south
- area borders: -3,333,076.28 m west and south, 3,333,076.28 m east and north
- spacial resolution: 801 px \times 801 px (1 px = 8,322.3 m \times 8,322.3 m)
- third party data: obtained as monthly averages
- time span: all data were averaged over 16 yr from 2003 to 2018

The dataset is based on the International Bathymetric Chart of the Southern Ocean (IBCSO) [bc], which provides the seabed depth information ([Arndt et al., 2013](#)). The thickness of the ice cap was taken from the data set BedMachine [bm] ([Morlighem et al., 2019](#)). The spatial resolution was cubic-spline interpolated using the gdal libraries [GDAL] (Fig. 4.20). Further references to land and sea were derived from the bathymetric map. Grid elements with positive elevation are referred to as land. Ice shelves with floating ice were determined from the surface and ice thickness.

Antarctic sectors are highlighted in figure 4.20b and were taken from [Saenz and Arrigo \(2014\)](#).

4. Methodology

(a)



(b)



Fig. 4.20 General overview of the Southern Ocean **a** Map modified according to the International Bathymetric Chart of the Southern Ocean (IBCSO) (Arndt et al., 2013). Polar stereographic south projection EPSG:3031. Depths and heights are shown in metres. **b** Map shows differentiated regions and their ocean sectors. Blue area is the ocean. Light blue is the coastal region of the ice shelf as part of the simulation space.



4.7 Environment and Boundaries

4.7.1 Net Primary Production *NPP*

Most of the available energy in the food chain is synthesised by sunlight. Plants and phytoplankton use solar radiation in the process of photosynthesis to convert carbon dioxide and water into longer organic molecules and oxygen (Ke, 2003). The organic matter produced is the first available source of food is therefore referred to as Net Primary Production *NPP*. Most of the production in the ocean takes place in the upper water layer, but a small part is also synthesised by ice algae in sea ice-covered regions. To account for both contributions to total *NPP* in the Antarctic, aquatic and ice *NPP* were considered separately. The mass of synthesised organic matter is proportional to its energy content (Platt and Irwin, 1973), with production rates depending on the following parameters:

- intensity of solar radiation
- amount of photosynthetic organisms
- and duration

Carbon content is thus expressed in mass per volume of water and time, here in grams of carbon per cubic metre per day. Remote sensing by satellite-based instruments provides data for large-scale calculations of net primary production. Morel (1991); Antoine and Morel (1996) developed a method that uses satellite data of chlorophyll concentration and solar irradiance to calculate primary production. A global application of the method with a seasonal overview is provided by Antoine et al. (1996). Morel proposed a set of equations to calculate *NPP* as a function of available light and chlorophyll (Eq. 4.85 by Morel (1991)).

$$P = \overline{PAR}(0^+) Chl_{tot} \Psi_l \quad (4.85)$$

Net production P , in $[g_C m^{-2} d^{-1}]$, is the product of photosynthetically available radiation $\overline{PAR}(0^+)$, in $[E m^{-2}]$ at the Earth's surface (indicated by the notation (0^+)) as a daily integrated quantity (indicated by the line above), the column-integrated chlorophyll content Chl_{tot} in $[g m^{-2}]$, and Ψ_l the *light use index*, in $[g_C g_{chl}^{-1} (E m^{-2})^{-1}]$ by (Falkowski, 1981). With a factor of $2.5 \cdot 10^{18}$ the form $[E m^{-2}]$ is converted to $[Quanta J^{-1}]$ (Morel and Smith, 1974).

Chlorophyll concentrations derived from satellite data cover only ice-free regions, but primary production also occurs in and under sea ice. Although rates are orders of magnitude lower than in open waters, ice algae are part of *NPP* in ice-covered areas. Both cases were treated separately, the monthly *NPP* data were merged and averaged over sixteen years. The basis for *NPP* in the ocean is chlorophyll data from satellite measurements, while *NPP* in sea ice was determined from ice thickness, light absorption and ice chlorophyll values.

To calculate the *NPP* P , according to equation 4.85, proposed by Morel (1991); Antoine and Morel (1996), the three terms for photosynthetically available radiation

4. Methodology

$\overline{PAR}(0^+)$, the column-integrated chlorophyll content Chl_{tot} and a light use index Ψ_l are first solved.

Solar Radiation PAR

Antoine proposes a method where the solar radiation on the sea surface can be calculated taking into account the cloud cover [p.53, Eq. A12] Antoine1996a.

$$PAR(0^+) = PAR(0^+)_{clear} \left[1 - \frac{0.75\Delta}{(1 - 0.25F_{vis})} \right] \quad (4.86)$$

The solar radiation at the Earth's surface $PAR(0^+)$, in $[J m^{-2} d^{-1}]$, is the solar radiation under clear skies reduced by a factor representing cloud cover. The solar radiation under clear sky $PAR(0^+)_{clear}$ is calculated according to the equation 4.86 (Frouin et al., 1989, p.9732, Eq. 6). The coefficient Δ describes a function of the cloud fraction c and the solar elevation angle α_c (Eq. 4.87). The latter was determined with the Python library *pysolar* [PS] for each 21st of a month between January 2003 and December 2018.

Cloud cover data is provided by NASA Earth Observations (NEO) [cl]. Cloud cover is a derived data set from the MODIS (MODerate resolution Imaging Spectrometer) cloud product (MODO6). It is a measure of what percentage of the sky is covered by clouds. Monthly cloud fraction datasets were downloaded at the highest available resolution $3,600 \text{ px} \times 1,800 \text{ px}$ for the years 2003 to 2018. The projection EPSG:4326 was transformed to EPSG:3031 using the open libraries of gdal [GDAL] and reduced to 60° southern latitude.

$$\Delta = 0.632c - 0.0019\alpha_c \quad (4.87)$$

Where c is the cloud fraction obtained and α_c is the solar altitude.

$$I_{\lambda_1-\lambda_2} = I_{0\lambda_1-\lambda_2} (d/d_0)^2 \cos\theta \frac{\exp[-(a+b/V)/\cos\theta]}{1-\bar{r}_{\lambda_1-\lambda_2}(a'+b'/V)} \exp[-a_v(U_v/\cos\theta)^{b_v}] \exp[-a_o(U_o/\cos\theta)^{b_o}] \quad (4.88)$$

The solar irradiance I , in $[W m^{-2} d^{-1}]$, for the wavelength range $\lambda_1 - \lambda_2$, here 400–700 nm, is a product of the solar extraterrestrial irradiance I_o and the three parameters: solar altitude, ozone and atmospheric water content. The solar angle θ is the angle between the zenith and the sun, so it is equal to $90^\circ - \alpha_c$. The intensity of solar radiation on the Earth's surface is also a function of the distance between the Earth and the Sun. This is represented by the fraction $(d/d_0)^2$, which establishes a relationship between the current distance at the time of calculation d and the mean distance between the Sun and the Earth d_0 :

$$d/d_0 = 1 - 0.01672 \cos(0.9856 (day - 4)) \quad (4.89)$$



4.7 Environment and Boundaries

Tab. 4.5 Solar radiation coefficients. List of coefficients used to calculate solar radiation in equation 4.88.

Coefficient	Value	Description
$I_{0\lambda_1-\lambda_2}$	531.2	extraterrestrial I (400–700 nm), in $[\text{W m}^{-2} \text{d}^{-1}]$
V	23	visibility in [km]
U_o	350	total ozone content in [DU]
U_v	2	precipitable water in $[\text{g cm}^{-2}]$
$\bar{r}_{\lambda_1-\lambda_2}$	6.6	reflectance factor at sea surface in %
a	0.068	
b	0.0379	
a'	0.117	
b'	0.493	
a_v	0.002	
b_v	0.870	
a_o	0.052	
b_o	0.990	

The coefficients were taken from Frouin et al. (1989, p.9733, table(1) and table(2)) and Antoine and Morel (1996, p.53, appenix(D)), listed in table 4.5 and applied to the current day of a month. Since solar radiation $[\text{W m}^{-2} \text{d}^{-1}]$ is independent of time and Joule over time in seconds is Watts, the solar radiation $PAR(0^+)_{clear}$ in $[\text{J m}^{-2} \text{d}^{-1}]$ is obtained by multiplying $I_{\lambda_1-\lambda_2}$ by the desired time period (here one month).

If the expression inside the brackets of the equation 4.86 is greater than 0.95, a constant reduction of 5% is applied to $PAR(0^+)_{clear}$. F_{vis} is set to 0.46 (Pinker and Laszlo, 1992; Antoine and Morel, 1996).

$$PAR(0^+)_{clear} = \begin{cases} PAR(0^+)_{clear} \cdot 0.95, & \text{if } \left[1 - \frac{0.75\Delta}{(1-0.25F_{vis})}\right] \geq 0.95 \\ PAR(0^+)_{clear}, & \text{else} \end{cases}$$

Chlorophyll as a Measure of Photosynthetically Active Biomass

Besides solar radiation, the energy source for the process of primary production, the amount of chlorophyll per unit area determines photosynthetic activity. The second term of the equation 4.85 represents the total chlorophyll content Chl_{tot} , which is integrated over the entire water column. Part of the polar oceans is covered with sea ice at times or even all year round. Thus, two different situations must be distinguished: ice-free parts of the open water and sea ice-covered areas. Some plankton species are specialised to live inside or below the ice. To determine their photosynthetic productivity, phytoplankton occurrences in sea ice according to Meiners et al. (2012); Zhang and Rothrock (2003) and light penetration measurements according to Little et al. (1972) were used. Ocean and ice chlorophyll were merged monthly, with ocean chlorophyll prioritised if both methods yielded chlorophyll values.

4. Methodology

Ocean Chlorophyll

Chlorophyll in ice-free regions is taken from satellite measurements Chl_{sat} in $[\text{mg m}^{-3}]$. The equation 4.90 of Antoine and Morel (1996) is used to convert Chl_{sat} into total chlorophyll Chl_{tot} data.

NASA Earth Observations (NEO) provides global long-term chlorophyll concentrations. NASA's Terra and Aqua satellites host the Moderate Resolution Imaging Spectroradiometer (MODIS), which takes daily colour images of the ocean. Chlorophyll a concentration is derived from the colour gradients and published by NEO [chl] (Hu et al., 2012). For the calculations, monthly datasets were downloaded at the highest available resolution $3,600 \text{ px} \times 1,800 \text{ px}$ for the years 2003 to 2018. A grid cell of the provided projection EPSG:4326 covers an area of $0,1^\circ \times 0,1^\circ$ geographic degrees. Each pixel or raster element therefore encloses an individual area. To bring all parameters into the same system, the data is transformed from EPSG:4326 to EPSG:3031 and reduced to 60° southern latitude using the open software libraries of gdal [GDAL].

$$y = 1.808 + 0.499x + 3.927 \cdot 10^{-2}x^2 - 8.574 \cdot 10^{-3}x^3 - 4.826 \cdot 10^{-3}x^4 \quad (4.90)$$

With the relations $y = \log_{10}(Chl_{tot})$ and $x = \log_{10}(Chl_{sat})$, a non-uniform chlorophyll distribution in the water column is represented by the equation 4.90. It applies to chlorophyll concentrations in the range of $0.02 \text{ mg}_{\text{Chl}} \text{ m}^{-3} < Chl_{tot} < 20 \text{ mg}_{\text{Chl}} \text{ m}^{-3}$ and extends to a depth where the light radiation PAR decreases to 0.1% (Antoine and Morel, 1996, p.53, Eq. A10b).

Ice Chlorophyll

Sea ice-covered areas were treated separately from the ice-free areas because ice thickness and snow cover strongly reduce light penetration to chlorophyll. Assuming that chlorophyll content is photosynthetically active within and at the ice-water interface, primary production depends on light penetration as a function of ice thickness in [%] and the presence of algal biomass.

Modelled ice thickness data from Zhang and Rothrock (2003) from the Polar Science Center in Washington, Seattle, WA replaced measured data here, as there was insufficient data available due to the lack of comprehensive long-term in situ measurements around the Antarctic continent. The simulated data are based on outputs of the Global Ice Ocean Modelling and Assimilation System (GIOMAS) [sit]. Monthly ice thickness values for 2003 to 2018 were trimmed to 60° south and missing values were linearly extrapolated over 77.25° S . Matrices were transformed to EPSG:3031 at 801 by 801 pixel resolution using gdal's coordinate transformation tools [GDAL]. The relative light intensity I_{rel} is the part of the sunlight that remains after absorption by the sea ice. The thicker the ice layer, the more light is therefore absorbed. I_{rel} is expressed as a function of ice thickness h_{eff} , in [m], and interpolated according to



4.7 Environment and Boundaries

photometric measurements by [Little et al. \(1972\)](#).

$$I_{rel} = \frac{0.04}{h_{eff} + 0.04} \quad (4.91)$$

The amount of organic carbon produced in sea ice continues to depend on photosynthetically active plankton. The amount of chlorophyll, in $[\text{mg}_{\text{Chl}} \text{m}^{-2}]$, was taken from ice core data, summarised and presented as monthly amounts in table 4.6 ([Meiners et al., 2012](#), p.3, Fig.(2)) and ([Saenz and Arrigo, 2014](#), p.3662, Fig.(12)).

Tab. 4.6 Sea ice chlorophyll. Monthly chlorophyll content, in $[\text{mg m}^{-2}]$. Data from ice cores taken in several campaigns and averaged over Antarctica. Data listed are from [Meiners et al. \(2012, p.3, Fig.\(2\)\)](#) and [Saenz and Arrigo \(2014, p.3662, Fig.\(12\)\)](#).

	Jan	Feb	Mar	Apr	May	Jun	Jul	Aug	Sep	Oct	Nov	Dec
Meiners	15.9	27.2	11.1	12.3	1.8	4.2	1.9	3.3	7.6	7.4	5.4	4.8
Saenz	8.1	8.6	8.8	5.7	3.1	1.6	0.5	0.6	2.1	5.7	10.9	9.2

Light Utilization

The last term of the equation 4.85, the *light utilisation factor* Ψ_l is expressed in $[g_C g_{Chl}^{-1} (E \text{m}^{-2})^{-1}]$ ([Antoine and Morel, 1996](#)).

$$\Psi_l = (12/4.6) \bar{a}^* \bar{\phi}_u \quad (4.92)$$

Since $\bar{\phi}_u$, is used in $[\text{mol}^C \text{E}^{-1}]$, the conversion factor $12 g_C \text{mol}$ was introduced. \bar{a}^* is set to $16 \text{m}^2 \text{g}_{\text{Chl}}^{-1}$ ([Bannister, 1974](#)).

4. Methodology

4.7.2 Energy Flux from the Surface to the Seafloor

Suess (1980) has proposed a general approach to estimate the carbon flux from the surface to the seabed:

$$C_{flux(z)} = \frac{C_{prod}}{0.0238z + 0.212} \quad (4.93)$$

The carbon $C_{flux(z)}$ at depth z , in [m], is thus a function of the carbon produced at the surface C_{prod} . Both the carbon content at the surface and that at the seabed are given in $[g_C m^{-2} d^{-1}]$ (Suess, 1980, p.260, Eq. 1). The depths required for the calculation were taken from the International Bathymetric Chart of the Southern Ocean (IBCSO) (Arndt et al., 2013).

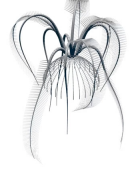
The main components of biomass are proteins, carbohydrates, lipids and various other molecules. The dominant source of energy is nevertheless provided by carbon and nitrogen. The average carbon content of phytoplankton is about 30%, while nitrogen contributes only about 10% (Platt and Irwin, 1973). Zooplankton contain similar amounts of both these energy sources (Harmelin-Vivien et al., 2019). Platt proposed two regressions that determine the energy content of either pure carbon only (Eq. 4.94) (Platt and Irwin, 1973, p.308) and one, which take nitrogen beside carbon into account (Eq. 4.95) (Platt and Irwin, 1973, p.309).

$$cal\ mg_{dry}^{-1} = 0.632 + 0.086(\%C) \quad (4.94)$$

This determines the caloric content of one milligram dry weight of phytoplankton into a function of pure carbon ratio.

$$cal\ mg_{dry}^{-1} = -0.555 + 0.113(\%C) + 0.054(C : N) \quad (4.95)$$

This somewhat extended equation determines the caloric content of a milligram dry weight of phytoplankton as a function of carbon content and carbon-to-nitrogen ratio. Since the absolute composition of the organic matter is unknown, a simplified general conversion by Platt and Irwin (1973) was used in this study. He applied a factor of $11.4\ cal\ mg_C^{-1}$, which as a simplified assumption sufficiently reflects the two calculations above.



4.7 Environment and Boundaries

4.7.3 Tide

The tidal currents were calculated using the core of the Tide Model Driver (TMD) toolbox for Matlab [TMD]. The circum-Antarctic CATS2008 model (Padman et al., 2002, 2008; King et al., 2011; Howard et al., 2019) served as the basis for the tidal predictions. The core from TMD Toolbox was translated into Scilab code for batch processing. The flow components u (east velocity) and v (north velocity) [cm s^{-1}] have been calculated hourly for all grid centre coordinates south of -60° of the EPSG:3031 projection over a 28-day period (1st – 28th January 2018). For this purpose, all available constituents for the Moon and Sun were considered (Tab. 4.7)³. For this purpose, the tidal velocities are integrated over the depths from eastward U and northward V transports, in [$\text{m}^2 \text{s}^{-1}$].

$$u_{ij(\text{IBCSO})} = \frac{u_{ij(\text{CATS2008})} d_{ij(\text{CATS2008})}}{100 d_{ij(\text{IBCSO})}} \quad (4.96)$$

$$v_{ij(\text{IBCSO})} = \frac{v_{ij(\text{CATS2008})} d_{ij(\text{CATS2008})}}{100 d_{ij(\text{IBCSO})}} \quad (4.97)$$

Tidal velocity components u and v , in [cm s^{-1}], obtained from the CATS2008 model, were corrected with the IBSCO bathymetry map (Arndt et al., 2013) and converted to standard units [m s^{-1}] so that all calculations performed in this study are based on the same bathymetric chart. Indices i and j represent a matrix operation over the simulation field of 801 by 801 grid cells.

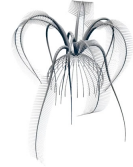
The maximum tidal velocities were derived from the flow cycles and averaged to mean maximum values. The mean maximum tidal velocity is the average of the incoming and outgoing maxima. Due to the nature of tidal currents flowing in opposite directions during a cycle, two flow fields had to be established. One combining ocean current and incoming tide, and the other combining ocean current and outgoing tide.

³A list of tidal constituents is provided by the National Oceanic and Atmospheric Administration NOAA in Washington DC and is available at <https://tidesandcurrents.noaa.gov/harcon.html?id=9410170> (August 2019)

4. Methodology

Tab. 4.7 Tidal constituents. List of lunar and solar constituents. The parameters are available in the tide model driver of the Earth & Space Research Institute in Seattle. A comprehensive list of tidal constituents is provided online by the National Oceanic and Atmospheric Administration NOAA in Washington DC.

Name	Symbol	Period [hr]	Type
Principle lunar	$m2$	12.4	semi-diurnal
Principle solar	$s2$	12.0	semi-diurnal
Larger lunar elliptic	$n2$	12.7	semi-diurnal
Lunisolar	$k2$	12.0	semi-diurnal
Lunar	$k1$	23.9	diurnal
lunar	$o1$	25.8	diurnal
Solar	$p1$	24.1	diurnal
Larger lunar elliptic	$q1$	26.9	diurnal
Lunisolar	mf	327.9	fortnight
Lunar	mm	661.3	monthly



4.8 Dispersal

4.8 Dispersal

4.8.1 Dispersal by Reproduction

Since juvenile *Promachocrinus kerguelensis* have a two to three months pelagic life phase, an average drift along ocean and tide currents of 75 days per year was chosen for the migration model.

Sea and tidal currents have a different influence on the resulting direction and bridged distance depending on their duration and strength. While the averaged ocean current flows constantly in the same direction, the tidal current represents a cyclic back and forth motion. The maximum distance in both directions of the tidal cycle is given by its velocity and was integrated over a quarter tidal period of three hours. The velocity profile of a half-day tide follows a sinusoidal function (Fig. 4.21a). Motionless still water occurs during low and high tide, while currents reach a maximum at mean sea level in between. The shaded area represents the integrated stretch of unidirectional flow until the current reverses.

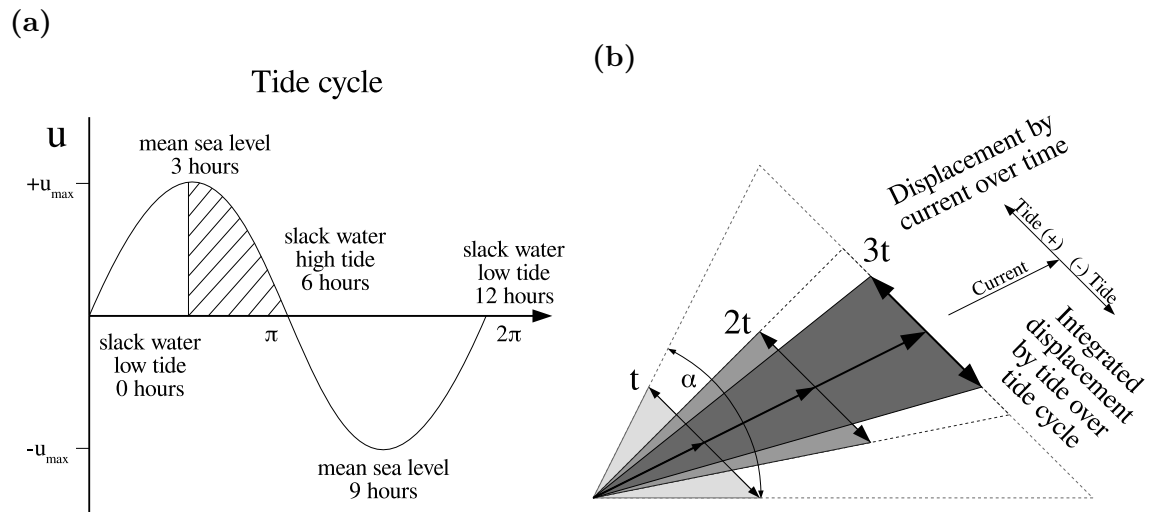


Fig. 4.21 Tidal drift. Illustration of a tidal cycle and its effect on a drifting object in relation to the current. **a** Velocity profile of a semi-diurnal tidal cycle over 12 h. The shaded area represents the integrated path of the unidirectional flow from mean sea level to high tide. **b** Schematic representation of the decreasing effect of the tidal current with increasing pelagic drift. The maximum displacement due to tidal drift is independent of the drift duration as long as the drift lasts at least half a tidal cycle. Less drift increases the included angle α , resulting in a wider offset.

The total semi-diurnal tide of 12h exhibits a sinusoidal velocity profile described over an angle of $0...2\pi$ (Eq. 4.98). The mean maximum amplitudes were determined for all grid points of the simulation room (detailed method is described in section

4. Methodology

(4.7.3) *Tide*).

$$u = A \sin(ct) \quad (4.98)$$

To determine the tidal velocity for a given time interval, a location-specific amplitude A and a time factor $c = \frac{2\pi}{43200}$ are used to convert the run-time variable t into the range $(0...2\pi)$ for 12 hours or 43,200 seconds respectively. The distance travelled s is obtained by integrating the velocity u over time.

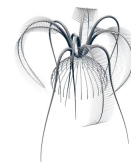
$$s(t) = \int u(t)dt = \int A \sin(ct)dt \quad (4.99)$$

By setting the limits from mean sea level (maximum velocity) after 3 h (10,800 s) to high tide after 6 h (21,600 s), the maximum distance in both directions of the tidal flow is integrated.

$$s_{max} = \int_{10,800}^{21,600} A \sin(ct)dt \quad (4.100)$$

$$\Rightarrow s_{max} = \left| -\frac{A}{c} \cos(ct) \right|_{10,800}^{21,600} \quad (4.101)$$

As long as the pelagic residence time is longer than 6 hours, the tidal current overlaps the main ocean current by zigzagging. Possible sites of settlement are located in a region along the ocean drift within the range of tidal displacement (Fig. 4.21b).



4.8 Dispersal

4.8.2 Dispersal and the Migration Model

Dispersal as a measure of evolutionary success is the time-dependent spatial spread of organisms. Their dispersal rate depends on their locomotion abilities, reproduction rate and chance of survival. I developed an algorithm for simulating the dispersal of crinoids, here in particular for *Promachocrinus kerguelensis*. The algorithm only considers the first two aspects because predation and accompanying survival rates require a more complex understanding of the entire ecosystem. The following parameters form the basis for the simulation of crinoid spatial dispersal:

- available and required energy for locomotion
- metabolic and reproductive energy requirements
 - primary carbon production as a food source
 - carbon transport to the seabed
 - energy content of available food
- swimming speeds
- drift by ocean and tidal currents
- bathymetry

The simulations include the entire area around the Antarctic continent, including the continental shelf and deep sea regions up to 60° southern latitude. Since the horizontal dimensions are orders of magnitude greater than the ocean depths, the potential energy for upward and downward motion has been neglected. The horizontal grid is limited by the resolution of the data, which were transformed into the stereopolar projection EPSG:3031 with a grid size of about 8 by 8 km.

By adjusting the parameters, the simulation can also be applied to other life forms or non-organic substances. The simulation of competing organisms helps to evaluate the locomotion capabilities of crinoids. For example, if the swimming speed is set to zero, this represents non-active swimmers such as drifting plankton. Dispersal by pure larval drift along currents and tides represents the life cycle of sessile organisms such as sea lilies, but also sponges and corals.

The algorithm is based on the assumption that current, tides and swimming speed are constant within the area of a grid cell. This means that the path from one to a neighbouring cell takes the shortest route with unchanged mean conditions. A second important assumption is: if at least 50% of a neighbouring cell is reached, it is assumed that the entire area of this cell has been colonised (Fig. 4.23). The reference point for this is always in the middle of the cell. At least half of the area of the cell is colonised if this point has been reached from the adjacent baseline. The baseline in this context represents a line from the centre of the source cell to the

4. Methodology

centres of its lateral neighbours, which lie across the target cell. Since EPSG:3031 represents a distorted non-isometric projection and the method requires true lengths and angles between two centres, the grid centres had to be transformed, primarily with `gdaltransform` from the `gdal` library [GDAL] into polar coordinates of the EPSG:4326 projection (Fig. 4.22). Distances and orientation of geographic relations were derived from the polar coordinates. True three-dimensional distances between two points were determined considering the sea depth from the bathymetric map and the position-dependent radius of the ellipsoidal earth shape. The true distance between two points that an organism has to travel is the resulting vector of flow and swimming direction. It starts at a point on the baseline and ends in the middle of a target cell. The aim of the dispersal algorithm is to find the starting point on the baseline within the source cell from which the least time t in seconds is required to reach the destination. Figure 4.23 shows a schematic representation of this concept and is solved analytically in equation 4.104. Since current direction and magnitude are individual for each grid cell, the mean value of both components was taken for the following calculation.

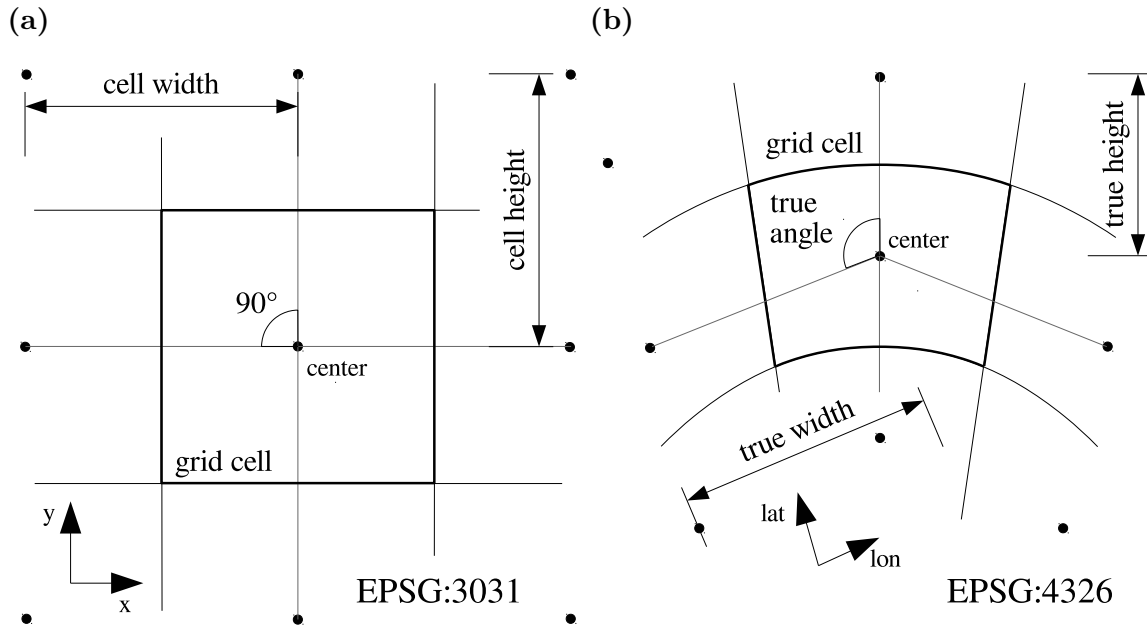


Fig. 4.22 Projection geometry. **a** Orientation and size of grid cells in polar stereographic projection EPSG:3031. **b** Grid cell transformed in EPSG:4326 in latitude and longitude coordinates. The square cells are deformed, but their extensions and angles are now isometric. The schematic drawing shows a example cell geometry. However, due to the polar stereographic projection, each cell has its individual shape.

$$y = y_1 + y_2 = U_{sy} t + U_{cy} t \quad (4.102)$$

The vertical distance of the true path y (y here stands for the direction to the target cell) consists of two components y_1 and y_2 , which are the vertical parts of the



4.8 Dispersal

swimming speed U_{sy} and the flow velocity U_{cy} multiplied by the time t .

$$y_1 = U_c \cos(\gamma) t \tan(\beta) \Rightarrow U_{cx} t \tan(\beta) \quad (4.103)$$

The component y_1 can be expressed as the product of the x-component of the current U_{cx} and the tangents of the angle β . The time can be obtained by substituting y_1 into equation 4.102 and solving it for the time t . Since the swimming vector U_s is perpendicular to the baseline, $U_{sy} = U_s \cos(\beta)$.

$$t = \frac{y_2}{U_s \cos(\beta) + U_{cy} - U_{cx} \tan(\beta)} \quad (4.104)$$

To test whether the target cell can be reached from a source cell, the horizontal component of the true path vector x must be less than half the source cell width.

$$reached = \begin{cases} true, if U_{cx} - U_s \sin(\beta) \leq width/2 \cos(\beta) \\ false, else \end{cases}$$

The light grey area in figure 4.23 represents all possible start and end points given by the boundaries of the source cell and defined by the true path vector.

Due to the fact that the swimming time is limited by the ratio of consumed and available energy, the time t is reduced to meet the constraints of food availability. Given the processes of primary production, carbon transport to the seabed and the energy content of carbon, a local specific energy fraction per area and time E_{avl} , in $[cal m^{-2} d^{-1}]$ is the limiting parameter for daily locomotion activity. The usable energy E_{uab} , in $[cal d^{-1}]$, for a crinoid is proportional to the ratio of the covered area of one square metre. A feeding crinoid is assumed to sit on the seabed with its arms spread out to the sides. Therefore, it covers a circular area a defined by its arm length l .

$$E_{uab} = l^2 \pi E_{avl} \quad (4.105)$$

Factor fac determines how much time of the day can be swum, determined by the ratio of required energy E_{swim} , in $[cal h^{-1}]$ to available energy E_{uab} .

$$fac = \frac{E_{swim} 24 h}{E_{uab}} \quad (4.106)$$

It follows that the required swimming time t_{trav} needed to cover the distance between two grid cells calculates the product of the time t given by equation 4.104 and the daily swimming factor fac .

$$t_{trav} = t fac \quad (4.107)$$

In a simulation, swim times were determined for all eight target cells surrounding a source cell when the following conditions apply:

- target cell is not populated yet

4. Methodology

- target cell provides enough energy for swimming
- target cell is part of the simulation area

The next occupied target cell is colonised and thus becomes a source cell itself. The simulation runs in a loop until all possible grid cells are occupied. By adjusting the parameters (swimming speed, tides, energy, depth range and starting point), different dispersal scenarios were simulated.

Ocean Current and Ice Drift

The surface current is provided by NASA's Ocean Surface Currents project OSCAR and was downloaded from the OPeNDAP server [oc]. OSCAR is a derived calculation of ocean surface currents from satellite-measured sea surface height, wind and temperature (Bonjean and Lagerloef, 2002). Since the surface current only covers ice-free areas, data gaps were filled by ice drift provided by the Integrated Climate Data Center of the University of Hamburg [id]. Both datasets were downloaded as monthly averages from January 2003 to December 2018, transformed to the polar stereographic projection EPSG:3031 and interpolated to 801 px \times 801 px resolution. The translation library gdal-2.2.3 [GDAL] was used for the transformation and interpolation. Ocean currents were prioritised so that gaps in the flow data were filled with ice drift values. The combined data sets were then averaged over the 192 months using scilab-6.0.2.

Metabolic and Reproductive Costs

A basic need for energy must be provided to enable the survival of *Promachocri-nus kerguelensis*. The metabolic expenditure keeps the animal alive, but does not cover the reproductive costs that guarantee survival over generations. Only the latter was the subject of the studies of *P. kerguelensis* (McClintock and Pearse, 1987). Metabolic costs were carried out by incubation experiments on conspecific crinoids and transferred to *P. kerguelensis* (Warnock and Liddell, 1985). Both parts were extrapolated according to a water temperature of -1.84°C and a body weight of 5.57 g. The oxygen consumption determined in $[\text{mgO}_2 \text{ g}^{-1} \text{ h}^{-1}]$ was converted with the relation $3.3 \text{ cal } (\text{mgO}_2)^{-1}$ (Elliott and Davison, 1975). The reproductive effort according to McClintock and Pearse was converted with the relation $1 \text{ cal}=4.1897 \text{ J}$.



4.8 Dispersal

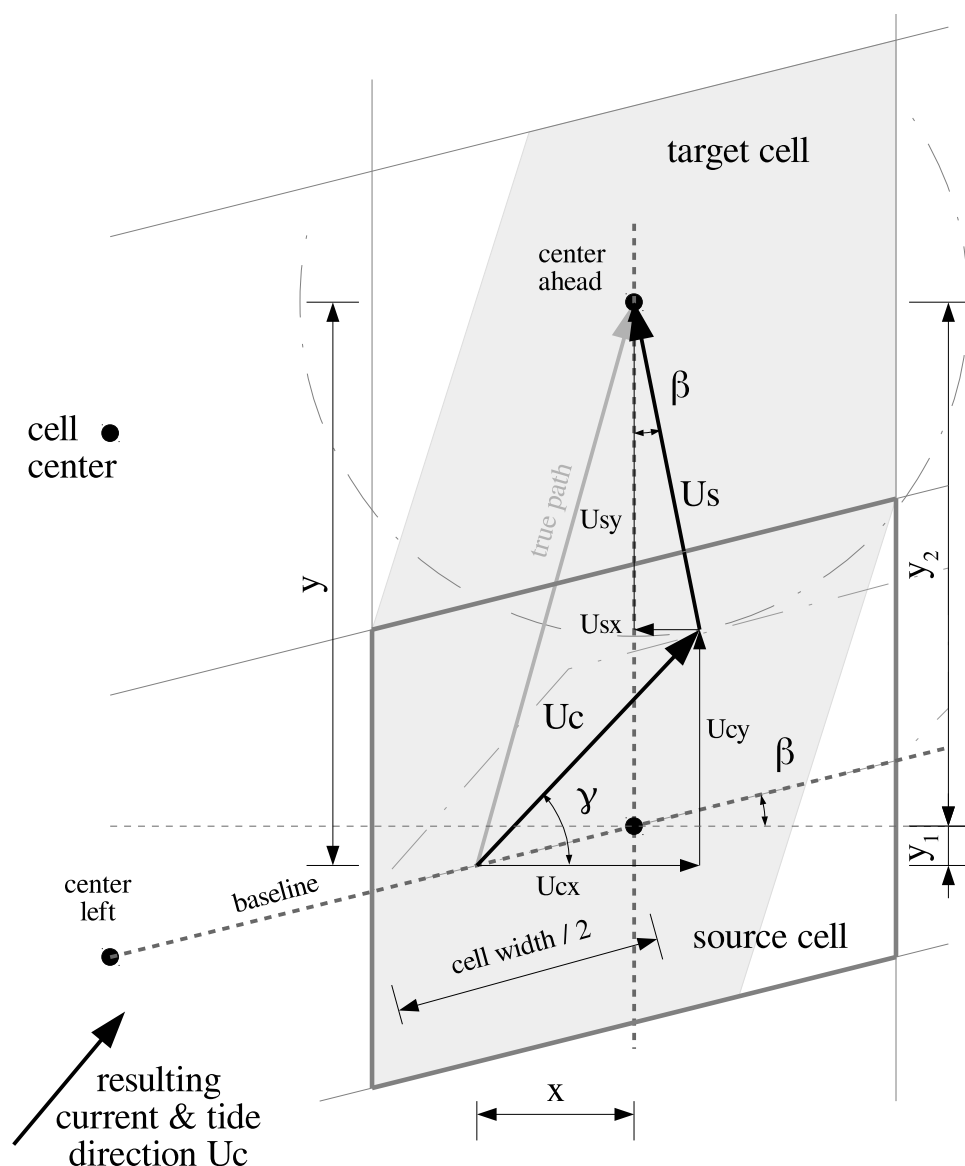
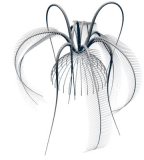


Fig. 4.23 Graphical representation of the algorithm. Visualisation of the mathematical algorithm to find the fastest path to a neighbouring grid cell. U_c : current speed (combines ocean and tidal currents), U_s : swimming speed, x and y are vertical and horizontal components of the true path vector, in metres. β is the difference between the true angle of the baseline to a cell on the left or right and its line perpendicular to the target cell. γ is the direction of the resulting current. The light grey area shows all possible start and end points given by the boundaries of the source cell and defined by the true path vector.

4. Methodology



5. RESULTS

5.1 Morphological-Physiological Computer Model

The morphological-physiological computer model of the crinoids serves as the basis for calculating the analytical dynamics, through which swimming speeds and energy consumption were determined. Measurements were carried out on eight adult crinoids caught during the *Polarstern* cruise ANT XXI/2 to the Weddell Sea in 2003. The virtual framework consists of simple geometric shapes strung together, cylinders for all elongated body parts brachials, pinnulars and cirrals, only the conical calyx was abstracted as a sphere. All dimensions of the individual segments were averaged and expressed as a function over their proximal-distal position. Cylinders are characterised by their length and diameter and placed either in relation to their specific position or in relation to the body parts they are connected to. Higher-level morphological features (arm, pinnules and cirri length) were taken from the video material and summarized with the composition of the virtual design in (Tab. 5.1). The dimensions of the passive body parts calyx, cirri and primibrachials are given in table 5.2 and compared with the data of [Clark \(1967\)](#).

Tab. 5.1 Composition of the virtual model. Derived from empirically collected body morphology of four twelve-armed samples. Dimensions were averaged from 53 tracked stroke cycles (data sources [cri] and [crii]) and measurements on eight specimen. The number of body segments n were derived from their individual relations to the corresponding body part as described below. Standard deviations are given in the brackets. See also appendix C for further details.

Video sample	RS600012	RS619007	RS620008	RS620018	total	kinematic mean
Tracked arms(strokes)	6(1)	5,6(2)	6(1)	6(5)	24(53)	1(53)
Virtual design					mean	kinematic mean
Arm length [m]	0.145(± 0.029)	0.128(± 0.012)	0.170(± 0.010)	0.120(± 0.011)	0.139(± 0.018)	140
Brachials n	82(± 18)	72(± 8)	98(± 7)	66(± 8)	79(± 14)	79
Pinnulars n	20	20	20	20	20	20
Pinnule length [m]	0.012	0.012	0.012	0.012	0.012	0.012
Calyx \emptyset	7 mm	7 mm	7 mm	7 mm	7 mm	7 mm
Primibrachials n	6	6	6	6	6	6
Cirri n	30	30	30	30	30	30
Cirrals n	29	29	29	29	29	29
Volume [cm ³]	5.13(± 0.09)	5.11(± 0.04)	5.18(± 0.01)	5.09(± 0.05)	5.13(± 0.04)	5.15
Weight [g]	5.55(± 0.10)	5.54(± 0.04)	5.61(± 0.01)	5.51(± 0.05)	5.55(± 0.04)	5.57
WiW [g]	0.29(± 0.00)	0.29(± 0.01)	0.29(± 0.00)	0.29(± 0.01)	0.29(± 0.00)	0.29

5. Results

Tab. 5.2 Morphology of the passive body parts. Calyx, primibrachials and cirri. Dimensions listed by [Clark \(1967\)](#) in comparison with measurements averaged from eight specimen and their derived geometry for the computer model.

calyx	Clark 1976	measurements (n=8)	model
diameter	7 mm–8 mm	5.1 mm±1.0	sphere \emptyset 7 mm
primibrachials	Clark 1976	measurements (n=8)	model
length	~ 5 mm	2.8 mm±0.5	cylinder $l=3$ mm
width	~ 5 mm	2.8 mm±0.5	cylinder $d=3$ mm
cirri	Clark 1976	measurements (n=5)	model
number	30–65	36±5	30 (29 segments)
length	40 mm–120 mm	34 mm±4	42 mm
dimensions	cylinder segments according to regression in figure 5.3		

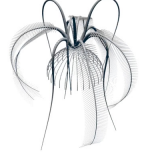
Brachials

The arms are composed of successive brachials. Starting at the proximal end, the first brachial is connected to the primibrachial axillary. Each brachial has two lateral pinnules, which are connected to the brachial cylinder in the middle in an idealised way. The brachial dimensions, length and diameter, are described as a function to their proximal-distal position number n_B ([Fig. 5.1](#)). The length l_B and diameter d_B of the brachial cylinders are exponentially related to their respective positions ([Eq. 5.1](#)). The first proximal brachial cylinder has a length of about 3.2 mm and a diameter of about 2.7 mm. At the other end is the most distal brachial cylinder with a length of about 1.6 mm and a diameter of about half a millimetre. The latter depends on the absolute arm length and the corresponding number of brachials.

$$\begin{aligned} l_B(n_B) &= 0.179e^{-0.109n_B+2.319} + 1.570 \quad R^2 = 0.882 \\ d_B(n_B) &= 0.297e^{-0.028n_B+2.232} + 0.010 \quad R^2 = 0.914 \end{aligned} \quad (5.1)$$

Pinnuls

The size ratio of pinnule cylinders is similar to that of brachials. The length of pinnules is given as a function of their absolute position n_P within a pinnule. Pinnular one is the most proximal segment next to a brachial, their length l_P decreases linearly outwards. In contrast to the length, the diameter of the pinnular is related to the diameter of the associated brachial $r_{d_P d_B}$. The regression follows an exponential trend in the direction of the pinnule end ([Eq. 5.2](#) and [Fig. 5.2](#)). The first segments are ~ 0.75 mm long and



5.1 Morphological-Physiological Computer Model

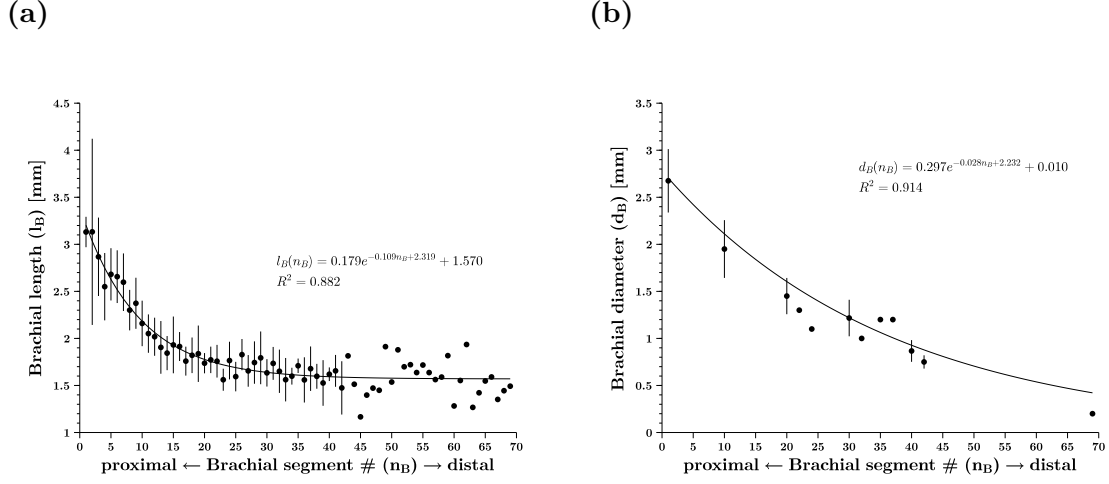


Fig. 5.1 Dimensions of brachial. **a** Brachial length l_B in [mm] over their proximal-distal position n_B . **b** Corresponding brachial diameter d_B in [mm]. Segment numbers start at the proximal end of the arm. Sample size $n=8$, black bars represent standard deviations.

have a diameter of about one third of the adjacent brachial.

$$\begin{aligned} l_P(n_P) &= -0.015n_P + 0.762 \quad R^2 = 0.951 \\ r_{d_P d_B}(n_P) &= 0.364e^{-0.054n_P} \quad R^2 = 0.987 \end{aligned} \quad (5.2)$$

Cirri

The cirrals are assumed to be of equal size, with a number of 30, evenly distributed around the calyx. Their dimensional relation over length are simplified linearly, averaged from $n=5$ samples (Eq. 5.3). A cirri consists of 29 cirral cylinders with a proximal length $\sim 1,6$ mm, decreasing to about 0,75 mm at the distal end. The corresponding diameter also decreases linearly from 0.72 mm to 0.65 mm (Fig. 5.3).

$$\begin{aligned} l_C(n_C) &= -0.032n_C + 1.659 \quad R^2 = 0.955 \\ d_C(n_C) &= -0.003n_C + 0.717 \quad R^2 = 0.447 \end{aligned} \quad (5.3)$$

The morphological measurements of the body parts of the crinoid ran a set of mathematical relations describing the shape of the individual body parts of *P. kerguelensis* and their mutual size relationships. These expressions provide the constructive blueprint for generating a computer model of the comatulid crinoid.

5. Results

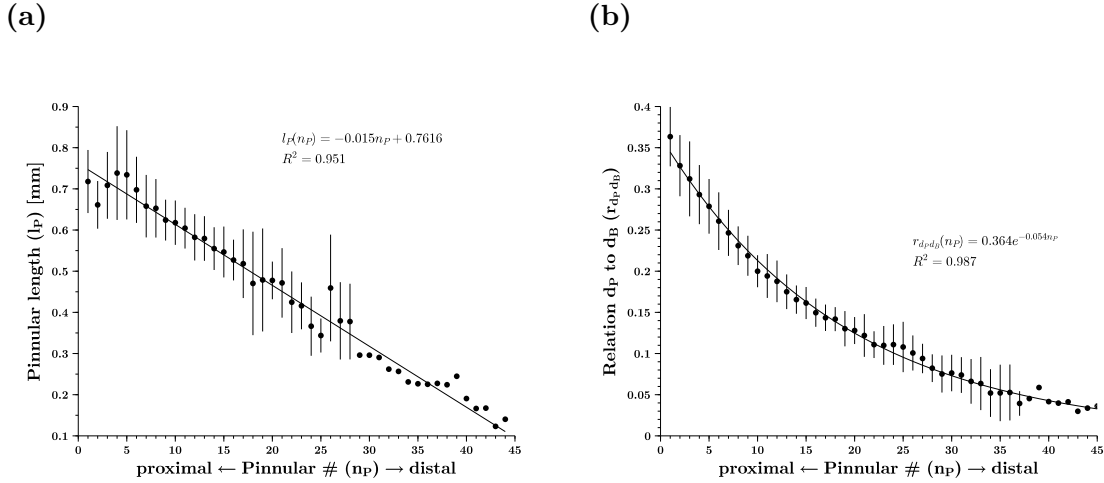


Fig. 5.2 Pinnular dimensions. **a** Pinnular length l_P is related to its proximal-distal position n_P . The position numbers start at the proximal end, which is connected to a brachial. **b** Shows the relation between the diameter of the pinnule and the brachial diameter associated to it $r_{d_P d_B}$. Sample size $n=63$, standard deviations are shown by black bars.

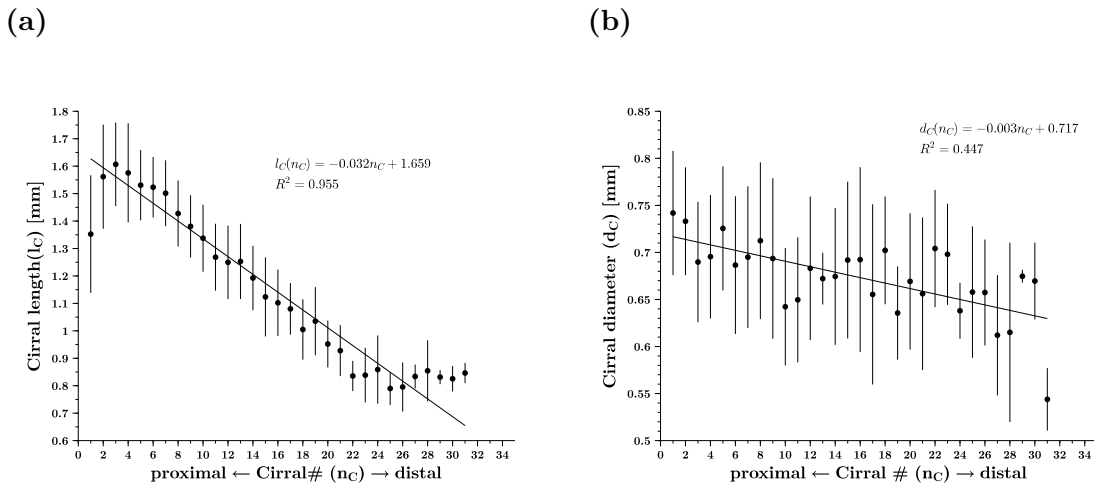
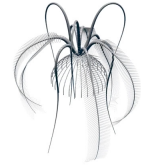


Fig. 5.3 Dimension of cirri. Size ratios were collected from a sample size of $n=5$. **a** Ratio of the cirral length l_C in relation to its proximal-distal position n_C . The first cirral at the proximal end is connected to the calyx. **b** Cirral diameter d_C over its proximal-distal position, their standard deviation is indicated as black bars.



5.2 Locomotion Kinematics

The kinematics of locomotion is a mathematical description of the course of the swimming motion; it provides the dynamic components that set the computational model in motion. Its kinematics of locomotion were analysed to calculate the fluid dynamic forces that occur during swimming, as well as to determine the cost of locomotion. The kinematics of the arm strokes are represented by its motion parameters of velocity and acceleration. Both were derived from image sequence tracking, which shows the motion over time. The arms were interpolated as natural splines, split according to morphological specifications of the individual brachials and calculated for each arm. The nature of the in-situ ROV (Remotely Operated Vehicle) operation initially required frame rectification and frame scaling.

Compensation of Perspective Distortion

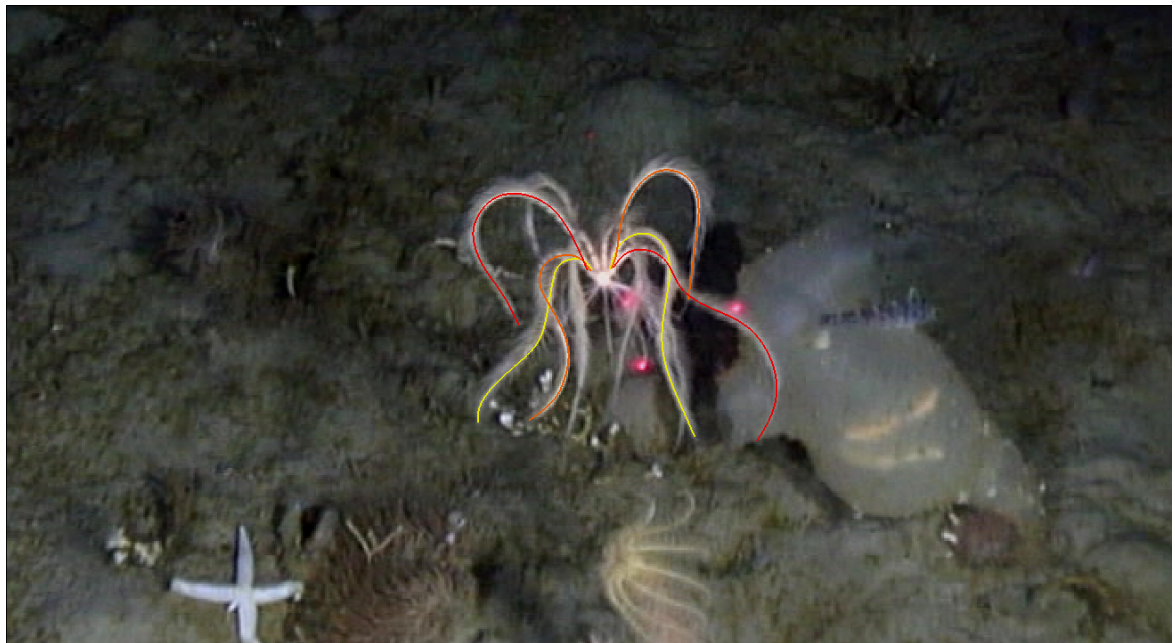


Fig. 5.4 Reference image. B-spline interpolation of six arms of a floating crinoid *Promachocrinus kerguelensis*. The laser dots represent a distance of 4 cm. The image (#128) was taken as a reference because the laser reflection on the organism shows the true scale of the crinoid. Images taken on the *Polarstern* cruise PS82 [crii].

Perspective distortions of the video material caused by camera movement, orientation and displacement of the organism were compensated before further processing of the image material. A viewing angle that deviates from the vertical makes an object

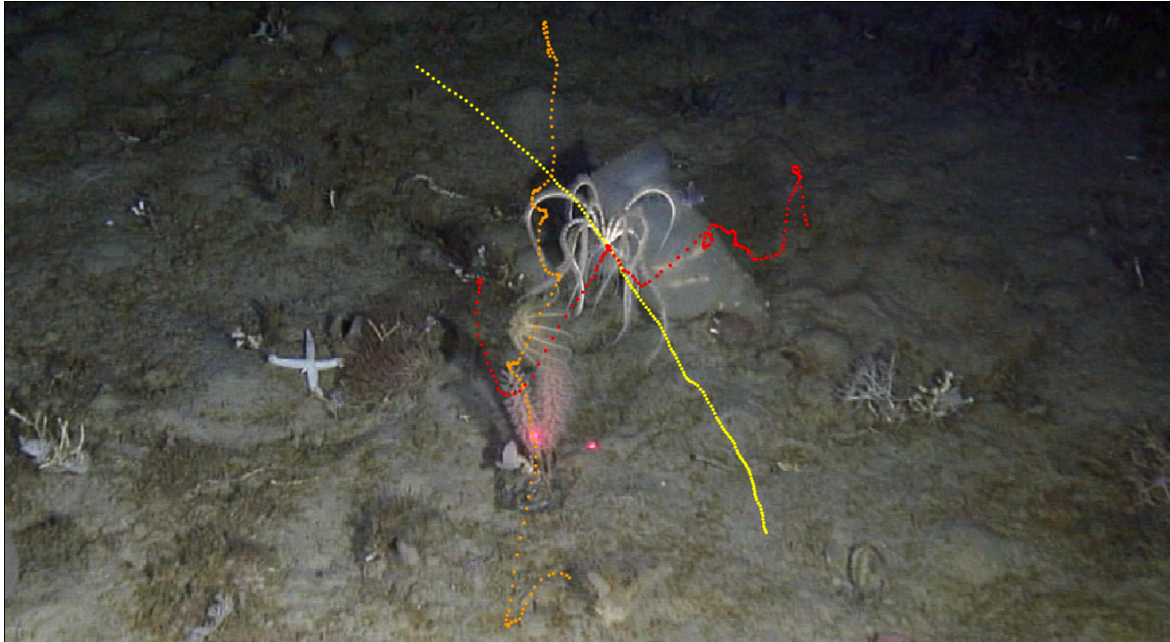
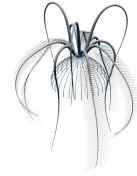


Fig. 5.5 Swim track Absolute swim track (yellow) of *Promachocrinus kerguelensis* derived from body track (red) and reference track (orange). The reference track was used to compensate for camera movement relative to the environment. Distance of laser dots 4 cm. Images taken on the *Polarstern* cruise PS82 [crii].

appear smaller in perspective, the tracking points were therefore rectified by trigonometric transformation. Scaling errors caused by different camera-object distances were reduced by determining the size of the crinoid on a scaled reference image. All other images in the same sequence were then scaled according to the arm length of the crinoid on the reference image. An example of the scaling of crinoid RS620018 is shown in figure 5.6 with reference to image #128 (Fig. 5.4). The absolute swim track (yellow) was derived from the body track (red) and a reference fixed point (orange) to correct for camera motion (Fig. 5.5). The effects on the angle of view and scale caused by a non-stationary camera setup are shown in figure 5.15 with the first and last image of the image sequences. Regressions for all crinoid samples and the corresponding video sequences are shown in table A.1.

Arm Kinematics

The arm kinematics were derived from arm movements on the video footage. The linear and angular motion of the brachials with their velocity and acceleration components are the first and second time derivatives of their displacement between two frames (Fig. 5.7 and Fig. 5.8). A stroke cycle is divided into a power phase and a recovery phase. The power phase (bold dots) was determined by its movement relative to the



5.2 Locomotion Kinematics

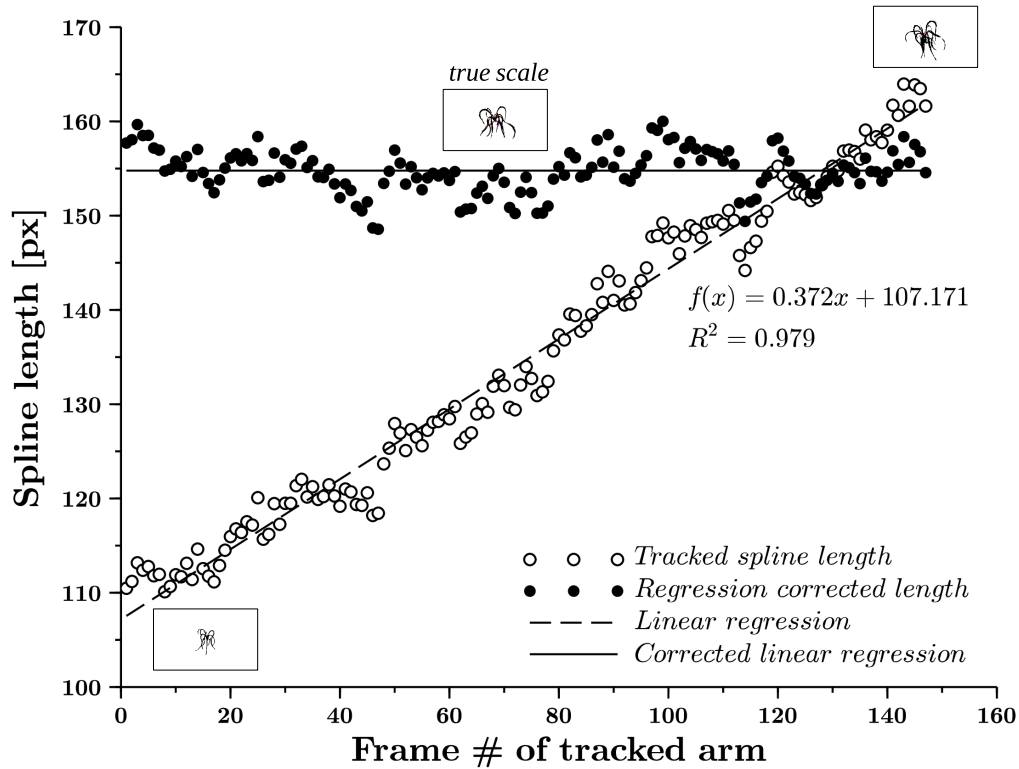


Fig. 5.6 Size compensation. Regression of the arm spline length and its correction according to frame #128. Due to the camera movement and the displacement of the organism, the perspective view and the scale have changed over time and had to be adjusted to the reference image.

swimming speed in the y-direction (Fig. 5.9). When a brachial moves backwards faster than the organism swims forwards, it generates a force that accelerates the organism in the swimming direction. All other states are considered recovery phases. Power stroke: the arm is extended outwards in a crescent shape while the pinnules are unfolded at an angle of 67° to form a banded paddle, then the arm is pulled backwards until it is fully extended backwards. The recovery stroke is initiated by aligning the pinnules along the major axis of the arm and pulling the arm towards the centre of the body and bringing it forward. It ends with the initial phase of the power stroke (Fig. 5.8a,b). With an arm on the right side of the body, the positive x-axis points away from the centre of the body and the positive y-axis points in the direction of swimming. The extension phase sideways occurs in the transition from the recovery to the power phase with a maximum velocity of 5 cm s^{-1} . The inward retraction reaches its maximum at the beginning of the recovery phase with a maximum -8 cm s^{-1} (Fig. 5.8a). Paddle strokes back (force) and forward (recovery)

5. Results

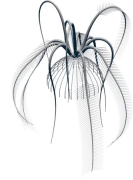
reach their maximum velocities at -14 cm s^{-1} and 12 cm s^{-1} . The absolute velocity in the middle phase of the power stroke is slightly higher than in the middle phase of the recovery stroke (Fig. 5.8b). Corresponding accelerations are shown in figure 5.8c,d. The acceleration reaches values in the range of -40 cm s^{-2} to 40 cm s^{-2} in the swimming direction and -20 cm s^{-2} to 40 cm s^{-2} laterally.

Angular velocities and accelerations are a measure of the brachials' rotational activity. The first brachial is located at the proximal end in the coordinate centre (Fig. 5.7a). Positive angular velocities represent counter-clockwise rotation. The maximum rotation of $\sim 4 \text{ rad s}^{-1}$ occurs at the distal end of the arm just before the transition from power stroke to recovery stroke, at the point where the arm is bent inwards and the tip tilts counter-clockwise. A second angular velocity peak is found in the last third of the recovery phase around the 25th brachial. Taking the example of maximum rotation at the tip of the arm, the change in velocity from one instance of time to the next is minimal and therefore not accelerated. Positively and negatively oriented angular acceleration are independent of direction and mean either acceleration or deceleration.

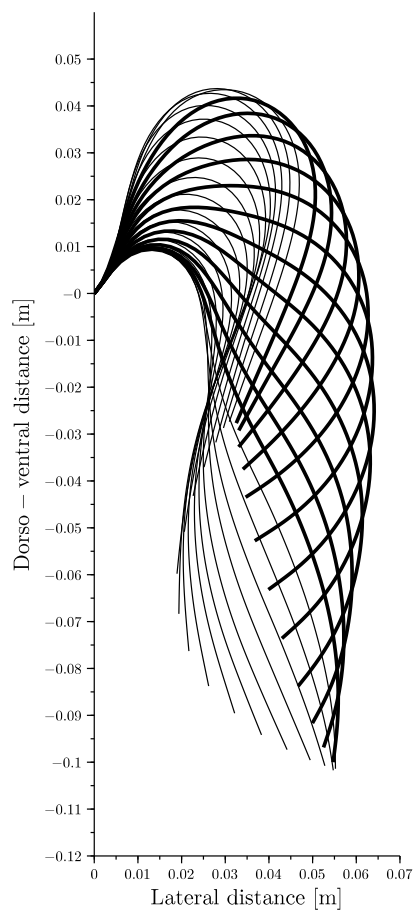
Pinnules alter the arm area and contribute either to increasing the projected area for a power stroke or to decreasing it for a recovery stroke. Power strokes are characterised by laterally unfolded pinnules. At the end of a power stroke, the pinnules fold inwards and align with the arm brachials to initiate the recovery stroke. Figure 5.9 shows the unfolded pinnules (bold dots) over a stroke cycle on the vertical axis. The relative arm position from proximal (left) to distal (right) shows the pinnule status during a time instance. Pinnule status is derived from the relative velocity field. Pinnules are unfolded when the backward arm movement is faster than the swimming speed of the crinoid. More than 10 % of the arm's proximal end is always slower than the swimming speed and thus creates permanent drag. The transition between power stroke and recovery stroke was defined here as one in which more than 40 % of the brachials generate thrust. The illustration of an arm stroke on the right side in figure 5.9 highlights power and recovery stroke poses.

The kinematic analysis of the swimming movements of *P. kerguelensis* provides information on the linear and angular velocities as well as the accelerations of all body segments (brachial, pinnule and cirri). The velocities relative to the surrounding fluid result in either drag or thrust depending on the direction of action, which are calculated in the Fluid Dynamics section. The accelerations calculated from the kinematics in conjunction with the segment masses provides the basis for energy calculations in the Inverse Dynamics section.

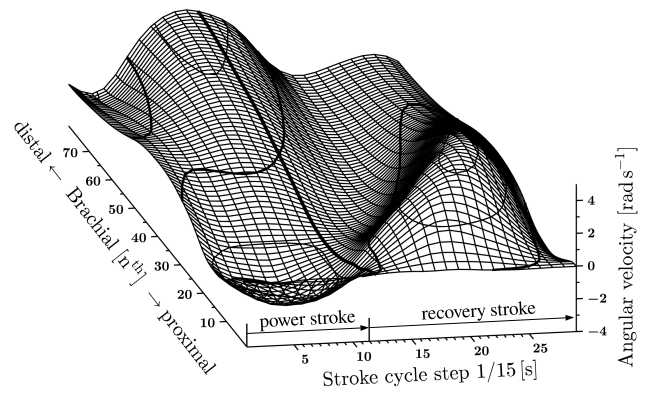
5.2 Locomotion Kinematics



(a)



(b)



(c)

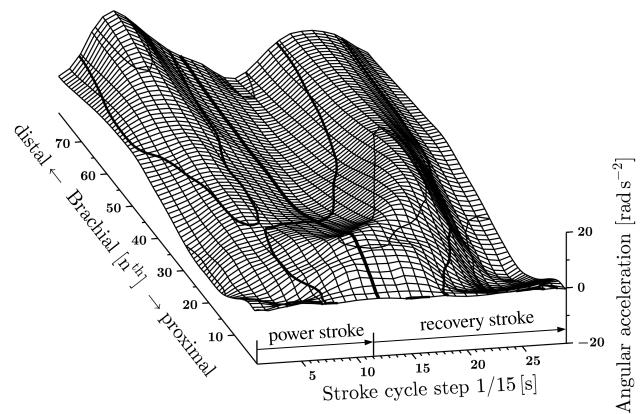


Fig. 5.7 Angular arm kinematics **a** Arm kinematics of a mean stroke cycle ($n=53$), thick lines indicate the power-stroke phase. **b** Angular velocity and **c** angular acceleration are shown for all brachial segments over one stroke period on the x-axis and the position on the arm on the y-axis.

5. Results

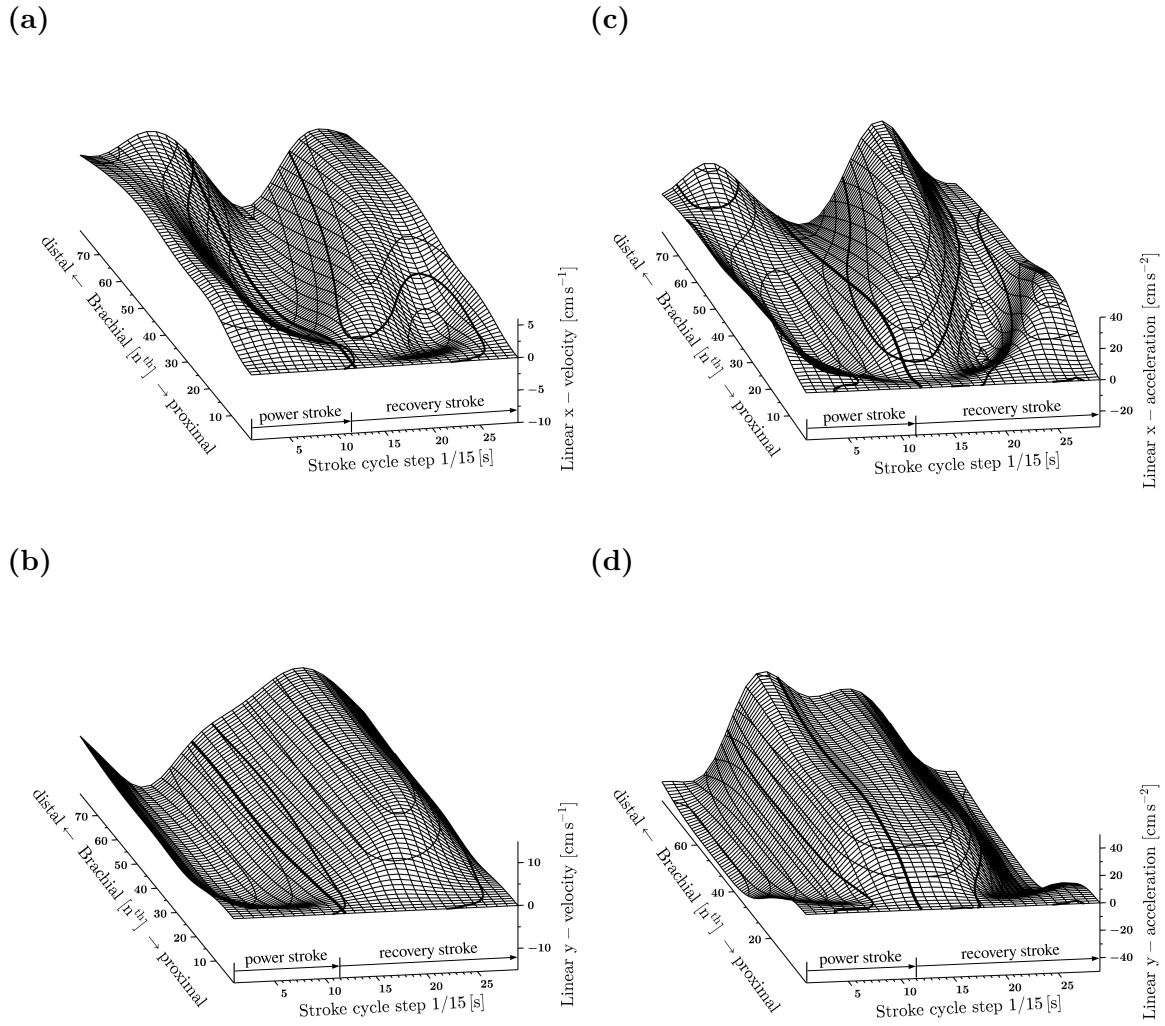


Fig. 5.8 Linear Arm Kinematics **a** x-velocity and **b** y-velocity components of brachials over a stroke cycle on the x-axis and along the arm on the y-axis, **c** and **d** show the corresponding acceleration components.



5.2 Locomotion Kinematics

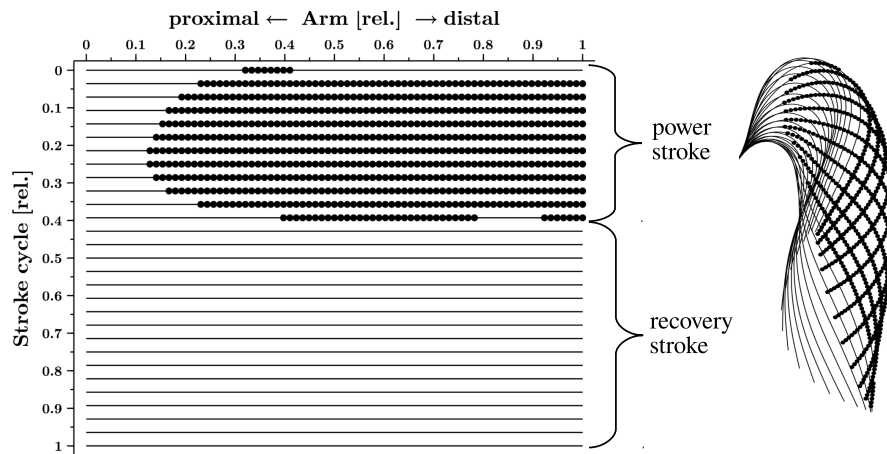


Fig. 5.9 Pinnule position during stroke phases. The kinematically averaged stroke cycle shows the pinnule phases of the power stroke and the recovery stroke. Bold dots mark the positions of the unfolded pinnules during a power stroke. The state of the pinnules, folded and unfolded, was automatically determined as a function of the relative speed of brachial to fluid. Thrust is only generated when the arm parts move backwards faster than the organism swims forwards. The principle of the algorithm for the iterative process is illustrated in the flowchart [4.11](#).

5.3 Fluid Dynamics

In order to determine the fluid-dynamical properties speed and maximum payload for the swimming crinoid, the hydrodynamic forces thrust and drag were first calculated using an analytical approach. These external forces acting on the organism are essential elements for carrying out the inverse dynamics, so that the Cost Of Transport *COT* (energy demand) for the locomotion of the crinoid can be determined later on. Fluid dynamic forces create a resistance on objects when moved through a fluid. The effect of a given force depends on its direction of action. Forces propelling the organism forward referred as *thrust* while forces acting in the opposite direction create drag. The ratio of drag and thrust thus determines the resulting swimming direction and velocity. Is an organism heavier than the surrounding fluid, part of the thrust generated must compensate for the weight pulling it downwards. The relationship between weight and thrust also determines the maximum payload, which is the maximum weight an organism can reach to still be able to lift itself off the ground. The trigonometric relationship for vertical swimming was used to calculate the horizontal swimming speed. This means if the vertical thrust component carries the dead weight and the excess forces can be used for horizontal swimming, they only have to work against the horizontal drag. Each simulation was derived from a single arm stroke and multiplied by twelve to represent a twelve-armed crinoid.

Reynold's realm

The analytical fluid dynamic equations apply only to low Reynolds numbers Re . While Lamb's approach covers a range of Re less than one (Lamb, 1932), Kümmel's equation increases the range and considers all Re less than 2,000 (Kümmel, 2007). However, analytical fluid dynamics can only lead to reasonable results if this condition is fulfilled.

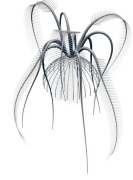
The mean Reynolds number of all brachials and pinnules is $Re_{mean} = 8.6$ with a maximum Re_{max} of about 138. Approximately 90% of brachials are in a range $Re < 20$ and about 23% are less than 1. These values are based on 190,008 segments calculated in one stroke cycle of averaged arm kinematics. The relative occurrence in the Re range is shown in figure 5.10.

Since all segments without exception are below Re 2,000, there are no restrictions on the Reynolds range for an analytical solution.

Thrust, Drag, and Velocity

A fluid dynamic force is the result of the mutual interaction between an object and the fluid surrounding it. Whether a force produces thrust or drag depends only on its direction of action; its ratio of the two determines the resulting velocity of propagation.

At constant speed, when the effective forces neither accelerate nor decelerate the organism, the thrust is equal to the drag plus its weight. Fluid dynamics were performed for ten swimming speeds at different paddle frequencies from 0.52 Hz (100%) down to 0.21 Hz (40%) of the observed paddle motion. The total thrust generated



5.3 Fluid Dynamics

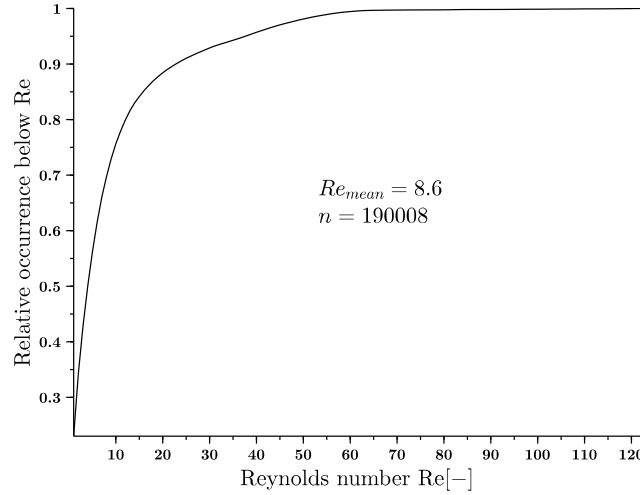


Fig. 5.10 Range of Reynolds numbers. Relative occurrence below a certain Reynolds number Re . About 23% of all segments have a Re less than 1 and about 90% less than 20. The data are based on a sample size of 190,008. The average Re of the whole organism is about 8.

ranges from $\sim 4 \text{ mN}$ (40%) to about 14 mN (100%) and the resulting swimming velocities from $\sim 4 \text{ mm s}^{-1}$ to $\sim 11 \text{ mm s}^{-1}$ vertically and respectively from $\sim 35 \text{ mm s}^{-1}$ to $\sim 45 \text{ mm s}^{-1}$ horizontally. Figure 5.11 shows the results averaged over 53 samples (open symbols) and those of the averaged kinematics (filled symbols).

The observed vertically swimming crinoid generates 13.72 mN of thrust, which is counteracted by 10.05 mN of resistance created by the arms themselves to this must be added 2.83 mN of weight and 0.84 mN body drag. Force components involved in observed swimming and predicted maximum range velocity MRV are shown in figure 5.12. The total thrust is the total force generated, while the effective thrust refers to the portion that leads to the change in position.

Where and when thrust or drag is generated during a stroke cycle is shown in figure 5.13. Negative values refer to drag when the incoming flow of the arms is faster than the absolute swimming speed of the crinoid. There is a region of $\sim 10\%$ at the proximal end of an arm where no thrust is generated at all (Fig. 5.13b), the maximum force impact velocity in this region is less than the absolute swimming velocity. Integrated values over a stroke cycle even show that more than 20% of the proximal arm generates resistance on average. Most of the thrust is generated in the middle phase of a force stroke with a maximum of $\sim 0.06 \text{ mN}$ (Fig. 5.13a). All the positive work is thus done by the distal 80% of the arm, with a slightly higher peak in the middle of the arm (about 50% of the arm length) (Fig. 5.13b).

Horizontal swimming speed is a measure of migration speed. The greatest distance is covered when the ratio of energy demand to speed reaches its minimum, which

5. Results

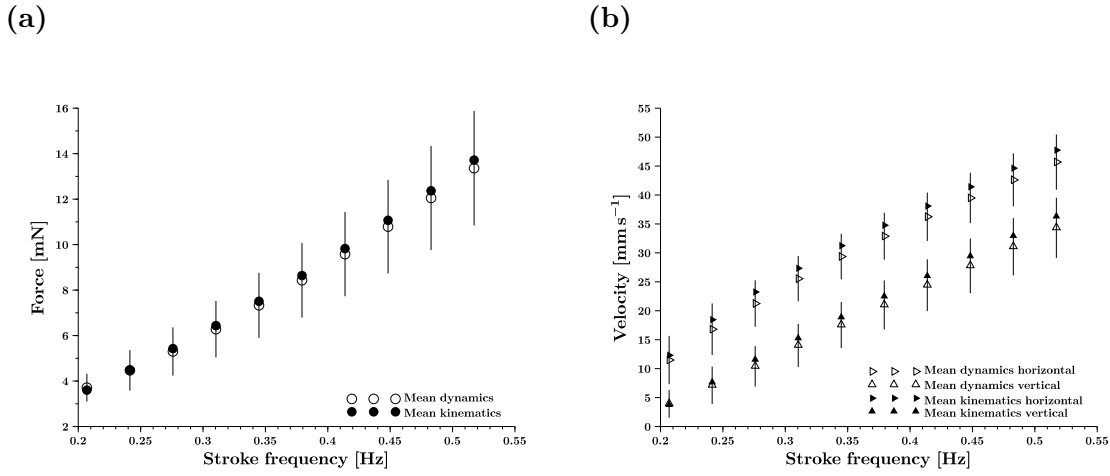
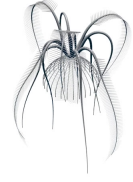


Fig. 5.11 Thrust force and velocity versus frequency. **a** Thrust force and **b** swimming velocities plotted over a stroke cycle. Fluid dynamic results from ten runs at increasing stroke frequency. The highest frequency represents the recorded swimming performance of the crinoids. Unfilled markers show standard deviation results (black bars) averaged from 53 individual stroke cycles. Filled markers are the results from the averaged kinematics.

is called Maximum Range Velocity *MRV*. Observed individuals are used to validate the results from the fluid dynamics approach (Fig. 5.14). The observed swimming velocities are 36.28 mm s^{-1} vertical and the derived horizontal velocity 47.75 mm s^{-1} . The kinematically averaged model shows slightly higher values than the mean values from fluid dynamics, but they are still within the range of the standard deviation. The swimming velocities at *MRV* are lower, 17.58 mm s^{-1} vertical, that is about 50% of the observed swimming, while the horizontal *MRV* with 28.95 mm s^{-1} reaches more than 60%. Inferred velocities from the video footage could only be estimated due to the two-dimensional nature of the imagery. The estimated height above the seabed and the individual derived image scaling are shown in figure 5.15. Derived velocities from height and temporal difference are summarised in table 5.3.



5.3 Fluid Dynamics

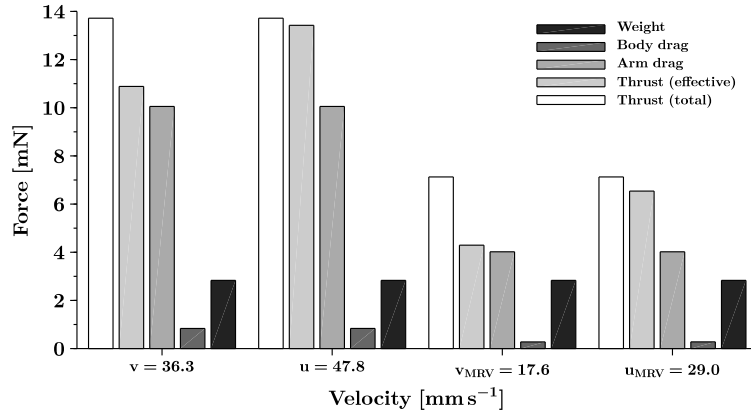
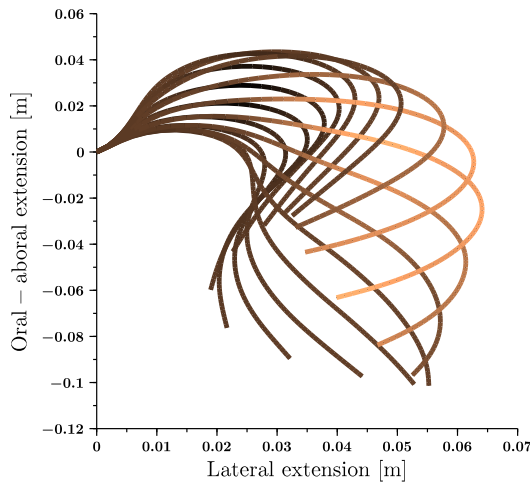


Fig. 5.12 Force components. Thrust and drag forces at observed and maximum range velocity MRV , vertical v and horizontal u . While total thrust is the total force generated, effective thrust refers to the part that results in progress (change of location). Body drag includes all passive elements calyx, cirri and primibrachials. Weight is given as weight in water.

(a)



(b)

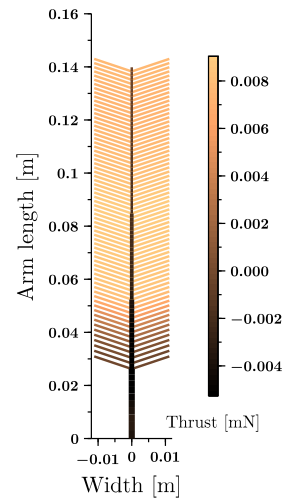


Fig. 5.13 Thrust force distribution over the stroke cycle and arm. **a** Pattern over one stroke cycle. **b** Average thrust during an entire stroke generated by brachials and pinnules. Areas with negative net forces generate less thrust than create drag.

5. Results

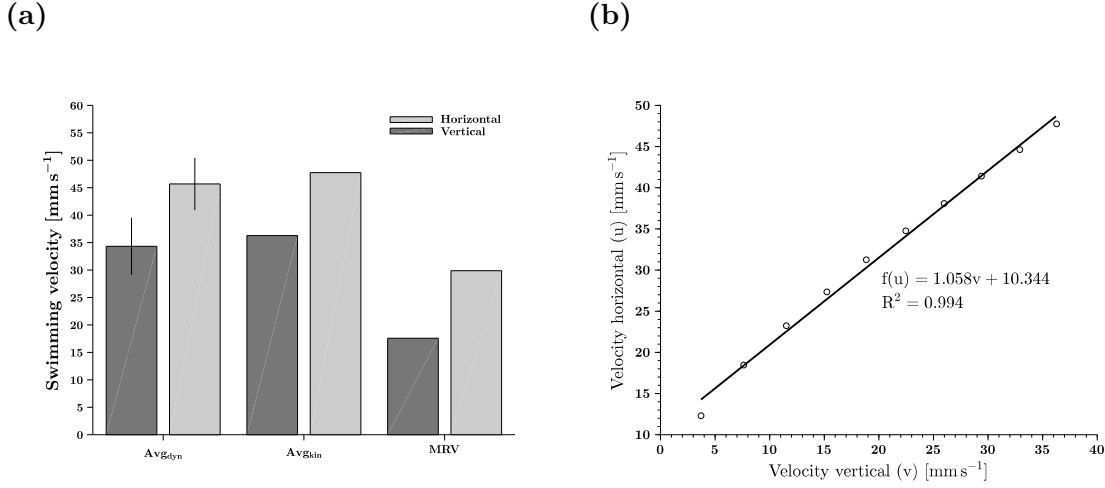
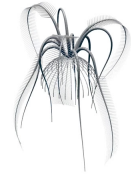


Fig. 5.14 Swimming velocity. **a** Vertical and horizontal swimming velocities derived from averaged fluid dynamics Avg_{dyn} including standard deviation ($n=53$), mean kinematics Avg_{kin} and Maximum Range Velocity MRV . **b** Relation between vertical and horizontal swimming velocity for different stroke cycle frequencies.

Tab. 5.3 Observed and calculated swimming velocities. Vertical swimming velocities v calculated in the analytical fluid dynamics (*values from the averaged kinematic model). Video-derived velocities were estimated from positions above the seabed on the first and last frames of the burst sequences (Fig. 5.15). Values in brackets refer to minimum and maximum estimates.

Sample	Fluid dynamics v [mm s^{-1}]	Digitized v [mm s^{-1}]
RS610012	33(± 9)	35 (34,38)
RS619007	30(± 5)	41 (34,49)
RS620008	42(± 5)	37 (30,43)
RS620018	32(± 4)	33 (30,36)
Average	35(± 5) 36*	37 (32,42)



5.3 Fluid Dynamics



Fig. 5.15 Travelled distances during a sequence. Distances to the seabed (yellow arrows). The left column shows the first images of each swim stroke, the right side the corresponding last image. Light blue numbers indicate the respective scale factors in [px m⁻¹], highlighted by light blue circles around the crinoids. Yellow values indicate the vertical distances to the estimated locations on the seafloor (yellow circles). Images taken on the *Polarstern* cruise PS82 [cri], [crii].

5. Results

5.3.1 Weight and Payload

Body weight and maximum load is the second parameter to evaluate the analytical approach. The average weight in water WIW is 0.29 g. The maximum lift-off weight (weight of the organism plus payload) is 1.40 g. It was solved numerically when the thrust is equal to the weight force (Fig. 5.14).

Tab. 5.4 Body weight and payload. Body mass of *P. kerguelensis* derived from density, volume and water properties. Maximum payload in water allowing lift-off from the seabed calculated for the average kinematic model Avg_{kin} , maximum range velocity MRV and as the mean of 53 calculations.

	Mass [g]
Wet mass	5.57
Mass in water	0.29
Max payload Avg_{kin}	1.40
Max payload $Avg_{kin} MRV$	0.73
Max payload Avg_{dyn}	1.36(± 0.26)

Most of the thrust is generated by the pinnules. An arm without pinnules still generates a positive thrust of 0.25 mN, but this is not sufficient to lift the crinoid off the ground. The increase in thrust respectively swimming speed is related to the angle of attack of the pinnules. A larger angle of attack leads to more thrust and higher swimming speeds (Tab. 5.5).

Tab. 5.5 Influence of pinnule's angle of attack. Maximum payload as a measure of generated thrust determined for different pinnule poses and without pinnules. Pinnule angle of attack refers to the angle between pinnule and major arm axis. Calculations were conducted on the average kinematic model at observed swimming velocity.

Angle of attack	without	20°	45°	67°	90°
Mass [g]	0.03	0.94	1.13	1.40	1.59
Thrust [mN]	0.25	9.26	11.03	13.73	15.62
Velocity v [mm s ⁻¹]	–	27.34	31.25	36.33	39.45

Fluid Properties

All values come from the calculation in the fluid dynamics section: Reynolds number, drag coefficient and forces depend on the fluid properties density and viscosity. Both parameters are functions of temperature, pressure and salinity. The values for the



5.3 Fluid Dynamics

Tab. 5.6 Fluid properties density, dynamic and kinematic viscosity derived from ambient properties of temperature, pressure and salinity (Rowe and Chou, 1970; Kuder, 2011). The values from the four stations on the Antarctic continental shelf were averaged and compared with the habitat on the Canadian west coast of *F. serratissima*, another comatulid crinoid of the Antedon family.

Measured data	Antarctic shelf	Canadian west coast
Temperature T [°C]	$-1.84 (\pm 0.03)$	10
Pressure p [MPa]	$2.70 (\pm 0.19)$	0.1
Salinity $NaCl$ [$g\ cm^{-3}$]	$0.0344 (\pm 0.0000)$	0.0344
Derived values		
Density ρ [$kg\ m^{-3}$]	1,026.66	1,024.70
Dynamic viscosity μ [Pa s]	1.860e-03	1.321e-03
Kinematic viscosity ν [$m^2\ s^{-1}$]	1.812e-06	1.289e-06

Antarctic continental shelf are compared with those for the Canadian west coast, where a related comatulid *Ferracrinus serratissima* lives (Tab. 5.6). The viscosity of the water at 280 m depth and -1.84°C water temperature is about one third higher than in the shallow waters of the Canadian coast. The salinity is assumed to be comparable in both regions.

The observed swimming comatulid crinoid *P. kerguelensis* generates an average thrust of 13.7 mN and achieves a vertical swimming speed of $36\ mm\ s^{-1}$ or could lift 1.4 g of body mass. Its most efficient horizontal locomotion speed, the Maximum Range Velocity *MRV*, was found to be about $29\ mm\ s^{-1}$. This plays a role in migration, as organisms tend to rely on efficient locomotion for long distances.

5.4 Inverse Dynamics

In contrast to fluid dynamics, inverse dynamics deals with the internal forces of a system. It is used to derive the load on the internal structure from external forces, fluid dynamic resistance, gravitational force (weight) and morphological dimensions (shape). This internal load is a measure of the required muscle activity. The locomotion-specific energy demand depends on the muscle contraction rate and the resulting internal load. The Cost Of Transport *COT* is then obtained by integrating all across all components involved. Since *COT* is a function of over time, it is minimum at the Maximum Range Velocity *MRV* when the distance travelled is maximum for a given energy fraction.

The following results were calculated for vertical swimming at observed paddle frequency and the kinematically averaged model. The resulting force components in lateral x and oral-aboral y directions are shown in figure 5.16. The forces exerted via a moment arm generate a torque [Nm] that acts on the corresponding joint (Fig. 5.17). They thus represent the rate of loading on the skeletal structure. The results presented here are oriented to the right side of the body. The forces in both directions are lower during the recovery stroke when the arm is pulled forward with the pinnules folded. Both components increase along the arm axis from the distal to the proximal end. The maximum lateral x -force 1.54 mN on a brachial occurs at the end of the first third of a power stroke when the arm is extended laterally. In contrast to the x -components, the oral-aboral forces are negative during the power stroke and slightly positive during the recovery phase. The maximum force backwards is transmitted in the middle of the power phase and reaches a value of up to -2.56 mN at the proximal end of the arm. The ratio between force and recovery stroke of 0.86 mN is about 1:3.

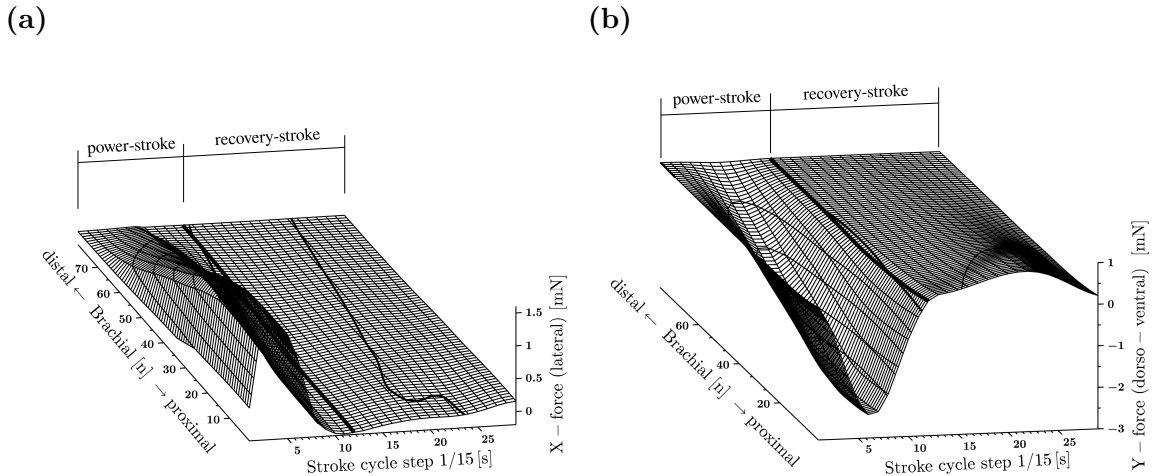


Fig. 5.16 Internal forces. Load on the brachial joints. **a** Lateral x -forces and **b** oral-aboral y -forces.

The moments [mNm] at the brachial joints are derived from the associated forces [mN] and the corresponding moment arms [m] (Fig. 5.17). The generated forces



5.5 Energetics: Cost Of Transport *COT*

dominate during power strokes with a maximum torque (counter-clockwise) of about -0.12 mNm at the most proximal arm end. Recovery strokes show a maximum value of about a quarter, 0.03 mNm clockwise.

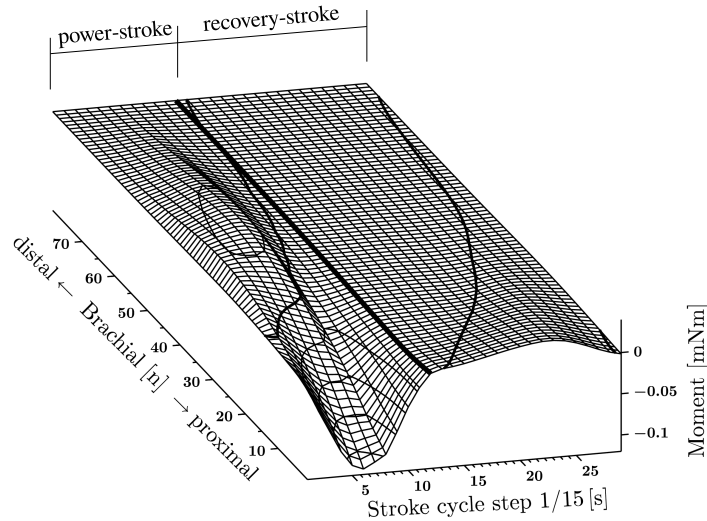


Fig. 5.17 Internal moments. Moments at brachial joints over one stroke cycle on the x-axis and along the arm on the y-axis.

5.5 Energetics: Cost Of Transport *COT*

The energy required to perform movements is the product of the torque generated and the resulting rotational movement (angular velocity from kinematics). The cost of transport is given both per time and per distance. The absolute energy requirement for locomotion per time is integrated over the arm length as well as the time and multiplied by the number of arms (Fig. 5.18). *Promachocrinus kerguelensis* requires 33.6 cal h^{-1} , which corresponds to $\sim 3 \text{ mg}$ organic carbon or $\sim 7 \text{ mg}$ plankton (dry weight) (Platt and Irwin, 1973; Percy and Fife, 1981; Schaafsma et al., 2018). The kinematically averaged model shows slightly lower values, but within the range of the standard deviation. The cost of transport at maximum range velocity *MRV*, which is assumed to be the most efficient or cheapest swimming, requires less than half the energy per time. Optimal horizontal migration under a given amount of available energy in the form of food is thus achieved at maximum range velocity.

5. Results

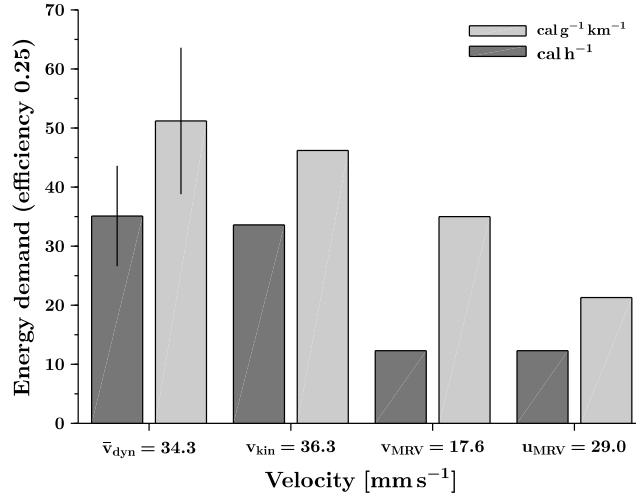


Fig. 5.18 Cost Of Transport COT . \bar{v}_{dyn} are average values from the dynamic calculations (n=53, black lines show standard deviation), v_{kin} are results from averaged kinematics, v_{MRV} show interpolated values at Maximum Range Velocity MRV , and u_{MRV} the corresponding transport costs for horizontal swimming.



5.6 Maximum Range Velocity *MRV*

5.6 Maximum Range Velocity *MRV*

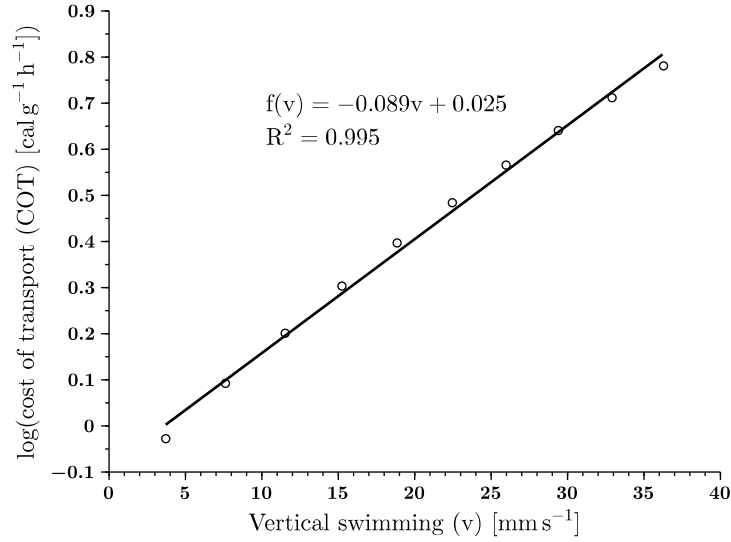
Tab. 5.7 Transport costs for different speeds. Vertical velocity v , horizontal velocity u and Cost Of Transport COT are given over different arm stroke frequencies.

Frequency [Hz]	v [mm s ⁻¹]	u [mm s ⁻¹]	COT [cal h ⁻¹]	COT [cal g ⁻¹ km ⁻¹]
0.21	3.7	12.3	5.2	70.3
0.24	7.6	18.5	6.9	45.1
0.28	11.5	23.2	8.9	38.3
0.31	15.2	27.3	11.2	36.7
0.34	18.9	31.3	13.9	36.8
0.38	22.5	34.8	17.0	37.7
0.42	26.0	38.1	20.5	39.4
0.45	29.4	41.4	24.4	41.3
0.48	32.9	44.6	28.7	43.5
0.52	36.3	47.8	33.6	46.2

The energy requirement for swimming, derived from inverse dynamics and expressed as a Cost Of Transport COT , is a function of the speed of movement. Assuming that the locomotion cost is simply changed by modulating the arm stroke frequency, it was adjusted by increasing the time interval between two adjacent video frames and calculated for ten speeds at rates between 6...15 frames per second *fps*. Corresponding arm beat frequencies, swimming speeds and transport costs are shown in table 5.7. Horizontal velocity u is related $Vf(v) = 1.058v + 10.344$ to vertical swimming velocity v , while COT per time increases with velocity from 5.8 cal h⁻¹ to 35.1 cal h⁻¹. The COT per weight and distance has a minimum of 35.0 cal g⁻¹ km⁻¹ at a velocity of 17.6 mm s⁻¹ (Fig. 5.19). The corresponding horizontal velocity u is then 29.0 mm s⁻¹ with a COT of 21.3 cal g⁻¹ km⁻¹. The requirement for *MRV* is then 12.3 cal h⁻¹. All energy values are corrected for the muscle power efficiency of 0.25 according to Hill (1950).

5. Results

(a)



(b)

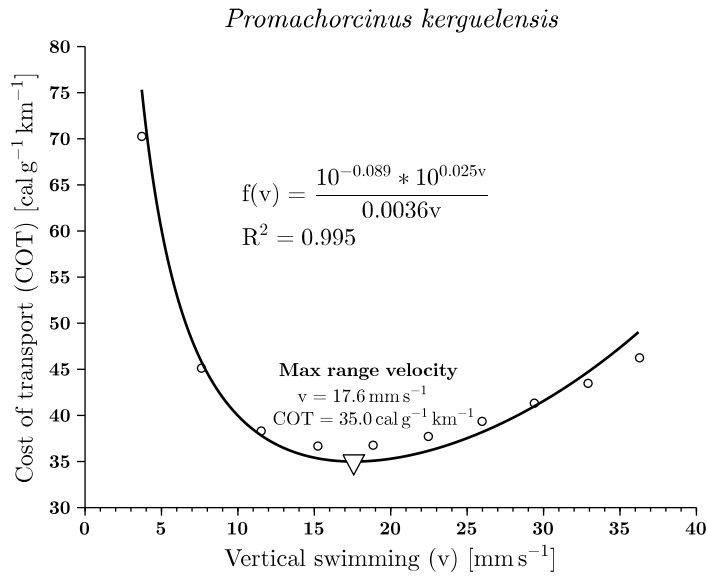


Fig. 5.19 Cost of transport over swimming velocity. **a** Relationship between Cost Of Transport COT per unit time ($\log(COT \text{ [cal g}^{-1} \text{ h}^{-1}])$) and swimming speed $v \text{ [mm s}^{-1}])$. **b** COT converted to distance-dependent energy demand $\text{[cal g}^{-1} \text{ km}^{-1}]$ and plotted versus v . The minimum COT is reached at the Maximum Range Velocity MRV .



5.7 Environmental Boundary Conditions

Migration rates of *Promachocrinus kerguelensis* and their resulting circum-Antarctic dispersal are influenced by the prevailing environmental conditions. The available energy in the form of food determines where individuals can survive, respectively how much energy is left for physical activity and therefore the distance they can swim each day. Another factor is the ocean and tidal currents, which can either support but also restrict migration. Under extreme strong currents, dispersal in a certain direction can even be prevented. This applies to both dispersal by drifting larvae and active swimming.

Food availability depends on primary production at the sea surface. How much of this ultimately reaches the seabed depends in turn on the water depth. The Net Primary Production *NPP* of organic carbon by phytoplankton is the process of photosynthesis, it takes place in the upper water layer of the ocean. The photosynthetic production rate is a function of the amount of phytoplankton and the available light. These parameters are influenced by the position of the sun, cloud cover, ice cover and its thickness. All these components were either modelled or taken from third-party sources, calculated monthly, merged and averaged over sixteen years (2003–2018) for the ocean south of -60° latitude at a resolution of 801×801 grid cells (about 8×8 km). All data shown below are displayed in a stereo polar projection EPSG:3031.

Sea Ice Thickness

Ice thickness determines the amount of light penetration and thus the rate of net primary production in ice-covered areas. The thicker the ice, the less light can shine through and the lower the primary production. The ice thickness is presented as an average of monthly data sets over the period of sixteen years (2003–2018) and their corresponding standard deviation (Fig. 5.20). It can be seen that the maximum average thickness of 2.4 m occurs in the western Weddell Sea. The standard deviation is a measure of annual variations. The lowest standard deviations are found in the Weddell Sea. This means that the ice cover and thickness is relatively constant in this area.

Chlorophyll

The ocean chlorophyll [mg m^{-3}] was derived from remote sensing in ice-free regions (satellite-based). It was integrated over the water column to total chlorophyll [g m^{-2}] (Fig. 5.21). Since ice-covered areas are not mapped by remote sensing, the ice chlorophyll was calculated separately, based on the chlorophyll content of the ice (Fig. 5.22). Part of the Weddell Sea is continuously covered by sea ice, as indicated by the white area east of the Antarctic Peninsula. In contrast, the greatest occurrence of chlorophyll occurs in a narrow band along the coastline. The standard deviation represents the seasonal variability over a year. Lower concentrations in the open ocean show

5. Results

relatively constant values, while the higher concentrations near the coast show greater variability, indicating strong seasonal differences.

Cloud fraction

Atmospheric properties influence the amount of sunlight reaching the Earth's surface. Clouds (water vapour) reduces the light transmission through the atmosphere and decreases therefore the radiation intensity. The cloud fraction (monthly data) as relative coverage was averaged over sixteen years (2003–2018) (Fig. 5.23). The densest coverage (almost 100%) was observed over the open ocean. It decreases towards the south, with a simultaneous increase in annual variation (standard deviation).

Light Radiation

The light radiation PAR in $[J\ m^{-2}\ day^{-1}]$ as the primary energy source on the Earth's surface is calculated from the extraterrestrial radiation that hits the Earth's atmosphere at an angle dependent on the position of the sun. It is reduced by the fraction absorbed by atmospheric conditions (clouds) (Fig. 5.24).

Net Primary Production

Net primary production NPP of organic carbon, the source of available energy for life forms, was calculated using chlorophyll concentration, which is representative of the level of photosynthetic activity, and the amount of available light that drives the process. Ice-free and sea-ice covered regions were treated separately, merged monthly, combined and averaged over the sixteen years period 2003 to 2018. Primary production inside and below sea ice is based on its chlorophyll content and light penetration as a function of ice thickness. Its maximum average value (Fig. 5.26) is about an order of magnitude lower than production in open waters (Fig. 5.25). Coastal areas show higher productivity, but also higher seasonal fluctuations, which are directly related to the prevailing chlorophyll concentrations (Fig. 5.21 and 5.22). The combined map (Fig. 5.27) shows values of organic carbon ranging from $0.0016\ g\ m^{-2}\ day^{-1}$ in the Weddell Sea east of the Antarctic Peninsula to $0.6\ g\ m^{-2}\ day^{-1}$ near the coast.

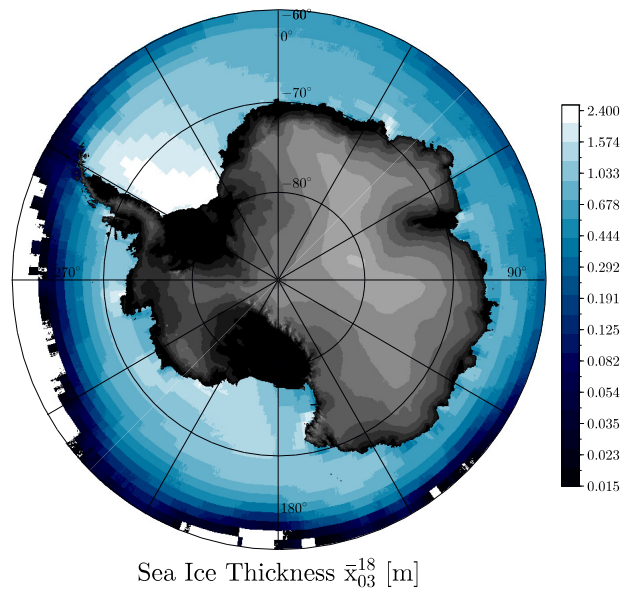
Available Energy at the Seafloor

The available energy stored in the form of organic particles arriving at the seabed is given as a factor $11.4\ cal\ mg_C^{-1}$ of organic carbon (Platt and Irwin, 1973). These are reduced on the way to the seabed via the food chain and are determined as a function of water depth. Shallow waters therefore generally provide more energy than deep-water regions (Fig. 5.28). Average values reach up to $14\ kcal\ m^{-2}\ day^{-1}$.



5.7 Environmental Boundary Conditions

(a)



(b)

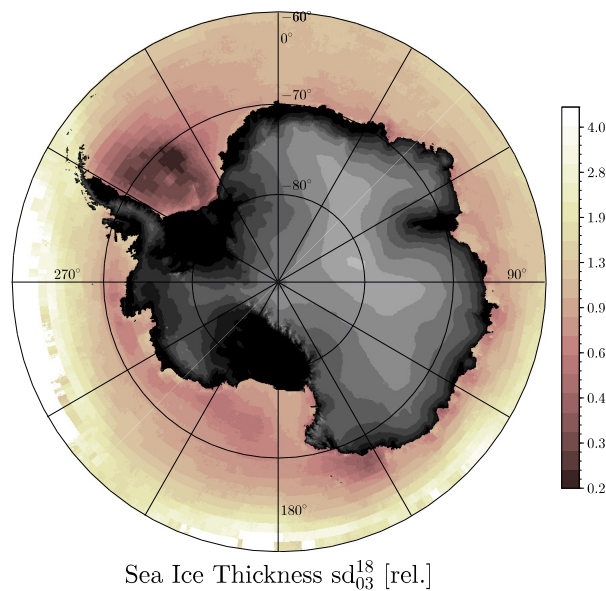
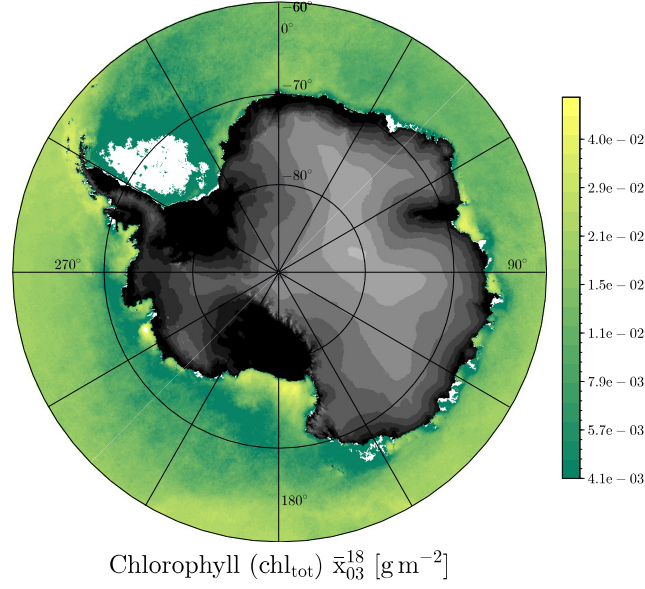


Fig. 5.20 Sea-ice thickness. Ice thicknesses were averaged from monthly datasets over sixteen years (2003–2018). Simulated polar ice data are provided by the Polar Science Center in Seattle, WA [sit]. **a** Mean values in metres; **b** Standard deviation shown relative to ice thickness.

(a)



(b)

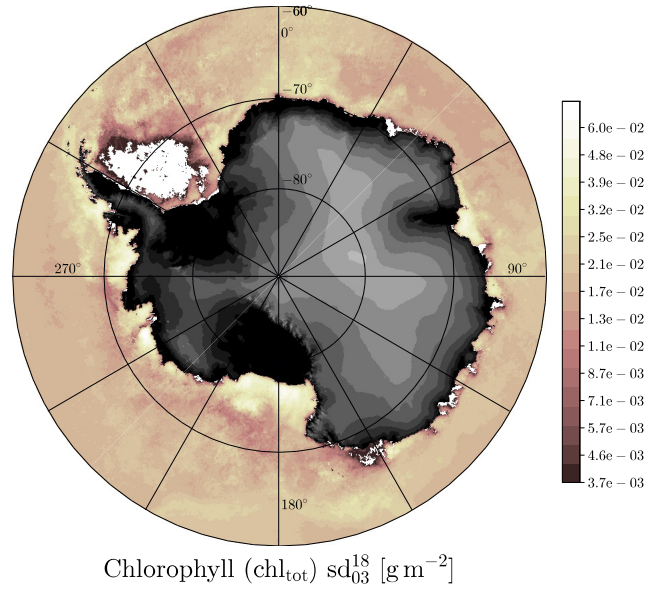
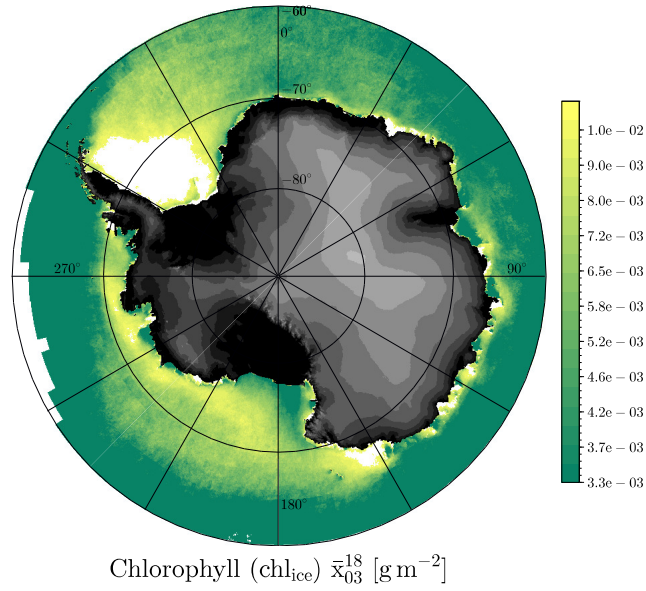


Fig. 5.21 Oceanic chlorophyll. Chlorophyll values in [g m^{-2}] were derived from remote sensing (satellite measurements) and integrated to total chlorophyll over the water column. **a** average values over the years 2003 to 2018; **b** standard deviation.



5.7 Environmental Boundary Conditions

(a)



(b)

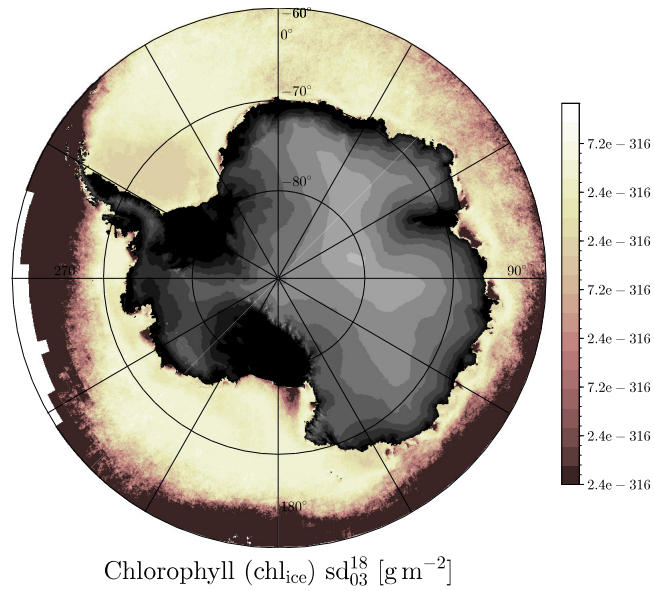
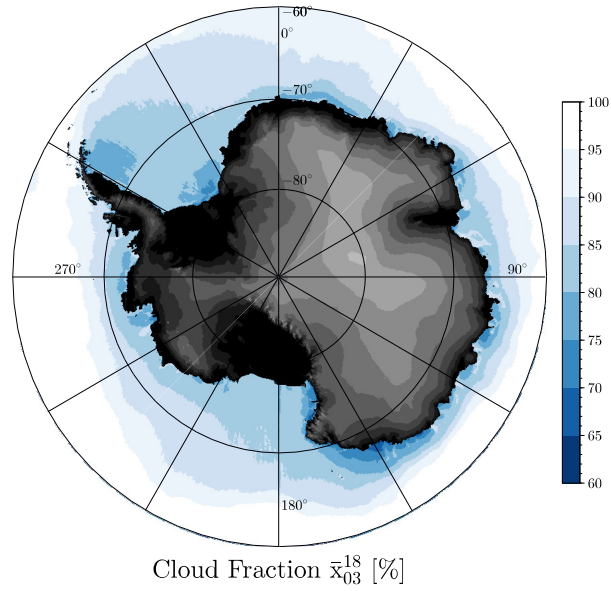


Fig. 5.22 Ice chlorophyll. Chlorophyll values in [g m^{-2}] derived from chlorophyll content according to [Saenz and Arrigo \(2014\)](#). **a** average values over the years 2003 to 2018; **b** standard deviation.

(a)



(b)

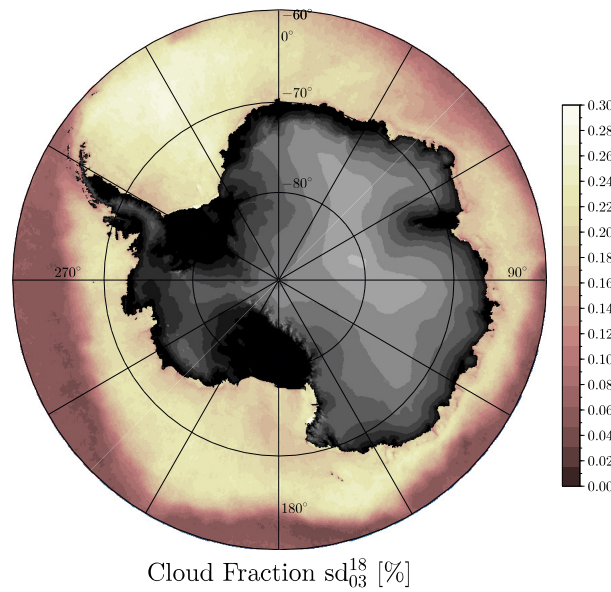
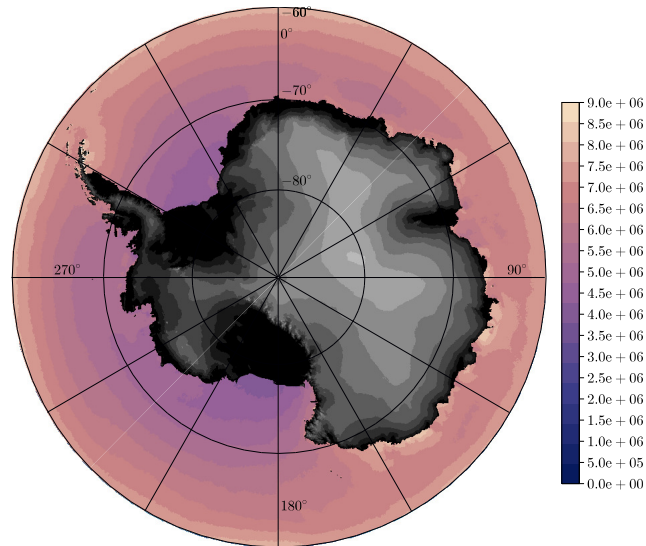


Fig. 5.23 Cloud fraction. Cloud cover, in [%], obtained from remote sensing. Data were downloaded from NASA Earth Observations as monthly data sets for the years 2003 to 2018 and averaged into a single data set [cl]. **a** Mean values; **b** Standard deviation.



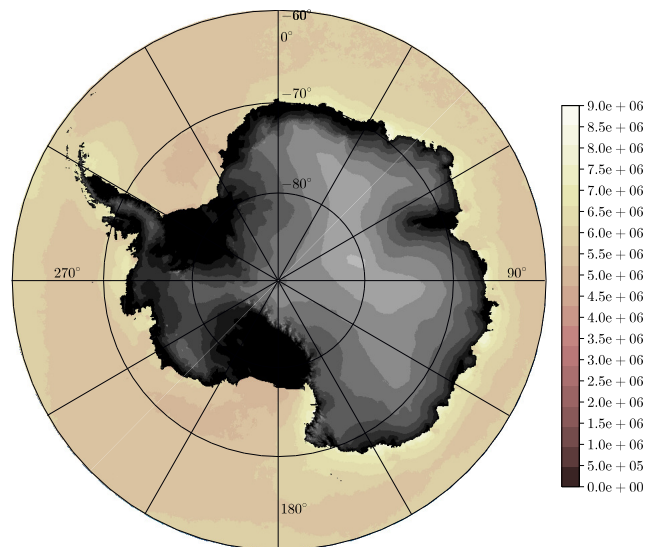
5.7 Environmental Boundary Conditions

(a)



Available Light (PAR) \bar{x}_{03}^{18} [$\text{J m}^{-2} \text{ day}^{-1}$]

(b)

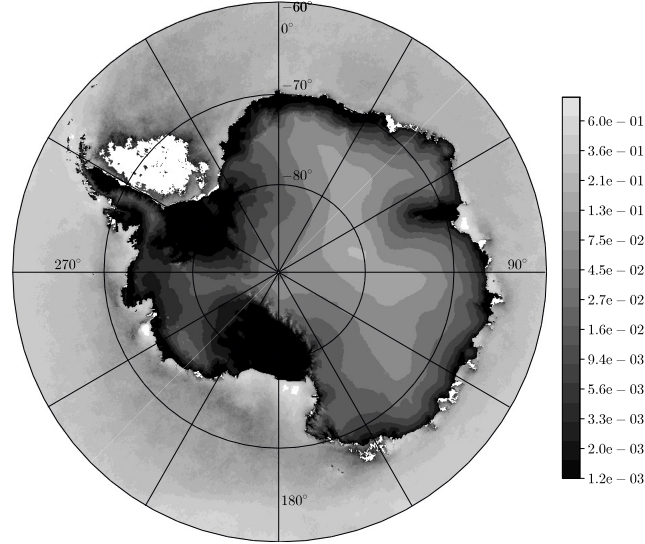


Available Light (PAR) sd_{03}^{18} [$\text{J m}^{-2} \text{ day}^{-1}$]

Fig. 5.24 Light radiation *PAR*. The values, in [$\text{J m}^{-2} \text{ day}^{-1}$], were calculated according to Morel 4.86 (Morel, 1991, p.265, Eq. 2). **a** Means; **b** Standard deviation.

5. Results

(a)



(b)

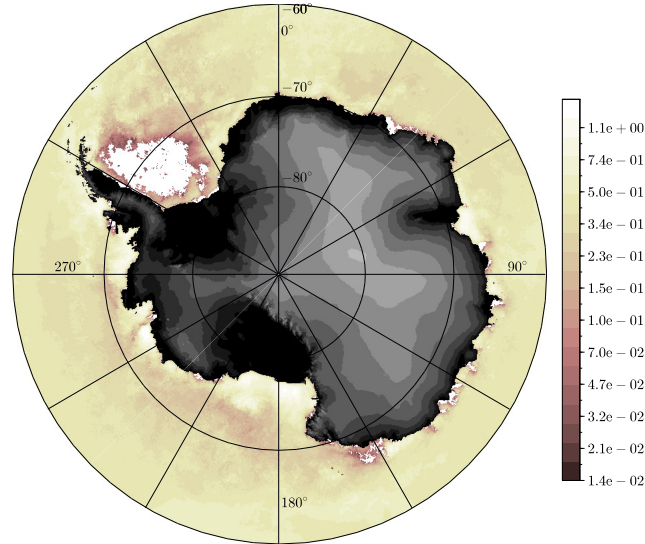
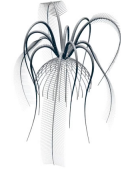
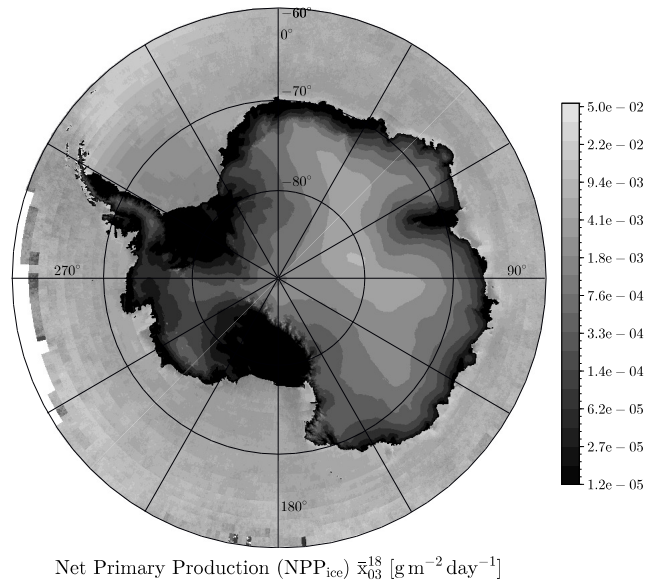


Fig. 5.25 The oceanic Net Primary Production NPP . Oceanic NPP of organic carbon, in [$\text{g m}^{-2} \text{ day}^{-1}$]. **a** Averaged over the years 2003 to 2018; **b** corresponding standard deviation.



5.7 Environmental Boundary Conditions

(a)



(b)

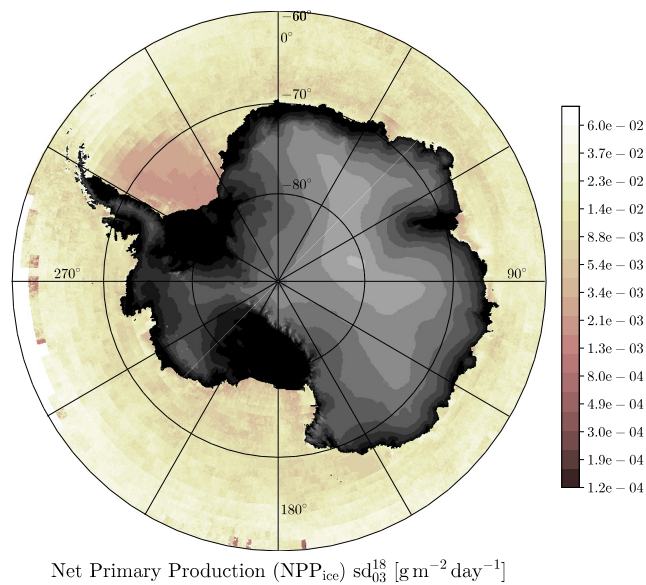
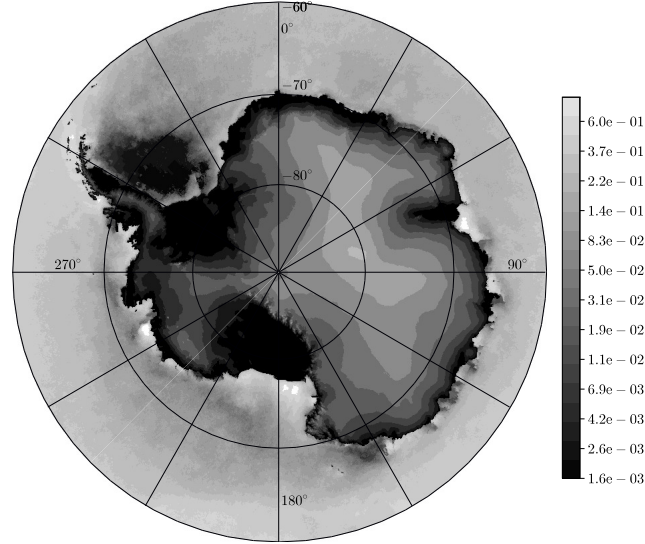


Fig. 5.26 Net Primary Production NPP of sea ice. Ice NPP of organic carbon, in [$\text{g m}^{-2} \text{ day}^{-1}$]. **a** Averaged over the years 2003 to 2018; **b** corresponding standard deviation.

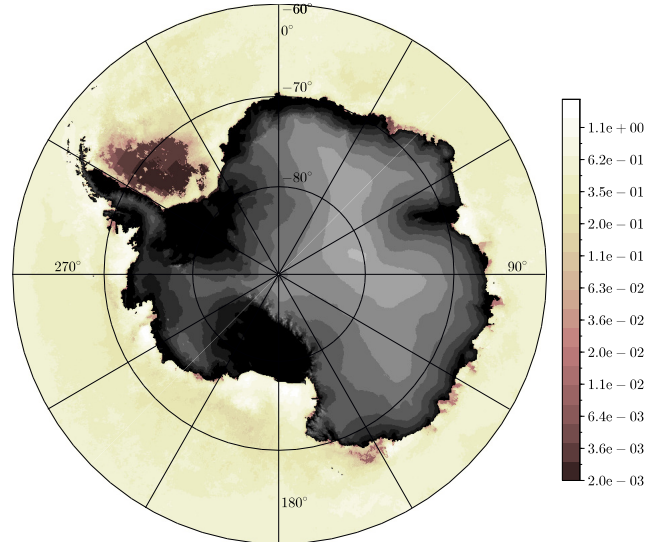
5. Results

(a)



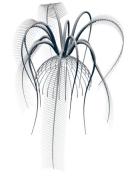
Net Primary Production (NPP) \bar{x}_{03}^{18} [$\text{g m}^{-2} \text{ day}^{-1}$]

(b)



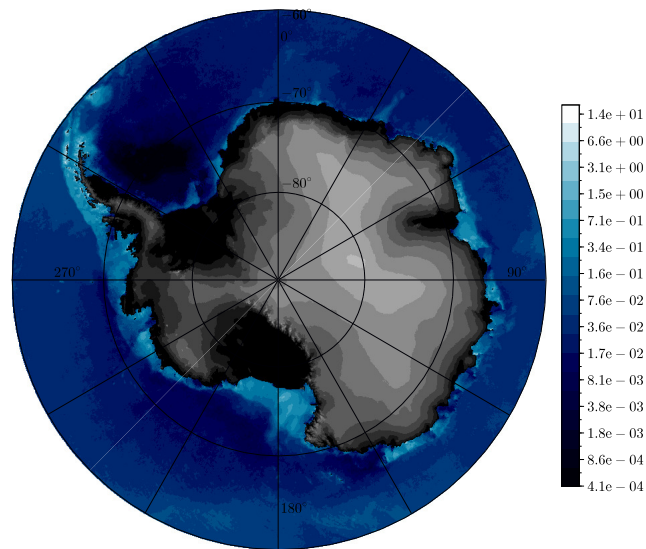
Net Primary Production (NPP) sd_{03}^{18} [$\text{g m}^{-2} \text{ day}^{-1}$]

Fig. 5.27 Total Net Primary Production NPP . Combined NPP of organic carbon, in [$\text{g m}^{-2} \text{ day}^{-1}$]. **a** Averaged over the years 2003 to 2018; **b** corresponding standard deviation.



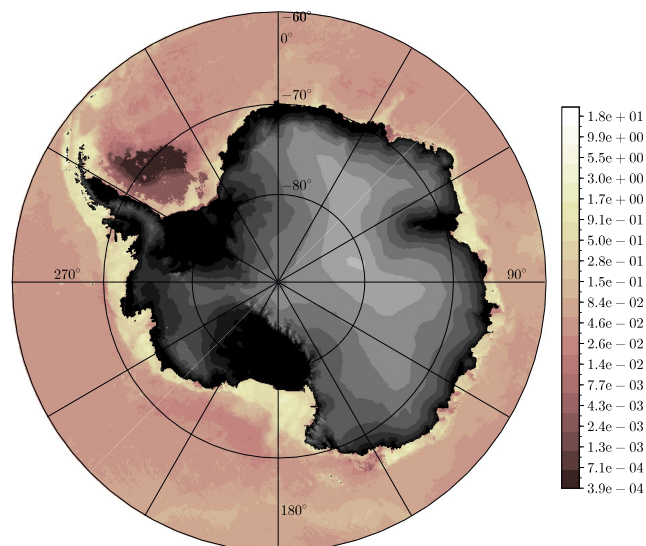
5.7 Environmental Boundary Conditions

(a)



Available Energy \bar{x}_{03}^{18} [$\text{kcal m}^{-2} \text{day}^{-1}$]

(b)



Available Energy sd_{03}^{18} [$\text{kcal m}^{-2} \text{day}^{-1}$]

Fig. 5.28 Available energy on the seabed. Energy content of organic matter, in [$\text{kcal m}^{-2} \text{day}^{-1}$], available at the seabed, previously produced at the sea surface and reduced by the food chain on its way to the seabed. **a** average values from 2003 to 2018; **b** corresponding standard deviation.

5. Results

Metabolic and Reproductive costs

Whether organisms are able to survive, reproduce and afford costly locomotion depends on the ratio of available and required energy. The costs of locomotion are discussed in the section on dynamics. Metabolic costs for life are derived from the regression: oxygen consumption as a function of ambient temperature, here -1.84°C (Fig. 5.29a). Reproduction costs were extrapolated from the relation in figure 5.29b for a wet body mass of 5.57 g.

Tab. 5.8 Costs for living. With their components for resting metabolism and reproduction.

	Costs [cal d^{-1}]
Metabolic	2.7
Reproductive	0.8
Total	3.5

The values for *Promachocrinus kerguelensis* were extrapolated and converted into the requirement of calories per day. The resting metabolic rate 2.7 cal d^{-1} is about three times higher than the average cost of reproduction 0.8 cal d^{-1} .

Cost of Living in Relation to the Productivity Surplus

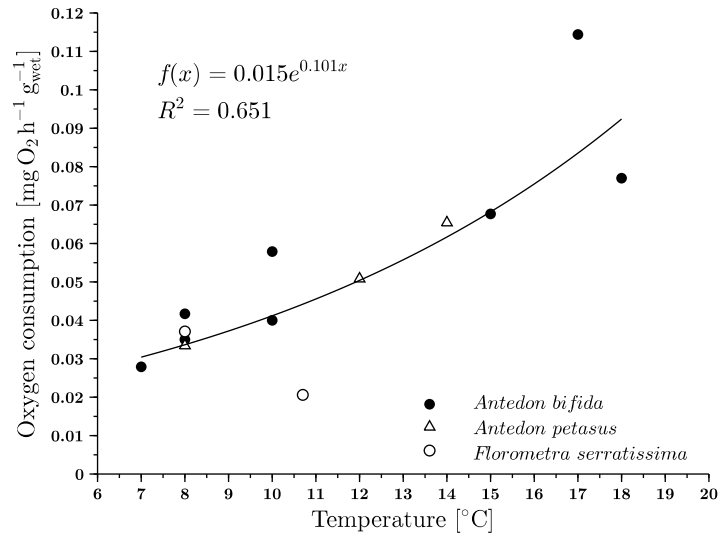
Productivity is a measure of the available amount of organic carbon produced, which corresponds to the amount of stored energy in the food source. In order to survive and reproduce, the available food must at least cover the cost of living of *P. kerguelensis* of 3.5 cal d^{-1} . Productivity in this study is therefore considered to be surplus productivity, as a ratio of sea area that provides more than the required cost of living. Annual mean values were obtained from monthly data and presented for the years 2003 to 2018 (Fig. 5.30). The year with the lowest production was 2014, with only about 6% of the seabed providing the required subsistence. The other end of the scale is 2010, when more than 9% of the ocean provided a sufficient amount of energy for *P. kerguelensis*. The records show a cyclical trend of successive high- and low-productive years (Fig. 5.30).

Local frequencies of available energy higher than the required limit for *P. kerguelensis* are shown for the years 2003 to 2018 in figure 5.31. The colour code from yellow to red represents the occurrence of local energy higher than $3.5 \text{ cal ind}^{-1} \text{ d}^{-1}$. In the yellow coloured area was at least this limit continuously maintained. The area shown in red provided such favourable conditions only in one out of the sixteen years. Although the red area corresponds well with the most productive year in 2010, local maxima partly occurred in other years as well.



5.7 Environmental Boundary Conditions

(a)



(b)

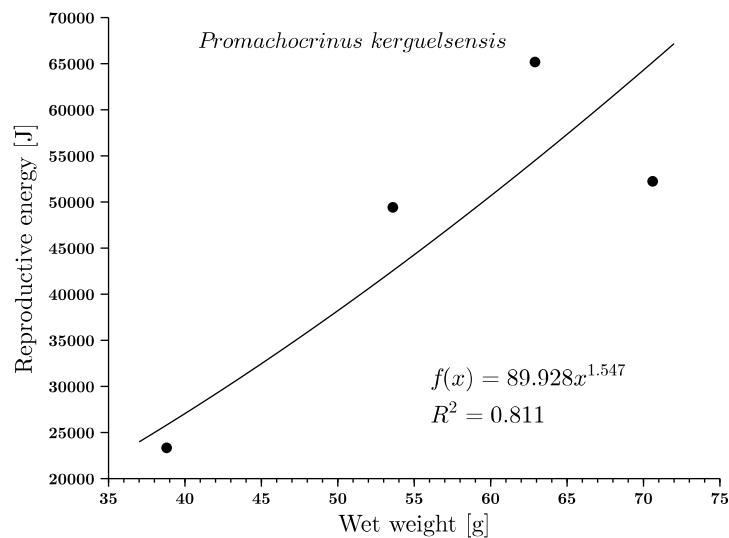


Fig. 5.29 Metabolic and reproductive costs. **a** Metabolic cost as a ratio of oxygen consumption to ambient temperature derived from several crinoid species. Data are based on incubation measurements from Fox (1936); La Touche (1976); Webster (1975); LaBarbera (1982); Warnock and Liddell (1985). **b** Regression of wet weight of crinoids on reproductive effort. Data provided by McClintock and Pearse (1987).

5. Results

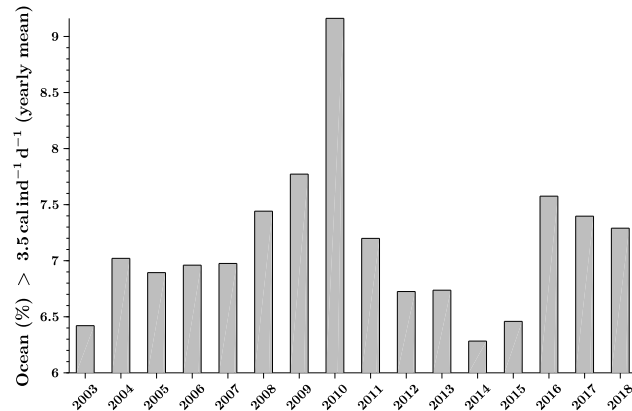


Fig. 5.30 Annual excess productivity from 2003 to 2018. Percentage of ocean (south of -60°) providing more than 3,5 calories per individual per day. Annual averages at the seabed are considered a measure of productivity.

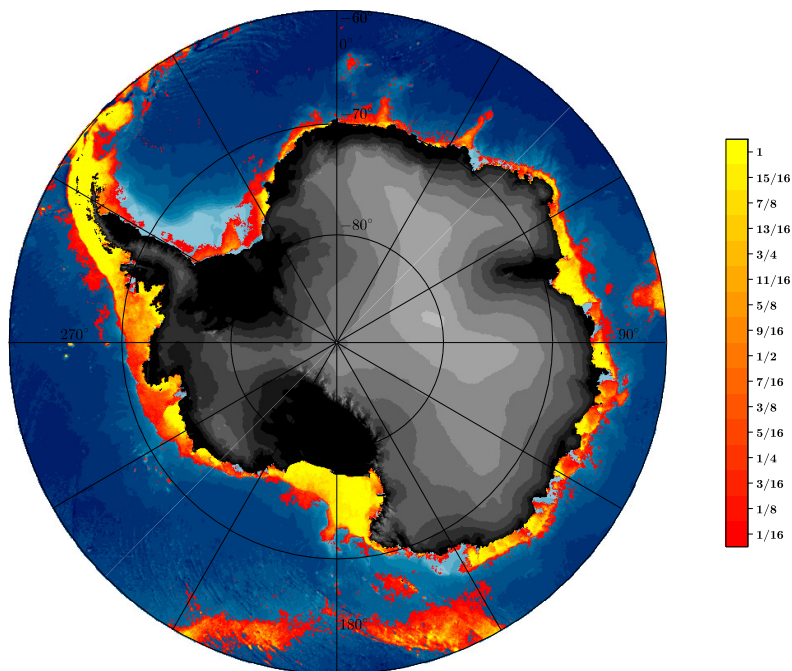


Fig. 5.31 Frequency of available energy. The diagram shows the range restricted to available energy at the seabed of more than $3.5 \text{ cal ind}^{-1} \text{ d}^{-1}$. The colour gradient represents the relative abundance of the ordered mean values. Red cells cover the region of the highest yielding year, which was reached only once ($1/16$) in the period between 2003 and 2018. Yellow represents the region that continuously delivers at least this yield, indicated by 1 or 100% of all years. The underlying bathymetric map is taken from IBCSO [bc] (Arndt et al., 2013).



5.7 Environmental Boundary Conditions

Ocean Current and Ice Drift

Water currents are another relevant parameter in two respects: They carry juvenile pelagic larvae until final settlement, and secondly they support or impede locomotion. Water currents were recorded remotely using satellite measurements, which cannot capture water movement under sea ice. In order to obtain a comprehensive and consistent picture of the overall current patterns, surface currents and ice drift were combined and averaged over 192 months from January 2003 to December 2018. Vector components u (east) and v (north) were transformed to cardinal direction and magnitude in $[\text{m s}^{-1}]$ (Fig. 5.32). The Antarctic Circumpolar Current *ACC* is clearly visible as a clockwise flow in light blue. A coastal counter-clockwise current extends from the Amundsen Sea to the Weddell Sea almost completely around the Antarctic continent, only the Antarctic Peninsula forms a natural barrier and prevents the current from forming a closed circuit. The boundary line between the two opposing currents is clearly visible in the velocity field. A distinct band of slow-flowing water masses can be seen on the corresponding map (Fig. 5.32b). Maximum current velocities of 0.5 m s^{-1} (about 1 kn) occur in the Drake Passage north of the Antarctic Peninsula (60° W) and are associated with the Pacific-Antarctic Ridge near the International Date Line *IDL* (170° E). Two other features of the southern ocean system can be identified. A northerly current along the eastern flank of the Antarctic Peninsula is diverted eastward. The current turns south again in the region behind Bouvet Island (30° E) and then westward into the Weddell Gyre. A similar circulation can be seen on the opposite side in the Amundsen Sea, where the water flows towards the coastline and westwards until it reaches the Ross Sea, where it is deflected northwards and then eastwards, forming the Ross Sea Gyre.

Tide Currents

Tides are the second important convective transport of water masses besides ocean currents. Additional transport by tidal currents can either increase the possible drift by ocean currents sideways if tides are perpendicular to the main current, or add to the maximum drift distance if they flow parallel to the main current. This takes into account both situations, swimming crinoids and pelagic larval drift. They were calculated hourly and averaged over 28 days from 1st to 28th January 2018, corresponding to a full monthly cycle (Fig. 5.33). The mean maximum tidal currents were averaged from the absolute values (Fig. 5.34). The magnitudes of the tidal currents range from millimetres per second in the deep sea region to several metres per second in shallow waters. The main direction of the tidal currents is east-west oriented as long as no geological barrier diverts the current, e.g. on the western flank of the Antarctic Peninsula or at continental slopes.

The region restricted by food availability show a fragmented habitable area along the Antarctic continental shelf. Only in highly productive years is a transfer across low-productive gaps possible and a circum-Antarctic connection occurs in only one

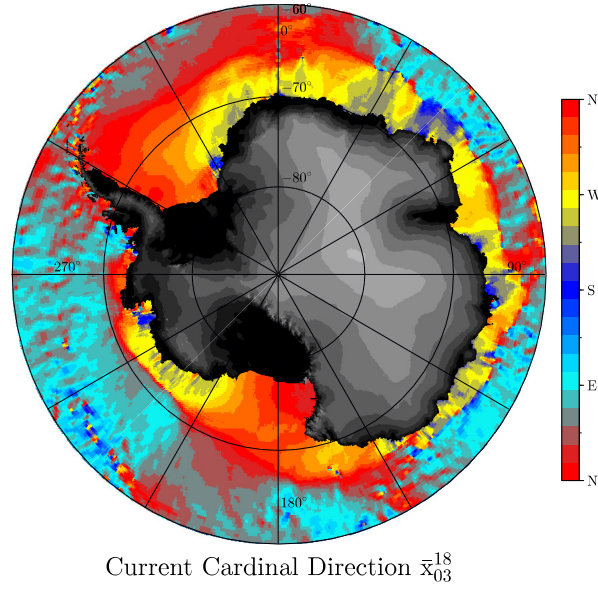
5. Results

out of sixteen years. Ocean currents promote a mainly westward migration along the Antarctic coast. Only the Antarctic Peninsula represents a natural barrier with other current conditions and exceptionally high productivity.



5.7 Environmental Boundary Conditions

(a)



(b)

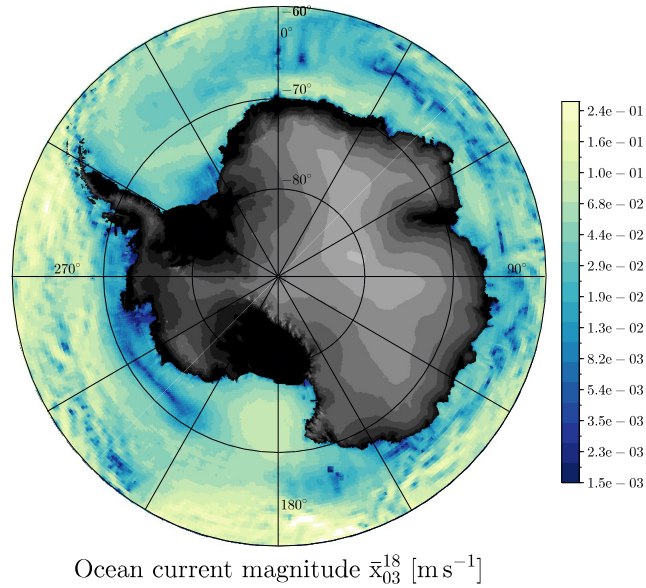


Fig. 5.32 Ocean currents. Combined ocean surface currents and ice drift averaged from monthly data from January 2003 to December 2018. **a** Cardinal direction with respect to geographic north in polar stereographic south projection EPSG:3031. Eastward (light bluish) is clockwise around the centred South Pole, or westward (yellowish) counter-clockwise. The northward flow in red points circularly outward while blue areas point southwards. **b** Corresponding current velocities in [m s^{-1}].

5. Results

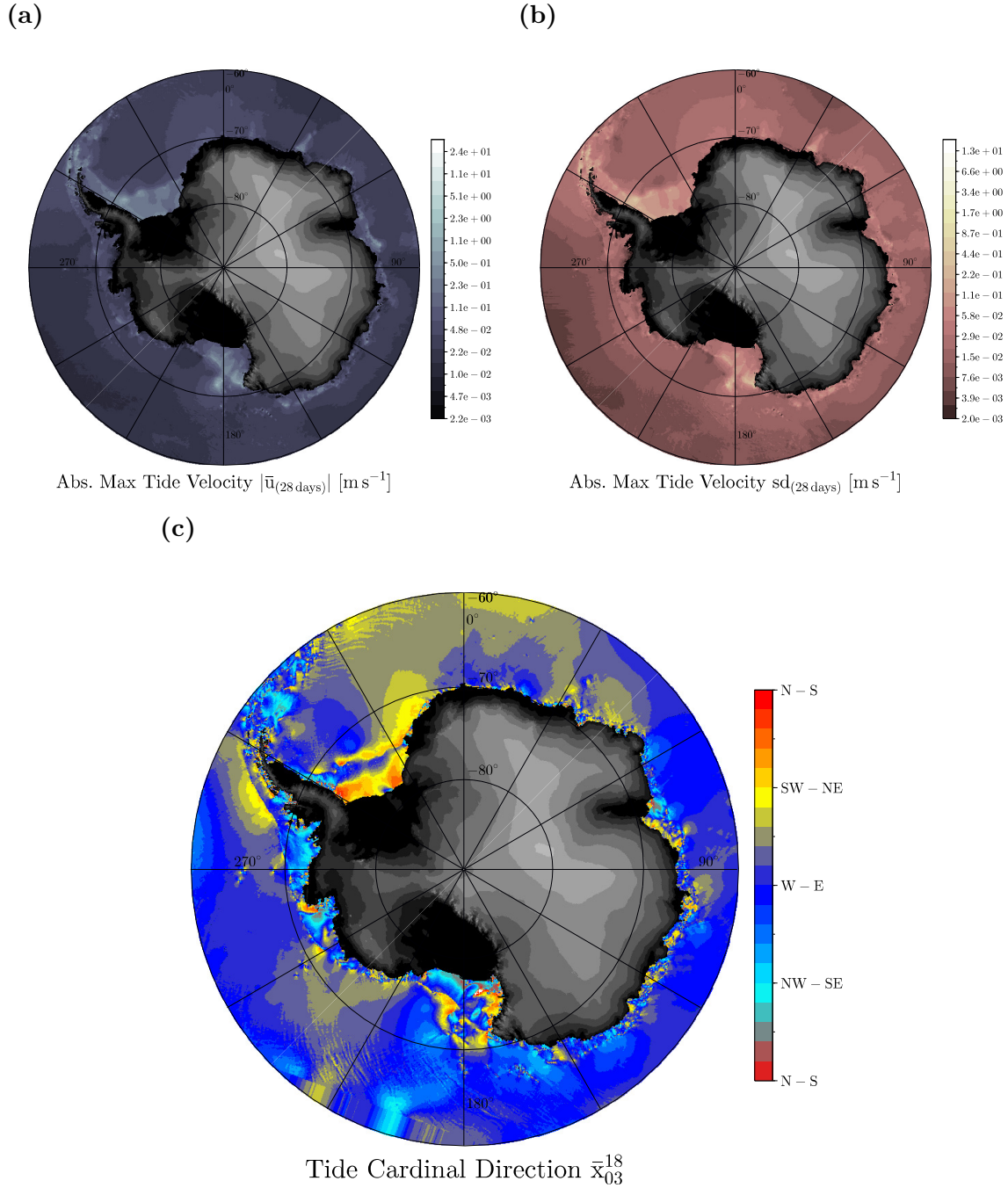


Fig. 5.33 Tidal current. Averaged maximum tidal currents calculated hourly over 28 days from 1st to 28th of January 2018. **a** Current speed in $[\text{m s}^{-1}]$. **b** Standard deviation. **c** Cardinal direction with respect to geographic north in polar stereographic south projection EPSG:3031. East refers clockwise around the centred South Pole, while counter-clockwise points westwards. The northerly flow in red points circularly outwards while the southerly flow in blue points inwards.



5.7 Environmental Boundary Conditions

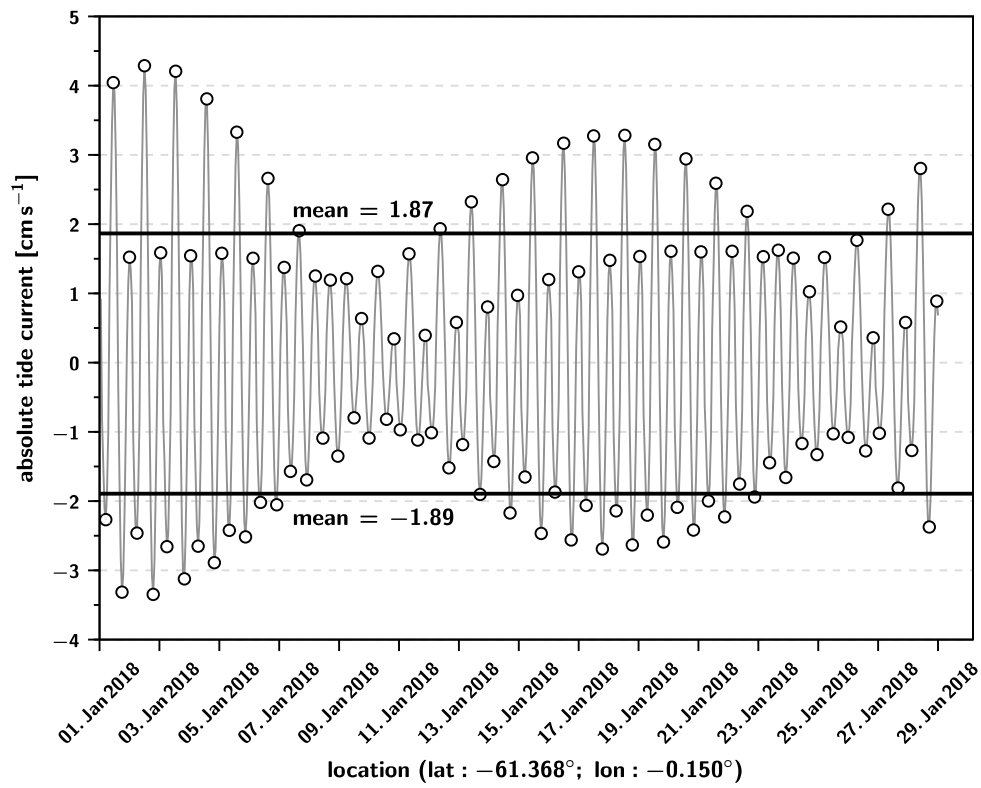


Fig. 5.34 Monthly tide cycle. Representative tidal cycle of a 28-day period, from 01 to 28 January 2018 at -61.368° latitude and -0.150° longitude. The circles show the maximum tidal velocities of a tidal cycle. These maximum velocities were averaged over 28 days for incoming and outgoing directions.

5.8 Dispersal

The dispersal of a species is a key aspect of its evolutionary success. Crinoids in general and comatulid crinoids in particular have been found in all oceans, from tropical warm to polar cold waters (Clark, 1967). *Promachocrinus kerguelensis* is the most abundant and diverse endemic species in the Southern Ocean (Speel and Dearborn, 1983). In order to analyse and evaluate the background of its success and dominance in the waters around Antarctica, *P. Kerguelensis*' migration that has led to its circum-Antarctic occurrence was simulated. The results of fifteen simulations, with different start and boundary conditions, are presented here to evaluate the influence of origin, swimming abilities and pelagic drift during their luvenile life stage.

The spatial simulation room is based on depths provided by the IBCSO (Bathymetric Chart of the Southern Ocean) (Arndt et al., 2013) and is limited to 60° southern latitude. Convective water transport is reflected by ocean currents and tidal cycles, where ocean currents were assumed to be a static mean of 192 monthly datasets from 2003–2018 assuming no temporal variations. Tides, on the other hand, were calculated hourly over a four-week period to determine a full monthly cycle. The horizontal extent of the simulation space is limited to the areas that provided at least the minimum required subsistence - consisting of metabolism 2.7 cal d^{-1} and demand for reproduction 0.8 cal d^{-1} . The food (energy) needed for this comes from primary production – synthesis of organic carbon by photosynthetically active phytoplankton at the sea surface. On the way to the seafloor, the organic particles pass through the food chain and are partially consumed, this reduction of food is here reproduced as a function of depth while its energetic content is assumed to be $11.4 \text{ cal mg}_C^{-1}$.

Dispersal can occur both by active swimming 29 mm s^{-1} and by drifting during the pelagic larval phase over which is assumed over a period of 75 days per year in this study. The swimming speed thus corresponds to horizontal locomotion at the most energy-efficient Maximum Range Velocity *MRV* with an energy demand of $12,3 \text{ cal h}^{-1}$ determined in the dynamic analysis (Tab. 5.9). The distances that can be covered daily are limited by the locally available energy minus the necessary living costs (metabolism and reproduction). Juvenile pelagic drift in contrast has no spatial borders but is temporally limited, providing the opportunity to overcome barren barriers with low productivity below the required cost of living of 3.5 cal d^{-1} .

Fluctuations in productivity due to fat and lean years alter the habitable regions so that the spread of *P. Kerguelensis* is in principle not spatially restricted, all scenarios are based on local maximum values of the sixteen years (2003 - 2018) (Fig. 5.35a). The resulting habitat (yellow) is patchy and does not form a closed area around Antarctica. Areas that can be reached during larval drift are shown in olive but also include yellow regions. These areas look different if the leanest year of this period is assumed. Large gaps divide the potential habitats of crinoids, which cannot be overcome even by 75 days of pelagic drift (Fig. 5.35c). Looking at the mean productivity of this period, both habitable area and areas reached by drift are increasing, although the circum-Antarctic link is still broken. Gaps in the western Ross Sea (150° E), between the



5.8 Dispersal

Kerguelen Plateau and the Antarctic continent (90° E), at the Indian sector (35° E) and in the Weddell Sea (30–60° W) seem to form insurmountable barriers (Fig. 5.35b). The situation is different under conditions of high productivity. Apart from a small gap in the Weddell Sea, the habitable and maximum drift areas form a contiguous zone along the Antarctic coast, connecting the continent with the Kerguelen Plateau and other sub-Antarctic islands (Fig. 5.35a). Only a transfer from the western Weddell Sea to the Antarctic Peninsula and vice versa seems to be impossible.

The results presented in this section are based on the expansion of the highest productivity, which indicates what is practically possible because it is only a matter of time before such conditions prevail.

The locomotion performance (speed and energy demand) of *P. kerguelensis* required for the simulation was determined in analytical fluid and inverse dynamics. For efficient migration, swimming speed and energy demand are assumed here for the *MRV*, this means a temporally maximum dispersal with available energy. Since *P. kerguelensis* is filter feeding, its catchment area depends on its size and determines how much food is accessible per time unit. The time span used for the annual drift during the larval stage is taken from the literature with 75 days per year (Tab. 5.9).

Tab. 5.9 Boundary conditions. List of start and boundary conditions used for the migration simulations of *P. kerguelensis*.

Parameter	Value
Swimming velocity	0.029 m s ⁻¹
Energy swimming	12.3 cal h ⁻¹
Energy metabolic	2.7 cal d ⁻¹
Energy reproduction	0.8 cal d ⁻¹
Arm length	0.142 m (area: 0.063 m ²)
Pelagic days	75
Current	on
Tide	on

Since *P. kerguelensis* occurs in all parts of the Southern Ocean, its origin is not certain. In order to cover a wide range of possible scenarios, five source locations were chosen that are roughly evenly distributed around the Antarctic continent (Tab. 5.10 and Fig. 5.35a). These consider an origin for both either on the Antarctic coast or on the sub-Antarctic islands.

In order to evaluate the different influences of origin, agility and larval drift, a total of 15 scenarios were simulated in different combinations. The resulting findings could provide circumstantial evidence on how *P. kerguelensis* was able to colonise the entire Antarctic continental shelf. For this purpose, five provenances were combined in three parameter combinations with and without swimming and varying pelagic lifetimes (75 and 10 days). The simulations were carried out under optimal environmental

5. Results

Tab. 5.10 Source localities. List of sites used as source sites for the migration simulations of *P. kerguelensis*.

Location	Latitude	Longitude
Antarctic Peninsula (AP)	62.676° S	54.646° W
Amundsen Sea (AS)	74.013° S	106.621° W
Kerguelen Plateau (KP)	60.513° S	81.952° E
Ross Sea (RS)	67.259° S	179.682° W
Weddell Sea (WS)	74.621° S	26.819° W

conditions and maximum swimming performance, i.e. as long as surplus energy is available, it is also used for locomotion. The determined migration times therefore represent a maximum possible dispersal, since ultimately only every sixteenth year offers such conditions for circum-Antarctic migration. However, since this should only influence the time frame and not the spatial extent, the dispersal periods are also given as a sixteenfold in the brackets.

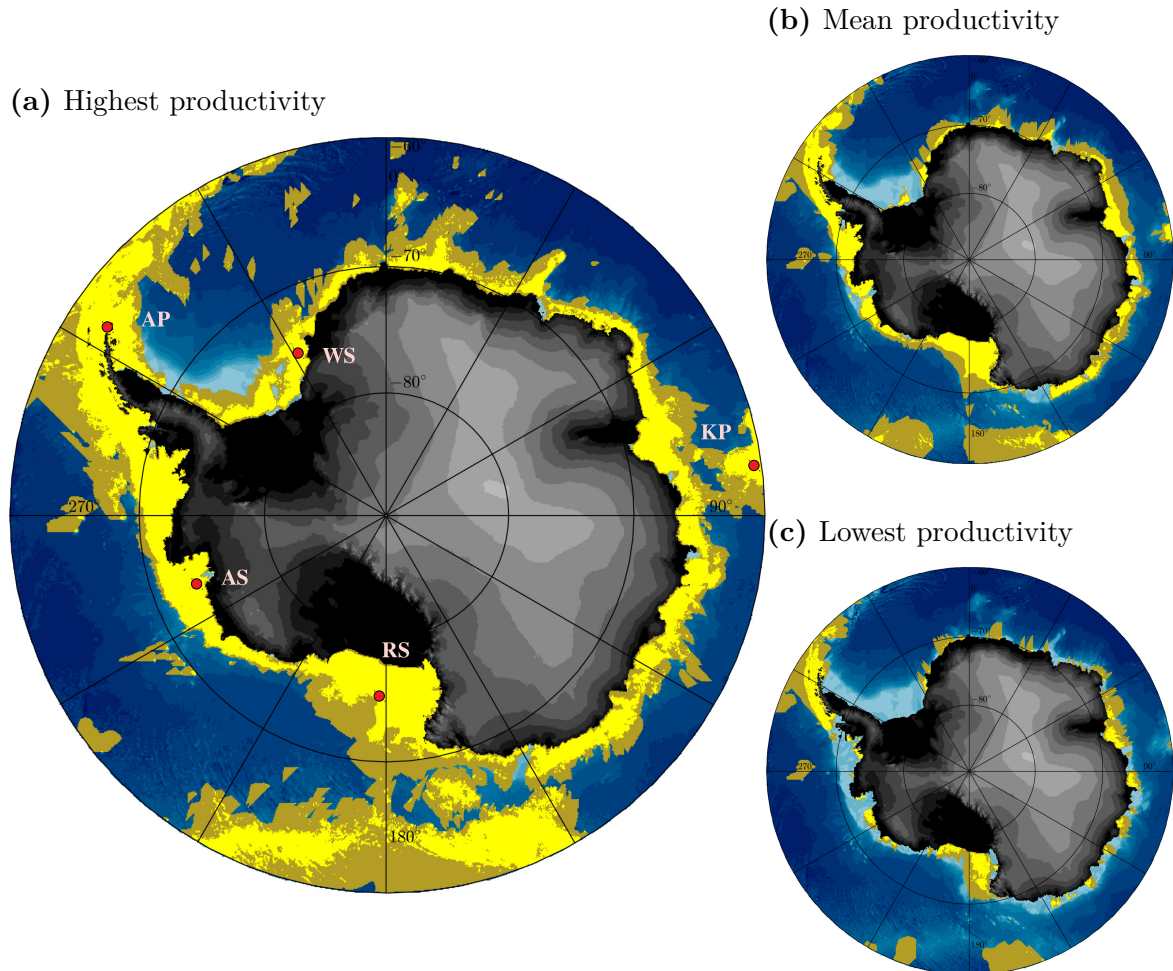
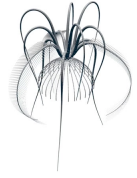


Fig. 5.35 Limits of spatial dispersal. The yellow area show the region that at least meets the life support requirements of *P. kerguelensis* of $3.5 \text{ cal ind}^{-1} \text{ d}^{-1}$. The underlying olive region also includes all yellow areas and represents the area of the ocean that can potentially be reached during 75 days of pelagic drift from any point within the yellow region. Olive regions provide less than *P. kerguelensis*' life support, but may allow transfer to an adjacent habitable area. **a** Highest productivity of sixteen annual averages (2003 – 2018), **b** their mean productivity and **c** the lowest productivity during this period. AP: Antarctic Peninsula, AS: Amundsen Sea, KP: Kerguelen Plateau, RS: Ross Sea, WS: Weddell Sea. The underlying bathymetry is taken from IBCSO [bc] (Arndt et al., 2013).

5. Results

Dispersal by swimming and 75 days of pelagic drift per year

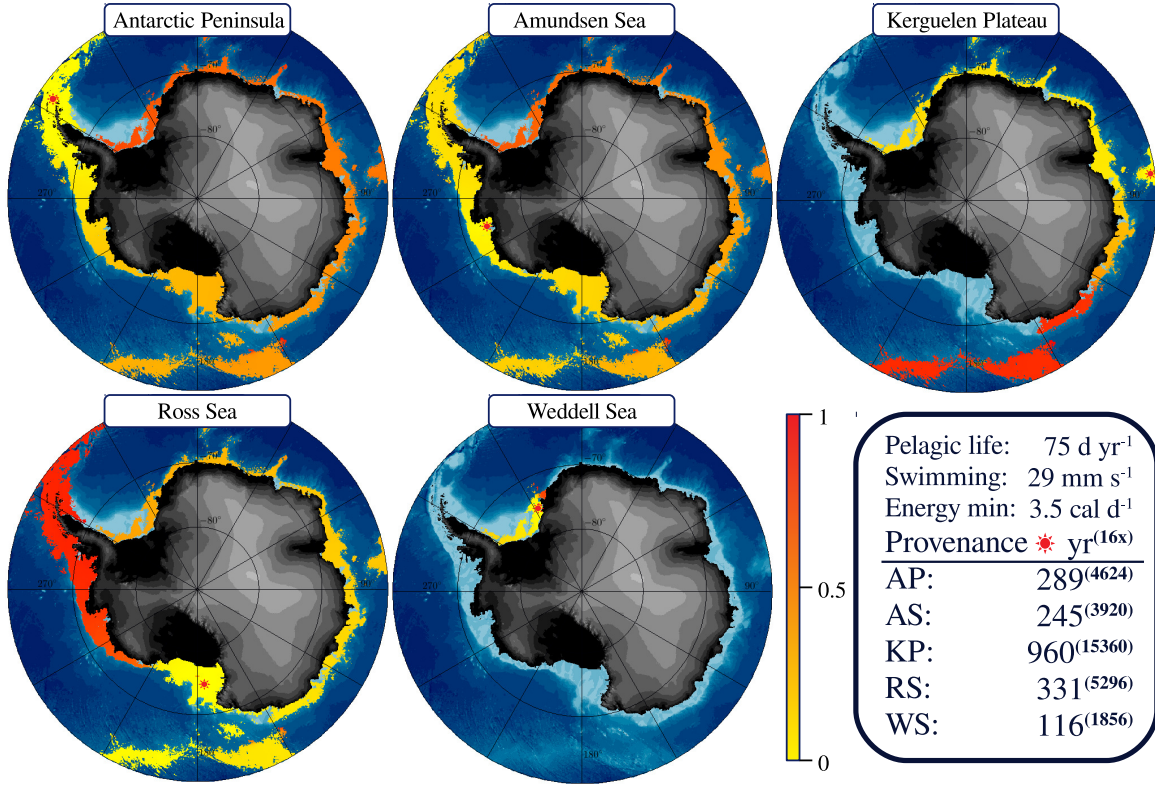


Fig. 5.36 Dispersal: full parameter set. Migration simulations of *P. kerguelensis* from five points of origin distributed around the Antarctic continent. Boundary conditions are set to: swimming with 2.9 cm s^{-1} and 75 pelagic days per year. The colour gradient represents the relative progress, 100% (red 1) corresponds to the dispersal time shown in the legend. The simulated migration times were determined for optimal environmental conditions and theoretical maximum swimming performance. The years in brackets represent sixteen times the simulated periods, as only every sixteenth year offered such conditions that allowed circum-Antarctic dispersal. The coloured area represents only the habitable region, without taking into account the areas that can be reached by pelagic drift. The underlying bathymetry is taken from the IBCSO [bc] (Arndt et al., 2013).

Promachocrinus kerguelensis habitable zone is primarily limited by food availability on the Antarctic continental shelf (Fig. 5.35). A counter-clockwise current dominates the coastal waters and supports westward migration (Fig. 5.32).

Simulations with provenance in West Antarctica – west of the Antarctic Peninsula to the Ross Sea (60° W to 150° E) – show the most promising results for circum-Antarctic settlement (Fig. 5.36 AP, AS, RS). The colour code from yellow to red expresses the temporal dimension. All simulations start at the location of the red star



5.8 Dispersal

on a yellow (0%) background, red 1 (100%) corresponds to the migration time shown in the legend. *P. kerguelensis* migration occurs along the colour gradient from yellow over orange to red. Westerly currents generally promote migration from the tip of the Antarctic Peninsula across the Amundsen Sea to the Ross Sea, continuing around East Antarctica past the Kerguelen Plateau south towards the Weddell Sea. Only the last end northwards along the east coast of the peninsula forms an insurmountable natural barrier under the given conditions, where the spreading is stopped. Strong westerly currents in combination with this barrier seem to have significant consequences if the provenance of *P. kerguelensis* is in the Weddell Sea or East Antarctica. This simulations end in an endemic colony extending into the south-eastern part of the Weddell Sea (Fig. 5.36 KP,WS). The Kerguelen simulation shows a transfer from the islands to the continental coast and a migration in both directions. The dispersal against the direction of the eastward coastal current takes longer than along the main westward current, as indicated by the colour code in figure 5.36 KP. The dispersal patterns from West Antarctica (Antarctic Peninsula, Amundsen Sea and Ross Sea) show the difference between migration towards or in the direction of currents. Eastward migration from the Ross Sea takes longer than westward migration from the Antarctic Peninsula. Circum-Antarctic migration from the Ross Sea thus takes 15-35% longer than from the Antarctic Peninsula. These boundary conditions also allow a transfer to the Kerguelen Plateau from the main continent. The islands north of the Ross Sea and the associated underwater mountain range are also accessible from the Antarctic coast. Under current conditions, settlement of the entire Antarctic waters appears to be limited to a provenance in the West Antarctic coastal region.

This setup allows also a transfer to the Kerguelen Plateau from the main continent. The islands north of the Ross Sea and the associated underwater mountain chain can also be reached from the Antarctic coast. Considering the present conditions a colonization of the entire Antarctic waters seem to be limited to a provenance in the West Antarctic coastal region.

Dispersal by swimming and 10 days of pelagic drift per year

Most of the global crinoid species have a juvenile pelagic life phase of only a few days. *P. kerguelensis*, in contrast, has a much longer period of two to three months. The following results were carried out under the assumption of only ten days of pelagic drift to illustrate the influence of their long larval life.

All simulations show spatial constraints with migration clearly limited to well-defined regions. West Antarctica still forms a contiguous area, but a transfer into the East Antarctic and vice versa seem to be not possible. The direction of dispersal in the West Antarctic show now a fourfold increase in the time required eastwards. Westward migration from the Antarctic Peninsula is much faster than eastward from the Ross Sea (Fig. 5.37 AP,AS,RS). The reduced pelagic drift also has a significant impact on the ability to cross barriers. The gap between the Kerguelen Plateau and the Antarctic coast appears to be too large for transfer. The same is true for the island and submarine mountain chain north of the Ross Sea (Fig. 5.37).

5. Results

Dispersal only by 75 days of pelagic drift per year

The third scenario represents non-mobile dispersal without the ability to swim. The boundary conditions are set to non-swimming and 75 pelagic days per year. This setup allows to assess the influence and contribution of *P. kerguelensis*' locomotion ability to their circum-Antarctic dispersal.

Dispersal without locomotion depends purely on ocean and tidal currents and the given drift time of 75 days per year. Migration is therefore mainly limited to a westerly dispersal. Only organisms with an origin in the Amundsen Sea encounter current conditions that allow drift almost around the entire Antarctic continent (Fig. 5.38 AS). The western coastal current is able to carry the descendants of *P. kerguelensis* from the Ross Sea and the Kerguelen Plateau into the Weddell Sea (Fig. 5.38 RS,KP). The Antarctic Circumpolar Current to the east is generally too far north to have a significant influence on coastal processes. An exception is the western flank of the Antarctic Peninsula, where the general westward coastal current is reversed to the sea gate between South America and the tip of the peninsula. This has a significant influence on the dispersal pattern for species with a provenance north-east of the Amundsen Sea. As shown in figure 5.38 AP, drifting larvae are picked up by the Circumpolar Current and carried north-east into the open sea. However, drifting along the main ocean currents takes too long to find new habitable areas.

The migration model shows that the circum-Antarctic success of *P. kerguelensis* most likely results from a combination of its swimming ability and an exceptionally long pelagic life phase. Another important factor seems to be its place of origin; provenances along the coast of West Antarctica led to the most promising results.



5.8 Dispersal

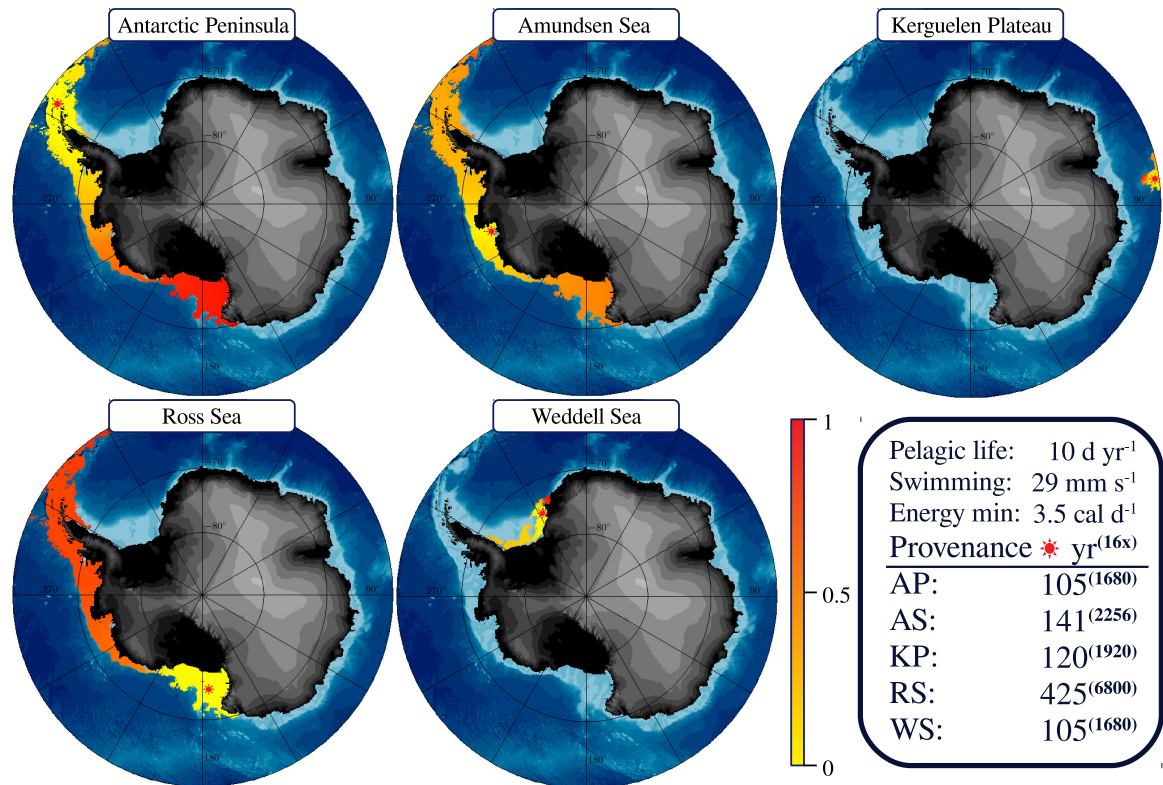


Fig. 5.37 Dispersal: 10 pelagic days. Migration simulations of *P. kerguelensis* from five points of origin distributed around the Antarctic continent. Boundary conditions are set to: swimming with 2.9 cm s^{-1} and 10 pelagic days per year. The colour gradient represents the relative progress, 100% (red 1) corresponds to the dispersal time shown in the legend. The simulated migration times were determined for optimal environmental conditions and theoretical maximum swimming performance. The years in brackets represent sixteen times the simulated periods, as only every sixteenth year offered such conditions that allowed circum-Antarctic dispersal. The coloured area represents only the habitable region, without taking into account the areas that can be reached by pelagic drift. The underlying bathymetry is taken from the IBCSO [bc] (Arndt et al., 2013).

5. Results

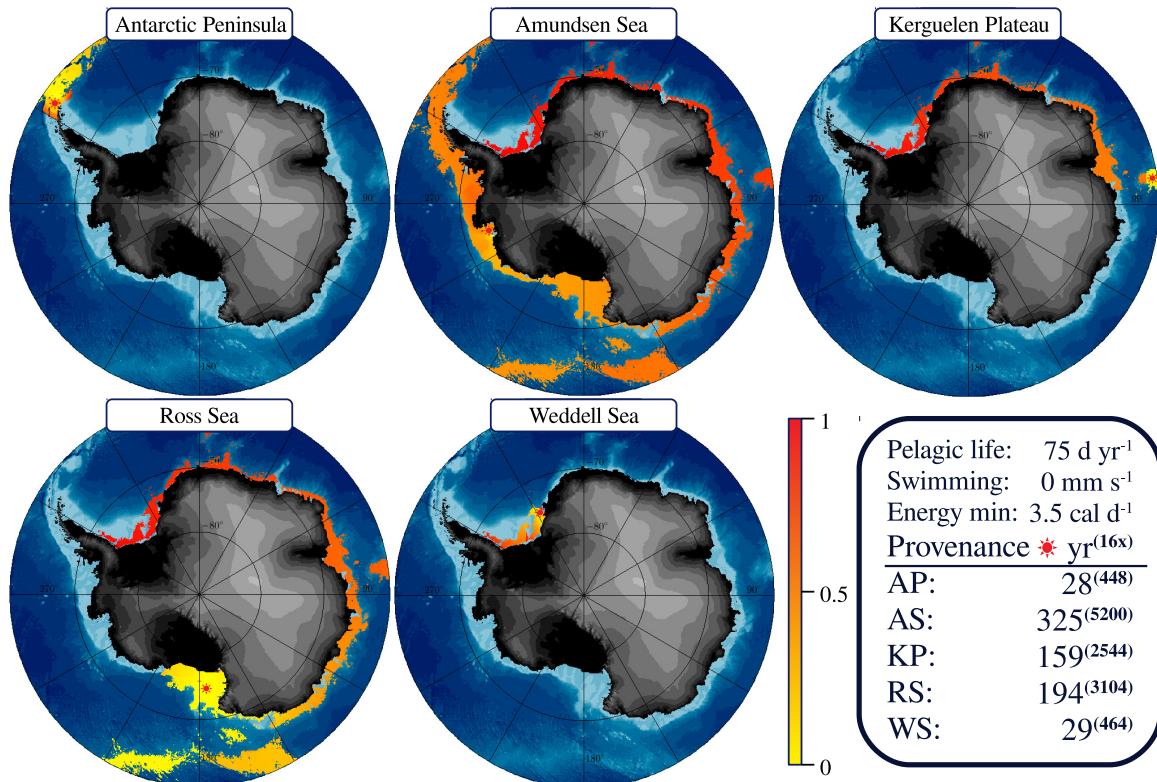


Fig. 5.38 Dispersal: no swimming. Migration simulations of *P. kerguelensis* from five sites of origin distributed around the Antarctic continent. Boundary conditions are set to: no active locomotion and 75 pelagic days per year. The colour gradient represents the relative progress, 100% (red 1) corresponds to the dispersal time shown in the legend. The simulated migration times were determined for optimal environmental conditions. The years in parentheses represent sixteen times the simulated periods, as only every sixteenth year offered such conditions that allowed circum-Antarctic dispersal. The coloured area represents only the habitable region, without taking into account the areas that can be reached by pelagic drift. The underlying bathymetry is taken from the IBCSO [bc] (Arndt et al., 2013).



6. DISCUSSION

The aim of the dynamic calculations of swimming crinoids is to characterise the internal and external processes of locomotion and to determine their forces, energy requirements and swimming speeds. These can be obtained experimentally for many organisms, but only partially for extremely small ones or those whose habitats are difficult to access. In addition, the natural behaviour of the animals can barely be reproduced in the laboratory, or only to a limited extent. The method presented here enables an indirect investigation of locomotion that is essentially based only on video recordings and thus enables an analysis of free-living organisms. On the other hand, the results obtained serve as a basis for the dispersal analysis of *P. Kerguelensis* around the Antarctic continent, which is part of the next section. The possibilities and limitations of this method are considered and discussed below.

6.1 Morphological Simplification and Kinematics

Morphology

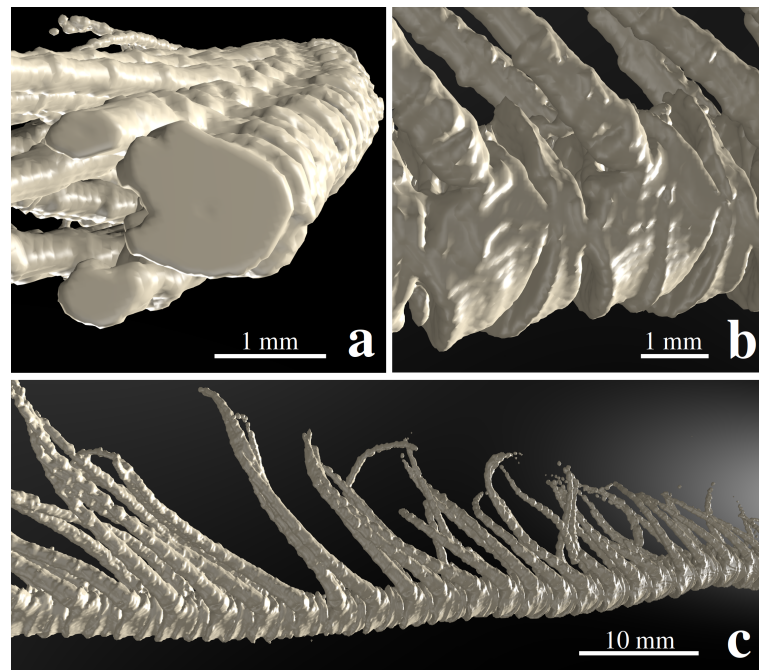


Fig. 6.1 Arm morphology. Computed tomographic scan of the arm of a comatulid crinoid. **a** Cross-sectional view at about two-thirds of the arm length. **b** Lateral view of the brachials **c** Wider section of the arm showing several brachials and their associated pinnules. Created in Blender [BL].

6. Discussion

The morphology of the crinoid was reduced to a sphere for the calyx (body) and cylinders for cirrals, brachials and pinnulars (Fig. 6.1). Their geometrical dimensions were determined on specimens stored in Formol, which was recently replaced by methylated alcohol. Measurements were expressed as functions of their respective positions within their associated body segments. Brachial length and diameter have exponential relationships along the proximal–distal arm axis. The diameter of the pinnulars was related to the size of their associated brachials with linearly decreasing length. The cirrals and the spherical body as passive elements were accordingly simply abstracted linearly.

The deformation of the skeleton and the shrinkage of the soft tissues caused by the long conservation period may have altered the morphological dimensions. These inaccuracies could not be quantified and therefore had to be neglected. Since crinoids have an exoskeleton where soft tissues are located inside the body, their shrinkage has probably minor effects on the outer dimensions of the body. Additional fragmentation of the incomplete specimens limited the available information to the proximal body parts. Distal structures could only be extrapolated from the data obtained. It was therefore not possible to determine a size relation of the body elements to the dimensions of the whole organism. Thus, it was also not possible to determine the arm length-diameter relationship. However, the arm length could be estimated from the video recordings, but the image resolution did not allow an exact measurement of arm diameters. However, all measurements were made on individuals with calyxes of approximately the same size and only slightly varying brachial diameters (see standard deviation in figure 5.1). This indicates that all examined individuals are of similar age and represent an average adult crinoid of the species *Promachocrinus kerguelensis*. Thus, the virtual model could only be designed under the given constraints (Fig. 6.2). For a more precise abstraction, further measurements on complete and especially recently collected samples would be necessary, but these were not available at the time of this study.

Additional artefacts are introduced by the geometric abstraction from non-circular organic shapes with rough surfaces to smooth cylindrical segments (Fig. 6.1b). However brachials are more disc-shaped with a lateral triangular projection, they form a circular cross-section and two adjacent brachials combined form a nearly cylindrical shape. Pinnulars and cirrals, on the other hand, are naturally nearly cylindrical, so this simplification should have little effect on their fluid dynamic properties (Fig. 6.1a).

Abstractions and mathematical idealisations of the organisms contain potential inaccuracies whose influence on the subsequent analysis is difficult to assess without additional sampling. The geometric reductions are nevertheless necessary to be able to apply analytical fluid dynamics, and despite all simplifications beside the poor conditions of the samples, the compilation of an idealised body structure established here currently reflects the most detailed morphological model of a crinoid (Fig. 6.2). In contrast, the latest dynamic analyses of swimming crinoids by [Janevski and Baumiller \(2009\)](#) are based on a highly simplified model, an oscillating permeable flat plate.



6.1 Morphological Simplification and Kinematics

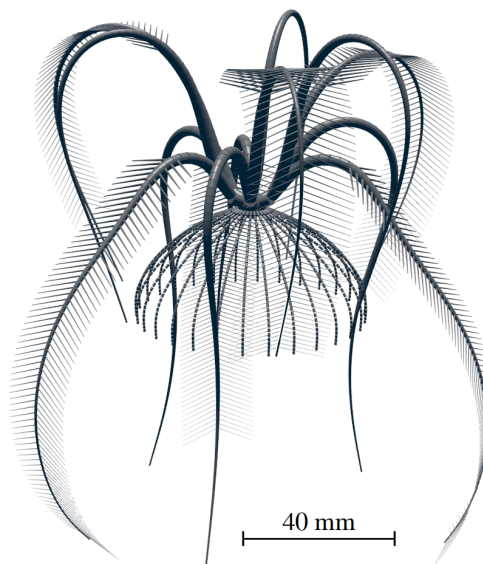


Fig. 6.2 Virtual model of *P. kerguelensis*. Rendered visualisation corresponding to the averaged morphology of the twelve-armed comatulid crinoid. The arm poses are taken from the mean kinematic analysis. Created in Blender [BL].

Kinematics

In general, the wave-like locomotion of undulating organisms, e.g. swimming fish, is often expressed by trigonometric time-dependent functions (Gray, 1968; Hertel, 1963; Oertel, 2008). However, they have a limited range of validity, restricted to small amplitudes in relation to their wavelength. Large amplitude motions require expressions with more degrees of freedom. A less common approach in aquatic locomotion is spline interpolation Ruiz-Torres et al. (2014); van Rees et al. (2015); Battista (2021). The arm paddling of a crinoid is comparable to a whip stroke, it follows a non-continuous path that would lead to a very complex function. The movement pattern of *P. kerguelensis* is described here by the individual kinematics of each arm. I follow a parametric approach, where x- and y-components (velocity and acceleration) are determined separately as parametric functions of a transit time variable. This approach seems to be sufficiently accurate to adequately represent arm flexion during an entire stroke cycle (see Fig. 5.4).

A second important feature of the arm movement is the folding in and out of the pinnules. Their movement was abstracted in only two states, either aligned along the arm axis during the recovery stroke or extended at an angle of 67° with respect to the main arm axis during power strokes. The temporal resolution of the video recordings was too low to accurately follow the folding and unfolding pinnular motion. Possible influences during the change of state on the fluid dynamic force components

6. Discussion

could therefore not be considered. The automated approach to determine the pinnule position as a function of thrust generation nevertheless revealed a characteristic pattern (Fig. 5.9) that would be expected during a flapping cycle. Pinnules folded out when an arm is pulled back and flapped in when the arm is brought forward again. This shows that both the algorithm for their movement and the underlying fluid dynamics seem plausible. The automation additionally helps to clearly determine the exact transition between recovery and power strokes. In contrast to the observations of Shaw and Fontaine (1990), who found a balanced ratio between power and recovery strokes in *F. serratissima*, the force stroke in *P. kerguelensis* occupies about 40% of the total arm stroke cycle and could thus be an indication of species dependence or the different fluid properties (Tab. 5.6).

6.2 Fluid Dynamics

To determine the interaction between fluid and the swimming crinoid, an analytical fluid dynamic approach was conducted to calculate the forces involved in their paddling movements. Depending on the direction of action, forces generate either drag (decelerating) or thrust (accelerating). While drag dominates recovery strokes, the mean force generated in power strokes lead to thrust. The effective total force is accordingly the sum of all forces at all time instances. However, the analytical approach only takes into account the generated forces and does not allow any conclusions to be drawn about the flow field. The mutual influence of wake and generated vortices of neighbouring arms is not considered, nor is the influence of the wave generated during the power stroke on the recovery stroke. In order to evaluate these influences, other fluid dynamic analyses are needed, e.g. experimental Particle Image Velocimetry *PIV* or Computational Fluid Dynamics *CFD*, which provide insights into the motion pattern of the fluid itself. However, one goal of this study was to reduce the large computational and time consuming efforts associated with these approaches.

Swimming speed and maximum payload were determined numerically using Newton's approximation method. Since drag is a function of velocity, the swimming speed is obtained when thrust and drag are equal, while the equilibrium of the maximum payload is reached when the weight balances the total thrust. This only applies to vertical swimming; to derive horizontal locomotion, a trigonometric approach was used for the transformation. A total of nine additional calculations with incrementally decreasing arm-paddle frequencies are used to analyse *Promachocrinus kerguelensis*' locomotion performance.

In order to be able to evaluate the underlying averaged kinematics, the fluid dynamics were calculated for all 53 arm strokes and compared with the kinematically averaged model (Fig. 5.11). Since all fluid dynamic parameters (velocities and forces) are well within the standard deviation from the 53 individual arm simulations, the following discussion refers only to the averaged model.



6.2 Fluid Dynamics

Thrust and Drag

Since the analytical approach only has a range of validity for low Reynolds numbers (Re), less than 2,000, its applicability to a swimming crinoid *Promachocrinus kerguelensis* must first be verified. Shaw and Fontaine (1990) determined a Re of 8,112 for a swimming *F. serratissima*, related to the size of the organism with an arm length of 16.2 cm. This is already in transition to turbulent flow and generally too high for a laminar-based approach. Since the analytics are applied to individual body segments with much smaller dimensions, the Reynolds numbers for each arm element (brachials and pinnulars) were determined in this study. This resulted in a mean Reynolds number of 8.6, in contrast to Shaw and Fontaine (1990) (Fig. 5.10). The Re -range shows that 90% of all segments are below 20. Flow around a cylinder at Re below 40 develops a stable steady flow field, while Re 300-100,000 lead to an unstable vortex street in the wake of the cylinder. The drag coefficient (cd) consequently decreases to ~ 1.2 by a quarter compared to 4.52 at Re 4 (Schlichting et al., 2006). A larger drag coefficient leads to a higher resistance and thus to more thrust. This means that drag-based propulsion is most efficient at low Re . Since more than 90% of the arm stroke takes place under laminar conditions, an analytical approach thus seems to be applicable.

The decentralised approach of calculating the fluid dynamics for each segment provides a novel view of the thrust distribution along the arm of crinoids (Fig. 5.13). Janevski and Baumiller (2009) derived from amputation experiments that only the proximal 9 cm (56%) of the 16 cm long arm contribute to thrust. However, the fluid dynamics here show a completely opposite pattern (Fig. 5.13). Almost all the thrust is generated on the distal 70% of the arm, while the proximal 10% only generate drag, i.e. the backstroke of this part of the arm never exceeds the swimming speed.

Neither the forces nor their distribution patterns can be checked directly. Only an indirect plausibility analysis can be done by means of the derived parameters swimming speed and maximum payload. This is part of the following sections.

Swimming Velocity

The observed swimming velocity was determined from the frame rate of the video recordings and is used to verify the results of the fluid dynamics. Perspective distortions, camera movement and the scaling error had to be corrected first. Nonetheless, inaccuracies remain that occurred when estimating the organism's position over ground. Therefore, these digitised swimming speeds provide only approximated values and should be viewed with caution. Nevertheless, the calculated swimming velocity of 36 mm s^{-1} agrees well with the observations from imaging 37 mm s^{-1} ; range: $32 - 42 \text{ mm s}^{-1}$ (Tab. 5.3). A vertical swimming of 54 mm s^{-1} ; range: $29 - 85 \text{ mm s}^{-1}$ was determined for a related Antedon species *Florometra serratissima* in the fjords of western Canada (Shaw and Fontaine, 1990). The *F. serratissima* individuals were slightly larger with arm lengths of 16.2 cm than the four *P. kerguelensis* specimens in this study. In addition, Shaw and Fontaine observed the swimming crinoids at a water temperature of 10°C in a depth of approximately 10 m. This means that the

6. Discussion

water's density, $1,024.70 \text{ kg m}^{-3}$, is 0.2% lower and their viscosity, 1.321 mPa s , which is 29% lower than the water properties on the Antarctic continental shelf. Species, size and environmental parameters can explain the different mobilities, but observed and calculated velocities agree quite well and support the analytical approach.

The horizontal swimming speed with 48 mm s^{-1} was geometrically derived from the total thrust minus the force needed to compensate for gravity. Shaw and Fontaine were able to observe *F. serratissima* lifting off the seabed and turning sideways until an orientation for horizontal swimming was achieved at a speed of 68 mm s^{-1} , equivalent to 126% of vertical swimming. The ratio obtained in this study between vertical and horizontal swimming of *P. kerguelensis* is slightly higher at 137%, but comparable. Impressively, the observations of Shaw and Fontaine show that comatulids are able to actively change their orientation and thus from vertical to horizontal swimming.

Maximum Payload

The maximum payload is a measure of the total thrust generated by the movement. *P. kerguelensis* is capable of lifting a total mass of 1.40 g, which agrees well with the thrust generated of 13.72 mN and the values calculated for *Florometra serratissima*. Janevski and Baumiller (2009) calculated a maximum Weight In Water *WIW* for a ten-armed *F. serratissima* of about 1,38 g. It follows that a slightly higher payload of about 15-17% could be expected for a twelve-armed crinoid. Using arm length as a measure of the organism's size, *P. kerguelensis* is about 12.5%, 140 mm, smaller than the individual with 160 mm from the study of Janevski and Baumiller (2009). According to the size difference, much less thrust would be expected, but this is partly compensated by the two additional arms. Nevertheless, calculation and reference are surprisingly close and confirm the results of the calculation.

Most of the thrust generated and the resulting swimming speed is attributed to the contribution of the pinnules (Tab. 5.5). The arms would still generate positive thrust of $\sim 0.3 \text{ mN}$ without pinnules, but not enough to lift the organism off the ground. This means that an arm that is extended outwards during a force stroke will produce more thrust than it will be subjected to drag when it is brought forward again near the centre of the body. The data also shows the influence of the increased projected arm area when the pinnules are extended laterally outwards. The greater the angle of attack, the greater the projected area and thus the greater the generated thrust respectively swimming speed (Tab. 5.5). This highlights two aspects: the important role of the pinnules themselves in the arm paddling movement of swimming crinoids and supports the plausibility of this analytical approach.

6.3 Inverse Dynamics

Inverse dynamics uses the external loads fluid dynamic forces, drag and thrust, body's inertia and kinematic acceleration to derive internal forces and moments within the



6.3 Inverse Dynamics

skeletal frame. The energy required to perform the swimming motion is derived from the internal joint moments and their angular velocities.

Maximum Range Velocity MRV

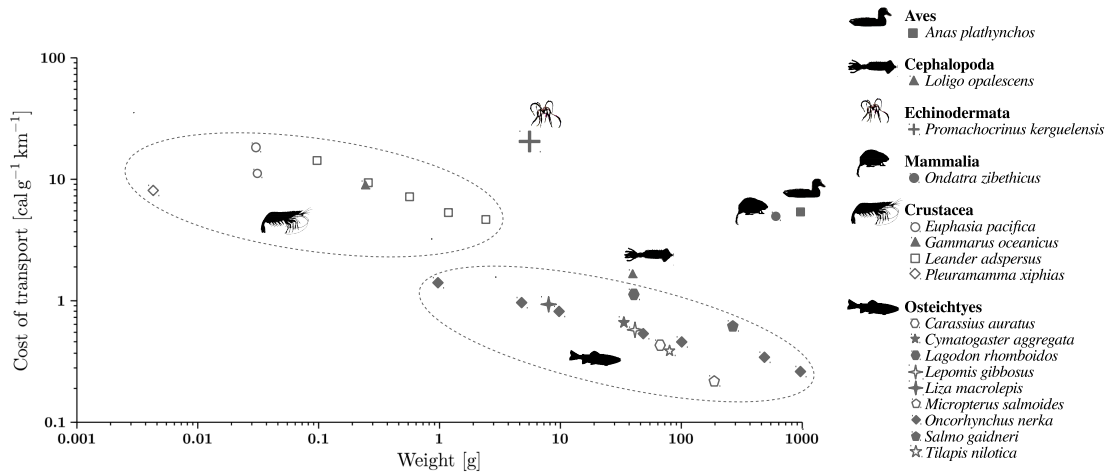


Fig. 6.3 Maritime Cost Of Transport COT . COT is here expressed as a function of weight for seventeen marine species (modified and supplemented from Torres (1984) after Schmidt-Nielsen (1972); Beamish (1978)). References of the individual species are: *Anas platyrhynchos* (Prange and Schmidt-Nielsen, 1970); *Carassius auratus* (Smit et al., 1971); *Cymatogaster aggregata* (Webb, 1975); *Euphausia pacifica* (Torres and Childress, 1983); *Gammarus oceanicus* (Halcrow and Boyd, 1967); *Lagodon rhomboides* (Wohlschlag et al., 1968); *Leander adspersus* (Ivlev, 1963); *Lepomis gibbosus* (Brett and Sutherland, 1965); *Liza macrolepis* (Kutty, 1969); *Loligo opalescens* (O'Dor, 1982); *Micropterus salmoides* (Beamish, 1970); *Oncorhynchus nerka* (Brett and Glass, 1973); *Ondatra zibethicus* (muskrat) (Fish, 1982); *Pleuromamma xiphius* (Morris et al., 1985); *Salmo gairdneri* (Webb, 1971); *Tilapia nilotica* (Farmer and Beamish, 1969).

Maximum Range Velocity MRV is the rate of locomotion at which an organism requires a minimum amount of energy to travel a given distance, or the distance travelled is maximal with a given amount of energy, usually denoted as u_{opt} in $[\text{cal g}^{-1} \text{km}^{-1}]$ (Alexander, 2006; Wakeman and Wohlschlag, 1981). The energy requirement for swimming of *P. kerguelensis* was determined for a muscle efficiency of 25% at MRV (Hill, 1950; Winter, 2009). The need for additional potential energy to overcome the height difference during vertical swimming can be invested in forward propulsion during horizontal swimming, leading to higher swimming speeds. The calculated optimal horizontal locomotion speed for *P. kerguelensis* is 29.0 mm s^{-1} with Costs Of Transport COT of $21.3 \text{ cal g}^{-1} \text{km}^{-1}$, thereby appearing extraordinarily inefficient compared to other organisms (Fig. 6.3). In order to be able to evaluate the results of *P. kerguelensis*, these values must first be put in relation to another organism, e.g. a swimming fish.

6. Discussion

With a body mass m of 5,57 g a fish *Oncorhynchus nerka* according to Brett and Glass (1973) would need $0,9 \text{ cal g}^{-1} \text{ km}^{-1}$: $COT = 1.416m^{-0.25}$. Videler (1993) presented a relation $COT = 1.1w^{-0.38}$ (w : weight in [g]) leading to $COT = 1.9 \text{ cal g}^{-1} \text{ km}^{-1}$ for the same weight of 5.57 g. Torres (1984) determined a COT -weight relationship for a crustacean *Euphausia pacifica* $COT = 6.26w^{-0.28}$. A 5.57 g crustacean would then require $3.9 \text{ cal g}^{-1} \text{ km}^{-1}$. This is still only about 1/5 of what *P. kerguelensis* needs. Only organisms that swim on the surface, such as muskrats and ducks, have comparably high transport costs (Fig. 6.3). Swimming humans also have a similar energy requirement of $35.4 \text{ cal g}^{-1} \text{ km}^{-1}$ (Andersen, 1960). For marine mammals, a regression COT to weight $COT = 7.79m^{-0.29}$ (m in [kg]) was assumed, although no marine mammal of 5.57 g exists, it would have a theoretical energy requirement for locomotion of $34.8 \text{ cal g}^{-1} \text{ km}^{-1}$, which is about 1.5 times that of *P. kerguelensis*.

Despite the simplifying assumption that only the arm stroke frequency is changed with changing speeds, the regression of log cost per hour and swimming speed correlates perfectly ($R^2=1$). Moreover, the derived COT over distance as a function of speed corresponds well to the expected asymmetry presented by Wakeman and Wohlschlag (1981) (Fig. 5.19). Since COT corresponds to energy per weight and distance [$\text{cal g}^{-1} \text{ km}^{-1}$], body mass and swimming speed have a direct influence on the transport costs. Videler (1993) proposed a relationship between most efficient speed and mass of fish $u_{MRV} = 0.47m^{0.17}$ (m in [kg]). This means that a fish weighing 5.57 g will swim with MRV of 194.5 mm s^{-1} , which is 6.7 times higher than the MRV of *P. kerguelensis*. Assuming a fish is neutral buoyant in water, its volume would be equal to the weight 5.57 cm^3 . Given velocity u 0.195 m s^{-1} , volume V $5.57 \text{e} - 6 \text{ m}^3$ and kinematic viscosity ν $1.8 \text{e} - 6 \text{ m}^2 \text{ s}^{-1}$ results in a volumetric Reynolds number Re_v of 1,920 and a volumetric drag coefficient cd_v of 0.107 (Eq. 6.1) (Nesteruk et al., 2014).

$$\begin{aligned} Re_v &= \frac{u_{\infty} V^{1/3}}{\nu} \\ cd_v &= \frac{4.708}{\sqrt{Re_v}} \end{aligned} \quad (6.1)$$

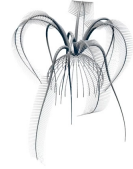
Bilo and Nchtigall (1980) derived a method for estimating the resistance of a swimming animal as a function of its body weight.

$$D = c m u^2 \quad (6.2)$$

Resistance D [N] results from body mass m [kg] times velocity u^2 [m s^{-1}] times a factor c). Whereas c is given as a function of drag coefficient cd_v , volume V , density ρ ($1,027 \text{ kg m}^{-3}$), and body mass m .

$$c = \frac{cd_v V^{2/3} \rho}{2m} \quad (6.3)$$

This results in a factor c of $3,112 \text{ m}^{-1}$ for a 5,57 g fish. The corresponding resistance force D is then 0.659 mN at u 0.195 m s^{-1} . An undulating body is subjected to about 3 times the resistance of an equivalent rigid object, so the effective resistance is 1.98 mN



6.3 Inverse Dynamics

Tab. 6.1 Motion energetics of *P. kerguelensis* vs. fish. Comparison of representatives of both organisms with an equivalent mass of 5.57 g. Speed at maximum range *MRV* and Cost Of Transport *COT* per distance in [$\text{cal g}^{-1} \text{km}^{-1}$] approximated for fish according to Videler (1993). *COT* per time derived from velocity. *COT* effective for *P. kerguelensis* with 92% from total thrust remaining after gravity compensation. Resistance for fish estimated from Nesteruk et al. (2014) and Bilo and Nchtigall (1980).

	<i>P. kerguelensis</i>	Fish	
u_{MRV} [mm s^{-1}]	29.0	195	$u_{MRV} = 0.47m^{0.17}$
<i>COT</i> [$\text{cal g}^{-1} \text{km}^{-1}$]	21.3	1.9	$COT = 1.1m^{-0.38}$
<i>COT</i> [$\text{cal g}^{-1} \text{h}^{-1}$]	2.2	1.3	
<i>COT</i> _{eff} [$\text{cal g}^{-1} \text{h}^{-1}$]	2.0		eff=0.92
Drag [mN]	6.5	2.0	
Drag _{u=195} [mN]	293.9	2.0	~147x of fish

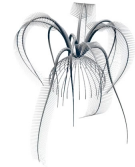
(Webb, 1975). Since the sum of all forces at constant velocity is zero, the thrust generated must also be 1.98 mN.

The transport cost per distance, at a known speed, can be converted into cost over time in [$\text{cal g}^{-1} \text{h}^{-1}$]. *P. kerguelensis* requires $2.21 \text{ cal g}^{-1} \text{h}^{-1}$ at *MRV* while a fish of the same weight requires only $1.3 \text{ cal g}^{-1} \text{h}^{-1}$. As shown in figure 5.12, the effective thrust at *MRV* is about 92% of the total thrust. Effective thrust in this context refers to the force vector in the swimming direction. The remaining 8% is used to overcome gravity to keep the non-neutral buoyant organism aloft, i.e. the effort for horizontal swimming is reduced to $2.03 \text{ cal g}^{-1} \text{h}^{-1}$ (Tab. 6.1). Assume that muscles have their optimal efficiency when the minimum energy requirement results in maximum output per time. If they are organism- and species-independent, we would expect similar energy demands regardless of distance travelled or swimming speed. The values of crinoids and fish are similar, suggesting that the magnitude of the calculated energy requirement of *P. kerguelensis* seems plausible. The difference to swimming fish could be due to hydrodynamic effects and lower efficiency. As deduced above, *P. kerguelensis* is already subjected to more than 3 times the drag of a comparable fish at about 11 times lower velocity. At the same *MRV* of the fish, *P. kerguelensis* would require 276.5 mN of thrust, a factor of about 147. Consequently, *P. kerguelensis* is obviously a very inefficient swimmer. This conclusion is supported by Shaw and Fontaine, who observed swimming crinoids *Florometra serratissima* with a maximum single swim burst of 5.4 m in 29 s. Such short periods also indicate high effort and thus certainly inefficient locomotion, so comatulids are certainly not optimised for locomotion.

Calculated Maximum Range Velocity *MRV*: 17.6 mm s^{-1} (vertical) is about half the observed vertical swimming speed of 36.3 mm s^{-1} . This means that the locomotion effort of the recorded specimens is higher than the most efficient cruising speed *MRV*. The observed behaviour of the recorded comatulids can therefore be seen as an escape reflex. A fleeing organism would activate all available resources simultaneously,

6. Discussion

i.e. maximum striking power in all arms at the same time. In addition to this, the standard deviation presented in figure 5.11 indicates an almost equal performance of all four individuals. The third piece of evidence is provided by the distribution of force along the arm (Fig. 5.13). The arm stroke forms a locomotion pattern with evenly distributed thrust over the 70% of the distal segments. Thus, except for the most proximal arm segments, the crinoid uses every available body part to achieve maximum swimming force.



6.4 Dispersal

6.4 Dispersal

The degree of dispersal is an indicator of the evolutionary success of a species. It is a measure of the ability to adapt to, tolerate and conquer a broad environmental spectrum. Crinoids have existed for more than 200 million years and are found in all oceans from tropical warm to polar cold waters (Clark, 1967). The comatulid crinoid (feather star) *Promachocrinus kerguelensis* is endemic to the Southern Ocean and is one of the most abundant local crinoids. It is native along the Antarctic coast and the sub-Antarctic islands including the Kerguelen Plateau (Eléaume et al., 2014).

Feather stars, unlike stalked crinoids, are able to swim. They are capable to perform paddling movements with their arms that generate enough thrust to leave the seabed and reach neighbouring sites. This ability is advantageous in at least two ways, firstly to escape benthic predators (Meyer and Macurda, 1977) and secondly to find places with better food supply. A key question of this work is: How did this ability support the circumpolar dispersal of *Promachocrinus kerguelensis* and its high abundance?

Here I have developed a computational model based on food availability, ocean and tidal currents and the physiological parameters of energy demand, swimming speed and reproductive life cycles to model and visualise the migration pattern of *P. kerguelensis* in the Southern Ocean. The simulation space is limited to 60° southern latitude, with water depths, as the third dimension, taken from the International Bathymetric Chart of the Southern Ocean (IBCSO) (Arndt et al., 2013). The available energy in the form of organic carbon at the seabed is derived from primary production at the sea surface and reduced by a function of depth, reflecting consumption down the food chain. *P. kerguelensis*' habitable areas are thereby limited by local food availability. Only areas that provide more than 3.5 cal d⁻¹ for metabolism and reproduction are potentially inhabitable (Fig. 5.35). *P. kerguelensis* dispersal by migration is distinguished in two mechanisms: once a year, larval offspring are released into the water column, which drift passively with the ocean and tidal currents for two to three months until they return to the seafloor where colonisation is initiated (McClintock and Pearse, 1987). This juvenile pelagic life stage allows transfer from one habitable area to a neighbouring one. Secondly, active swimming, which offers the possibility of controlled migration even towards the ocean currents. However, the additional energy required for locomotion prevents a transfer across low-yield gaps between habitable areas. The necessary information on swimming speed and energy demand was calculated using analytical fluid and inverse dynamics.

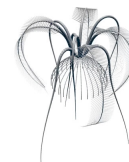
Locomotion is costly and takes *P. kerguelensis* about a hundredfold compared to their metabolism and reproduction, it is thus only practicable under sufficient food supply (swimming: ~ 300 cal d⁻¹; living: ~ 3.5 cal d⁻¹). Consequently, it is logical that comatulids would only swim when a situation makes it absolutely necessary. Albeit the daily activity of *P. kerguelensis* could not be determined so far, the focus in this study is set on the best possible daily performance, knowing that the actual activity is only a fraction of the results obtained. It is also assumed that the tidal currents always support the migration, thus covering the maximum possible range,

6. Discussion

which statistically also happens at some point but also leads to an underestimation of the time required. The determined settlement times therefore reflect a best possible performance rather than a realistic picture. To be able to determine the relationship between drifting and floating contribution to migration, three scenarios with different boundary conditions are simulated. A simulation with the full set of parameters, both 75 days of pelagic drift per year and active swimming, may reflect the behavior of *P. kerguelensis* best (Fig. 5.36). Since the actual duration of the larval stage of *P. kerguelensis* is unknown and was estimated by McClintock and Pearse (1987) to be 60–90 days, a drift phase of 75 days is assumed to be reasonable for first approximations. A second run without swimming illustrates the contribution of active locomotion (Fig. 5.38). Since *P. kerguelensis* has an exceptionally long pelagic life phase compared to other crinoid species, a third model is calculated with only ten pelagic days per year (Fig. 5.37). En bloc fifteen simulations from five different points of origin allow an assessment of *P. kerguelensis* most likely provenance around the Antarctic continent and thus emphasizes the hydrographic influence of ocean currents on the migration pattern.

Since no individual behaviour is implemented, it is assumed that daily migrations take place according to the available energy. Consequently, the obtained dispersal times are based on maximum migration rates, but realistic dispersal would take much longer. Decadal productivity cycles also inhibit continuous migration (Figs. 5.31 and 5.35), a full circumpolar connection of areas that can be reached by drift or swimming occurs only once in sixteen years (based on data from 2003–2018). These productive years may allow transfer across wider gaps between regions with more stable conditions. Multiples of the calculated dispersal periods are most likely, so simulation results are listed in parentheses according to a factor of sixteen (Fig. 5.36, 5.37, 5.38). The determined dispersion periods can therefore only be put into relation and do not reflect absolute values. The results of the three origins in West Antarctica (Antarctic Peninsula, Amundsen Sea and Ross Sea) lead to a circum-Antarctic spreading in about 4,000 to 5,000 yr, assuming a frequency of productive periods every sixteen years. This would have allowed about three complete circulations since the last glacial period about 15,000 yr ago (Clark et al., 2009). Greater ice cover during this phase, and consequently less available food, must have forced the crinoids to retreat to the sub-Antarctic islands, from where they began their new campaign of conquest. Despite the simplicity of the model and the lack of long-term environmental data, besides uncertain pelagic life stages and swimming behaviour, the simulated dispersal periods are plausible and their possible locations are congruent with the locations where *P. kerguelensis* has been found to date (Eléaume et al., 2014).

A striking common feature of all migration runs is a strong link to ocean dynamics. The coastal current counter-clockwise supports westward migration, which means that circumpolar dispersal most likely originates in West Antarctica. The continental shelf between the Antarctic Peninsula and the Ross Sea offers the best conditions for dispersal (Fig. 5.36). The region that benefits most from ocean dynamics is in the Amundsen Sea between 90–120° W. Near-circumpolar dispersal from this region is supported even



6.4 Dispersal

by drift with the currents (Fig. 5.38 AS). A combination of swimming and drifting starting in the Amundsen Sea takes about 245 yr, while pure drifting takes 325 yr, implying a maximum contribution of swimming of 25%. Swimming performance, on the other hand, depends on individual behaviour, supporting or inhibiting currents and food supply. This means that the benefits of swimming are less and probably have a greater influence on local rather than large-scale dispersal. Steep slopes can present insurmountable barriers to non-swimming organisms, and newly developed areas destroyed by iceberg scouring can be easily colonised.

Circumpolar migration, on the other hand, seems impossible if the pelagic life phase is reduced to ten days per year, as is common in other crinoid species (Mladenov and Chia, 1983; McClintock and Pearse, 1987). The distances between habitable zones are too far and the drift periods too short to overcome the gaps of low productivity. This does not necessarily mean that such environmental conditions prevent passive circumpolar dispersal. Continental drift and climate changes over Earth-historical time spans have certainly provided better conditions at some point within the crinoids' two hundred million years of existence. The simulations performed can only reflect present-day conditions and only provide a glimpse of a possible scenario in current decades. The patterns with 75 and 10 pelagic days indicate a possible adaptation to the barren Antarctic ambient conditions. Only long-drifting organisms can thus reach the local restricted habitable sites and are able to establish distant colonies. McClintock and Pearse (1987) already suspected a connection between long pelagic life phases and the wide distribution.

Only under the assumption of a long-term energy supply of $3,5 \text{ cal d}^{-1}$ is it possible to ensure a permanent settlement of *P. kerguelensis*. Years of lower productivity can be compensated by resuspension, uptake and horizontal transport of organic particles deposited on the seabed (Lampitt, 1985; Jago et al., 2002; Souza, 2004). *P. kerguelensis* is theoretically also able to survive with only 2.7 cal d^{-1} (metabolic cost at rest). However, to do this, reproduction must be interrupted for a few seasons until the food supply recovers. However, we have to bear in mind that metabolic and reproductive costs have been strongly extrapolated from either related species or individuals with up to ten times the body mass.

Since net primary production and ice cover are derived from satellite imagery, algal activity and associated carbon transport to the seafloor can also only be within the range of accuracy of the raw data. All assumptions aside, the results show very good agreement in the long-term mean with the findings of *P. kerguelensis* around Antarctica Eléaume et al. (2014) (Fig. 6.4). Most locations where *P. kerguelensis* was found (brown dots) fall within the predicted range providing full life support (yellow, 3.5 cal d^{-1}).

The only circum-Antarctic representative of stalked crinoids is, to my knowledge, *Feracrinus heinzelleri* (Eléaume et al., 2014) beside *Bathycrinus australis*, which is only native to the South Atlantic and sub-Antarctic islands (Gutt et al., 2011). *F. heinzelleri* is by far not as common as *P. kerguelensis*, but both share at least partly the same habitat, thus illustrating the consequences of their different morphology

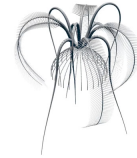
6. Discussion

and associated mobilities (Fig. 6.4). Passive simulation scenarios using only pelagic drift without self-propulsion therefore represent the dispersal of stalked crinoids in particular, but also of sessile organisms (corals, sponges, etc.) in general. Strictly speaking, stalked crinoids are not sessile, they are not able to swim per se (Janevski and Baumiller, 2009) but can crawl across the seafloor, which results in a limited degree of freedom (Baumiller and Messing, 2007). As this subaquatic locomotion is by far slower and restricted by bathymetric barriers, crawling as a form of active migration was omitted in this study. The distribution pattern of *F. heinzelleri* indicates a somewhat deeper water occurrence than that of *P. kerguelensis*, which may also indicate a more frugal lifestyle, as simplistically food availability decreases with depth. As the purely passive migration simulations show, the best chance for circum-Antarctic dispersal is in the Amundsen Sea, where *F. heinzelleri* was also found. An origin from this region thus seems likely. The apparent dominance of *P. kerguelensis* already indicates a strong advantage of advanced locomotion. Although *P. kerguelensis* benefits from the ability to escape benthic predators, the capability to swim provides a more effective migration, especially to encounter currents and tides, overcome bathymetric barriers and occupy local areas more quickly. Gutt (2001) predicts that the seabed on the Antarctic continental shelf above 500 m water depth is destroyed by iceberg scour once in 340 yr. More pessimistic assumptions even arrive at a destruction of 30% of the extremely shallow regions annually (Peck et al., 2010; Barnes, 2016; Barnes et al., 2018). These huge devastated fields thus offer great potential for pioneer species. Images taken on the *Polarstern* cruise PS96 in the Weddell Sea by Piepenburg et al. (2017) show the early stage of the recolonised seafloor of an iceberg scour with a high proportion of comatulid crinoids (Fig. 6.5) [pip].

6.5 Evaluation of the Model

The quality of a computational model essentially depends on the underlying input data, the complexity of the factors involved and the degree of their abstraction. While parameters of lesser relevance can change the results to a certain degree, incorrect implementation of relevant parameters can even lead to contrary results. It is important to understand that computational models only ever reflect an idealistic image of reality. Natural variations and unknown components make precise predictions difficult or impossible. An evaluation of the model identifies its reliability and possible weaknesses.

At the beginning, there is the time limitation of the available underlying data on which the model is based (chlorophyll, solar radiation, ocean currents, ice cover, etc.), and the ocean bathymetry, which determines the simulation room, were obtained in the last two decades. They thus only provide a basis for predictions under present-day conditions. Geology has also changed greatly in the two hundred million years of crinoid's existence. Climate change and continental drift have continuously shaped the environment, the end of the last supercontinent Pangaea was just about 150 million



6.5 Evaluation of the Model

years ago, so the actual process of circum-Antarctic colonisation of *P. kerguelensis* was certainly different. Accordingly, the simulation can only reproduce today's migration processes, but cannot take earth-historical events into account.

In contrast to the results of the locomotion dynamics, which can be compared and verified with observations and findings from previous studies, a direct assessment of the dispersal model results is difficult. The only available view of the current status of the circum-Antarctic dispersal of *P. kerguelensis* is a dispersal picture compiled over more than a century, which is certainly not complete either (Fig. 6.4). All other components involved in the migration, temporal aspects and earlier environmental conditions, however, are unknown. Only the fact that the results are within the realm of possibility since the last glacial period points to a somehow realistic model.

Nevertheless, a plausibility analysis as well as an evaluation of the input parameters will help to identify limitations, strengths and weaknesses of the model.

Net Primary Production *NPP*

A brief overview of the procedure for determining Net Primary Production *NPP* and its components involved can help to grasp the complexity of this issue. Phytoplankton, as the primary producer of organic carbon in the oceans, is represented by its chlorophyll content and the resulting photosynthetic activity. This process is driven by solar radiation reaching the Earth's surface. In other words, the photosynthetic biomass exposed to light determines the rate of *NPP*. The global chlorophyll *a* of the ocean is observed and quantified by satellite measurements. A small contribution, about two orders of magnitude lower, is provided by ice algae, but these cannot be detected by the satellites (Figs. 5.25 and 5.26). Especially in polar regions with partly permanent sea ice cover, ice algae are the only suppliers of organic carbon, e.g. in the western Weddell Sea. The light reduction through the ice was expressed as a function of ice thickness neglecting snow cover, as shown by Saenz and Arrigo (2014). Since ice generally contributes less than 2% to total productivity, I have simplified the calculation of primary production contributed by ice accordingly.

The *NPP* of carbon synthesised by phytoplankton in open waters was calculated according to Antoine and Morel (1996). It shows seasonally averaged global data (from 1978 to 1986) based on satellite chlorophyll *a* measurements with a spatial resolution of about 78 km², with the projection increasing towards the poles (Antoine et al., 1996). A large area south of 60° southern latitude shows values between 0.1 – 0.2 g_C m⁻² d⁻¹ in the late summer to autumn months of January to March. The spring to early summer period from October to December shows wide ranges up to 0.3 g_C m⁻² d⁻¹. The winter period is accompanied by complete ice cover and thus no primary production. Absolute values averaged over 16 yr including ocean and ice production yield 0.19 (±0.07) g_C m⁻² d⁻¹ in this study (based on data in Fig. 5.27). Despite different chlorophyll *a* measurements, both results show similar circum-Antarctic *NPP* of the same order of magnitude. While most of the Antarctic waters have ice-free phases associated with algal blooms and high *NPP* in summer, some parts are permanently covered by sea ice. The hotspot of high ice concentration is in the central and western

6. Discussion

Tab. 6.2 Net primary production *NPP* of sea ice. Results, in $[\text{mg}_\text{C} \text{m}^{-2} \text{d}^{-1}]$, from [Saenz and Arrigo \(2014\)](#) compared to the mean values of this study. The mean values were formed assuming a minimum ice thickness of 0.05 m.

Sector	Saenz and Arrigo	This study
Amundsen	2.26	3.96
Indian	3.71	4.70
Pacific	3.85	5.29
Ross	4.09	4.01
Weddell	4.18	4.09
Circum-Antarctic	4.10	4.30

Weddell Sea (Fig. 5.20). As the mean carbon production of sea ice is fifty times lower (ocean: $0.19 \text{ g}_\text{C} \text{m}^{-2} \text{d}^{-1}$; sea ice: $0.004 \text{ g}_\text{C} \text{m}^{-2} \text{d}^{-1}$, Table 6.2), this area is characterised by correspondingly low productivity (Fig. 5.27). Despite its low contribution of organic carbon, sea ice is nevertheless the only source of organically available energy in some places.

[Saenz and Arrigo \(2014\)](#) proposed a comprehensive model based on ice thickness and snow cover to calculate ice algal production. In this study, I adopted a simpler approach that greatly reduces the complexity, as I found it less important for the dispersal simulations. However, despite local differences, the overall Antarctic average still corresponds well to the results of Saenz and Arrigo (Tab. 6.2).

Ocean Currents, Migration, and Pelagic Drift

Currents are probably the most important part of the dispersal model. However, satellite remote sensing only allows measurements of surface currents, which may be different from midwater or seabed currents. Seabed features (canons, seamounts and continental slopes) deflect the main currents and can even reverse them. Superimposed tidal currents increase their complex structure and add a time-dependent component to the system. As tides cycle forth and back with local amplitudes and velocities, they return objects approximately to their original position. Consequently, objects picked up on the seabed and transported along tidal currents are carried a maximum of twice the tidal amplitude. Tidal currents perpendicular to the main current, on the other hand, increase the opening angle for lateral transport and thus increase the area of the dispersal zone.

Nevertheless, the main currents in the ocean below the surface are largely unknown or only locally determined. Since the spatial dispersal of *P. kerguelensis* is dominated by its larval progeny and they have positive buoyancy, they are largely at the sea surface [McClintock and Pearse \(1987\)](#). Therefore, surface currents seem to provide a good basis for dispersal through their larval migration. Horizontal drift by the unknown near-bottom currents during swimming, on the other hand, is uncertain and



6.5 Evaluation of the Model

cannot be evaluated with the given information.

Final considerations on the migration model of *P. kerguelensis*

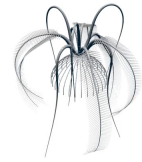
Spatial changes, on large time scales, by continental drift and climate variations cannot be represented due to lack of long term data. On the other hand, the behaviour of individuals is not taken into account on smaller time scales. All migration simulations reflect an optimal situation in which all available surplus energy is used for swimming. However, this does not correspond to reality, as organisms generally only move when external influences trigger this behaviour. That means, relocation to another site would only be worthwhile if either a lack of food, changing environmental characteristics (temperature, salinity, etc.), emerging threats or reproduction required it. Without any external trigger, crinoids would most likely stay where they are. Realistic migration rates by swimming are therefore probably orders of magnitude lower. Decadal fluctuations in ambient conditions are already considered to be sixteen times higher, but this figure is only based on available data between 2003 to 2018, which may vary within longer time periods. Random parameters could pick up the environmental variability and would be able to emulate the natural swimming behaviour of individuals or group dynamics. Despite all assumptions and simplifications introduced, the results nevertheless provide a good insight into the general mechanisms of mobile, but also sessile circum-Antarctic migration. By adjusting the boundary conditions, the model offers the potential to also predict and trace the spatial dispersal of other organisms or marine pollutants introduced by humans.

In the end, not all processes involved in the circum-Antarctic success of *Promachocrinus kerguelensis* are fully understood, however, the almost perfect match of *P. kerguelensis*' findings and the areas of high productivity is remarkable. Considering the simplified mathematical algorithm, remotely sensed satellite data averaged over sixteen years, and strongly extrapolated energetics, the model provides a reasonable representation of the processes involved. Since earlier ambient conditions are unknown, the conclusions drawn apply only to the recent environment. However, crinoids have existed for hundreds of millions of years, witnessing global changes such as continental drift and ice ages, magnetic field upheavals and global catastrophes such as asteroid impacts or volcanic eruptions, which probably strongly influenced their dispersal. Considering that evolution is still ongoing and the spread of species is a dynamic process that permanently adapts to changing conditions, the success story of *P. kerguelensis* is not over yet. Climate fluctuations will open or close habitable zones and continuously change the map of the fertile seabed. Echinoderms release countless offspring every year that can quickly colonise new areas, but they can also disappear at the same pace from places with deteriorating conditions.

In summary, *P. kerguelensis*' success is most likely a combination of several aspects. The ability to escape predators, as suggested by Meyer and Macurda (1977), is

6. Discussion

certainly crucial, but due to their relatively slow escape speed ($\sim 5 \text{ cm s}^{-1}$) this probably only affects threats from benthic predators, escaping pelagic predators is rather unlikely. Swimming itself plays a smaller role in large-scale migration than in local small-scale space. The simulations show that *P. kerguelensis*, in contrast to purely pelagic larval drift, is able to migrate slowly against the main ocean currents at migration speeds (maximum range velocity: $2,9 \text{ cm s}^{-1}$). Nevertheless, I believe that other adaptations must be involved in their success. Other Comatulid species have evolved the same ability and are present in the circum-Antarctic, but not as abundant and as diverse as *P. kerguelensis*. An estimated mean annual fecundity of 29,000 (max: 264,000) buoyant eggs with a pelagic residence time of two to three months allows for long range drift and thus wide distribution [McClintock and Pearse \(1987\)](#). Another aspect is metabolic life support costs, as the amount of energy available in Antarctica is very limited. *P. kerguelensis* is among the lightest crinoids with a body mass of only $\sim 5 \text{ g}$ for a 12-armed representative, *Florometra serratissima* in comparison has a body mass about twice as high ([Janevski and Baumiller, 2009](#)). Since metabolic costs are a function of body mass (Fig. 5.29), the light physiology of *P. kerguelensis* requires less metabolic energy, which in turn increases its potential habitat and the chance to survive lean years. *P. kerguelensis*' circum-Antarctic success is therefore most likely a combination of different adaptations and species-dependent characteristics.



6.5 Evaluation of the Model

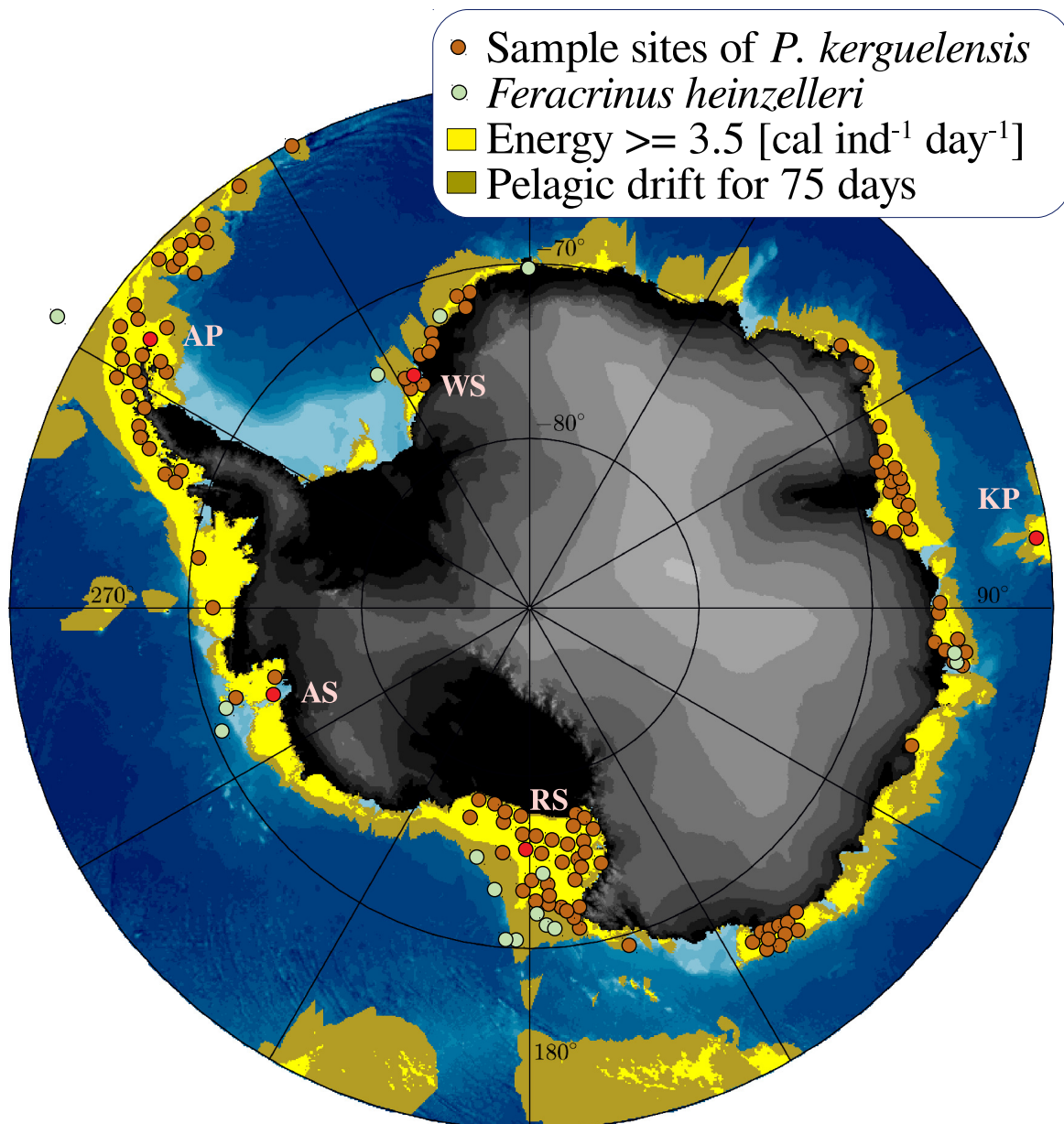


Fig. 6.4 Energy-dependent possible occurrence ranges of *P. kerguelensis*. The yellow region provides more than 3.5 calories per day per individual (long-term average: 2003-2018) total metabolic cost required by *P. kerguelensis* for survival. The underlying olive region also includes all yellow areas as well. This part of the ocean represents the area that can be reached during 75 days of pelagic drift from any point within the yellow region. The olive areas provide less than *P. kerguelensis*' life support, but may allow transfer to an adjacent habitable area. Brown dots mark in-situ findings according to (Eléaume et al., 2014). Red dots show the sites of origin used as starting points for the migration simulation. Green dots show the sites of a circum-Antarctic stalked crinoid *Feracrinus heinzelleri* for comparison. The underlying bathymetric map is taken from the IBCSO model [bc] (Arndt et al., 2013).

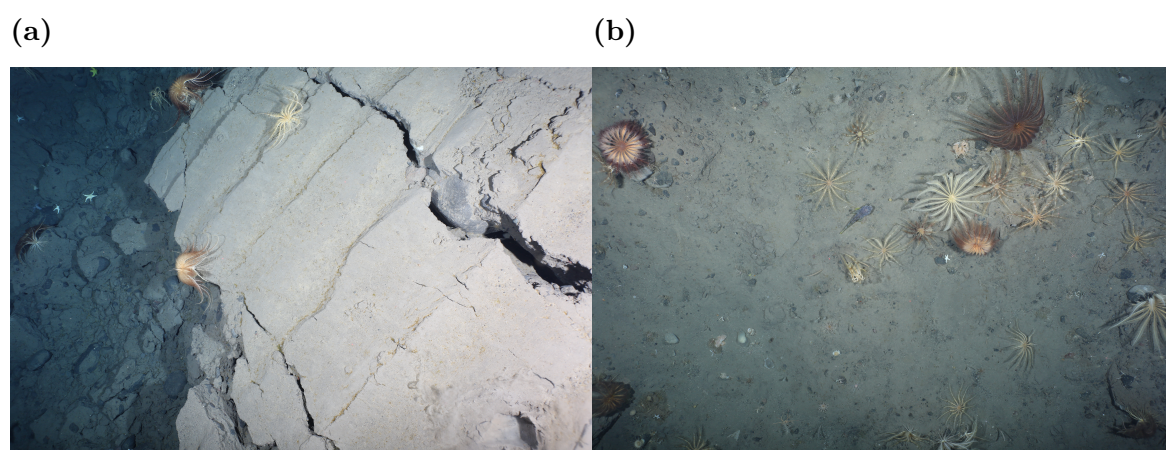
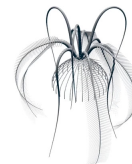


Fig. 6.5 Early stage of recolonisation of an iceberg scour. Pioneer comatulids as initial colonisers on destroyed seabed. The images were taken by Dieter Piepenburg on the *Polarstern* cruise PS96 in the Weddell Sea (Piepenburg et al., 2017) [pip].

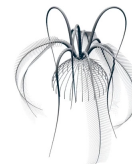


BIBLIOGRAPHY

- Alexander, R. M. (2006). *Principles of Animal Locomotion*. Princeton University Press.
- Allen, R. M., Metaxas, A., and Snelgrove, P. V. (2018). Applying movement ecology to marine animals with complex life cycles. *Annual Review of Marine Science*, 10(1):19–42.
- Ameziane, N. and Roux, M. (1997). Biodiversity and historical biogeography of stalked crinoids (Echinodermata) in the deep sea. *Biodiversity and Conservation*, 6(11):1557–1570.
- Andersen, K. L. (1960). Energy cost of swimming. *Acta chirurgica Scandinavica Supplementum*, (253):169–174.
- Antoine, D., André, J.-M., and Morel, A. (1996). Oceanic primary production 2. Estimation at global scale from satellite (coastal zone color scanner) chlorophyll. *Global Biogeochemical Cycles*, 10(1):57–69.
- Antoine, D. and Morel, A. (1996). Oceanic primary production 1. Adaptation of a spectral light-photosynthesis model in view of application to satellite chlorophyll observation. *Global Biogeochemical Cycles*, 10(1):43–55.
- Arndt, J. E., Schenke, H. W., Jakobsson, M., Nitsche, F. O., Buys, G., Goleby, B., Rebesco, M., Bohoyo, F., Hong, J., Black, J., Greku, R., Udintsev, G., Barrios, F., Reynoso-Peralta, W., Taisei, M., and Wigley, R. (2013). The International Bathymetric Chart of the Southern Ocean (IBCSO) Version 1.0-A new bathymetric compilation covering circum-Antarctic waters. *Geophysical Research Letters*, 40(12):3111–3117.
- Au, L. T. K., Phan, H. V., and Park, H. C. (2017). Comparison of aerodynamic forces and moments calculated by three-dimensional unsteady blade element theory and computational fluid dynamics. *Journal of Bionic Engineering*, 14(4):746–758.
- Bannister, T. T. (1974). Production equations in terms of chlorophyll concentration, quantum yield, and upper limit to production. *Limnology and Oceanography*, 19(1):1–12.
- Barnes, D. K. A. (2016). Iceberg killing fields limit huge potential for benthic blue carbon in Antarctic shallows. *Global Change Biology*, 23(7):2649–2659.
- Barnes, D. K. A., Fleming, A., Sands, C. J., Quartino, M. L., and Deregibus, D. (2018). Icebergs, sea ice, blue carbon and Antarctic climate feedbacks. *Philosophical Transactions of the Royal Society A: Mathematical, Physical and Engineering Sciences*, 376(2122):20170176.

Bibliography

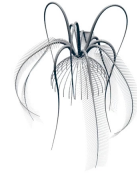
- Batchelor, G. K. (1967). *An Introduction to Fluid Dynamics*. Cambridge University Press, 8 edition.
- Battista, N. A. (2021). Fluid-structure interaction for the classroom: Interpolation, hearts, and swimming! *SIAM Review*, 63(1):181–207.
- Baumiller, T. K. and Janevski, G. A. (2011). On the swimming function of crinoid cirri. *Swiss J. Palaeontol.*, 130:19–24.
- Baumiller, T. K. and Messing, C. G. (2007). Stalked crinoid locomotion, and its ecological and evolutionary implications. *Paleontological Society*, 10(1):1–10.
- Beamish, F. W. H. (1970). Oxygen consumption of largemouth bass, *Micropterus salmoides*, in relation to swimming speed and temperature. *Canadian Journal of Zoology*, 48(6):1221–1228.
- Beamish, F. W. H. (1978). Swimming capacity. *Fish physiology*, 7:101–187.
- Behbahani, S. B. and Tan, X. (2016). Bio-inspired flexible joints with passive feathering for robotic fish pectoral fins. *Bioinspiration & Biomimetics*, 11(3):036009.
- Beyer, O., Bittner, L., Boseck, H., Bothe, H. G., Czichowski, G., Frischmuth, C., Göhde, D., Göhler, W., Görke, L., Gottwald, S., Hellwich, M., Here, H., Herrmann, M., Kästner, H., Lißke, G., Lorenz, G., Maeß, G., Müller, W., Neigenfind, F., Nožicka, F., Oberländer, S., Peschel, M., Pietzsch, G., Renschuh, B., Sachs, H., Salié, H., Schlosser, H., Schröder, E., Stammler, L., Steger, A., Sulanke, R., Thiele, H., Tuschke, W., Vahle, H., Wagner, L., Walsch, W., Wunsch, V., Wußing, G., and Wußing, H. (1977). *Kleine Enzyklopädie Mathematik*. H. Deutsch, Thun Switzerland.
- Bi, S., Ma, H., Cai, Y., Niu, C., and Wang, Y. (2014). Dynamic modeling of a flexible oscillating pectoral fin for robotic fish. *Industrial Robot: An International Journal*, 41(5):421–428.
- Bilo, D. and Nchtigall, W. (1980). A simple method to determine drag coefficients in aquatic animals. *Journal of Experimental Biology*, 87(1):357–359.
- Bonjean, F. and Lagerloef, G. S. E. (2002). Diagnostic model and analysis of the surface currents in the tropical pacific ocean. *Journal of Physical Oceanography*, 32(10):2938–2954.
- Bottjer, D. J. and Jablonski, D. (1988). Paleoenvironmental patterns in the evolution of post-paleozoic benthic marine invertebrates. *PALAIOS*, 3(6):540.
- Brett, J. R. and Glass, N. R. (1973). Metabolic rates and critical swimming speeds of sockeye salmon (*Oncorhynchus nerka*) in relation to size and temperature. *Journal of the Fisheries Research Board of Canada*, 30(3):379–387.



-
- Brett, J. R. and Sutherland, D. B. (1965). Respiratory metabolism of pumpkinseed (*Lepomis gibbosus*) in relation to swimming speed. *Journal of the Fisheries Research Board of Canada*, 22(2):405–409.
- Broyer, C. D., Koubbi, P., Griffiths, H., Raymond, B., d’Udekem d’Acoz, C., de Putte, A. V., Danis, B., David, B., Grant, S., Gutt, J., Held, C., Hosie, G., Huettmann, F., Post, A., and Ropert-Coudert, Y. (2014). *Biogeographic atlas of the Southern Ocean*. The Scientific Committee on Antarctic Research, Scott Polar Research Institute, Lensfield Road, Cambridge, CB2 1ER, United Kingdom. ISBN: 978-0-948277-28-3.
- Buchli, J., Kalakrishnan, M., Mistry, M., Pastor, P., and Schaal, S. (2009). Compliant quadruped locomotion over rough terrain. In *2009 IEEE/RSJ International Conference on Intelligent Robots and Systems*. IEEE.
- Burgess, R. W. (1916). *The Uniform Motion of a Sphere through a Viscous Liquid*. PhD thesis, Graduate School of Cornell University. Reprinted from American Journal of Mathematics Vol. XXXVIII, No. 1 January, 1916.
- Byron, C. J. and Burke, B. J. (2014). Salmon ocean migration models suggest a variety of population-specific strategies. *Reviews in Fish Biology and Fisheries*, 24(3):737–756.
- Carpenter, P. H. (1879). Preliminary report upon the comatulæ of the challenger expedition. In *Proceedings of the Royal Society of London*, volume 28, pages 383–395.
- Carpenter, W. B. (1866). Researches on the structure, physiology, and development of antedon (*Comatula, Lamk. rosaceus*). part i. *Phil. Trans. R. Soc. Lond.*, 156:671–756.
- Chadwick, H. C. (1907). Antedon. In Hardman, W. A., editor, *L.M.B.C. Memoirs*, volume 15, pages 1–47. Liverpool Marine Biology Committee. with 7 plates.
- Clark, A. H. (1915). *A Monography of the existing crinoids, Vol. 1, Part 1*. Number 82 in Bulletin of the United States National Museum. U. S. government printing office, Washington.
- Clark, A. H. (1921). *A Monography of the existing crinoids, Vol. 1, Part 2*. Number 82 in Bulletin of the United States National Museum. U. S. government printing office, Washington.
- Clark, A. H. (1967). *A Monography of the existing crinoids, Vol. 1, Part 5*. Number 82 in Bulletin of the United States National Museum. U. S. government printing office, Washington.
- Clark, P. U., Dyke, A. S., Shakun, J. D., Carlson, A. E., Clark, J., Wohlfarth, B., Mitrovica, J. X., Hostetler, S. W., and McCabe, A. M. (2009). The last glacial maximum. *Science*, 325(5941):710–714.

Bibliography

- Colgate, J. E. and Lynch, K. M. (2004). Mechanics and control of swimming: A review. *IEEE Journal of Oceanic Engineering*, 29(3):660–673.
- Daniel, T. L. (1984). Unsteady aspects of aquatic locomotion. *American Zoologist*, 24(1):121–134.
- Drzewiecki, M. S. (1892). Méthode pour la détermination des éléments mécaniques des propulseurs hélicoïdaux. In *Bulletin de l'Association Technique Maritime*, volume 03, pages 11–31.
- Drzewiecki, M. S. (1900). Des hélices propulsives. In *Bulletin de l'Association Technique Maritime*, volume 12, pages 71–91.
- Drzewiecki, M. S. (1901). Du choix des éléments déterminant les hélices propulsives, permettant leur facile comparaison entre elles. In *Bulletin de l'Association Technique Maritime*, volume 11, pages 91–116.
- Durst, F. (2006). *Grundlagen der Strömungsmechanik*. Springer Verlag.
- Elliott, J. M. and Davison, W. (1975). Energy equivalents of oxygen consumption in animal energetics. *Oecologia*, 19(3):195–201.
- Eléaume, M., Hemery, L. G., Roux, M., and Améziane, N. (2014). *Biogeographic atlas of the Southern Ocean*, chapter 5.25. Southern Ocean Crinoids, pages 208–212. The Scientific Committee on Antarctic Research, Scott Polar Research Institute, Lensfield Road, Cambridge, CB2 1ER, United Kingdom.
- Falkowski, P. G. (1981). Light-shade adaptation and assimilation numbers. *Journal of Plankton Research*, 3(2):203–216.
- Farin, G. (1990). *Curves and Surfaces for Computer Aided Geometric Design - A Practical Guide*. Academic Press Inc.
- Farin, G. E. and Hansford, D. (2000). *The Essentials of CAGD*. A K Peters, Ltd.
- Farmer, G. J. and Beamish, F. W. H. (1969). Oxygen consumption of *Tilapia nilotica* in relation to swimming speed and salinity. *Journal of the Fisheries Research Board of Canada*, 26(11):2807–2821.
- Fish, F. E. (1982). Aerobic energetics of surface swimming in the muskrat *Ondatra zibethicus*. *Physiological Zoology*, 55(2):180–189.
- Fox, H. M. (1936). The activity and metabolism of poikilothermal animals in different latitudes. *Proceedings of the Zoological Society of London*, 106(4):945–955.
- Frouin, R., Lingner, D. W., Gautier, C., Baker, K. S., and Smith, R. C. (1989). A simple analytical formula to compute clear sky total and photosynthetically available solar irradiance at the ocean surface. *Journal of Geophysical Research*, 94(C7):9731–9742.



-
- Gray, J. (1968). *Animal Locomotion*. Weidenfeld and Nicolson.
- Grimm, V., Berger, U., Bastiansen, F., Eliassen, S., Ginot, V., Giske, J., Goss-Custard, J., Grand, T., Heinz, S. K., Huse, G., Huth, A., Jepsen, J. U., Jørgensen, C., Mooij, W. M., Müller, B., Pe'er, G., Piou, C., Railsback, S. F., Robbins, A. M., Robbins, M. M., Rossmanith, E., Rüger, N., Strand, E., Souissi, S., Stillman, R. A., Vabø, R., Visser, U., and DeAngelis, D. L. (2006). A standard protocol for describing individual-based and agent-based models. *Ecological Modelling*, 198(1-2):115–126.
- Gutt, J. (2001). On the direct impact of ice on marine benthic communities, a review. *Polar Biology*, 24(8):553–564.
- Gutt, J., Barratt, I., Domack, E., d’Udekem d’Acoz, C., Dimmler, W., Grémare, A., Heilmayer, O., Isla, E., Janussen, D., Jorgensen, E., Kock, K.-H., Lehnert, L. S., López-González, P., Langner, S., Linse, K., Manjón-Cabeza, M. E., Meißner, M., Montiel, A., Raes, M., Robert, H., Rose, A., Schepisi, E. S., Saucède, T., Scheidat, M., Schenke, H.-W., Seiler, J., and Smith, C. (2011). Biodiversity change after climate-induced ice-shelf collapse in the Antarctic. *Deep Sea Research Part II: Topical Studies in Oceanography*, 58(1-2):74–83.
- Halcrow, K. and Boyd, C. (1967). The oxygen consumption and swimming activity of the amphipod *Gammarus oceanicus* at different temperatures. *Comparative Biochemistry and Physiology*, 23(1):233–242.
- Harmelin-Vivien, M., Bánaru, D., Dromard, C. R., Ourgaud, M., and Carlotti, F. (2019). Biochemical composition and energy content of size-fractionated zooplankton east of the Kerguelen Islands. *Polar Biology*, 42(3):603–617.
- Heath, T. L. (1897). *The works of archimedes*. Cambridge University Press.
- Hertel, H. (1963). *Struktur, Form, Bewegung*. Krausskopf-Verlag, Mainz.
- Hess, H., Ausich, W., Brett, C., Simms, M. J., and Taylor, W. L. (2003). *Fossil Crinoids*. Cambridge University Press.
- Hill, A. V. (1950). The dimensions of animals and their muscular dynamics. *Science Progress (1933-)*, 38(150):209–230.
- Hirt, C., Amsden, A., and Cook, J. (1974). An arbitrary lagrangian-eulerian computing method for all flow speeds. *Journal of Computational Physics*, 14(3):227–253.
- Hirt, C., Cook, J., and Butler, T. (1970). A lagrangian method for calculating the dynamics of an incompressible fluid with free surface. *Journal of Computational Physics*, 5(1):103–124.
- Hoerner, S. (1965). *Fluid-Dynamic Drag - Aerodynamic Drag and Hydrodynamic Resistance*. Published by the Author, 1 edition.

Bibliography

- Hoerner, S. (1975). *Fluid-Dynamic Lift - Aerodynamic and Hydrodynamic Lift*. Published by Mrs. Liselotte A. Hoerner, 1 edition.
- Hopkins, M. A., Hong, D. W., and Leonessa, A. (2015). Compliant locomotion using whole-body control and divergent component of motion tracking. In *2015 IEEE International Conference on Robotics and Automation (ICRA)*. IEEE.
- Howard, S. L., Padman, L. H., and Erofeeva, S. (2019). Cats2008: Circum-Antarctic tidal simulation version 2008.
- Hu, C., Lee, Z., and Franz, B. (2012). Chlorophyll *a* algorithms for oligotrophic oceans: A novel approach based on three-band reflectance difference. *Journal of Geophysical Research: Oceans*, 117(C1).
- Hui, C. A. (1988). Penguin swimming. I. Hydrodynamics. *Physiological Zoology*, 61(4):333–343.
- Isla, E., Gerdes, D., Palanques, A., Gili, J.-M., and Arntz, W. (2006). Particle fluxes and tides near the continental ice edge on the eastern weddell sea shelf. *Deep-Sea Research II*, 53:866–874.
- Isla, E., Gerdes, D., Palanques, A., Gili, J.-M., Arntz, W. E., and König-Langlo, G. (2009). Downward particle fluxes, wind and a phytoplankton bloom over a polar continental shelf: A stormy impulse for the biological pump. *Marine Geology*, 259:59–72.
- Ivlev, V. S. (1963). Energy consumption during the motion of shrimps. *Zool. Zh.*, 42:1465–1471.
- Jago, C., Jones, S., Latter, R., McCandliss, R., Hearn, M., and Howarth, M. (2002). Resuspension of benthic fluff by tidal currents in deep stratified waters, northern North Sea. *Journal of Sea Research*, 48(4):259–269.
- Janevski, G. A. and Baumiller, T. K. (2009). Could a stalked crinoid swim? A biomechanical model and characteristics of swimming crinoids. *Society for Sedimentary Geology*, 25(9):588–596.
- Jansen, J., Hill, N. A., Dunstan, P. K., McKinlay, J., Sumner, M. D., Post, A. L., Eléaume, M. P., Armand, L. K., Warnock, J. P., Galton-Fenzi, B. K., and Johnson, C. R. (2017). Abundance and richness of key Antarctic seafloor fauna correlates with modelled food availability. *Nature Ecology & Evolution*, 2(1):71–80.
- Kalakrishnan, M., Buchli, J., Pastor, P., Mistry, M., and Schaal, S. (2010). Learning, planning, and control for quadruped locomotion over challenging terrain. *The International Journal of Robotics Research*, 30(2):236–258.
- Kato, N. and Kamimura, S. (2008). *Bio-mechanisms of Swimming and Flying - Fluid Dynamics, Biomimetic Robots, and Sports Science*. Springer Verlag, 1 edition.



-
- Ke, B. (2003). *Photosynthesis*, volume 10. Kluwer Academic Publishers.
- King, M. A., Padman, L., Nicholls, K., Clarke, P. J., Gudmundsson, G. H., Kulesa, B., and Shepherd, A. (2011). Ocean tides in the Weddell Sea: New observations on the Filchner-Ronne and Larsen C ice shelves and model validation. *Journal of Geophysical Research*, 116(C6).
- Kuder, J. (2011). Methoden zur berechnung von fluidparametern. Technical report, Leibniz-Institut für Angewandte Geophysik Hannover.
- Kutty, M. N. (1969). Oxygen consumption in the mullet *Liza macrolepis* with special reference to swimming velocity. *Marine Biology*, 4(3):239–242.
- Kümmel, W. (2007). *Technische Strömungsmechanik: Theorie und Praxis (German Edition)*. Vieweg+Teubner Verlag.
- La Touche, R. W. (1976). The feeding behaviour and food of the shallow-water crinoid *Antedon bifida* (pennant) and some aspects of its ecology. mthesis, University of Dublin. 214 pp.
- LaBarbera, M. (1982). Metabolic rates of suspension feeding crinoids and ophiuroids (Echinodermata) in a unidirectional laminar flow. *Comparative Biochemistry and Physiology Part A: Physiology*, 71(2):303–307.
- Lake, T. (2017). *Computational Modelling of Interactions of Marine Mammals and Tidal Stream Turbines*. PhD thesis, College of Engineering, Swansea University.
- Lamb, S. H. (1932). *Hydrodynamics*. Dover Publications, Inc., 6 edition.
- Lampitt, R. (1985). Evidence for the seasonal deposition of detritus to the deep-sea floor and its subsequent resuspension. *Deep Sea Research Part A. Oceanographic Research Papers*, 32(8):885–897.
- Langeloh, H.-P. (1937). Über die bewegung von *Antedon rosaceus* und ihre nervöse regulierung. In Hartmann, M. and Hesse, R., editors, *Zoologische Jahrbücher*, volume 57, chapter Abteilung für allgemeine Zoologie und Physiologie der Tiere, pages 235–279. Gustav Fischer-Jena. plates VI+VII.
- Lauer, J., Rouard, A. H., and Vilas-Boas, J. P. (2016). Upper limb joint forces and moments during underwater cyclical movements. *Journal of Biomechanics*, 49(14):3355–3361.
- Lighthill, M. J. (1969). Hydromechanics of aquatic animal propulsion. *Annual Review of Fluid Mechanics*, 1(1):413–446.
- Little, E. M., Allen, M. B., and Wright, F. F. (1972). Field measurement of light penetration through sea ice. *Institute of Marine Science contribution*, 25(1):28–33. ASTIS record 10171.

Bibliography

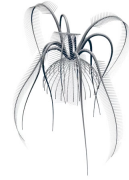
- Liu, H. (2005). Simulation-based biological fluid dynamics in animal locomotion. *Applied Mechanics Reviews*, 58(4):269–282.
- Macurda, D. Bradford, J. and Meyer, D. L. (1983). Sea lilies and feather stars. *American Scientist*, 71(4):354–365.
- Marshall, A. M. (1884). On the nervous system of *Antedon rosaceus*. *Journal of Cell Science*, 2(24):507–548.
- McClintock, J. B. and Pearse, J. S. (1987). Reproductive biology of the common antarctic crinoid *Promachocrinus kerguelensis* (Echinodermata: Crinoidea). *Marine Biology*, 96(3):375–383.
- McEdward, L. R. and Miner, B. G. (2001). Larval and life-cycle patterns in echinoderms. *Canadian Journal of Zoology*, 79(7):1125–1170.
- Meiners, K. M., Vancoppenolle, M., Thanassekos, S., Dieckmann, G. S., Thomas, D. N., Tison, J.-L., Arrigo, K. R., Garrison, D. L., McMinn, A., Lannuzel, D., van der Merwe, P., Swadling, K. M., Jr., W. O. S., Melnikov, I., and Raymond, B. (2012). Chlorophyll *a* in Antarctic sea ice from historical ice core data. *Geophysical Research Letters*, 39:1–5.
- Messing, C. G. (1997). Living comatulids. *The Paleontological Society Papers*, 3:3–30.
- Meyer, D. L. (1985). Evolutionary implications of predation on recent comatulid crinoids from the Great Barrier Reef. *Paleobiology*, 11(2):154–164.
- Meyer, D. L., LaHaye, C. A., Holland, N. D., Arneson, A. C., and Strickler, J. R. (1984). Time-lapse cinematography of feather stars (Echinodermata: Crinoidea) on the Great Barrier Reef, Australia: demonstrations of posture changes, locomotion, spawning and possible predation by fish. *Marine Biology*, 78:179–184.
- Meyer, D. L. and Macurda, D. B. (1977). Adaptive radiation of the comatulid crinoids. *Paleobiology*, 3(1):74–82.
- Mladenov, P. V. and Chia, F. S. (1983). Development, settling behaviour, metamorphosis and pentacrinoid feeding and growth of the feather star *Florometra serratis-sima*. *Marine Biology*, 73(3):309–323.
- Moore, A. R. (1923). The nervous mechanism of coordination in the crinoid, *Antedon Rosaceus*. *The Journal of General Physiology*, 6(3):281–288.
- Morel, A. (1991). Light and marine photosynthesis: A spectral model with geochemical and climatological implications. *Prog. Oceanog.*, 26:263–306.
- Morel, A. and Smith, R. C. (1974). Relation between total quanta and total energy for aquatic photosynthesis. *Limnology and Oceanography*, 19(4):591–600.



-
- Morlighem, M., Rignot, E., Binder, T., Blankenship, D., Drews, R., Eagles, G., Eisen, O., Ferraccioli, F., Forsberg, R., Fretwell, P., Goel, V., Greenbaum, J. S., Gudmundsson, H., Guo, J., Helm, V., Hofstede, C., Howat, I., Humbert, A., Jokat, W., Karlsson, N. B., Lee, W. S., Matsuoka, K., Millan, R., Mouginot, J., Paden, J., Pattyn, F., Roberts, J., Rosier, S., Ruppel, A., Seroussi, H., Smith, E. C., Steinhage, D., Sun, B., van den Broeke, M. R., van Ommen, T. D., van Wessem, M., and Young, D. A. (2019). Deep glacial troughs and stabilizing ridges unveiled beneath the margins of the Antarctic ice sheet. *Nature Geoscience*, 13(2):132–137.
- Morris, M. J., Gust, G., and Torres, J. J. (1985). Propulsion efficiency and cost of transport for copepods: a hydromechanical model of crustacean swimming. *Marine Biology*, 86(3):283–295.
- Nesteruk, I., Passoni, G., and Redaelli, A. (2014). Shape of aquatic animals and their swimming efficiency. *Journal of Marine Biology*, 2014:1–9.
- O’Dor, R. K. (1982). Respiratory metabolism and swimming performance of the squid, *Loligo opalescens*. *Canadian Journal of Fisheries and Aquatic Sciences*, 39(4):580–587.
- Oertel, H. (2008). *Bioströmungsmechanik*. Vieweg + Teubner, 1 edition.
- Oertel, H., Böhle, M., and Dohrmann, U. (2009). *Strömungsmechanik*. Vieweg + Teubner, 5 edition.
- Oertel, H. J. (2006). *Strömungsmechanik (German Edition)*. Vieweg+Teubner Verlag.
- Oji, T. (1996). Is predation intensity reduced with increasing depth? Evidence from the west Atlantic stalked crinoid *Endoxocrinus parrae* (Gervais) and implications for the Mesozoic marine revolution. *Paleobiology*, 22(3):339–351.
- Oji, T., Ogawa, Y., Hunter, A. W., and Kitazawa, K. (2009). Discovery of dense aggregations of stalked crinoids in Izu-Ogasawara Trench, Japan. *Zoological Science*, 26(6):406–408.
- Owsianowski, N. and Kesel, A. (2008). Drag reduction in schooling fish? — a CFD approach. *Comparative Biochemistry and Physiology Part A: Molecular & Integrative Physiology*, 150(3):S85.
- Padman, L., Erofeeva, S. Y., and Fricker, H. A. (2008). Improving antarctic tide models by assimilation of ICESat laser altimetry over ice shelves. *Geophysical Research Letters*, 35(22).
- Padman, L., Fricker, H. A., Coleman, R., Howard, S., and Erofeeva, L. (2002). A new tide model for the Antarctic ice shelves and seas. *Annals of Glaciology*, 34:247–254.

Bibliography

- Palanques, A., Isla, E., Puig, P., Sanchez-Cabeza, J. A., and Masqué, P. (2002). Annual evolution of downward particle fluxes in the Western Bransfield Strait (Antarctica) during the FRUELA project. *Deep-Sea Research II*, 49:903–920.
- Paul, C. R. C. and Smith, A. B. (1984). The early radiation and phylogeny of Echinoderms. *Biological Reviews*, 59(4):443–481.
- Peck, L. S., Barnes, D. K. A., Cook, A. J., Fleming, A. H., and Clarke, A. (2010). Negative feedback in the cold: ice retreat produces new carbon sinks in Antarctica. *Global Change Biology*, 16(9):2614–2623.
- Percy, J. A. and Fife, F. F. J. (1981). The biochemical composition and energy content of Arctic marine macrozooplankton. *Arctic*, 34(4):307–313.
- Piepenburg, D., Buschmann, A., Driemel, A., Grobe, H., Gutt, J., Schumacher, S., Segelken-Voigt, A., and Sieger, R. (2017). Seabed images from Southern Ocean shelf regions off the northern Antarctic Peninsula and in the southeastern Weddell Sea. *Earth System Science Data*, 9(2):461–469.
- Pinker, R. T. and Laszlo, I. (1992). Global distribution of photosynthetically active radiation as observed from satellites. *Journal of Climate*, 5(1):56–65.
- Platt, T. and Irwin, B. (1973). Caloric content of phytoplankton. *Limnology and Oceanography*, 8(2):306–310.
- Porro, L. B., Collings, A. J., Eberhard, E. A., Chadwick, K. P., and Richards, C. T. (2017). Inverse dynamic modelling of jumping in the red-legged running frog, *Kassina maculata*. *The Journal of Experimental Biology*, 220(10):1882–1893.
- Prange, H. D. and Schmidt-Nielsen, K. (1970). The metabolic cost of swimming in ducks. *Journal of Experimental Biology*, 53(3):763–777.
- Richards, C. T. (2008). The kinematic determinants of anuran swimming performance: an inverse and forward dynamics approach. *Journal of Experimental Biology*, 211(19):3181–3194.
- Rossington, K. and Benson, T. (2020). An agent-based model to predict fish collisions with tidal stream turbines. *Renewable Energy*, 151:1220–1229.
- Rowe, A. M. J. and Chou, J. C. S. (1970). Pressure-volume-temperature-concentration relation of aqueous naci solutions. *Journal af Chemical and Engineering Data*, 15(1):61–66.
- Ruiz-Torres, R., Curet, O. M., Lauder, G. V., and MacIver, M. A. (2014). Kinematics of the ribbon fin in hovering and swimming of the electric ghost knifefish. *Journal of Experimental Biology*, 217(20):3765–3766.



-
- Saenz, B. T. and Arrigo, K. R. (2014). Annual primary production in Antarctic sea ice during 2005-2006 from a sea ice state estimate. *Journal of Geophysical Research: Oceans*, 119(6):3645–3678.
- Saunders, F., Trimmer, B. A., and Rife, J. (2010). Modeling locomotion of a soft-bodied arthropod using inverse dynamics. *Bioinspiration & Biomimetics*, 6(1):016001.
- Schaafsma, F. L., Cherel, Y., Flores, H., van Franeker, J. A., Lea, M., Raymond, B., and van de Putte, A. P. (2018). Review: the energetic value of zooplankton and nekton species of the Southern Ocean. *Marine Biology*, 165(129):1–35.
- Schlichting, H., Gersten, K., Krause, E., and Oertel, H. (2006). *Grenzschicht-Theorie*. Springer-Verlag GmbH, 10 edition.
- Schmidt-Nielsen, K. (1972). Locomotion: Energy cost of swimming, flying, and running. *Science*, 177(4045):222–228.
- Shanks, A. L. (2009). Pelagic larval duration and dispersal distance revisited. *The Biological Bulletin*, 216(3):373–385.
- Shaw, G. D. and Fontaine, A. R. (1990). The locomotion of the comatulid *Florometra serratissima* (Echinodermata: Crinoid) and its adaptive significance. *Can. J. Zool.*, 68:942–950.
- Sigloch, H. (2008). *Technische Fluidmechanik*. 6. Springer-Verlag Berlin Heidelberg.
- Siniff, D. and Jessen, C. (1969). A simulation model of animal movement patterns. In *Advances in Ecological Research*, pages 185–219. Elsevier.
- Smit, H., Amelink-Koutstaal, J., Vijverberg, J., and Vaupel-Klein, J. V. (1971). Oxygen consumption and efficiency of swimming goldfish. *Comparative Biochemistry and Physiology Part A: Physiology*, 39(1):1–28.
- Smith, C. R., Mincks, S., and DeMaster, D. J. (2008). The FOODBANCS project: Introduction and sinking fluxes of organic carbon, chlorophyll *a* and phytodetritus on the western Antarctic Peninsula continental shelf. *Deep Sea Research Part II: Topical Studies in Oceanography*, 55(22-23):2404–2414.
- Sonntag, R., Hoffmann, F., Stamhuis, E., and Kesel, A. B. (2018). Potential of a flapping fish-like propulsion system for application on a micro-rov. In *Bionik: Patente aus der Natur - Tagungsbeiträge zum 9. Bremer Bionik Kongress*, pages 277–281. Bionik-Innovations-Centrum (B-I-C), 5 edition.
- Sonntag, R. and Kesel, A. B. (2011). Alternative antriebssysteme: Dreidimensionale nachlaufuntersuchungen an modellen mit fischähnlichen biegesteifigkeitsgradienten. In *Bionik: Patente aus der Natur - Tagungsbeiträge zum 5. Bremer Bionik Kongress*, pages 348–353. Bionik-Innovations-Centrum (B-I-C).

Bibliography

- Soontiens, N., Binding, C., Fortin, V., Mackay, M., and Rao, Y. R. (2019). Algal bloom transport in Lake Erie using remote sensing and hydrodynamic modelling: Sensitivity to buoyancy velocity and initial vertical distribution. *Journal of Great Lakes Research*, 45(3):556–572.
- Souza, A. J. (2004). Tidally induced turbulence and suspended sediment. *Geophysical Research Letters*, 31(20).
- Speel, J. A. and Dearborn, J. H. (1983). Comatulid crinoids from *R/V Eltanin* cruises in the Southern Ocean. In *Biology of the Antarctic Seas XIII*, pages 1–60. American Geophysical Union.
- Staaterman, E. and Paris, C. B. (2013). Modelling larval fish navigation: the way forward. *ICES Journal of Marine Science*, 71(4):918–924.
- Stamhuis, E. J., Videler, J. J., van Duren, L. A., and Müller, U. K. (2002). Applying digital particle image velocimetry to animal-generated flows: Traps, hurdles and cures in mapping steady and unsteady flows in re regimes between 10^{-2} and 10^{-5} . *Experiments in Fluids*, 33:801–813.
- Stokes, G. G. (1850). On the effect of the internal friction of fluids on the motion of pendulums. In *Transactions of the Cambridge Philosophical Society*, volume IX, page 8. Cambridge University Press.
- Suess, E. (1980). Particulate organic carbon flux in the oceans—surface productivity and oxygen utilization. *Nature*, 288(5788):260–263.
- Swearer, S. E., Treml, E. A., and Shima, J. S. (2019). A review of biophysical models of marine larval dispersal. In *Oceanography and Marine Biology*, pages 325–356. CRC Press.
- Torres, J. J. (1984). Relationship of oxygen consumption to swimming speed in *Euphausia pacifica*. *Marine Biology*, 78(3):231–237.
- Torres, J. J. and Childress, J. J. (1983). Relationship of oxygen consumption to swimming speed in *Euphausia pacifica*. *Marine Biology*, 74(1):79–86.
- Triantafyllou, G., Triantafyllou, M., and Grosenbaugh, M. (1993). Optimal thrust development in oscillating foils with application to fish propulsion. *Journal of Fluids and Structures*, 7(2):205–224.
- Triantafyllou, M. S. and Triantafyllou, G. S. (1995). An efficient swimming machine. *Scientific American*, 272(3):64–70.
- van Rees, W. M., Gazzola, M., and Koumoutsakos, P. (2015). Optimal morphokinematics for undulatory swimmers at intermediate Reynolds numbers. *Journal of Fluid Mechanics*, 775:178–188.



-
- Videler, J. J. (1993). *Fish Swimming*. Springer Netherlands.
- Vogel, S. (1996). *Life in Moving Fluids*. Princeton University Press.
- Wagner, W., Cooper, J. R., Dittmann, A., Kijima, J., Kretzschmar, H.-J., Kruse, A., Mareš, R., Oguchi, K., Sato, H., Stöcker, I., Šifner, O., Takaishi, Y., Tanishita, I., Trübenbach, J., and Willkommen, T. (2000). The IAPWS industrial formulation 1997 for the thermodynamic properties of water and steam. *J. Eng. Gas Turbines & Power*, 122:150–182.
- Wakeman, J. M. and Wohlschlag, D. E. (1981). Least-cost swimming speeds and transportation costs in some pelagic estuarine fishes. *Fisheries Research*, 1:117–127.
- Warnock, R. E. and Liddell, W. (1985). Oxygen consumption in two shallow-water comatulid crinoids. *Journal of Experimental Marine Biology and Ecology*, 91(1-2):169–182.
- Webb, P. W. (1971). The swimming energetics of trout. (i) oxygen consumption and swimming efficiency. *J. exp. Biol.*, (55):521–540.
- Webb, P. W. (1975). Efficiency of pectoral-fin propulsion of *Cymatogaster Aggregata*. In *Swimming and Flying in Nature*, pages 573–584. Springer US.
- Webster, S. K. (1975). Oxygen consumption in echinoderms from several geographical locations, with particular reference to the Echinoidea. *The Biological Bulletin*, 148(1):157–164.
- Wefer, G. and Fischer, G. (1991). Annual primary production and export flux in the Southern Ocean from sediment trap data. *Marine Chemistry*, 35:597–613.
- Willis, J. (2011). Modelling swimming aquatic animals in hydrodynamic models. *Ecological Modelling*, 222(23-24):3869–3887.
- Winter, D. A. (2009). *Biomechanics and Motor Control of Human Movement*. Wiley John + Sons.
- Wohlschlag, D. E., Cameron, J. N., and Joseph J. Cech, J. (1968). Seasonal changes in the respiratory metabolism of the pinfish (*Lagodon rhomboides*). *Contrib. mar. Sci.*, 13:89–104.
- Zhang, J. and Rothrock, D. A. (2003). Modeling global sea ice with a thickness and enthalpy distribution model ingeneralized curvilinear coordinates. *Mon. Weather Rev.*, 131(5):845–861.

Data Sources

- [bc] Arndt, J. E. International Bathymetric Chart of the Southern Ocean (IBCSO) [elevation]. Dataset accessed [June 2014] at <https://doi.pangaea.de/10.1594/PANGAEA.805734?format=html>. doi: 10.1594/PANGAEA.805734.
- [bm] Morlighem, M. 2019. MEaSURES BedMachine Antarctica, Version 1. [bed, thickness, surface]. Boulder, Colorado USA. NASA National Snow and Ice Data Center Distributed Active Archive Center. doi: <https://doi.org/10.5067/C2GFER6PTOS4>. [20 January 2020].
- [chl] NASA Earth Observations (NEO). MODIS ocean color imaging. Dataset accessed [08 Juli 2019] at https://neo.sci.gsfc.nasa.gov/view.php?datasetId=MY1DMM_CHLORA and doi: 10.5067/AQUA/MODIS/L3B/CHL/2014.
- [cl] NASA Earth Observations (NEO). MODIS ocean color imaging. Dataset accessed [08 Juli 2019] at https://neo.sci.gsfc.nasa.gov/view.php?datasetId=MODAL2_M_CLD_FR.
- [cri] Owsianowski, Nils; Federwisch, Luisa; Kluibenschedl, Anna; Casado de Amezua, Maria del Pilar; Richter, Claudio (2017): Sea-floor videos (benthos) along ROV profile PS82/049-1 during POLARSTERN cruise PS82, links to videos. Alfred Wegener Institute, Helmholtz Centre for Polar and Marine Research, Bremerhaven, PANGAEA, <https://doi.org/10.1594/PANGAEA.879289>.
- [crii] Owsianowski, Nils; Federwisch, Luisa; Kluibenschedl, Anna; Casado de Amezua, Maria del Pilar; Richter, Claudio (2017): Sea-floor videos (benthos) along ROV profile PS82/128-1 during POLARSTERN cruise PS82, links to videos. Alfred Wegener Institute, Helmholtz Centre for Polar and Marine Research, Bremerhaven, PANGAEA, <https://doi.org/10.1594/PANGAEA.879524>.
- [id] Monthly mean sea-ice motion vectors derived from Tschudi, M., W. N. Meier, J. S. Stewart, C. Fowler, and J. Maslanik. 2019. Polar Pathfinder Daily 25 km EASE-Grid Sea Ice Motion Vectors, Version 4.1. Boulder, Colorado USA. NASA National Snow and Ice Data Center Distributed Active Archive Center. doi: <https://doi.org/10.5067/INAWUWO7QH7B>. [26 April 2019] were provided in netCDF format (file version fv0.01) by the Integrated Climate Data Center (ICDC, icdc.cen.uni-hamburg.de) University of Hamburg, Hamburg, Germany.
- [oc] ESR. 2009. OSCAR third degree resolution ocean surface currents. Ver. 1. PO.DAAC, CA, USA. Dataset accessed [12 Juli 2019] at <https://doi.org/10.5067/OSCAR-03D01>.



[pip] Piepenburg, Dieter (2016): Seabed photographs taken along OFOS profiles during POLARSTERN cruise PS96 (ANT-XXXI/2 FROSN). Alfred Wegener Institute, Helmholtz Centre for Polar and Marine Research, Bremerhaven, PANGAEA, <https://doi.org/10.1594/PANGAEA.862097>.

[sit] Polar Science Center at University of Washington, Seattle, WA. Global Ice Ocean Modeling and Assimilation System (GIOMAS), variable [heff] (sea ice thickness). Dataset accessed [30 October 2019] at https://pscfiles.apl.uw.edu/zhang/Global_seaice/.

Software

[BL] Blender 2.79, <https://blender.org/>.

[FIJI] Fiji based on ImageJ version 1.52, available on <https://imagej.net/Fiji/Downloads>

[FFP] ffmpeg version 3.4.8, available on <https://ffmpeg.org/download.html>

[GDAL] Gdal libraries version 2.2.3, <https://gdal.org/>. Documentation under <https://gdal.org/gdal.pdf>.

[PS] Pysolar [Juli 2019] <https://pysolar.org/>. Documentation available under <https://buildmedia.readthedocs.org/media/pdf/pysolar/latest/pysolar.pdf>.

[SCI] Scilab in the versions 5.5.2 and 6.1.0 are available under <https://www.scilab.org/> (September 2019).

[TMD] The Tide Model Driver v2.05 by the Earth & Space Research institute in Seattle, available on <https://www.esr.org/research/polar-tide-models/tmd-software/> (Juli 2019).

Data Sources



A. LIST OF SCALE COEFFICIENTS

Tab. A.1 Scaling coefficients. Regression coefficients (a) and (b) to compensate for tracking perspectives. Arm size is scaled with respect to arm length on a reference image.

Sample	Arm	Ref. frame	a	b	std
RS600012	A	1	1.050	154.750	3.512
	B	1	1.261	88.338	2.587
	C	1	2.304	128.827	10.914
	D	1	0.573	161.340	3.794
	E	1	2.970	123.868	4.739
	F	1	1.997	162.701	4.894
RS619007	A	51	1.452	77.466	10.116
	B	51	0.844	86.598	6.231
	C	51	0.735	98.498	4.619
	D	51	1.012	85.142	3.767
	E	51	0.701	72.711	3.774
	F	51	0.650	100.072	6.958
RS620008	A	1	0.679	168.963	5.716
	B	1	-0.072	175.018	5.889
	C	1	1.442	152.451	4.864
	D	1	0.917	154.426	3.902
	E	1	-0.527	177.672	5.945
	F	1	-0.319	173.482	4.391
RS620018	A	128	0.424	75.186	7.724
	B	128	0.380	75.295	3.816
	C	128	0.365	75.992	5.662
	D	128	0.329	62.655	4.227
	E	128	0.419	75.504	8.513
	F	128	0.274	67.068	4.355

Appendix



B. TABLES OF VISCOSITY AND DENSITY COEFFICIENTS

Tab. B.1 Volumetric expressions. List of expressions necessary to calculate the specific volume in Eq. 4.36 (Rowe and Chou, 1970; Kuder, 2011).

Coefficient
$A = 5.916365 - 0.01035794 \cdot T + 0.9270048 \cdot 10^{-5} \cdot T^2 - 1,127.522/T + 100,674.1/T^2$
$B = 0.5204914 \cdot 10^{-2} - 0.10482101 \cdot 10^{-4} \cdot T + 0.8328532 \cdot 10^{-8} \cdot T^2 - 1.1702939/T + 102.2783/T^2$
$C = 0.118547 \cdot 10^{-7} - 0.6599143 \cdot 10^{-10} \cdot T$
$D = -2.5166 + 0.0111766 \cdot T - 0.170552 \cdot 10^{-4} \cdot T^2$
$E = 2.84851 - 0.0154305 \cdot T + 0.223982 \cdot 10^{-4} \cdot T^2$
$F = -0.0014814 + 0.82969 \cdot 10^{-5} \cdot T - 0.12469 \cdot 10^{-7} \cdot T^2$
$G = 0.0027141 - 0.15391 \cdot 10^{-4} \cdot T + 0.22655 \cdot 10^{-7} \cdot T^2$
$H = 0.62158 \cdot 10^{-6} - 0.40075 \cdot 10^{-8} \cdot T + 0.65972 \cdot 10^{-11} \cdot T^2$

Tab. B.2 [Viscosity coefficients v1 to v6. Empirical determined constants to calculate the viscosity of sea water containing NaCl used in equation 4.40 according to (Kuder, 2011).

NaCl
v1 16.222
v2 1.3229
v3 1.4849
v4 0.0074691
v5 30.78
v6 2.0583

Tab. B.3 Viscosity parameter. Parameter I, J and n to calculate the viscosity equation 4.41 (Kuder, 2011).

Index i	I _i	J _i	n _i	Index i	I _i	J _i	n _i
1	0	0	0.513204700	11	2	2	-1.263184000
2	0	1	0.320565600	12	3	0	0.177806400
3	0	4	-0.778256700	13	3	1	0.460504000
4	0	5	0.188544700	14	3	2	0.234037900
5	1	0	0.215177800	15	3	3	-0.492417900
6	1	1	0.731788300	16	4	0	-0.041766100
7	1	2	1.241044000	17	4	3	0.160043500
8	1	3	1.476783000	18	5	1	-0.015783860
9	2	0	-0.281810700	19	6	3	-0.003629481
10	2	1	-1.070786000				

Tab. B.4 Viscosity parameter n^0 . Parameter n^0 to calculate the viscosity equation 4.42 (Kuder, 2011).

Index i	n_i^0
0	1.000000
1	0.9781970
2	0.5798290
3	-0.2023540



C. MORPHOLOGICAL DATA

Tab. C.1 Arm length. Empirically determined arm length [m]. Numbers in brackets are standard deviations.

Arm sample	RS600012	RS619007	RS620008	RS620018
A	0.160	0.115	0.171	0.130
B	0.094	0.132	0.178	0.126
C	0.140	0.138	0.156	0.124
D	0.167	0.138	0.157	0.105
E	0.137	0.110	0.179	0.130
F	0.173	0.135	0.176	0.104
mean	0.145(± 0.029)	0.128(± 0.012)	0.170(± 0.010)	0.120(± 0.011)

Tab. C.2 Number of brachials. Numbers in brackets are standard deviations.

Arm sample	RS600012	RS619007	RS620008	RS620018
A	92	63	99	73
B	50	74	103	70
C	79	78	89	69
D	96	78	90	57
E	77	60	104	73
F	100	76	102	56
mean	82(± 18)	72(± 8)	98(± 7)	66(± 8)

Appendix

Tab. C.3 Body volume. Volume in [cm³]. Numbers in brackets are standard deviations.

Arm sample	RS600012	RS619007	RS620008	RS620018
A	5.17	5.08	5.18	5.13
B	4.95	5.13	5.18	5.11
C	5.15	5.14	5.17	5.11
D	5.18	5.14	5.17	5.03
E	5.14	5.05	5.18	5.13
F	5.18	5.14	5.18	5.02
mean	5.13(±0.09)	5.11(±0.04)	5.18(±0.01)	5.09(±0.05)

Tab. C.4 Body weight. Weight in [g]. Numbers in brackets are standard deviations.

Arm sample	RS600012	RS619007	RS620008	RS620018
A	5.60	5.50	5.61	5.55
B	5.36	5.55	5.61	5.54
C	5.57	5.57	5.60	5.53
D	5.60	5.57	5.60	5.45
E	5.56	5.47	5.61	5.55
F	5.61	5.56	5.61	5.43
mean	5.55(±0.10)	5.54(±0.04)	5.61(±0.01)	5.51(±0.05)

Tab. C.5 Body weight in water. Weight in [g]. Numbers in brackets are standard deviations.

Arm sample	RS600012	RS619007	RS620008	RS620018
A	0.29	0.28	0.29	0.29
B	0.28	0.29	0.29	0.29
C	0.29	0.29	0.29	0.29
D	0.29	0.29	0.29	0.28
E	0.29	0.28	0.29	0.29
F	0.29	0.29	0.29	0.28
mean	0.29(±0.00)	0.29(±0.01)	0.29(±0.00)	0.29(±0.01)



ACKNOWLEDGEMENTS

Prof. Dr. Julian Gutt (Alfred Wegener Institute): My first supervisor, for his valuable support and trust.

Prof. Dr. Pedro Martínez Arbizu (Deutsches Zentrum für Marine Biodiversitätsforschung): My second referee, for his kind willingness to review my work.

Prof. Dr. Antonia B. Kesel (Bremen University of Applied Sciences): My second supervisor, for her support and valuable contributions and her great enthusiasm for my project. As my professor, she has supervised me since the beginning of my biomimetics studies in 2003 and offered me many opportunities to realise my ideas. I owe her a lot.

Prof. Dr. Drik Carl Albach (University of Oldenburg): For his willingness to participate in my defence as a third examining member and representative of the doctoral committee.

Prof. Dr. Albert Baars (Bremen University of Applied Sciences): For his great support in fluid dynamics matters and his valuable ideas and contributions.

Dr. Marc Eléaume (Muséum national d'Histoire naturelle): For his help in identifying the crinoid species.

Prof. Kirby A. Baker (UCLA, Department of Mathematics): For his work on spline interpolation and his kind support.

Prof. Dr. Eize Stamhuis (University of Groningen): For his support and encouragement to write the PhD thesis. Unfortunately, our long distance collaboration was not feasible for me.

Kerstin Beyer (Alfred Wegener Institute): She provided the crinoid samples from the AWI collection.

Prof. Dieter Piepenburg (Alfred Wegener Institute): For his contribution of images of the seafloor.

Dr. Johannes Freitag (Alfred Wegener Institute): For his time and effort in making the computer tomographic scans of the crinoid samples.

Prof. Dr. Claudio Richter (Alfred Wegener Institute): For giving me the opportunity to reduce my contract at AWI for this study.

I would like to thank all the researchers, founders and institutions, organisations and governments that have made this scientific work possible. This project benefits

to a large extent from methods, measurements and results provided by a great community. All the efforts that have been made and all the knowledge that has been gathered contribute to a comprehensive understanding of our world. My thanks also go to a huge group of computer specialists who have invested a great part of their spare time in open source projects to provide an endless list of useful software tools, accessible to everyone without financial interest. I appreciate your immense commitment, your work supports people like me and gives us a chance to realise our ideas.

Special thanks to my family for their endless patience and mental support.



BIOGRAPHY

Nils Owsianowski is a scientist and engineer who completed his bachelor's and master's degrees in bionics. During his studies he acquired an extensive portfolio of programming languages, computer programmes and electronics. His great passion is the fluid dynamics and biomechanics of locomotion and their computer-aided analyses and simulations.

During his studies, Nils Owsianowski already worked on scientific projects in paleontology, forensics and archaeology. After completing his studies, he worked at the University of Applied Sciences in Bremen, where he was involved in the simulation of fish shoals. In addition to various lectures in CAD, FEM, optimisation and statistics, he introduced the module terrestrial locomotion, which he still teaches today after a break.

When Nils Owsianowski got a job at the Alfred Wegener Institute, his field of responsibility changed. From now on, he is responsible for the technical and scientific supervision of underwater robotics in marine biology. This includes the preparation and implementation of polar expeditions, data processing and their publication. In addition to his work at the AWI, he began writing his doctoral thesis on the swimming and Antarctic dispersal of feather stars.

Selection of publications

First author publications

Owsianowski, N., Richter, C. (2021): Exploration of an ice-cliff grounding zone in Antarctica reveals frozen-on meltwater and high productivity. *Commun Earth Environ* 2, 99. <https://doi.org/10.1038/s43247-021-00166-y>

Owsianowski, N. , Nachtsheim, D. , Held, C. , Richter, C. , Steinmetz, R. and Bornemann, H. (2017): Under-shelf ice sampling by ROV reveals specimens of ice-associated crustaceans , XIIth Biology Symposium of the Scientific Committee of Antarctic Research (SCAR) “Scale Matters”, Leuven, Belgium, 10 July 2017 - 14 July 2017.

Owsianowski, N., Kesel, A. (2008): Drag reduction in schooling fish? - a CFD approach. *Comparative Biochemistry and Physiology Part A: Molecular & Integrative Physiology*, Elsevier BV, 2008, 150, S85. <https://doi.org/10.1016/j.cbpa.2008.04.148>

Owsianowski, N. (2007): Finite-Elemente-gestützte bionische Bauteiloptimierung. *Bionik und Nachhaltigkeit – Lernen von der Natur* (2007), ISBN 3503103252

Data publications

Owsianowski, Nils; Richter, Claudio (2020): Glacial dynamics, distribution of cryobenthic algae and fish and a 3D model of the grounding zone of a tidewater cliff in front of Coats Land's coast. *PANGAEA*, <https://doi.org/10.1594/PANGAEA.924822>

Owsianowski, Nils; Schröder, Henning; Maier, Sandra; Richter, Claudio (2019): Shelf ice and sea bed videos of the Remotely Operated Vehicle "Ocean Modules V8 Sii" from the continental shelf of the Weddell Sea during Polarstern cruise PS111. *PANGAEA*, <https://doi.pangaea.de/10.1594/PANGAEA.909258>

Owsianowski, Nils; Held, Christoph; Nachtsheim, Dominik A; Richter, Claudio; Steinmetz, Richard; Bornemann, Horst (2018): Under-shelf ice video footage and hydrographic data from ROV transects at Drescher Inlet. *PANGAEA*, <https://doi.org/10.1594/PANGAEA.892762>

Owsianowski, Nils; Federwisch, Luisa; Kluibenschedl, Anna; Casado de Amezua, Maria del Pilar; Richter, Claudio (2017): Sea-floor videos (benthos) along 12 ROV profiles during POLARSTERN cruise PS82 (ANT-XXIX/9). Alfred Wegener Institute, Helmholtz Centre for Polar and Marine Research, Bremerhaven, *PANGAEA*, <https://doi.org/10.1594/PANGAEA.879283>